Preparation and Characterisation of Poly(ethylene terephthalate) Nanocomposites

Sarah Lindsay Grant

A thesis submitted to the Department of Pure and Applied Chemistry, University of Strathclyde, in part fulfilment of the requirements for the degree of Doctor of Philosophy

October 2011

DECLARATION

ACKNOWLEDGEMENTS

Firstly, I would like to thank my supervisor Dr. John Liggat for all the guidance, support and patience he has shown during the course of my doctorate. In addition I would like to thank my industrial supervisors Dr. Duncan MacKerron and Dr. Simon Mortlock for all their support, guidance and assistance.

I would also like to express my gratitude to the EPSRC and DuPont Teijin Films Ltd. for funding the research and allowing me this opportunity.

I would also like to show my appreciation to several members of staff who have been invaluable not only by providing technical support, but who have always been extremely generous with their time and provided top notch banter! In particular I would like to thank Jim Morrow, John Carruthers, Dr. Ian Rhoney, Dr. Allan Mackintosh, Dr. John Daly and Dr. David Hayward. You guys truly are the Chuck Norris's of the research world!

A special thanks also goes out to everyone from TG521 (or TG315 if we're talking old school!) and beyond, from past and present, whether you're still here plodding away or have moved on, for making this experience what it was. It would never have been the same without you!

Lastly, thank you to my mum, dad, wee sister Hilary and all of my friends who have supported me through my doctorate. A special thank you goes out to everyone who has regularly asked me what I was doing and then had the patience to actually listen to me witter on about it for the following 20 minutes! You know who you are. You have all stopped me going insane with the chemistry! I love you all.

OVERVIEW

Polymer nanocomposites are considered the next generation in polymers due to the belief that the incorporation of a nanoclay into a polymer matrix may enhance properties such as gas permeability, resistance to degradation and chemical attack or elastic modulus. Numerous complications however during the research and development stages have resulted in little breakthrough and production of a polyester nanocomposite on a commercial scale in particular is considered somewhat of a 'holy grail'. Issues vary considerably at each stage of production and include: ensuring compatibility between the nanoclay and the monomer or polymer, degradation of surface modifiers during synthesis and processing, incorporating the nanoclay at a desirable loadings, brittleness of polymer film on melt processing and clarity in the final polymer nanocomposite film. As a result of these issues there has been a rapid rise in the number of polymer nanocomposite research groups in the past few decades, a larger number of which are on this last crusade to find the holy grail in the field of polymer science.

An investigation into nanoclay and monomer compatibility was the first study performed within this thesis as compatibility was crucial in ensuring nanoclay exfoliation and intercalation. If exfoliation and intercalation were not successful in the liquid monomer there would be little point in continuing the *in situ* polymerisation procedure method with the aim of preparing a polymer with nanoclay dispersed throughout the matrix. The study focused on a range of commercially available, surface modified nanoclays marketed under the trade names Cloisite® and Garamite®. All surface modifiers were based upon an alkyl ammonium; however a range of surface hydrophobicities were created through varying the structure of the alkyl chains and the modifier surface concentration. The dispersing agents were selected in order to examine the influence of permittivity and polarity, both of which were observed to influence exfoliation to a substantial degree. Permittivity was as a variable to explore as it influences the ability of a dispersant to shield or dampen the attractive interplatelet forces which would result in the reformation of tactoids. A high permittivity related to an effective shielding ability. Polarity was observed to give an

indication of the extent of interactions possible with the nanoclay surface and/or surface modifiers through interactions such as hydrogen bonding.

Subsequently, the *in situ* polymerisation method was investigated in order to prepare a series of poly(ethylene terephthalate) based nanocomposites. Foaming due to the degradation of the organic modifiers was observed as expected during small scale laboratory tests, and as a result an antifoaming agent was incorporated in order to manage the reaction more effectively. After a series of trials at Strathclyde, poly(ethylene terepthalate)-Garamite® nanocomposites were successfully prepared at nanoclay loadings of 0.5% w/w and 1.0% w/w at DuPont Teijin Films' research and development facility at Wilton. The incorporation of nanoclay at loadings higher than 1.0% w/w was unviable as the foaming became uncontrollable. In addition, the polymer film exhibited an increase in brittleness during melt processing to uniaxial film, and as such a nanoclay loading higher than 1.0% w/w would again have been unfeasible.

Characterisation of the polymer nanocomposites by ^{13}C NMR, ^{1}H NMR and FTIR confirmed the Garamite® had no effect on the polymers structure during synthesis. Determination of the molar mass however through both GPC and intrinsic viscosity measurements illustrated the degradative effect of the Garamite® during melt processing within an oxidative environment. In addition the nanoclay content dispersed within the polymer was not observed to be directly proportional to the extent of degradation and decrease in molar mass.

Characterisation of the Garamite® nanoclay during a three month exchange at the University of Ottawa allowed the nanoclay group and identity to be determined. Previously, Garamite® had been suspected to consist of both a plate-like and a fibrous aluminosilicate nanoclay. The predominant nanoclay however was identified as sepiolite, a fibrous aluminosilicate belonging to the hormite group.

A study into the crystallisation behaviour of the polymer and polymer nanocomposites illustrated the Garamite® acted as a heterogeneous nucleating agent. With respect to the

neat polymer, crystallisation of the amorphous chip was hampered due to a high molar mass which caused a decrease in chain mobility. The nucleating ability of the Garamite® however was observed to offset the molar mass effects and act as the dominant influence over the crystallisation process. Experimentally, the nucleating ability of the Garamite® was observed through the shift in the crystallisation peak on cooling. This illustrated the polymer crystallites were able to melt and re-crystallise before the maximum temperature at which a crystallite could exist in the melt was reached. In order to investigate the mode of crystallite growth the crystallisation kinetics were determined for both the amorphous chip and uniaxial film. The modified Avrami model in particular illustrated the differing crystalline growth morphologies for the pure polymer and polymer nanocomposites. It was illustrated the pure polymer increased in dimensions from a disc-like to spherulitic crystalline morphology. The polymer nanocomposites however both exhibited sheaf like growth, illustrating heterogeneous nucleating ability of the sheaf-like fibrous sepiolite nanoclay. In contrast the Ozawa model illustrated that the mode of crystalline growth for the pure polymer did not alter as a result of melt processing and suggested a more sheaf-like growth morphology. The polymer nanocomposites were also suggested to decrease in crystalline dimensions from spherulitic to disc-like lamellae. It was concluded that the modified Avrami model best described the crystalline growth morphologies of the polymer and polymer nanocomposites under study due to knowledge of the sepiolite nanoclay structure.

With respect to the thermal degradation behaviour, the presence of the Garamite® was observed to have no effect on the thermogravimetric and energetic degradation of the bulk polymer matrix. Only the onset of energetic degradation was effected and was observed to decrease. It was suggested that the onset of degradation indicated the thermal stability at the polymer and nanoclay interface, and that the Garamite® was accelerating degradation in some manner. In addition, an investigation into the thermal degradation kinetics also suggested that the Garamite® accelerated degradation. An examination of the Arrhenius parameters also suggested that the effect of the Garamite® on the kinetics was not proportional to Garamite® loading, and that there appeared to be a limit to the effect of the Garamite® on degradation. An investigation into the thermo-oxidative degradation

behaviour illustrated that the systems which possessed the highest maximum temperatures of degradation also possessed the highest molar masses. As a result the samples possessed a high melt viscosity which slowed oxygen diffusion and delayed the degradation process. Samples which contained the Garamite® nanoclay were also observed to possess a higher maximum temperature of degradation due to a further impedance of oxygen diffusion. It was noted at the highest Garamite® loading that the barrier effect was counteracted within the uniaxial film samples, which suggested the Garamite® accelerated the thermo-oxidative process. Stabilisation was also observed however through delays in the energetic onset of degradation. No effect on the degradation of the bulk polymer matrix was observed however, indicating that the degradation of the bulk polymer was neither inhibited nor catalysed, and that only the physical transport of the oxygen and small organics was affected. These competing effects were observed in the degradation kinetics. The Arrhenius model and ASTM 1641 illustrated the catalytic effect of the Garamite®, whereas the physical barrier effect was observed through the Kissinger model and ASTM E698.

The final study provided insight into the thermal degradation products and mechanisms though thermal volatilisation analysis. The primary degradation products were identified as carbon monoxide, carbon dioxide, acetaldehyde, water and benzaldehyde. It was observed during degradation of the polymer nanocomposites that the evolution of the minor products ethene and acetylene was inhibited. This was attributed to some degree to the barrier effect by the nanoclay which slowed the transport of the volatiles through the polymer matrix. Mass spectrometry also revealed that the presence of the Garamite® drives the production of acetaldehyde during degradation, and therefore alters the degradation mechanism of poly(ethylene terephthalate). It was suspected that the polymer nanocomposite undergoes a heterolytic degradation mechanism as an increase in acetaldehyde was observed without an accompanying increase in carbon dioxide. Finally, the catalytic activity of the Garamite® was attributed to the Brønsted acid sites on the nanoclay which were predominantly produced during the degradation of the ammonium surface modifiers through the Hoffman elimination. The presence of Brønsted acid sites was significant as they allowed the polyester to undergo acid catalysed ester hydrolysis when free protons were available.

TABLE OF CONTENTS

Appendices on Disc

LIST OF FIGURES

CHAPTER 1 INTRODUCTION

CHAPTER 2 INSTRUMENTAL AND THEORY

CHAPTER 3 EXPERIMENTAL

CHAPTER 4 DISPERSION EFFECTS

CHAPTER 5 CHARACTERISATION

CHAPTER 6 CRYSTALLISATION

CHAPTER 7 DEGRADATION

LIST OF TABLES

CHAPTER 4 DISPERSION EFFECTS

CHAPTER 5 CHARACTERISATION

CHAPTER 6 CRYSTALLISATION

CHAPTER 7 DEGRADATION

CHAPTER 1 INTRODUCTION

1.1 CLAY MINERALS

The clay mineral group is classified as belonging to the hydrous phyllosilicates family (stemming from the Greek word *phyllon* which means leaf) and as such they are commonly described as sheet silicates. They possess distinctive parallel sheets of silicate tetrahedra, and although the major octahedral substituent is generally assumed as aluminium it can vary dramatically due to isomorphous substitution and environmental conditions on formation.

1.1.1 ALUMINOSILICATES

1.1.1.1 MONTMORILLONITE

Clay minerals such as montmorillonite belong to the smectite group and exist in distinctive platelet structures. Montmorillonite platelets are planar crystalline sheets of octahedrally co-ordinated metals sandwiched between tetrahedral silica layers. There are various types of platelet structure and the simplest contains a single tetrahedral and octahedral sheet (1:1) as in kaolinite. Montmorillonite clays however are 2:1 layered aluminosilicates, and have the general formula $[M_x[Al_{4-x}Mg_x](Si_8)O_{20}(OH)_4]$. M_x is a counter-ion which is present to balance the increase in negative surface charge if isomorphous substitution has occurred, and in the case of montmorillonite is usually sodium or calcium. Montmorillonite platelets are generally between 70-150 nm in length and approximately 1 nm in thickness.[1, 2]

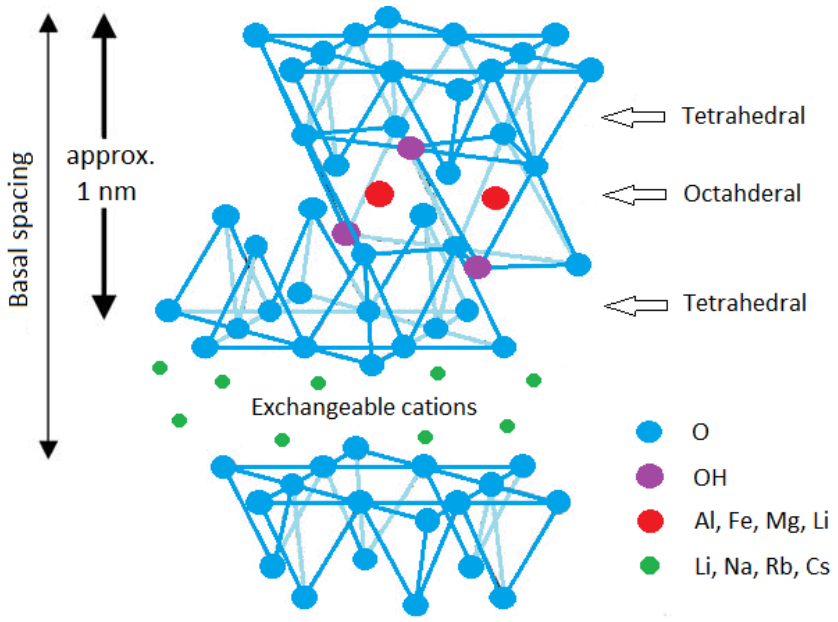

Figure 1 Reproduced illustration of the montmorillonite sheet structure[3]

Grimshaw *et al*. described the bonding within the silicate sheet as both ionic and covalent in character.[4] Bond directionality and electron sharing are present suggesting a covalent character, however silicon is also considered in the oxidised Si^{4+} state, with electron transfer from the O^{2-} ions. In addition within the silicate sheet not all of the oxygen's electrons are used in bonding to the silicon. Those which are not bridging (or basal) electrons still possess an electron which can either coordinate to the octahedral metal or remain to produce the platelets' negative surface charge. Within the octahedral layer there are various metal cations which can be present such as Al^{3+} and Mg^{2+} mentioned above, and the metal cations present determine the octahedral network produced within the platelet. The networks within montmorillonite are described as dioctahedral when the majority of sites are occupied by trivalent cations (i.e. Al^{3+}), and trioctahedral when sites possess primarily divalent cations (i.e. Mg^{2+}). The octahedral layer also possesses hydroxyls which can be positioned in a trans or cis formation with respect to the central cation.

Collectively, montmorillonite platelets exist in flocculated structures. The structure of the platelet flocculate is determined by electrostatic interactions which may be altered by a variety of factors. On formation, the most commonly observed flocculates in literature are

tactoids, whereby the platelets form various stacked arrangements.[2] The stacked book house structure is considered the most stable tactoid structure due to a stabilising attraction between the negative face and positive edge charges. Further stability may be imparted if the platelets exist in a card house structure which removes all repulsive forces.[5] Lambe and Whitman described how platelet flocculation on formation differs in salt and fresh waters.[6] During salt water flocculation the platelets preferentially sediment in a parallel fashion due to a high concentration of ions allowing an electrical double layer between individual platelets. This electrical double layer dampens interfacial repulsions favouring a book house type arrangement. Fresh water environments which lack the presence of salts tend to favour a card house structure which minimises the interfacial repulsions to the greatest degree.

Figure 1.2 Illustration of an individual platelet with surface and edge charges, an individual tactoid with hydrated counter-ions, card-house structure and book-house structure.

As previously stated, electrostatic interactions are one of the most substantial influences for clay microstructure. Electrostatic interactions are to some degree determined by the extent of isomorphous substitution within a clay mineral, itself determined through the ion content during formation and altering environmental conditions post-formation. As such clay minerals exist in isomorphous series with a range of available ion contents within one general structural form. Isomorphous substitution is also a process which may occur within both octahedral and tetrahedral layers, however in the majority of literature concerning montmorillonite substitution is reported to occur predominantly or only within the octahedral layer.[7-11]

Montmorillonite is an excellent example of a clay mineral isomorphous series and within the octahedral layer may contain varying proportions of aluminium and magnesium. Isomorphous substitution is a process in which an ion of similar size substitutes for an ion of a lower charge within the platelet structure. In the case of montmorillonite Mg^{2+} substitutes for Al^{3+}, and in turn Fe^{+} can substitute for Mg^{2+}. With respect to alterations in electron density, the substitution of an ion for one of a lower valency is the equivalent to adding an additional electron to the structure. however it has been observed that the oxygen atoms immediately adjacent to the substitution increase in electron density no more than 4%.[8] This indicates the majority of the additional charge is dispersed through the platelet. Due to the addition of counter-ions however there is no difference in the overall platelet charge.

1.1.1.2 SEPIOLITE

Sepiolite is a hydrous phyllosilicate which belongs to the hormite group and possesses a fibrous structure which has the general formula $[(OH_2)_4(Mg,Al,Fe)_5(OH)\cdot 2Si_8O_{20}]\cdot 4H_2O$.[12] Sepiolite is classified as a phyllosilicate due to a continuous tetrahedral sheet throughout its structure, however it lacks the continuous octahedral layer characteristic of montmorillonite. As a result the tetrahedral layer contains inversions at a general width of three pyroxene-type units ($(X,Y)_4O_6$).[13] These inversions along the Si-O-Si bonds result in the formation of regular channels or pores throughout the length of the fibre through the linking of individual tetrahedral sheets with each inversion resulting in a new octahedral section.[13] Counter-ions may again be present where there is isomorphous substitution however sepiolite dominantly contains magnesium within the octahedral layer.[10] The low extent of isomorphous substitution is as a result reflected through a low ion exchange capacity of between 5 – 40 meq/100g.

As the octahedral sheet is discontinuous the outer cations within the unit will be charge balanced by co-ordinated water molecules. Any remaining uncoordinated oxygens will be charge balanced by hydrogen ions, water and to a small extent other exchangeable cations. The octahedral cations may vary as for montmorillonite however the octahedral cations

within sepiolite are predominantly magnesium with a maximum of 10% aluminium.[14, 15]

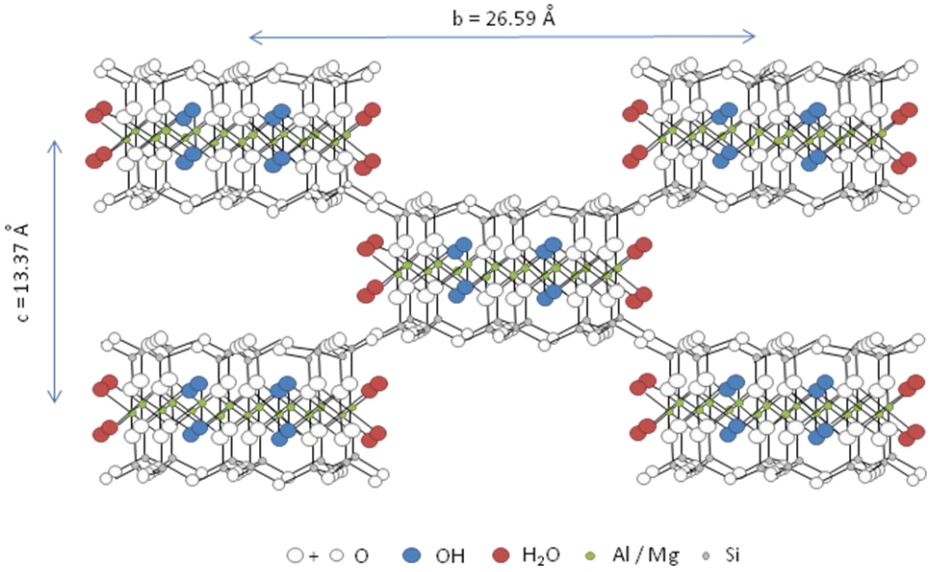

Figure 1.3 Reproduced illustration of the sepiolite unit structure[14]

1.1.2 SORPTIVE PROPERTIES

The ability of a nanoclay to absorb species and form electrostatic interactions determines to what extent it can be surface modified by organic molecules. It also determines to what extent a nanoclay surface may be tailored for particular applications and therefore its adaptability. Within both montmorillonite and sepiolite, organic molecules may form electrostatic interactions at unprotonated oxygens within the silica tetrahedral layer and Al^{3+} and Mg^{2+} ions at platelet edges or fibre channels. Channel size will be an additional factor in sepiolite absorptivity, and varies due to the polydispersity of the fibres. Typically, sepiolite contains mesopores of approximately 45 Å in diameter and micropores of 15 Å and may account for up to 50% of the surface area. It is therefore obvious that the surface area available to a sorbate molecule will depend upon its own physical parameters such as size, shape and polarity. Generally it is only ions and polar organic molecules which enter the fibre channels, and non-polar organic molecules and gases remain on the fibre surface. Non-polar organic molecules can only interact with the fibres through van der Waals forces, although a small amount of nanoclay mediated hydrogen bonding may occur due to

silanol groups. Polar organic molecules may also coordinate directly to exposed octahedral ions within the channels in a similar fashion to counter-ions or coordinated water molecules. The surface modification of a nanoclay involves the exchange of counter-ions such as sodium for organic cations. Generally, the role of the counter-ions is to balance the negative face charge present as a result of isomorphous substitution. The number of counter-ions at a platelets surface is therefore representative of the extent of isomorphous substitution within that platelet. The charge balancing role of the counter-ions also allow the formation of an electrical double layer between platelets which facilitates stacking and tactoid formation.

In order to incorporate a nanoclay into a material the compatibility of the nanoclay surface must be tuned to its desired environment. This is often achieved through increasing the organophilicity and hydrogen bonding capability of the platelet surface through surface modification.[16, 17] Commonly the surface modifier is similar to a surfactant in morphology. The ionic head groups tend to be ammonium or phosphonium ions, with the organic substituents consisting of alkoxy groups or long chain alkyl tallows. The extent of an organic modifier to absorb onto a nanoclay surface is largely dependent upon the number of counter-ions and therefore extent of isomorphous substitution within the structure. As previously stated, sepiolite has a relatively low cation exchange capacity of between 5 – 40 meq/100g. Montmorillonite, in comparison, is far better suited for surface modification as it has a relatively high cation exchange capacity of 70 - 120 meq/100g.[18] The cation exchange capacity is determined directly by the extent of isomorphous substitution within a nanoclay, and describes the quantity of cations a surface can accommodate with relation to the accumulated negative charge. Montmorillonite will therefore absorb a greater number of alkyl ammonium anions onto its' surface, leading to a better surface coverage and alteration of surface chemistry.

In addition, the surface modifier not only improves compatibility but increases the intergallery spacing, increasing the intercalative and/or exfoliative ability of the nanoclay through increasing the ease at which a material may penetrate the gallery spacings. The mode of modifier packing on the platelet surface may therefore have a significant impact

on the ability of the nanoclay to intercalate/exfoliate. It will be affected by both the cation exchange capacity of the nanoclay and the structure of the organic modifier. Larger CEC values will force modifiers into more structured, vertical arrangements, whereas low CEC values may enable the tallows to lie along the platelet surface if the chain length allows. The degree of organisation within the alkyl chains will also be dependent on temperature, with a more disorganised state existing as temperature increases.[16] A more structured modifier arrangement may or may not encourage easier exfoliation of the platelets depending on both the modifier arrangement and material in which it is to be exfoliated.

1.1.3 RHEOLOGICAL PROPERTIES

If a nanoclay is exfoliated efficiently in a liquid there is potential for the suspension to gel. This is due to the formation and extension of nanoclay network structures throughout the medium. Various degrees of structure formation have been observed in literature, and it is more aptly described as a series of potential structures rather than discrete structural types. Stable suspensions range between stable colloids in which there are no interparticle interactions to gelled systems which possess fully flocculated structures. Unstable suspensions may range from those where the nanoclay is completely sedimented to systems in which there is partially formed floccs. The formation of structure within a system is dependent on the solvent–platelet and platelet-platelet interactions. In addition if the nanoclay is surface modified this must also be taken into account as the modifier has the ability to both enhance or remove structure formation depending on the systems under study.[5]

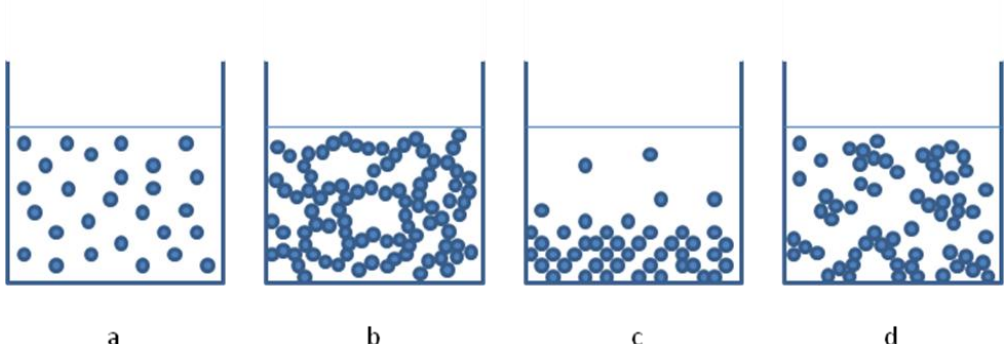

Figure 1.4 Reproduced illustration of the end members in the structural formations series within stable and unstable suspensions. Suspension types are; a, stable with no interparticle interactions; b, stable with extensive structure formation; c, unstable sedimented; d, unstable with partial structure formation[19].

Structures within montmorillonite suspensions are based upon the formation of card-house or book-house structures. The structures are formed due to the favourable attractive interactions between the negatively charged platelet surfaces and the platelet edges. The edge charges are pH dependent; the edge will possess a negative charge at an alkaline pH due to unprotonated oxygen anions, and a positive charge at acidic pH due to protonation.[20] Sepiolite fibre suspensions however are not well characterised within the literature and structure formation is suggested to be a result of hydrogen bonding interactions between the silanol functionalities.[21] With respect to structural formations sepiolite is suggested to form some type of matchstick structure, which would have a similar two-dimensional illustration to that of the card-house structure of montmorillonite platelets within figure 1.2.

The structures which are formed may be observed through the rheological analysis of the suspensions. Viscosity profiling, for example, examines the change in viscosity on increasing shear and consequently may provide valuable insights not only with regards to the formation of interplatelet structure but also its breakdown. Typically, suspensions follow the shear thinning behaviour as described. At low shear rates the particles have sufficient time to align with the flow direction and a greater degree of interaction will therefore occur between the platelets and the medium, resulting in a higher viscosity. At higher shear rates the platelets will not have sufficient time to align themselves with the flow direction, and as a consequence viscosity building platelet-medium interactions will be smaller in number, resulting in a lower observed suspension viscosity.

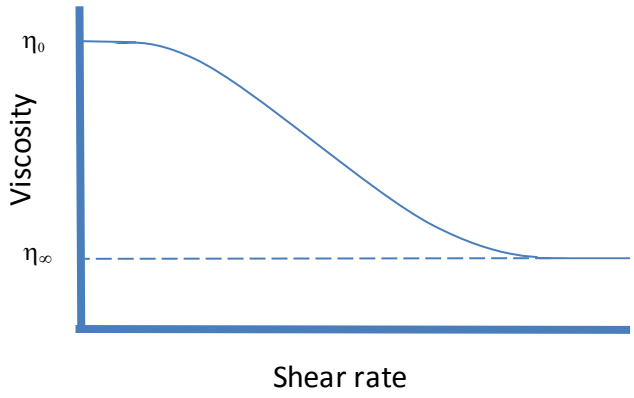

Figure 1.5 Example of an ideal shear thinning viscosity profile.

Particle size and shape have also been observed to influence viscosity. Generally larger and bulkier particles (ie those which are less geometrically uniform) will occupy a greater phase volume within a suspension, and as a consequence the suspension viscosity increases.[22] It is also observed through the aspect ratio that more uniform particles also occupy a greater phase volume and hence increase in viscosity.

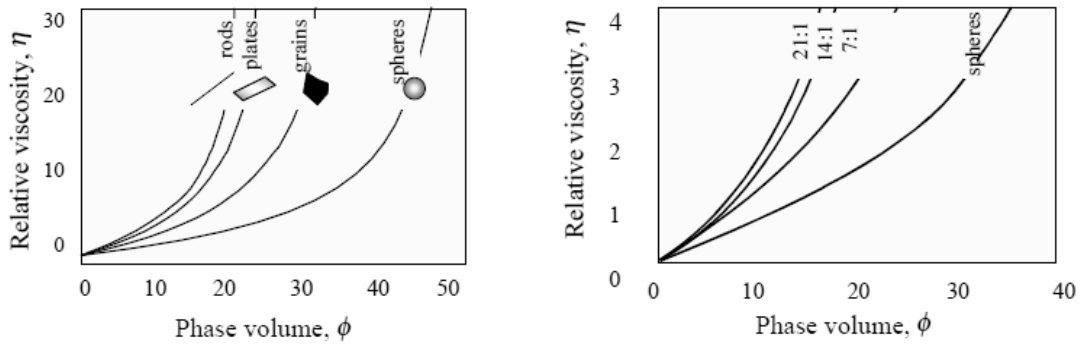

Figures 1.6a and 1.6b The effect of particles size and aspect ratio on phase volume and resulting suspension viscosity. [22, 23]

1.1.4 APPLICATIONS

The rheological and sorptive properties of montmorillonite and sepiolite have allowed them to be employed in a vast number of applications within many different industrial settings. Nanoclays are now widely known and employed, for example, as catalytic supports. During the Heck reaction, the coupling of aryl halides and styrene molecules yields stilbenes in the presence of a palladium catalyst. A nanoclay support not only allows the palladium to leach out into the solvent and catalyse the reaction but also re-adsorbs the catalyst after the reaction has run to completion.[24, 25] This is an extremely efficient and simple method in which to apply and extract a catalyst, without need for complicated purification methods. Nanoclays may also be employed during the pelletizing of a wide range of materials from iron ore to animal foodstuffs. This is due to its extremely efficient ability to extract moisture.[26] In addition nanoclays may even be employed in nuclear waste management. Mixtures of smectite and sand are often employed as protective buffer layers between waste canisters to minimise the leeching of radioactive materials into the

surrounding environment.[27] There are numerous other current and potential applications for nanoclays, for example:

Pesticide industry	carrier for herbicides and insecticides
Chemical industry	catalytic supports, filtration, anti-settling agent, pelletizing
Cosmetics industry	filler, pigment supports
Petrochemical industry	drilling fluids, thickening/thixotropic additives
Building industry	foundry mouldings, cement/mortar additives

1.2 POLY(ETHYLENE TEREPHTHALATE)

1.2.1 GENERAL PROPERTIES

Poly(ethylene terephthalate), PET, is a step-growth polymer which can be formed from a variety of monomers. The most basic monomers are ethylene glycol and terephthalic acid which produce water as the condensation by-product.

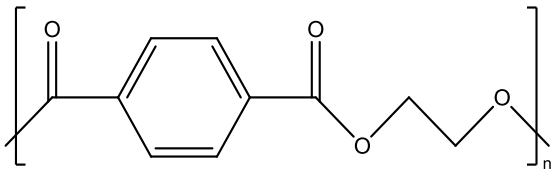

Figure 1.7 Repeat unit of poly(ethylene terephthalate)

PET is a linear semi-crystalline polymer, with a glass transition temperature between 75 – 80°C and crystalline melting region around 250°C. It is also a thermoplastic polymer, and can be re-melted once prepared and re-moulded or drawn into films. This ability to

recycle the material repeatedly is one of PET's most valuable qualities, and is due to the absence of curing during polymerisation.

The molar mass of the PET chains will vary depending on the desired application. Low molar masses are generally used in the film and fibre industries, whereas a high molar mass polymer is more desirable in packaging for items such as bottles. The molar mass has a direct influence on the crystallinity of the polymer, as smaller chains crystallise at faster rates. Crystallisation can be controlled however through processing techniques such as biaxial orientation, which imparts a controlled level of crystallinity and morphological structure to a polymer film during film production.

1.2.2 SYNTHESIS AND CATALYSIS

1.2.2.1 ESTERIFICATION

The synthesis of PET is a two-step process consisting of an esterification reaction followed by a polycondensation reaction. There are two esterification routes which are available and both lead to the preparation of bis-hydroxyethyl terephthalate oligomers. Direct esterification involves terephthalic acid and ethylene glycol, and water is produced as the condensation product. It is performed under temperature and pressure (230 – 255°C, 3.675 atm) and requires no catalyst. Transesterification however employs a terephthalate derivative, most commonly dimethyl terephthalate which forms a methanol condensation product. It also requires a catalyst which is commonly a metal acetate. Calcium acetate is the most common catalyst employed in trans-esterification, and is preferable at the laboratory scale compared to other transition metal acetates such as zinc or manganese. Initially the alkoxy group of the catalyst acts as a nucleophile which facilitates the formation of an anhydride. An alkoxy exchange then occurs resulting in the deprotonation of ethylene glycol, and hence encouraging the nucleophilic attack of the anhydride.

Although transition metal acetates are more efficient catalysts they also require an extremely efficient removal of reaction by-products due to their additional ability to

catalyse de-esterification reactions. As a result they produce a more thermally sensitive polymer are therefore generally only used in industrial scale preparations.[28] In addition the exact mechanism of transition metal acetate catalysis is still under debate, however it has been suggested that the anion either acts in the same manner as its calcium based analogue or the metal acts as an electrophile with respect to the carbonyl oxygen as illustrated in figure 1.9.[28, 29] For zinc-based catalysts it has also been demonstrated that both of these mechanisms may be present.[29] The greater efficiency of the transition metal catalysts may then be attributed to either a steric influence during the initial dissociation and solvation of the metal cations, or an enhancement of interaction between with the glycol due to a concerted mechanism not available to the alkaline metals.

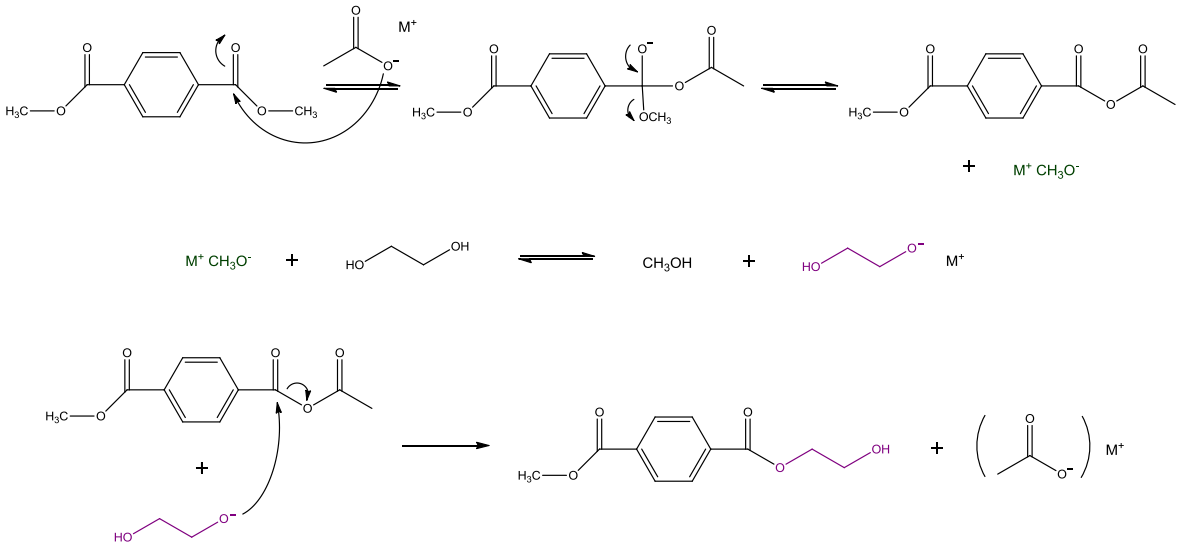

Figure 1.8 Alkali-metal catalysed trans-esterification mechanism of dimethyl terephthalate and ethylene glycol

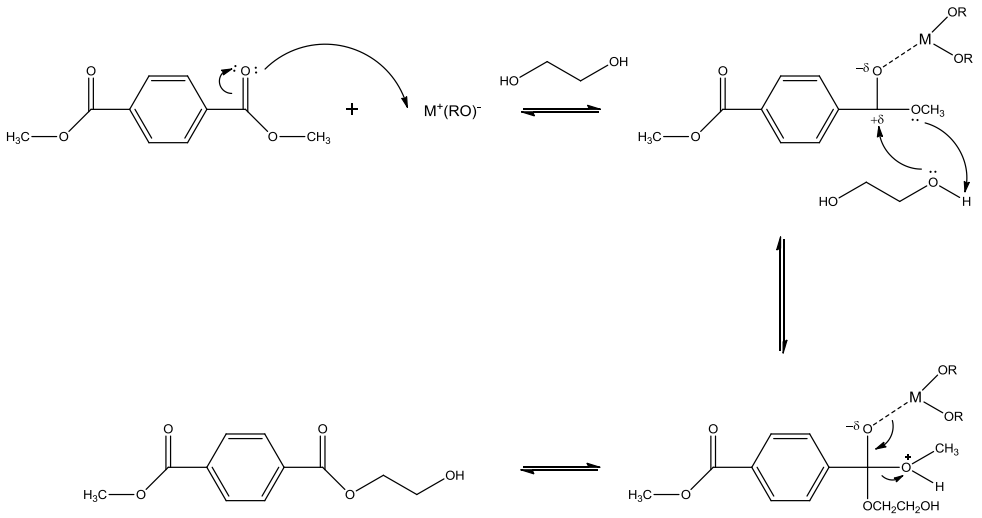

Figure 1.9 Transition metal catalysed trans-esterification mechanism of dimethyl terephthalate and ethylene glycol

1.2.2.2 POLYCONDENSATION

The polycondensation step polymerises the bis-hydroxyethyl terephthalate oligomers into polymeric chains, and is typically performed under vacuum and temperatures of 270 - 290°C.[30, 31] Transition metal oxides and alkoxides are the most commonly employed catalysts, an example of which is antimony trioxide. Initially, the antimony trioxide will form antimony glycolates with excess ethylene glycol. Polycondensation then proceeds through the nucleophilic attack of the carbonyl carbons within the bis(2-hydroxyethyl) terephthalate oligomers.[32] It is the formation of the antimony glycolate capped oligomers which drives the polycondensation reaction through a higher reactivity (and therefore lower activation energy) than the hydroxyethyl end capped oligomer.[32] Antimony trioxide is a frequently employed catalyst as it has a low tendency to catalyse de-esterification and side reactions whilst possessing a relatively high catalytic activity.[32] In contrast to many other transition metal catalysts and does not taint the final product colour. Titanium based catalysts possess the highest catalytic activity of any polycondensation catalysts currently used, however suffer the drawback of catalysing de-esterification reactions.[33] It is suggested that the enhanced ability of the titanium to catalyse de-esterification reactions is due to its ability to accept electron density from the lone electron pairs within the carboxyl group. As a consequence the acidity of the α-methylene protons increases which facilitates a 1,2 internal elimination mechanism to form carboxyl and vinyl ester moieties.[30]

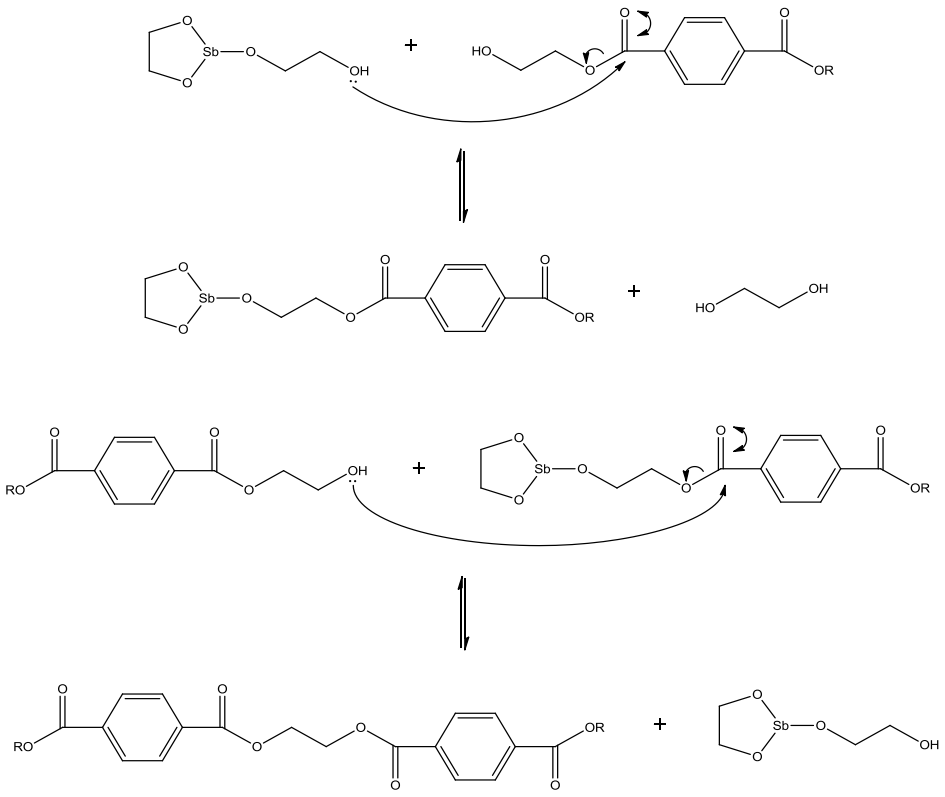

Figure 1.10 Polycondensation mechanism of bis (2-hydroxyethyl) terephthalate catalysed by antimony glycolate

1.2.2.3 SIDE REACTIONS

The most prevalent side reaction during the synthesis of PET is the formation and subsequent incorporation of DEG into the polymer backbone, with the extent of incorporation determining the effect on final polymer properties. It has been quoted that for every percentage increase in DEG concentration there is a 5°C decrease in the thermal stability.[34] It is therefore imperative that formation of DEG is prevented in any manner possible.

DEG segments are known to form through etherfication (or dehydration) reactions between the hydroxyl groups of ethylene glycol and bis-hydroxyethyl terephthalate. The etherfication reaction is acid catalysed in the following manner:

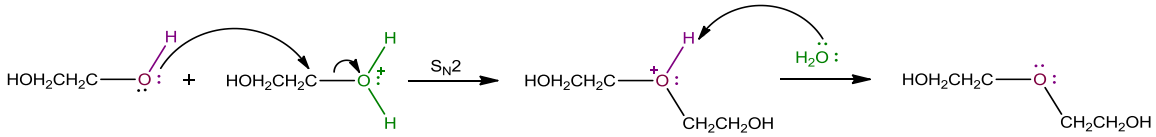

Figure 1.11 Acid-catalysed etherfication mechanism of ethylene glycol[35]

The most critical stage for DEG formation is dependent on the synthetic route however there is opportunity for DEG formation at either stage during polymerisation.[36] Direct esterification routes generally yield higher DEG contents due to the protons released from the terephthalic acid monomers. As the protons possess a catalytic effect up to 80% of total the DEG content may then be formed within this initial stage.[37] Transesterification routes therefore tend to yield lower DEG contents and the polycondensation step is critical.[34] In addition catalytic choice also possesses a significant influence in DEG formation and the least acidic catalysts are observed to lead to the formation of the lowest DEG content. Calcium acetate and antimony oxide for example have been determined as most inhibitive catalysts with respect to DEG formation.[38]

Another major side reaction which occurs during reprocessing leads the discolouration of PET. There is still much debate over the exact cause of the discolouration and little evidence to support or refute the claims of various authors. Yoda *et al*. has previously suggested that the discolouration is due to crosslinking reactions between the vinyl esters and aryl segments. This assumption was made as discolouration was observed in conjunction with an increase in the rate of gelation which would suggest the formation of polyene and conjugated aryl species.[39] Edge has also reviewed the current literature but was less specific suggesting the species responsible for discolouration rose as a result of the hydroxylation of the aromatic ring and the formation of vinyl esters.[36] Other authors have suggested the discolouration is due to the accumulation of acetaldehyde within the degrading matrix. It has previously been proven that acetaldehyde is a major degradation product during PET degradation in both thermal and thermo-oxidative environments.[35, 40, 41] The predominant pathway for acetaldehyde formation is through the degradation of backbone segments which have been re-formed during the trans-esterification of vinyl esters. It is also suggested to form during the degradation of dioxane

or 2-methyl-1,3-dioxolane due to excess ethylene glycol within the matrix or DEG segments within the polymer backbone.[36]

1.2.3 CRYSTALLINE STRUCTURE

PET chains are fairly rigid due to the presence of aromatic rings and carboxylate groups, with flexibility imparted only by the segments originating from the glycol. The rigidity is attributed to the near planarity of the conjugate system which produces a repeat distance of 10.75 Å, close to the calculated distance of 10.9 Å for a completely planar chain.[42, 43] It also increases the ease at which the polymer chains crystallise through maximising the probability of favourable chain alignment. With regard to bonding forces, intermolecular distances suggest there are few strong intermolecular forces apart from Van der Waals. Daubeny *et al.* investigated the cohesion energies and melting behaviour of several structurally different polymers in order to assess the intermolecular bonding in PET.[42] It was determined that the cohesion energy of PET chains was only slightly higher than that observed for aliphatic polymers, and therefore the aromatic rings were considered to contribute little to intermolecular bonding. A melting point comparison between PET, other aliphatic polyesters and nylon however highlighted a higher melting point for PET, which was attributed to a greater rigidity in structure due to the presence of the aromatic rings.

PET also has a triclinic crystal structure, where the crystal dimensions are described by vectors which are of unequal length and are non-orthogonal. The dimensions of a PET unit cell are as follows: a = 4.56 Å, b = 5.94 Å, c = 10.75 Å, $\alpha = 98.5^{\circ}$, $\beta = 118^{\circ}$, $\gamma = 112^{\circ}$.[42]

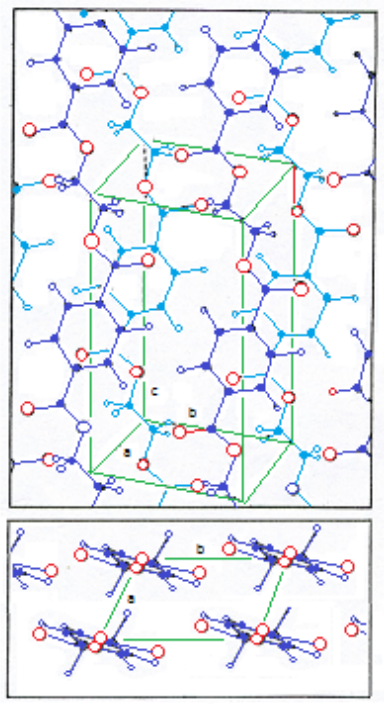

Figure 1.12 PET crystal structure reproduced from Werner. Above: Projection along the 010 plane. Below: projection along the c axis. Carbon atoms are represented as large black dots, hydrogen atoms as small black dots and oxygen atoms as large open dots.[44]

1.2.4 PROCESSING: FILM MELT EXTRUSION[44-47]

PET is an ideal polymer for the film manufacturing industry due to the combination of a variety of distinctive qualities. A selection of the attributes which contribute to the invaluable nature of PET include: a well defined glass transition and crystalline melt temperatures, can be easily synthesised to the moderate molar masses required for melt extrusion and the formation of high strength films, possesses a regular, linear and ordered structure which facilitates chain orientation and thermal stability, and possesses an inherent chemical structure which allows for the efficient recycling of scrap or waste material generated during processing.[48]

The film drawing process imparts a controlled degree of crystallinity and orientation within the polymer which is otherwise considered an unordered two phase matrix of crystalline and amorphous domains. Biaxial drawing at the most basic level may be considered as four separate processes: melt extrusion and quenching, drawing in the machine or longitudinal

direction, drawing in the transverse direction and heat setting. Various other auxiliary treatments may also be included at various stages during the extrusion and drawing process depending on the desired film application. Some examples of common treatments are in-line coatings, electrical discharge and etching which may impart an increased degree of slip control, weatherability, anti-static or barrier properties.

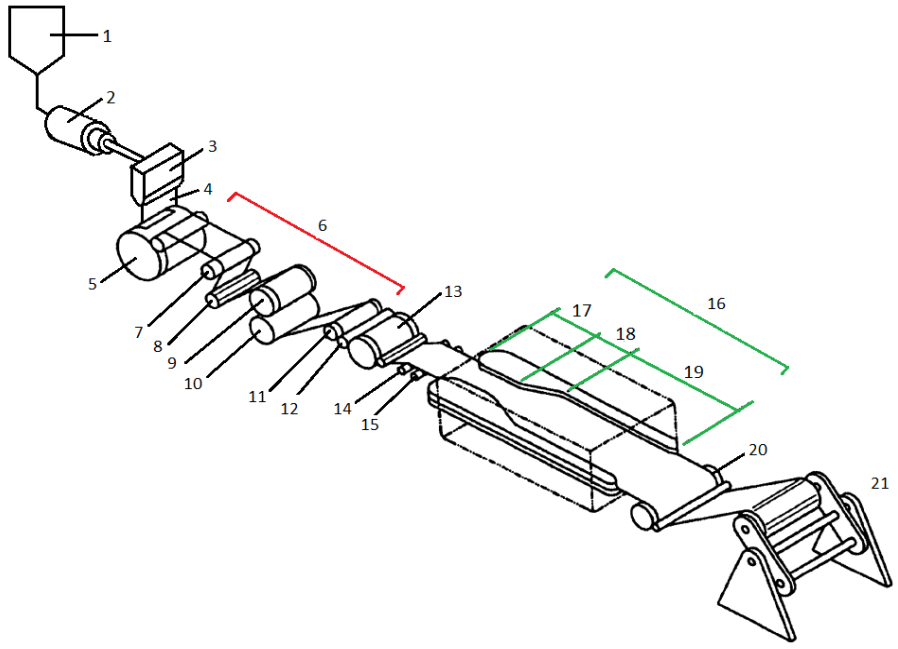

Figure 1.13 Adapted illustration of the melt extrusion process for polymer film. Section parts are as follows: 1 hopper, 2 extruder, 3 slot die, 4 slot die output, 5 chill roller, 6 stretching section for machine direction orientation, 7 and 8 idler rollers, 9 and 10 pre-heat rollers, 11 slow roller, 12 fast roller, 13 roller, 14 - 15 tandem idler rollers, 16 lateral stretching section transverse direction, 17 pre-heat, 18 stretching or draw section with tenter clips, 19 annealing section, 20 chill roller for biaxial film, 21 spools.[49]

During melt extrusion the molten (pre-dried) polymer is extruded through a slotted die and quenched onto a water-chilled cooling drum in order to form polymer film in an unorientated, amorphous state. The quenching process must be efficient as if the temperature of the drum is too high or the cooling rate too slow crystallisation will occur which may render the film brittle and hence unable to undergo further processing.

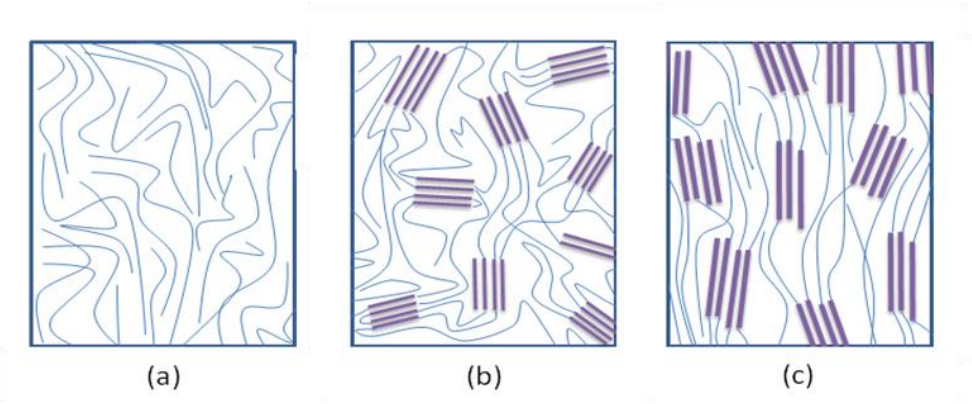

Figure 1.14 Illustration of (a) amorphous, randomly orientated polymer film, (b) semi-crystalline polymer film in which the lamellae are randomly oriented and (c) semi-crystalline polymer film in which the lamellae are linearly orientated.

After quenching the amorphous sheet is reheated to approximately 15 – 20°C above the glass transition temperature which is between 68 – 70°C for PET. This provides the polymer chains with enough thermal energy and molecular mobility to be drawn in the machine direction up to 400% the original film length. The stress imposed on the polymer chains within the uniaxial drawing process tends to align the molecules in the direction of the applied stress and orientate the aromatic rings parallel to the film surface. As a consequence the crystalline content of the film is increased through stress induced crystallisation.[50] Crystalline phase within uniaxially drawn films accounts for 10 – 20 % of the matrix and the films are typically between 50 – 1200 μm in thickness. After uniaxial stretching the tensile strength of the film is dramatically increased along the machine direction, however applications are limited as the film is easily ruptured along the transverse direction.

Biaxial stretching may then be performed in the transverse direction. The film is again reheated but to a higher temperature which provides the extra molecular mobility and thermal energy to the remaining partially restricted amorphous domain. Generally temperatures over 100°C are employed and the uniaxially drawn film may be stretched up to 400% in the transverse direction. This aligns additional polymer chains within the amorphous domain increasing the crystalline volume to between 25 – 40 %. In addition previously formed crystallites orientated in the machine direction are also aligned with

respect to the transverse direction.[50] Again, applications are limited to shrink wrap films as the polymer is thermally unstable and shrinks if exposed temperatures above 100°C.

Biaxial orientated films are then heat set between 180 – 220°C for a time period in the order of seconds. During this time polymer chains under stress within the amorphous domain relax, partial crystalline melting and further crystallisation and/or re-crystallisation may occur. This increases the crystalline content to approximately 50% and allows the stabilisation of the crystalline structure and orientation formed during the drawing processes.

The applications of biaxially orientated PET films are extremely varied after the heat setting process as it imparts an extremely high tensile strength in the planar direction, and thermal stability up to temperatures of 150°C. The films are generally between 5 – 180 μm in thickness and may be employed in the following industries:

Photographic:	dental and medical x-ray films, 35 mm slides, photographic film
Data storage:	audio and video tape, floppy discs, magnetic cards, microfilm
Packaging:	food wrap, metallised barrier wrap (e.g. in coffee packaging), medical devices
Electrical:	capacitors, wire and cable insulation, photoresist films for use in printed microcircuits, encapsulants for OLED displays
Other:	hot stamping (e.g. synthetic wood grain), stationary, photocopier and typewriter belts

1.2.5 DEGRADATION

PET can degrade through various mechanisms depending on the environmental conditions, and the mechanisms themselves can also be described through various nomenclatures. The degradation mechanisms of polymer chains may be described as belonging to one or more of the following classes: heterolytic, homolytic, hydrolytic, and photolytic. The definitions of these mechanisms can be found below.

Heterolytic scission: The cleavage of a covalent bond in such a manner that both bonding electrons remain with one of the two molecular or atomic fragments. For example,

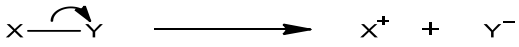

Homolytic scission: The cleavage of a covalent bond in such a manner that both molecular or atomic fragments retain one of the bonding electrons. For example,

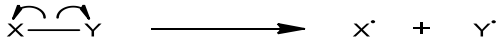

Hydrolytic scission: The reaction of a molecule with water (solvolysis) resulting in the cleavage of one or more bonds.

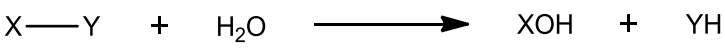

Photolytic scission: The cleavage of one or more covalent bonds in a molecule due to the absorption of light. For example,

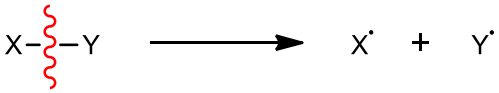

1.2.5.1 THERMAL DEGRADATION

Despite decades of research into the thermal degradative processes of PET, there is still much debate over the evidence or lack thereof for heterolytic or homolytic based initiation mechanisms. Various authors throughout the years have continually published literature which has supported both postulates.[40, 41, 51]

1.2.5.1.1 HETEROLYTIC INITIATION AND MECHANISMS OF THERMAL DEGRADATION

The heterolytic degradative initiation of PET may also be described as a McLafferty rearrangement. The McLafferty rearrangement is a commonly adopted mechanism in literature and is favoured by authors such as Grassie.[40] It proceeds through the formation of a cyclic six-membered transition state which subsequently facilitates electron rearrangement. The formation of the transition state is dependent upon the molecular conformation of the polymer backbone, and requires a trans glycol arrangement alongside a gauche structure with respect to the CH_2-O bonds. Electron induction effects due to the polarity differences in the ring structure then produce the molecular rearrangement. As a consequence scission occurs via a concerted mechanism at the alkyl-oxygen bond of the glycol unit, leading to vinyl ester and carboxylic acid end groups. Scission in this manner is of course random, and is dependent upon the availability of β-methylene groups.

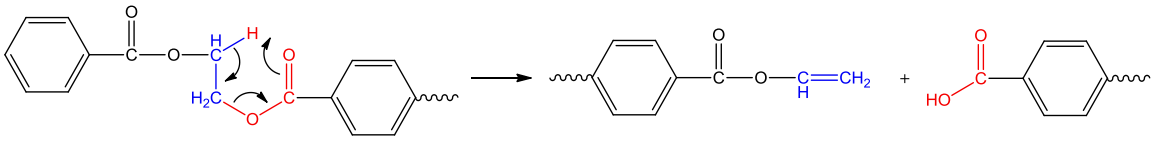

Figure 1.15 Heterolytic initiation mechanism for the thermal degradation of PET

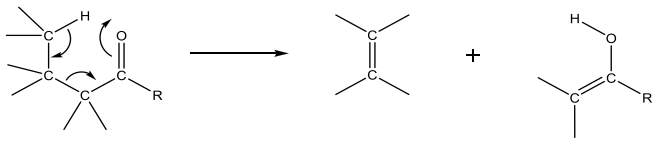

Figure 1.16 M^{c}Lafferty rearrangement[35]

Arguments in support of a heterolytic mechanism tend to focus upon the favourable induction effects which exist upon the formation of a six-membered ring.[52] In addition, literature has stated that the degradation of PET is not known to be inhibited by free-radical trapping agents, therefore favouring a heterolytic mechanism.

Acetaldehyde is one of the major products during PET degradation and is formed as by-product during transesterification reactions between vinyl benzoate and hydroxyethyl moieties. The transesterification reaction regenerates the polymer chain through the reformation of the ethoxy repeat unit and is irreversible. The vinyl alcohol formed as the by-product then immediately undergoes keto-enol tautomerisation to acetaldehyde.[35] The regeneration of the polymer backbone in this manner is suggested as the major secondary reaction involving vinyl ester end groups, due to the amount of acetaldehyde released during degradation.[53]

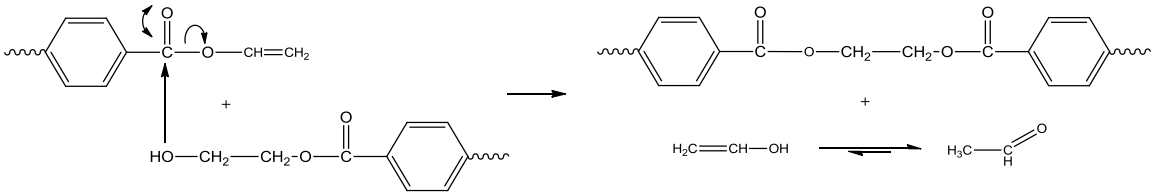

Figure 1.17 Re-polymerisation of vinyl benzoate and hydroxy ethyl end groups leading to the formation of acetaldehyde

A second major degradative pathway of vinyl benzoates involves a rearrangement to dicarbonyl moieties, which then undergo decarbonylation to yield acetophenone and carbon monoxide.[40] Other suggested mechanisms include decarboxylation to yield conjugated vinyl moieties and the acid or base catalysed hydrolysis of the ester bond which yields carboxylic acid and vinyl alcohol. A mechanism which has been postulated numerous times in literature is a repolymerisation of the vinyl moieties to yield polyethylene-type segments with terephthalate-based pendant groups.[40, 53] Little evidence however has been observed in literature, likely due to low probabilities of formation and high probabilities of further degradation once formed.

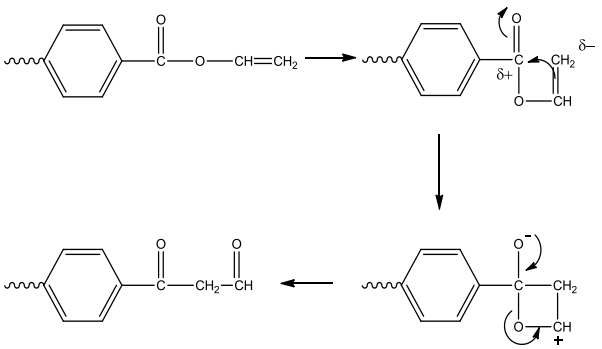

Figure 1.18 Proposed mechanism for the rearrangement of vinyl benzoate to 3-oxo-3-propanal prior to decarbonylation

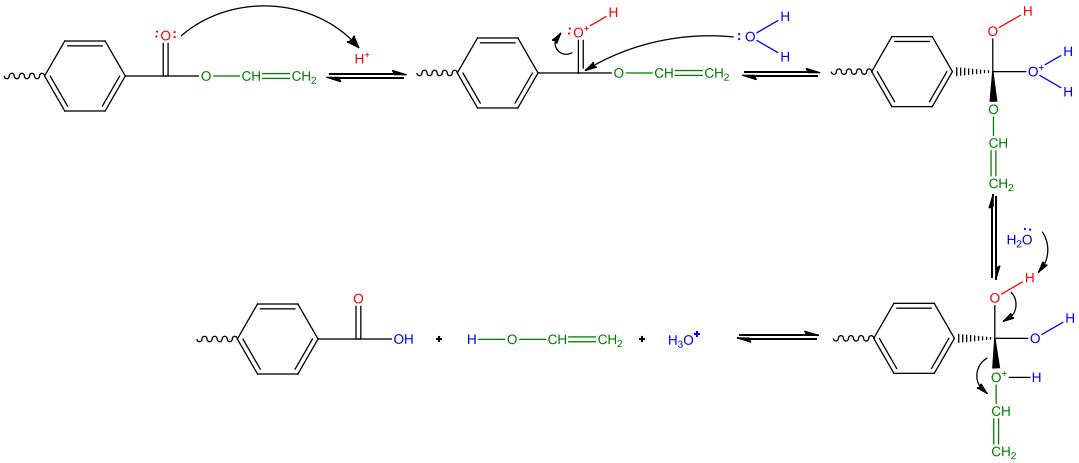

Figure 1.19 Degradative mechanism for the acid catalysed hydrolysis of a vinyl benzoate moiety[35]

Secondary heterolytic reactions of the carboxylic acid moieties formed after initiation involve a homo-nucleophilic attack to form an anhydride. The formation of anhydrides is theoretically possible and has been suggested in numerous degradation schemes.[53, 54] It is uncommon to find anhydride formation reported in the literature, and it is concluded to be of minor importance during PET degradation.[41] The lack of experimental data supporting anhydride formation may also be accounted for due to the possibility of transesterification reactions between the anhydride and hydroxyl groups, potentially reforming the polymer backbone.[54]

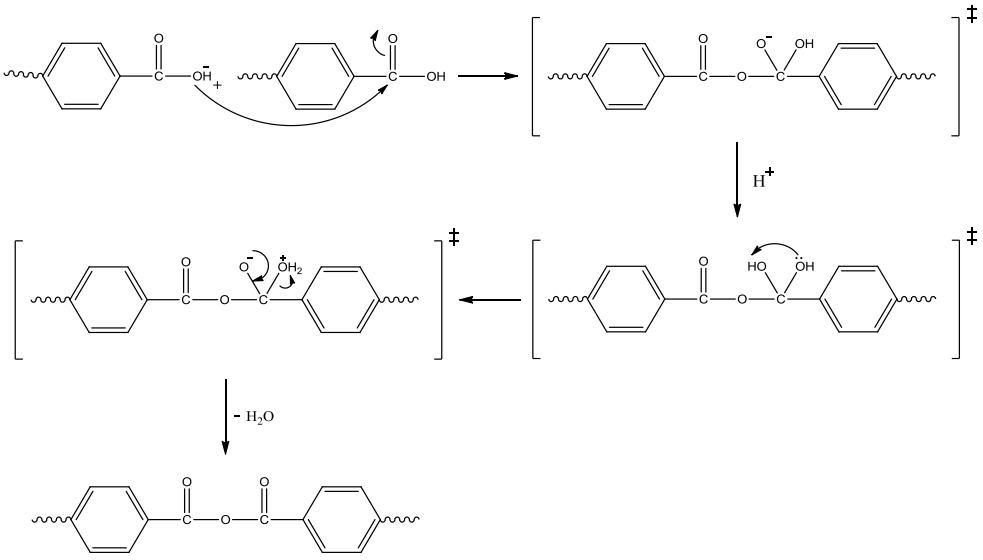

Figure 1.20 Mechanism for the homo-nucleophilic attack of carboxylic acid moieties

1.2.5.1.2 HOMOLYTIC INITIATION AND MECHANISMS OF THERMAL DEGRADATION

The thermal degradation of PET may also be described through a homolytic mechanism which is favoured by authors such as McNeill and Bounekhel.[41] The mechanism proceeds through the cleavage of the ester bond as in the heterolytic mechanism, however in contrast can occur at either side of the carboxy bond.[55] Cleavage and proton abstraction at the aromatic carboxyl bond yields either carbon dioxide and a vinyl ester terminated moiety or carbon monoxide and an ethoxy terminated moiety respectively. In addition a benzyl terminated moiety is formed regardless of the route. Initiation at a/b as shown in figure 1.21 to yield carbon monoxide would be considered the more likely position for scission due to the increased stability of the acyl-oxygen bond because of conjugation and electron induction effects from the aromatic ring. Depending on the functional groups present additional cleavage and proton abstractions can degrade the molecules or chain sections further.

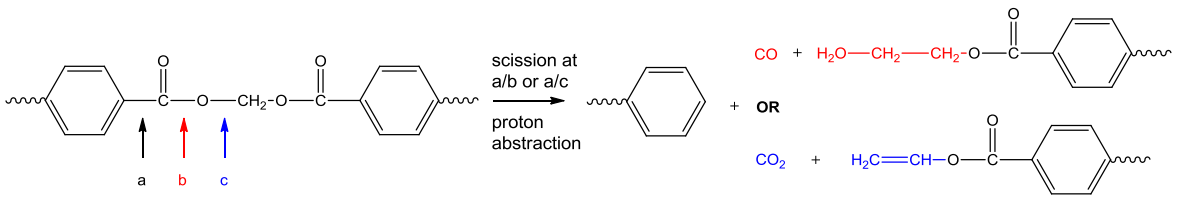

Figure 1.21 Homolytic initiation mechanism for the thermal degradation of PET

McNeill and Bounekhel present the case for a homolytic initiation employing the argument that free-radical trapping agents would only inhibit chain reactions.[41] This is a differing interpretation of experimental data than that taken by Grassie.[40] In addition evidence for a homolytic mechanism is observed in the volatile release during degradation. Carbon monoxide and carbon dioxide are evolved at the lowest observed temperatures of degradation and indeed throughout the degradative process. It has been argued that if a heterolytic mechanism were prevalent carbon monoxide and carbon dioxide would only be formed and observed at the highest degradative temperatures.

Acetaldehyde formation may be accounted for homolytically through scission of the acyl-oxygen bonds within vinyl benzoate moieties. Proton abstraction would result in the formation of vinyl alcohol, with the molecule then preferentially tautomerising to acetaldehyde.

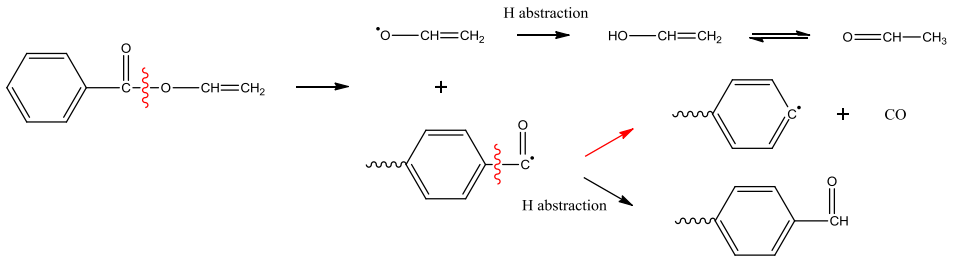

Figure 1.22 Homolytic degradation mechanism of vinyl benzoate moieties to yield benzene and benzaldehyde moieties, acetaldehyde and carbon monoxide

The formation of additional products may be accounted for in a relatively straightforward manner. Chain scission at the olefinic-oxygen bond for example will yield terephthalic acid, with further degradation resulting in the formation of carbon dioxide.[41]

Acetaldehyde, benzaldehyde, carbon monoxide and carbon dioxide are only a few of the major degradation products cited in literature and final products are indeed diverse. There has been a vast range of products reported due to a vast series of complicated side reactions. These include anhydrides, benzoic acid, p-acetyl benzoic acid, acetophenone, vinyl benzoate, ketones, methane, ethylene and acetylene.[56] Products specifically reported to originate from carboxylic acid moieties are cyclic ketones, cyclic aldehydes and water.[40] Vinyl ester moieties are reported to yield aldehydes, dienes and cyclic ethers.[40] It is important to note that not every degradation product may be formed through both heterolytic and homolytic routes and this may give an indication of the mechanism type. An abundance of carbon monoxide for example may indicate a homolytic initiation mechanism as opposed to a heterolytic mechanism.

1.2.5.2 THERMO-OXIDATIVE DEGRADATION

PET degradation under thermo-oxidative environments follows a homolytic or radical-based depolymerisation mechanism with the major products consisting of carbon monoxide, acetaldehyde, formaldehyde, benzene, styrene and aliphatic hydrocarbons. The composition of the products is dependent upon the temperature of degradation, with lower temperatures favouring low molar mass products such as carbon monoxide, acetaldehyde and formaldehyde.[51]

In contrast to thermal degradation, PET also undergoes gelation due to crosslinking during thermo-oxidative degradation. Literature has stated crosslinking may occur within PET at temperatures between 230 – 300°C under air. There is still a significant amount of debate over whether the crosslinks are formed through the aromatic or aliphatic segments of the polymer after initiation. The initial degradation of the polymer backbone leads to the formation of carboxylic acids, vinyl esters, aldehydes and carbon dioxide. As vinyl esters accumulate within the matrix further reaction occurs with the possibility of network structures being formed. The oxygen within the system is then postulated to purge the system of degradation products which may consume the vinyl esters in reverse reaction, accelerating chain scission and crosslinking.[51] Other authors have suggested it is the

aromatic fragments which are responsible for cross-linking through the formation of aryl radicals after the initial oxidation step.[57, 58] In addition Yoda *et al.* have suggested it is a combination of both aliphatic and aromatic crosslinking which gives rise to gelation.[39]

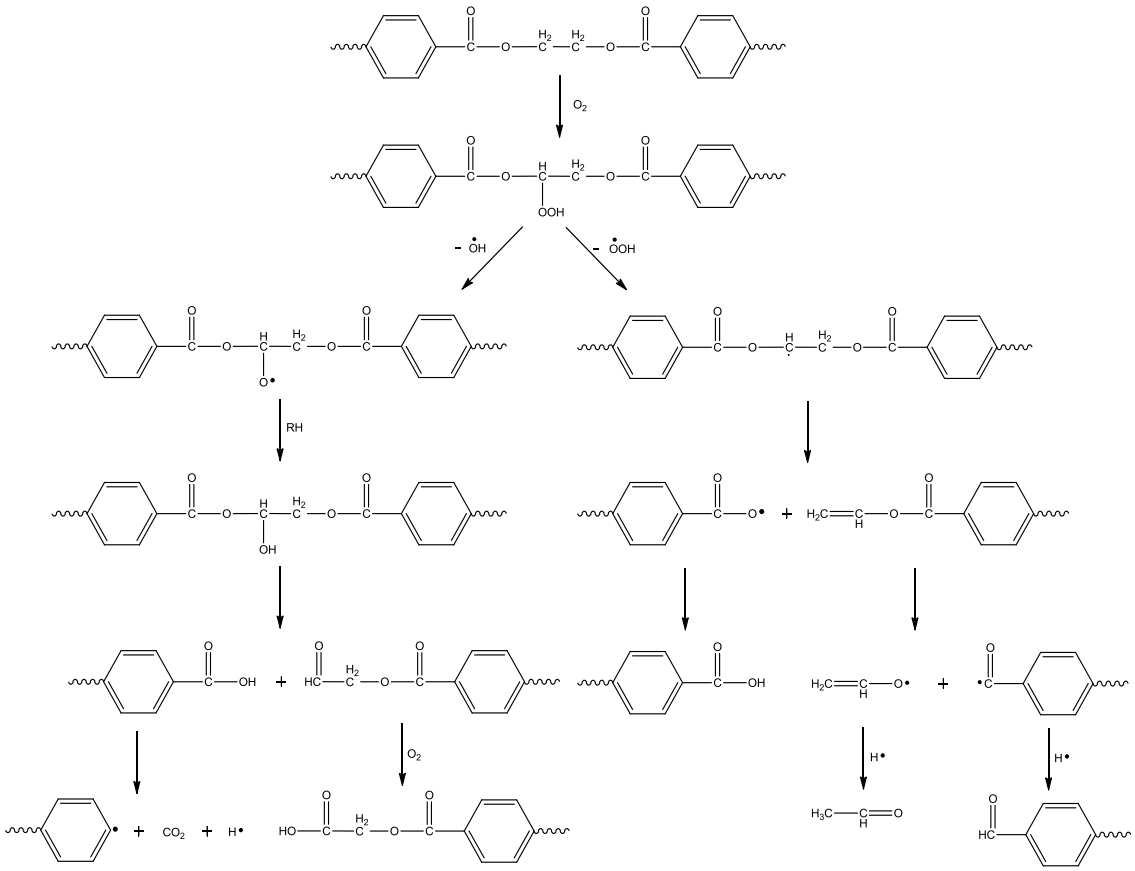

Figure 1.23 Homolytic or radical-based depolymerisation of PET under thermo-oxidative conditions[51]

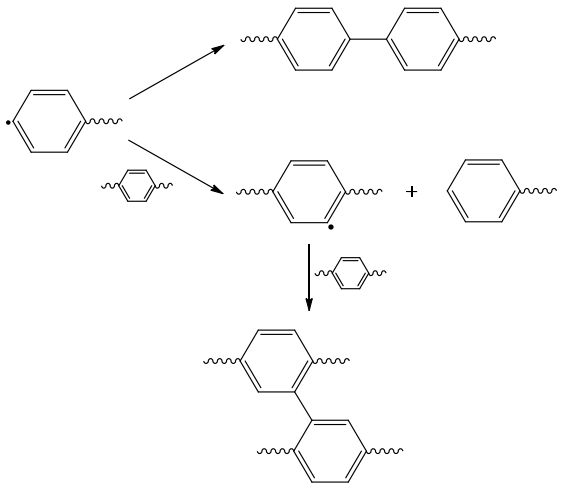

Figure 1.24 Aryl crosslinking mechanism of PET under thermo-oxidative conditions[51]

1.3 POLYMER NANOCOMPOSITES

Over the past few decades polymer composite research has received a significant degree of interest due to the potential enhancement of properties. The literature indicates that some of the enhancements that composites tend to exhibit are: an increased flexural modulus (and limited increase in distortion temperature under load), increased tensile elongation and strength, increased barrier properties and decreased flammability (due to an increase in barrier properties and char formation).[59-61] The nanomaterials which have been studied in polymer systems are as numerous as the polymers themselves, and so it is understandable why this area of research has received such widespread attention.

1.3.1 PREPARATION

Literature has illustrated there are several routes available to polymer nanocomposite preparation.[60] The most commonly adopted routes by researchers are *in situ* polymerisation and melt intercalation, as they can be adopted into the industrial manufacturing level with minimal disruption and cost.[62-66] An additional route which may be undertaken is the exfoliation-adsorption method, however the need for an

additional solvent increases the complexity and as such it is only generally employed when melt intercalation and *in situ* polymerisation are not suitable.[67, 68]

During preparation it is essential that the filler is adequately dispersed within the liquid monomer or molten polymer matrix. If this is not achieved, aggregation of the nanoclay within the matrix may occur, which may be detrimental to the final composite properties. It is therefore necessary that the filler and monomer/polymer are complementary and encourage favourable intermolecular interactions. Generally surface modification is a technique which is commonly employed to increase the compatibility of the nanoclay with the matrix without the need for adaption of the experimental equipment or procedures. Surface modification has previously been discussed within section 1.1.2.

Melt intercalation is the route which is the most straightforward and demands the least in the way of alterations to pre-existing extrusion equipment at both the research and manufacturing level. It assumes the nanoclay (if compatible) should shear into the molten polymer as the polymer and nanoclay passes through the twin screw of the extruder. Depending on the degree of compatibility the polymer chains may enter the nanoclay galleries to various degrees and hydrid morphologies are common.[69, 70]

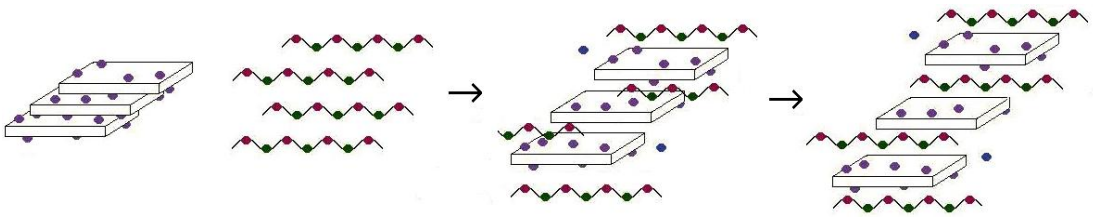

Figure 1.25 Simplified schematic illustrating melt intercalation

The *in situ* polymerisation route requires the nanoclay is compatible with both monomer and polymer matrices. Initially the platelets or fibres are swollen in the presence of liquid monomer and this process is often facilitated by ultra-sonication. Additional monomers may then be added to the reaction vessel and the system is polymerised incorporating the nanoclay in the matrix as the molecular size increases. It is generally assumed that the

intercalation and/or exfoliation is near completion prior to polymerisation, however the nanoclay may re-agglomerate or exfoliate further during the process.[70]

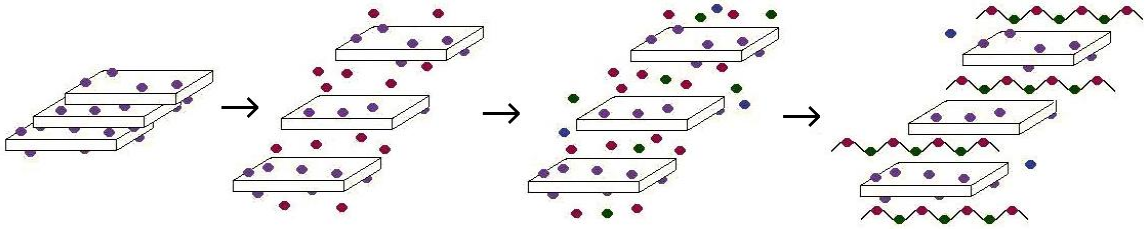

Figure 1.26 Simplified schematic illustrating *in situ* polymerisation

The exfoliation-adsorption method is the most demanding route for composite preparation and requires the greatest alteration to current preparative equipment and procedures. As a result this method is the least preferred preparative method and is only employed when the desired nanoclay will not shear directly into the monomer or molten polymer. The nanoclay is initially exfoliated in a solvent in which it is compatible and the polymer is soluble. The solvent swells the nanoclay allowing the polymer to enter the galleries with greater ease, and the solvent is then evaporated and as a result entraps the nanoclay between the polymer chains.

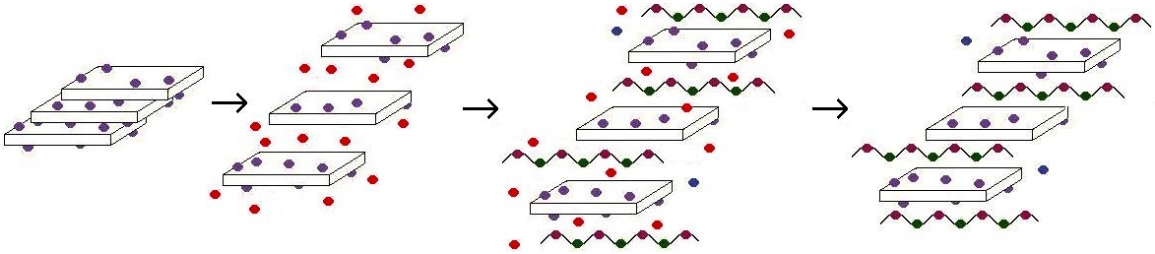

Figure 1.27 Simplified schematic illustrating the exfoliation – adsorption method

1.3.2 THERMODYNAMICS OF FORMATION

The entropic influences during intercalation can be said to originate from the nanoclay, alkyl ammonium surface modifier and the polymer. The nanoclay would be expected to influence the entropy of the system as it intercalates or exfoliates with the polymer. As platelets are substantial in size however and their structure is unaffected by intercalation

their contribution to the total entropy change is negligible. When considering the modifier however the entropy is observed to increase as intercalation occurs as the configurational freedom of the alkyl chains is proportional to the intergallery height. When the intergallery height increases to the point where the alkyl chains are fully extended with no hindrance the maximum potential gain in entropy will have been achieved. Finally the confinement of a polymer from a bulk, molten state to a polymer–modifier solution will cause a decrease in entropy within the system due to confinement, and hence decreasing the favourability of the process. Within the melt intercalation process, this gain in entropy due to an increase in conformational freedom is the only process which may counteract the unfavourable influence of the polymer. Intercalation from solution however is far more favourable as the entropy loss on confinement is compensated for by an entropy gain associated with the desorption of the solvent molecules. If the nanoclay has been intercalated (or rather exfoliated) efficiently within either method, the entropy loss on confinement may approach zero if the intergallery distance is greater than the radius of gyration of the polymer. No negative entropic influence would therefore affect the intercalative process and it would be entropically favourable.

The major enthalpic contributions originate from the confinement of the polymer within the galleries, conformational changes of the modifier alkyl chains and the intermolecular interactions between the polymer, modifier and the silicate surface. The enthalpic contribution of the polymer is lowest or negligible when the intergallery distance approaches the radius of gyration of the polymer. Similarly, the conformational freedom of the alkyl tallows imparts the lowest enthalpic contribution when there is no influence from the opposing platelet surface. As the surface modifier commonly possesses apolar alkyl tallows the predominant intermolecular interactions will be between the polymer and the silicate surface. It could be assumed that due to a change in surface-surface and polymer-polymer interaction energies that the intercalative process may be enthalpically unfavourable. On the contrary, polymers which possess polar functionalities may cause a favourable decrease in enthalpy due to the establishment of a variety of favourable polymer-surface interactions. In addition, the sole purpose of a surface modifier is to establish favourable interactions between both the polymer and silicate surface and hence

facilitate intercalation. Specific modifiers may therefore be employed to lower the enthalpic contribution and impart and drive the polymer intercalative process.

1.3.3 NANOCLAY LOADING AND COMPOSITE MORPHOLOGY

The platelet morphology in the polymer composite may vary substantially within the matrix. Intercalated and exfoliated forms are the most commonly employed morphologies in literature however both structures are actually the end members of a series of possible platelet arrangements. Intermediate morphologies may be described as either ordered or disordered to various extents and in addition non-homogeneity may yield a variety of structures.

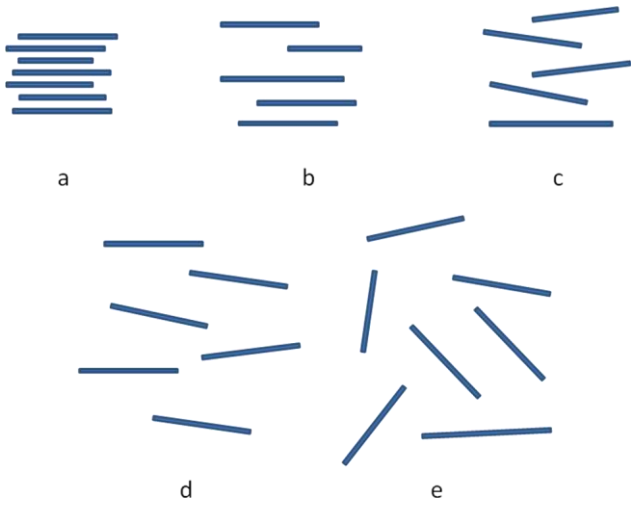

Figure 1.28 Illustration of nanoclay morphology types within a nanocomposite; a, book-house; b, ordered intercalated; c, disordered intercalated; d, ordered exfoliated; e, disordered exfoliated

Nanoclay loading has a significant impact on morphology in the final polymer and there is a specific range in which exfoliation is homogeneous with no or little agglomeration.[66, 71-73] Literature tends to suggest a low nanoclay loading of between 1 – 2% allows homogenous exfoliation whilst allowing the alteration of polymer properties.[66, 71, 73] A greater efficiency in exfoliation is observed at lower loadings due to the larger free volume available for platelet movement which lowers the probability of collision between platelets. At higher loadings agglomeration may occur and therefore homogeneous exfoliation is less

probable. Higher loadings however are required for applications where improvements in the gas barrier properties are desirable, and so a less than ideal degree of exfoliation or intercalation may have to be tolerated. It has been illustrated that above a 3% loading agglomeration increases substantially and by a 15% loading there is near complete agglomeration and very little exfoliation.[72]

1.3.4 CRYSTALLISATION WITHIN A POLYMER NANOCOMPOSITE

During crystallisation the nanoclay acts as a ready-made, heterogeneous nucleating surface for the polymer chains which removes the free energy penalty required when forming a new crystalline surface. As a result the crystallisation rate is observed increase and crystallisation occurs earlier or at a higher temperature during dynamic runs.[59] It has also been noted by Wang *et al.* that the lowest nanoclay loadings appears to have the most significant effect on crystallisation. Although further additions above a 1% loading are observed to increase the crystallisation rate and temperature their effect is not as marked as that of the initial loading. As the majority of composites do not exhibit an ideal exfoliated state this suggests that sufficient nucleant material may in fact be present at the lower loadings. If the extent of exfoliation could be improved the lower nanoclay loadings may produce equal results to the higher loadings. Crystallite size is also known to decrease and crystallite number increase on incorporation of nanoclay into the polymer. This is due to the large number of ready-made nuclei which encourage a greater number of spherulitic growth centres in the molten polymer.[72, 73]

1.3.5 DEGRADATION WITHIN A POLYMER NANOCOMPOSITE

Literature has also suggested that ammonium organoclays enhance the thermal stability of PET under thermal (non-oxidative) conditions. Wang *et al.* and Chung *et al.* have both observed an increase in onset temperatures and temperatures of maximum degradation at loadings up to 8% w/w.[72, 74] In contrast, literature concerning the thermo-oxidative degradation suggests the opposite.[75] Osman *et al.* have also observed a difference in degradative behaviour during thermogravimetric analysis and postulated degradation

occurs in a different manner for the ammonium organoclays during thermal and thermo-oxidative degradation.[76] Cervantes-Uc *et al.* have examined the degradation products of the common alkyl ammoniums employed in montmorillonite and sepiolite surface modification under both thermal and thermo-oxidative conditions. It was observed that during thermal degradation products characteristic of the Hoffman elimination are present.[77] The thermo-oxidative process also yielded aldehyde and carboxylic acid functionalities due to the oxidation of the alkene products. It is probable that the subsequent formation of RCOO• and RCO• radicals then catalyse the degradation of the polymer chain resulting in lower thermal stability.[77] It is generally accepted that the thermal stability of the polymer is lowered due to an increase in Brønsted acid sites as a result of modifier degradation. However Hoffman elimination reactions would form Brønsted acid sites in both thermal and thermo-oxidative environments and a decrease in thermal stability is only observed during thermo-oxidative degradation. It is therefore suggested by the author, in contrast to popular opinion, that it may be the formation of free radicals under thermo-oxidative conditions that leads to the decrease in stability within PET and not an increase in Brønsted acid sites on the nanoclay surface. In addition, it has been illustrated by Xu *et al.* that during shearing on processing (under air) a more exfoliated structure results which further accelerates the degradative process.[75] This illustrates a greater volume of exposed modifier decreases the thermal stability of the polymer, and is despite a greater degree of montmorillonite exfoliation (which has previously been suggested to inhibit oxygen diffusion and therefore the thermo-oxidative degradation of the polymer).

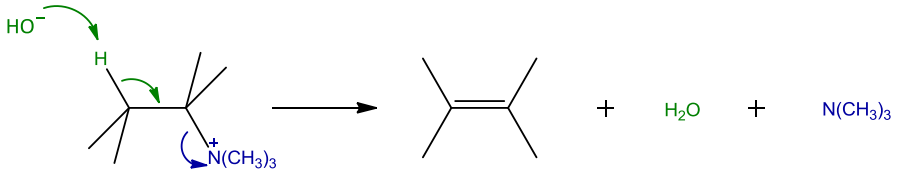

Figure 1.29 Hoffman elimination of a quaternary ammonium salt[35]

1.3.6 ADDITIONAL PROPERTIES AND APPLICATIONS

Polymer-nanoclay composites are widely considered to represent the next generation of polymers, predicted on the supposition that the composite exhibits enhanced properties with respect to the original polymer thermally, mechanically or chemically. The initial driving forces for the development of polymer-nanoclay composites were the enhancement of the elastic modulus and a decrease in gas permeability. It was considered a significant enhancement in these properties would open up various structural and packing applications previously unavailable to the traditional polymers.

One of the typical enhancements on the incorporation of a nanoclay into a polymer is indeed an increase in modulus, which is due to a restriction in polymer mobility at the polymer-nanoclay interface (the extent of which is dependent upon the extent of exfoliation of the nanoclay). An enhancement in the permeability however is dependent not only on the extent of exfoliation but also platelet orientation. A random exfoliated state would not be expected to enhance gas barrier properties. Orientation such as is observed during the uniaxial and biaxial drawing process however would achieve an increase in barrier properties however due to an increase in the tortuous path length the gas was required to travel to diffuse through the film. Typically, an increase in modulus is also accompanied by a decrease in the impact resistance. This has previously been compensated for within polypropylene composites by compounding with rubber nanoparticles.[78] Flame retardancy has also been observed to increase as the presence of the nanoclay alters the char structure, decreases the mass loss on degradation and reduces the flammability at low percentage contents, whilst allowing a decrease in co-monomer content within co-polyesters.[78, 79]

As a result polymer-nanoclay composites have found use in an extensive number of applications within various industries, a selection of which are illustrated below.[80-82] In spite of this poly(ethylene terephthalate) nanoclay composites in particular have not found widespread use as the polymer suffers from brittle behaviour at relatively low smectite loadings. Cement nanoparticles however have been successfully incorporated as an

additive during recycling and an improvement in mechanical properties such as an increase in toughness has been claimed on reprocessing.[83] This increase in toughness is apparently due to the ability of the nanoparticles to absorb water from the polymer which would otherwise have resulted in hydrolytic degradation on reprocessing.

Automotive industry:	engine covers, timing belt covers, oil reservoir tanks, petrol tanks
Home applications:	coverings for electrical appliances, storage tanks, pipelines, furniture
Leisure/sporting activities	boat hulls, hand-glider frames, skis, surfboards, racquets
Defence applications:	ballistic protection, electrostatic charge dissipation, sensors, UV resistance

1.4 REFERENCES

1. Kato, M., Usuki, A., *Polymer-Clay Nanocomposites*, ed. Pinnavaia, T.J.,Beall, G.W., 2000, John Wiley & Sons Ltd, Chichester.
2. Hast, N., *Structrue of Clay*, Nature, 1947, **159**, 354-356.
3. Grim, R.E., *Applied Clay Minerology*, 1962, McGraw-Hill, New York.
4. Grimshaw, R.W., Searle, A.B., *The Chemistry and Physics of Clays*, 1959, Ernest Benn Limited, London.
5. McAlpine, M., Hudson, N.E., Liggat, J.J., Pethrick, R.A., Pugh, D., Rhoney, I., *Study of the Factors Influencing the Exfoliation of an Organically Modified Montmorillonite in Methyl Methacrylate/Poly(methyl methacrylate) Mixtures*, Journal of Applied Polymer Science, 2005, **99**, 2614-2626.
6. Lambe, T.W., Whitman, R.V., *Soil Mechanics*, 1969, John Wiley and Sons, New York.

7. Theng, B.K.G., *The Chemistry of Clay-Organic Reactions*, 1974, Adam Hilger, London.
8. Aronowitz, S., Coyne, L., Lawless, J., Rishpon, J., *Quantum-chemical modelling of smectite clays,* Inorganic Chemistry, 1982, **21**, 3589-3593.
9. Chatterjee, A., Iwasaki, T., Hayashi, H., Ebina, T., Torii, K., *Electronic and structural properties of montmorillonite - a quantum chemical study,* Journal of Molecular Catalysis A: Chemical, 1998, **136**, 195-202.
10. Guven, N., *Hydrous Phyllosilicates (exclusive of micas): Smectites*, Reviews in Mineralogy, ed. Bailey, S.W., Vol. 19, 1988, Mineralogical Society of America, Washington.
11. Bray, H.J., Edfern, A.T.R., Clark, S.M.C., *The kinetics of dehydration in Ca-montmorillonite; an in situ X-ray diffraction study* Mineralogical Magazine, 1998, **62**(5), 647-656.
12. Frost, R.L., Ding, Z., *Controlled rate thermal analysis and differential scanning calorimetry of sepiolites and palygorskites,* Thermochima Acta, 2003, **397**, 119-128.
13. Barron, P.F., Frost, R.L., *Solid state ^{29}Si NMR examination of the 2:1 ribbon magnesium silicates, sepiolite and palygorskite*, American Mineralogist, 1985, **70**, 758-766.
14. Jones, B.F., Galan, E., *Hydrous Phyllosilicates (exclusive of mica) : Sepiolite and Palygorskite*, Reviews in Mineralogy, ed. Bailey, S.W., Vol. 19, 1988, Mineralogical Society of America, Michigan.
15. Serna, C., VanScoyoc, G.E., Ahlrichs, J.L., *Hydroxyl groups and water in palygorskite*, American Mineralogist, 1977, **62**, 784-792.
16. Park, S.J., Seo, D.I., Lee, J.R., *Surface modification of montmorillonite on surface acid-base characteristics of clay and thermal stability of epoxy/clay nanocomposites,* Journal of Colloid and Interface Science, 2002, **251**, 160-165.
17. Dowling, A.H., Stamboulis, A., Fleming, G.J.P., *The influence of montmorillonite clay reinforcement on the performance of a glass ionomer restorative*, Journal of Dentistry, 2006, **34**, 802-810.

18. Bergaya, F., Lagaly, G., Vayer, M., *Cation and Anion Exchange*, Handbook of Clay Science, ed. Bergaya, F., Theng, B.K.G.,Lagaly, G., 2006, Elsevier, Oxford.
19. Ferguson, J., Zemblowski, Z., *Applied Fluid Rheometry*, 1990, Elservier Applied Science, London.
20. Zhao, H., Bhattacharjee, S., Chow, R., Wallace, D., Masliyah, J.H., Xu, Z., *Probing Surface Charge Potentials of Clay Basal Planes and Edges by Direct Force Measurements*, Langmuir, 2008, **24**, 12899-12910.
21. Maqueda, C., Partal, P., Villaverde, J., Perez-Rodriguez, J.L., *Characterisation of Sepiolite-gel-based Formulations for Controlled Release of Pesticides*, Applied Clay Science, 2009, **46**, 289-295.
22. Barnes, H.A., Hutton, J.F., Walters, K., *An Introduction to Rheology*, 1989, Elsevier Science, Amsterdam.
23. Barnes, H.A., *Industrial Processes and Suspensions*, 2006, Unilever, Port Sunlight.
24. Zhao, F.Y., Bhanage, B.M., Shirai, M., Arai, M., *Heck Reactions of Iodobenzene and Methyl Acrylate with Conventional Supported Palladium Catalysts in the Presence of Organic and/or Inorganic Bases Without Ligands*, Chemistry - A European Journal, 2000, **6**, 843-848.
25. Adams, J.M., McCabe, R.W., *Clay Minerals as Catalysts*, in Handbook of Clay Science, ed. Bergaya, F., Theng, B.K.G.,Lagaly, G., 2006, Elsevier, Oxford.
26. Harvey, C.C., Lagaly, G., *Conventional Applications*, in Handbook of Clay Science, ed. Bergaya, F., Theng, B.K.G.,Lagaly, G., 2006, Elsevier, Oxford.
27. Pusch, R., *Clays and Nuclear Waste Management*, in Handbook of Clay Science, ed. Bergaya, F., Theng, B.K.G.,Lagaly, G., 2006, Elsevier, Oxford.
28. Tomita, K., Ida, H., *Studies on the Formation of Poly(ethylene terephthalate): 3. Catalytic Activity of Metal Compounds in Transesterification of Dimethyl Terephthalate with Ethylene Glycol*, Polymer, 1975, **16**, 185-190.
29. Otton, J., Ratton, S., *Investigation of the formation of poly(ethylene terephthalate) with model molecules: Kinetics and mechanisms of the catalytic esterification and alcoholysis reactions: II Catalysis by metallic derivatives (monofunctional reactants)*, Jounral of Polymer Science: Part A: Polymer Chemistry, 1988, **26**, 2199-2224.

30. Tomita, K., *Studies on the Formation of Poly(ethylene terephthalate): 6. Catalytic Activity of Metal Compounds in Polycondensation of Bis(2-hydroxyethyl) Terephthalate,* Polymer, 1976, **17**, 221-224.
31. Awaja, F., Pavel, D., *Recycling of PET*, European Polymer Journal, 2005, **41**, p. 1453-1477.
32. Duh, B., *Effect of antimony catalyst on solid-state polycondensation of poly(ethylene terephthalate),* Polymer, 2002, **43**, 3147-3154.
33. Fiorini, M., Pilati, F., *Reactive blending of poly(ethylene terephthalate) and bisphenol-A polycarbonate: effect of various catalysts and mixing time on the extent of exchange reactions,* Polymer, 1996, **38**(2), 413-419.
34. Chen, J.W., Chen, L.W., *The Kinetics of Diethylene Glycol Formation in the Preparation of Polyethylene Terephthalate,* Journal of Applied Polymer Science Part A: Polymer Chemistry, 1998, **36**(17), 3073-3080.
35. McMurray, J., *Organic Chemistry*, 2000, Brooks/Cole, Pacific Grove.
36. Edge, M., Wiles, R., Allen, N.S., McDonald, W.A., Mortlock, S.V., *Characterisation of the Species Responsible for Yellowing in Melt Degraded Armoatic Polyesters - I: Yellowing of Poly(ethylene terephthalate),* Polymer Degradation and Stability, 1996, **53**, 141-151.
37. Chen, J.W., Chen, L.W., *Effect of TPA addition at the initial feed on DEG formation in the perparation of PET and the kinetics of ethylene glycol with protons in the etherification reaction,* Journal of Applied Polymer Science Part A: Polymer Chemistry, 1998, **36**(17), 3081-3087.
38. Rozengauz, S.S., Repina, L.P., Aizenshtein, E.M., *Formation of Diethylene Glycol in the Polycondensation Stage of Polyethylene Terephthalate Synthesis,* Khimicheskie Volokna, 1976, **6**, 34-35.
39. Yoda, K., Tsuboi, A., Wada, M.L., Yamadera, R., *Network Formation in Poly(ethylene Terephthalate) by Thermo-oxidative Degradation,* Journal of Applied Polymer Science, 1970, **14**, 2357-2376.
40. Grassie, N., Gerald, S., *Polymer Degradation and Stabilisation*, Vol. 5, 1985, Cambridge University Press, Cambridge.

41. McNeill, I.C., Bounekhel, M., *Thermal Degradation Studies of Terephthalate Polyesters: 1. Poly(alkylene terephthalate),* Polymer Degradation and Stabilisation, 1991, **34**, 187-204.

42. Daubeny, P., Bunn, C.W., *The Crystal Structure of Polyethylene Terephthalate* Proceedings of the Royal Society of London: Series A - Mathematical and Physical Sciences, 1954, **226**(1167), 531-542.

43. Tsu, J.S., Mak, T.C.W., *Refinement of the Crystal Structure of Polyethylene Terephthalate,* Journal of Crystal and Molecular Structure, 1975, **7**, 75-80.

44. Werner, E., *Polyester, Films*, in Encyclopedia of Polymer Science and Engineering, Vol. 12, 1988, Wiley, New York.

45. Kanai, T., Campbell, G., *Film Processing*, 1999, Hanser Publishers, Munich.

46. Brooks, D.W., Giles, G., *PET Packaging Technology*, 2002, Blackwell Publishing, Stevenage.

47. Fakirov Weinheim, S., *Handbook of Thermoplastic Polyesters, Vol. 1*, 2002, Wiley-VCH, Weinheim.

48. Kurokawa, H., Ohshima, M.A., Sugiyama, K., Miura, H., *Methanolysis of Polyethylene Terephthalate (PET) in the Presence of Aluminium Tiisopropoxide Catalyst to From Dimethyl Terephthalate and Ethylene Glycol,* Polymer Degradation and Stability, 2003, **79**(3), 529-533.

49. Hanya, A., Hicks, B.W., Fina Technology Inc., *Heat-sealable Films*, 6641913, 2003, United States Patent Office.

50. Cakmak, M., Spruiell, J.E., White, J.L., *Small-Angle and Wide Angle X-Ray Pole Figure Studies on Simultaneous Biaxially Stretched Poly(ethylene terephthalate) (PET) Films,* Polymer Engineering and Science 1987, **27**(12), 893-905.

51. Levchik, S.V., Weil, E.D., *A Review on Thermal Decomposition and Combustion of Thermoplastic Polymers,* Polymers for Advanced Technologies, 2004, **15**, 691-700.

52. Macooll, A., *Gas-phase eliminations. Part I. The Unimolecular Gas-phase Pyrolysis of Some Esters and Analogus Compounds,* Journal of the Chemical Society, 1958, 3398-3402.

53. Zimmerman, H., *Developements in Polymer Degradation*, 1984, Applied Science Publishers, Essex.

54. Levchik, S.V., Weil, E.D., *A Review on Thermal Decomposition and Combustion of Thermoplastic Polyesters,* Polymers for Advanced Technologies, 2004, **15**, 691-700.

55. Zhu, H., Kelley, M.J., *IR Spectroscopic investigation of the effect of deep UV irradiation of PET films,* Polymer, 2005, **46**(20), 8883-8891.

56. Brandup, J., Immergut, E.H., *Polymer Handbook*, 3rd ed, 1989, John Wiley & Sons, London.

57. Nealy, D.L., Adams, L.J., *Oxidative Crosslinking in Poly(ethylene terephthalate) at Elevated Temperatures* Journal of Polymer Science Part A-1: Polymer Chemistry, 1971, **9**(7), 2063-2070.

58. Spanninger, P.A., *Thermoxidative Degradation Leading to Gel in Poly(ethylene terephthalate),* Journal of Polymer Science Part A-1: Polymer Chemistry, 1974, **12**(4), 709-717.

59. Ray, S.S., Okamoto, M., *Polymer/Layered Silicate Nanocomposites: A Review From Preparation to Processing,* Progress in Polymer Science, 2003, **28**, 1539-1641.

60. Pinnavaia, T.J., Beall, G.W., *Polymer-Clay Nanocomposites*, 2000, Wiley, Chichester.

61. Brink, A.E., *Thermoplastic Polyester Composites*, in *Modern Polyesters: Chemistry and Technology of Polyesters and Copolyesters*

Ed. Scheirs, J. 2003, Wiley, Chichester.

62. Vaia, R.A., Ginnelis, E.P., *Polymer Melt Intercalation in Organically-Modified layered Silicates: Model Predictions and Experiment,* Macromolecules, 1997, **30**, 8000-8009.

63. Barber, G.D.C., B. H.; Moore, R.B., *Poly(ethylene terephthalate) Ionomer Based Clay Nanocomposites Produced Via Melt Extrusion* Polymer, 2005, **46**, 6706-6714.

64. Yang, H., Song, Y., Xu, B., Qiang, Z., *Preparation of Exfoliated Low-density Polyethylene/Montmorillonite Nanocomposites Through Melt Extrusion* Chemical Research in Chinese Universities, 2006, **22**, 383-387.

65. Ke, Z.Y., B., *Improve the Gas Barrier Property of PET Film with Montmorillonite by In Situ Interlayer Polymerization* Materials Letters, 2005, **59**, 3348-3351.

66. Chang, J.H.K., S. J.; Joo, Y. L.; Im, S., *Polymer-layered Oxide Nanocomposites*, Polymer, 2004, **45**, 919-926.

67. Enomoto, H.L., M. M., *Synthesis and Characterisation of Polymer/TaS2 Layered Nanocomposites* Journal of Physics and Chemistry of Solids, 2004, **65**, 587-590.

68. Li, B.H., Y.; Lui, J.; Chen, Z.; Fan, W., *Preparation of Poly(methyl methacrylate)/LDH Nanocomposite by Exfoliation-Adsorption Process*, Colloid Polymer Science, 2003, **281**(10), 998-1001.

69. Vaia, R.A., Ginnelis, E.P., *Lattice model of polymer melt intercalation in organically-modified layered silicates* Macromolecules, 1997, **30**, 7990-7999.

70. Alexandre, M., Dubois, P., *Polymer-Layered Silicate Nanocomposites: Preparation, Properties and Uses of a New Class of Materials* Materials Science and Engineering R: Reports, 2000, **28**(1,2), 1-63.

71. Ou, C.F., Ho, M.T., Lin, J.R., *Synthesis and Characterisation of Poly(ethylene terephthalate) Nanocomposites with Organoclay* Journal of Applied Polymer Science, 2004, **91**(1), 140-145.

72. Wang, Y., Gao, J., Ma, Y., Agarwal, U.S., *Study on Mechanical Properties, Thermal Stability and Crystallisation Behaviour of PET/MMT Nanocomposites* Composites Part B: Engineering, 2006, **37**(6), 399-407.

73. Ke, Y.C., Yang, Z.B., Zhu, C.F., *Investigation of Properties, Nanostructure, and Distribution in Controlled Polyester Polymerization with Layered Silicate*, Journal of Applied Polymer Science, 2002, **85**(13), 2677-2691.

74. Chung, J.W., Son, S.B., Chun, S.W., Kang, T.J., Kwak, S.Y., *Thermally Stable Exfoliated Poly(ethylene terephthalate) (PET) Nanocomposites as prepared by Selective Removal of Organic Modifiers of Layered Silciate*, Polymer Degradation and Stability, 2008, **93**, 252-259.

75. Xu, X., Ding, Y., Qian, Z., Wang, F., Wen, B., Zhou, H., Zhang, S., Yang, M., *Degradation of Poly(ethylene terephthalate)/clay nanocomposites during melt extrusion: Effect of Clay Catalysis and Chain Extension*, Polymer Degradation and Stability, 2009, **94**, 113-123.

76. Osman, M.A., Ploetze, M., Suter, U.W., *Surface Treatment of Clay Minerals - Thermal Stability, Basal - Plane Spacing and Surface Coverage*, Journal of Materials Chemistry, 2003, **13**, 2359-2366.

77. Cervantes-Uc, J.M., Cauich-Rodriguez, J.V., Vazquez-Torres, H., Garfias-Mesias, L.F., Paul, D.R., *Thermal Degradation of Commerically Available Organoclays studied by TGA-FTIR*, Thermochimica Acta, 2007, **457**, 92-102.

78. Ruiz-Hitzky, E., Meerbeek, A.V., *Clay Mineral- and Organoclay-Polymer Nanocomposite*, in *Handbook of Clay Science*, Ed. Bergaya, F., Theng, B.K.G.,Lagaly, G. 2006, Oxford, Elsevier.

79. Ge, X.G., Wang, D.Y., Wang, C., Qu, M.H., Wang, J.S., Zhao, C.S., Jing, X.K., Wang, Y.Z., *A Novel Phosphorus-Containing Copolyester/Montmorillonite Nanocomposite with Improved Flame Retardancy*, European Polymer Journal, 2007, **43**, 2882-2890.

80. Kurahatti, R.V., Surendranathan, A.O., Kori, S.A., Singh, N., Ramesh Kumar, A.V., Srivastava, S., *Defence Applications of Polymer Nanocomposites*, Defence Science Journal, 2010, **60**(5), 551-563.

81. Yasue, K., Katahira, S., Yoshikawa, M., Fujimoto, K., *In Situ Polymerization Route to Nylon 6-Clay Nanocomposites*, in *Polymer-Clay Nanocomposites*, Ed. Pinnavaia, T.J.,Beall, G.W. 2000, John Wiley & Sons, Chichester.

82. Kandola, B.K., Horrocks, A.R., *Composites*, in *Fire Retardant Materials*, Ed. Horrocks, A.R.,Price, D. 2000, CRC Press, Cambridge.

83. Simmons, W.J., Simmons, W.N., Terrasimco Inc., *Toughened Polyethylene Terephthalate*, 7351756, 2008, United States Patent Office.

CHAPTER 2 INSTRUMENTAL & THEORY

2.1 SONICATION [1, 2]

Ultrasonication is an efficient and widely documented method of preparing nanocomposite suspensions.[3-5] Ultrasound lies within a frequency range of 20 – 100 kHz, which is just above the upper limit for human hearing (18 kHz).

Acoustic energy may be considered to consist of alternating compression and stretching (rarefaction) waves over time in a manner similar to a sine curve and is transmitted through a medium by the enhancement of molecular vibrational motion. As the molecules will physically compress and stretch, the molecular spacing will also alter as the acoustic energy is transmitted. If a large negative pressure is applied during a stretching wave the molecules may exceed the critical molecular distance required to keep the liquids molecular structure intact. This will result in the formation of microbubbles. Subsequent stretching waves will increase the size of the cavitation bubble through vapourisation of the surrounding medium until an equilibrium state is reached. At this point the frequency of the bubbles resonance will equal that of the vibrational energy. Due to the simultaneous formation and resonance of cavitation bubbles individual bubbles will not be surrounded by stable acoustic fields. As a consequence individual bubbles will undergo rapid expansions. The major of expansion produce unstable microbubbles which subsequently violently collapse. As a result high shear forces are felt by the medium with localised temperatures reaching up to 5500 K. With respect to exfoliation of nanoclays, this shearing effect and the formation of cavitation bubbles will result in the expansion of nanoclay microstructures. Platelet tactoids will form intercalated or exfoliated states and fibre bundles will separate into loose clusters. Ideally a homogenous dispersion of the nanoclay would be formed in the liquid medium.

The ultrasonic probe which delivers the acoustic energy consists of a generator, transducer and sonic horn. The generator is the source of the alternating energy which supplies the transducer, which converts the electrical energy to vibrational energy. The sonic horn then modifies the acoustic vibrational output to an amplitude which can be taken in by the medium. The amplitude may be altered through variation in the shape of

the horn tip. Cone, tapered and stepped tips for example magnify the negative rarefraction wave to varying degrees. Typically, the extent of amplitude gain from a probe tip is described through a ratio of the probe entrance and exit diameters.

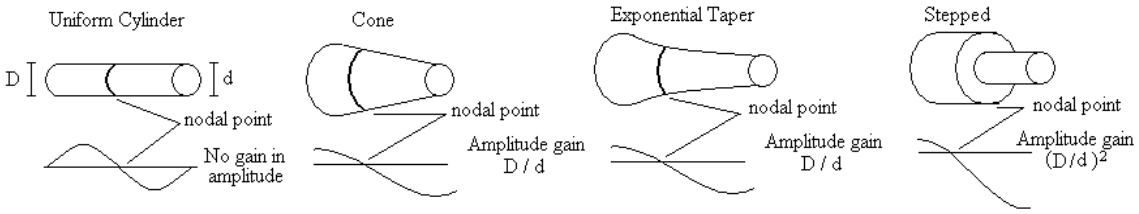

Figure 2.1 Reproduced illustration of horn shapes and their effect on amplification[2]

2.2 RHEOLOGY [6, 7]

Rheology is a useful tool when examining suspensions as it may allow the ability of a nanoclay to exfoliate in a particular medium to be determined. It may also provide information on interplatelet morphology which can provide an indication of bonding interactions. Rheology is therefore a technique which is sensitive to structure formation, particle size, particle shape and molecular interactions.

Viscosity (η) is the "measure of resistance to flow that a fluid offers when it is subjected to shear stress," and was first introduced through Newton's postulate which related the shear stress (σ) and shear strain rate (γ) through the equation 2.2.[8] The postulate was derived as shown in figure 2.2, by considering two parallel plates, both of area 'A' and distance 'd' apart, with the gap between the plates filled with the fluid which is to be sheared. In this instance the lower plate remains constant, and the upper plate will move with velocity, U. As a result not all the fluid within the gap will feel the same shear force and a velocity gradient equal to U/d (or dγ/dt) will exist. This is known as the shear strain rate, γ, measured in s^{-1}. The force required per unit area to produce the plate motion is equal to F/A, and is termed the shear stress (σ), measured in Pascals (Pa).

$$\sigma = \eta\, U/d$$

Equation 2.1

$$\sigma = \eta\, \dot{\gamma}$$

Equation 2.2

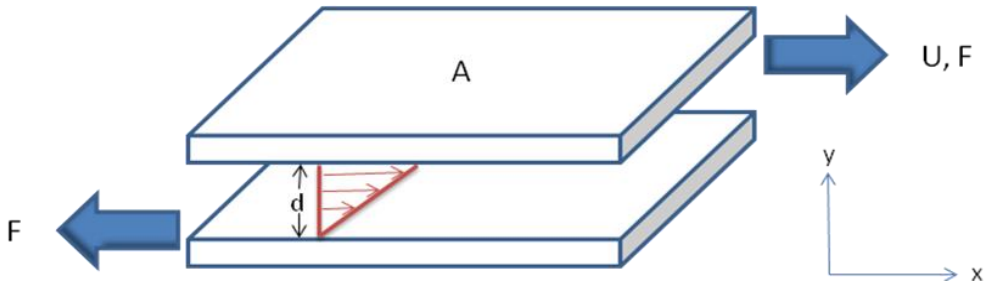

Figure 2.2 Adapted illustration of the velocity gradient produced when a fluid is sheared. The velocity gradient is represented by the red arrows. [9]

In the simplest fluids there is a direct relationship between shear stress and rate i.e. the viscosity is constant. These fluids are known as elastic or Newtonian fluids and must also possess the following qualities:

- The stress in the fluid must fall to zero immediately after shearing is finished.
- In any subsequent shearing the previously measured viscosity must be observed regardless of the time period between measurements.
- The viscosity measurements of different types of deformation are always in simple proportion to one another.

A large number of fluids, however, vary in viscosity with shear rate i.e. they possess a non-linear relationship between shear stress and rate, and these are termed non-Newtonian or viscous fluids. The viscosity is now a function of shear rate and therefore Newton's postulate must be amended to equation 2.3.

$$\sigma = \eta(\dot{\gamma})\dot{\gamma}$$

Equation 2.3

If the fluid obeys all the other conditions however it is known as a generalised Newtonian fluid. Examples of generalised Newtonian fluids are shear thinning, shear thickening and Bingham plastics, all of which have distinctive and characteristic viscosity profiles. Shear thickening fluids are rare and increase in viscosity on shear, an example of which is a solution of cornstarch in water. Bingham plastics exhibit a yield stress, and as long as the yield stress limit is not reached the material behaves like an

elastic solid. If the stress applied exceeds the yield limit the material behaves like a viscous fluid.

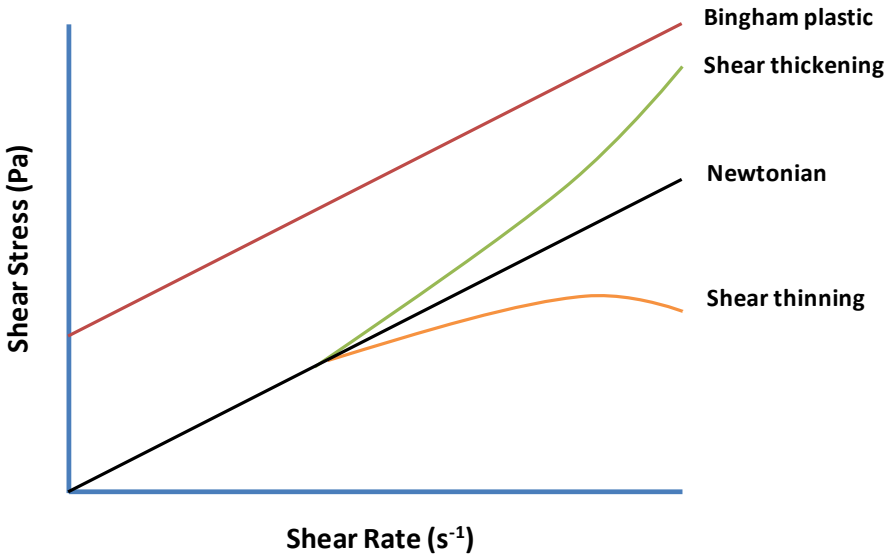

Figure 2.3 Shear stress against shear rate for generalized Newtonian fluids.

The rheological behaviour of nanoclay suspensions has already been discussed in section 1.1.3 and will not be discussed further.

2.3 THERMOGRAVIMETRIC ANALYSIS [10]

Thermogravimetric analysis is a relatively simple method which determines the change in the mass of a sample with temperature. Despite its simplicity, thermogravimetric analysis is a highly useful tool in determining the moisture, organic and inorganic content of a material. In addition insight into the kinetics of various processes may be gained through the onset and maximum temperatures of transitions such as degradation, which may be examined in various environmental conditions.

The sample under analysis is generally held within a quartz or platinum pan which is offset by a counter balance at the back of the instrument. During analysis the furnace encloses the sample and the thermocouple allowing the desired atmosphere and temperature to be maintained.

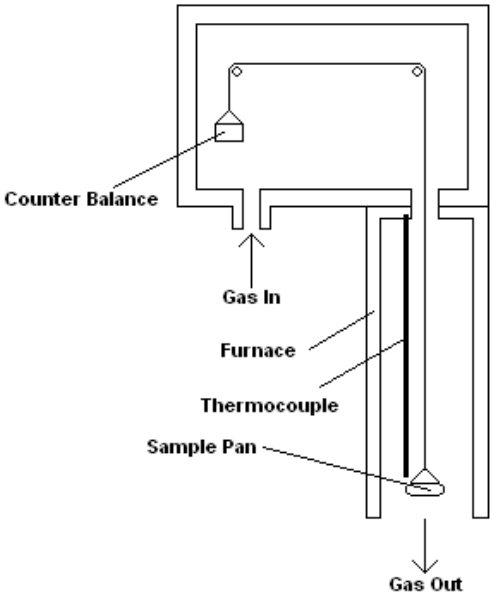

Figure 2.4 Schematic of thermogravimetric analysis instrument.

2.4 DIFFERENTIAL SCANNING CALORIMETRY [11, 12]

DSC is a quantitative and qualitative method of thermal analysis which allows the physical and chemical transitions of a material to be determined through the measurement of energy fluctuations in a system with temperature. During analysis a sample and inert reference are placed in an appropriate form of sample pan and subjected to an identical temperature regime. During analysis the energy required to maintain the sample at a particular temperature is monitored and compared with the reference, with data displayed as a plot of changing heat capacity against temperature. DSC is commonly employed in determining the enthalpy and temperatures of events such as the glass transition, crystallisation, crystalline melting and degradation.

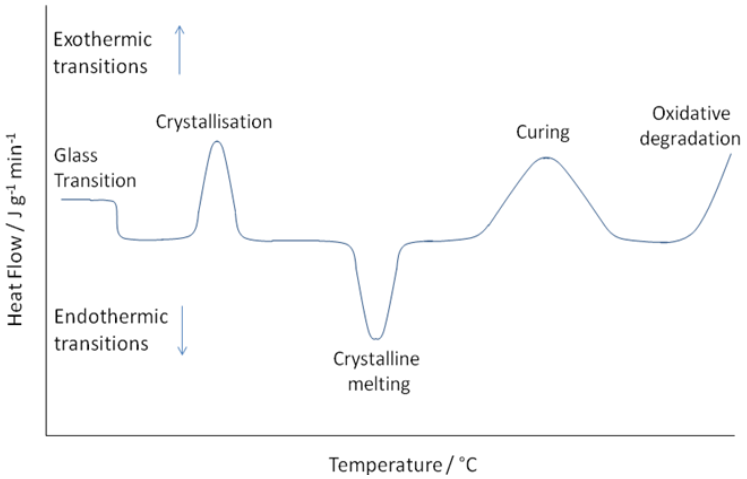

Figure 2.5 Illustration of energetic transitions which may be observed by DSC.

DSC instruments offer the choice of two systems for analysis; heat-flux and power compensation. Power compensation systems employ two separate identical furnaces for the sample and reference set at identical conditions. The variation in power required to keep the furnace at a temperature equal to that of the reference determines the heat capacity. Within heat-flux systems a single furnace is employed containing both samples. The samples are connected by a metal disk with a low resistance to heat flow. Any change in sample heat capacity again causes a difference in temperature in comparison to the reference.

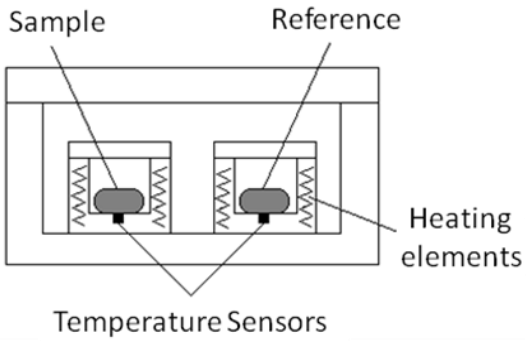

Figure 2.6 Illustration of typical heat-flux measuring cell as employed in the DSC Q1000.

The heat flow curve which is expressed within the DSC thermogram, which describes the change in enthalpy (ΔH) over a specific temperature range (ΔT), or ΔH/ΔT, and is expressed within the DSC thermogram is calculated as a function of both the heating rate and effective heat capacity via equation 2.4, where C_p is the effective heat capacity at a constant pressure (J/ °C) and ΔT/Δt is the heating rate (°C min^{-1}). f(T,t) is the

contribution to the heat flow from the kinetic processes in a sample and illustrates that a samples response to a change in temperature is not instantaneous.

$$\frac{\Delta H}{\Delta T} = Cp\frac{\Delta T}{\Delta t} + f(T,t) \qquad \text{Equation 2.4}$$

The effective heat capacity is calculated by multiplying the specific heat capacity by the mass of the sample under study. The specific heat capacity itself may be defined as the energy required to alter the temperature of a substance by 1°C (without a transition in structure), with units are in J g^{-1} $°C^{-1}$. As the heat capacity is a measure of the molecular motion of a material, an increase in heat capacity will be accompanied by an increase in the vibrational, rotational or translational movement of a material's molecules. As a result, temperature transitions which are accompanied by a change in molecular movement, for example crystallisation or crystalline melting, may easily be observed through a change in heat capacity.

2.5 TRANSMISSION ELECTRON MICROSCOPY[12, 13]

Within transmission electron microscopy an electron source such as an electron gun emits electrons which are condensed though an anode plate into the main microscope column. The beam is then focused into a fine, intense beam using electromagnetic lenses in a similar manner to light microscopy. The beam passes through the sample stage and then an objective lens re-focuses the electron beam. A projector lens then magnifies the image further onto a fluorescent screen which converts the electron energy into a visual image.

The resolution of an electron microscope is determined by the wavelength of the electrons, in the same manner that the wave length of optical microscopy is determined by the wavelength of light. The shorter the wavelength the better the resolving power of the microscope. The wavelength may be tuned through altering the electron potential difference at the source, as described through the relationship in equation 2.7.

$$eV = {}^{1}/_{2}mv^{2} \qquad \text{Equation 2.5}$$

$$\lambda = h / mv \qquad \text{Equation 2.6}$$

Therefore, $$\lambda = h / 2eV.v \qquad \text{Equation 2.7}$$

where eV is the energy of the electron (equal to the accelerating voltage at the potential difference), m is the mass of the electron, v is the velocity of the electron, λ is the wavelength of the electron and h is Planck's constant.

The tone (or greyscale) within the electron micrograph are due to differing levels of electron scattering. Materials such as metals with high atomic numbers scatter electrons to a greater degree and therefore regions appear dark in the micrograph. Organic compounds with lower atomic numbers scatter weakly and therefore appear more brightly.

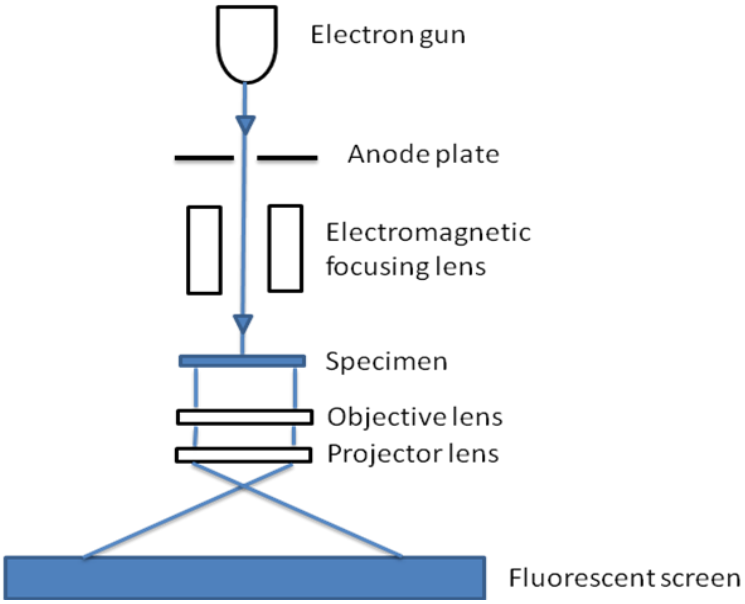

Figure 2.7 Schematic of a transmission electron microscope.

2.6 SCANNING ELECTRON MICROSCOPY (SEM) [14, 15]

In SEM an electronic image of a material is generated by rastering a high energy electron beam over its surface. As a result deflected primary electrons (originally from the electron beam itself), ejected secondary electrons or emitted x-ray photons may all be detected and compositional and/or topographical information may be gained.

Firstly an electron beam is generated by an electron gun, most commonly a thermionic emission gun. The current is initially adjusted by a Wehnelt electrode carrying a negative voltage before the beam is focused by an anode. The smallest diameter the electron beam achieves is known as the crossover and is regarded as comparative to diameter of the electron beam as it is ejected from the source. The beam is then passed through at least one magnetic condenser lens which alters the diameter and current of the electron beam before passing through the scan coils. The scan coils direct the position of the beam allowing it to sweep or raster over the sample at a pre-determined rate. The beam then finally passes though a magnetic objective lens which re-focuses the beam prior to it hitting the sample under study. Figure 2.8 contains a schematic of a typical SEM instrument.

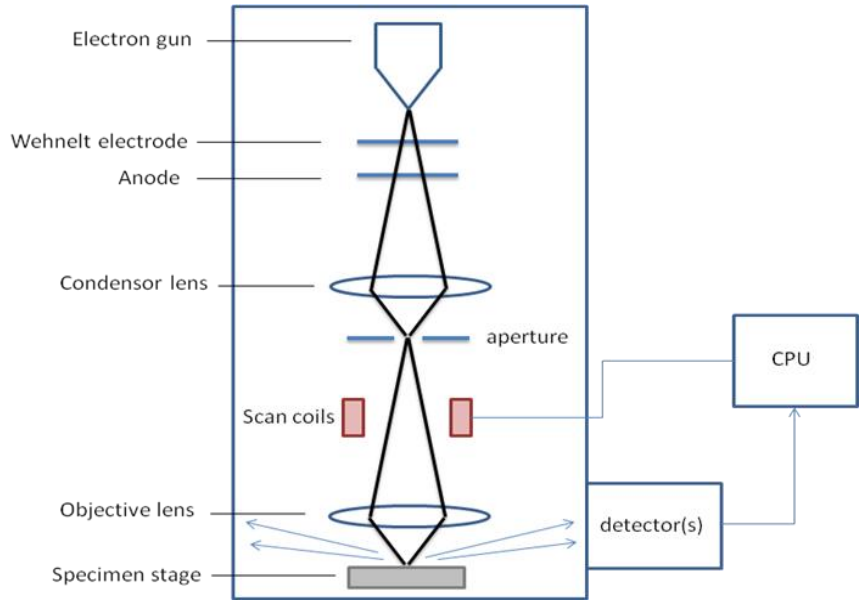

Figure 2.8 Schematic of a typical SEM instrument.

Compositional information may be gained from both backscattered electrons and ejected photons (or x-rays). Backscattered electrons are electrons which originate directly from the electron beam and have been scattered elastically (i.e. without the loss of energy) from the atomic nuclei. The extent of backscattering from a particular atom is directly related to the atomic number. Higher atomic numbers are more efficient at scattering the electron beam elastically. Regions containing atoms of a high atomic number such as metal particulates therefore appear brighter than those with a low atomic number for example organic substances. X-ray photons provide information on

the energy required for particular electronic transitions within an atom and as a result allow the qualification of a substance or particulate. X-rays are generated due to an outer shell electron dropping into an inner shell vacancy. This vacancy has been created as a result of the electron beam interacting with the atomic electrons, ejecting so-called secondary electrons from within the atom.

Topographical information may be gained from the secondary electrons ejected on interaction with the electron beam. If the electrons originate from within a surface indentation or pit it is likely they will collide with the banks of the indentation and therefore not reach the detector. Small extrusions or mounts however will eject a greater proportion of secondary electrons into free space and therefore a greater proportion of electrons will reach the detector. As a result indentations will appear as dark regions within the SEM image and extrusions will appear brighter.

Scanning electron microscopy differs from transmission electron microscopy as the image is generated due to reflected electrons, rather than those which have been transmitted through the sample. The image is also built up step by step rather like a jigsaw, and therefore the electron beam at no point carries the full set of information for the specimen area under study as is the case for transmission electron microscopy. In addition, due to the lower energy electron beam (and hence longer wavelength), scanning electron microscopy also carries a lower resolution.

2.7 X-RAY DIFFRACTION [16, 17]

X-rays are a form of electromagnetic radiation which have a wavelength of between 0.01 and 10 nm. X-rays are generally generated by x-ray tubes for laboratory scale experiments when a high energy electron beam bombards a metal target. As the electrons collide with the atoms in the metal they decelerate and a spectrum of x-rays are emitted. The high energy electrons are also able to eject inner shell electrons. When an electron is ejected electrons at a higher orbital are able to fall down to fill the empty space and restore equilibrium. This occurs with the emission of an x-ray photon with a characteristic energy. The energy of the photon is related to its wavelength through the equation $E = hc/\lambda$, where h is Planck's constant and c is the speed of light.

When an x-ray comes into contact with an atom its electrons will oscillate at the same frequency as the incoming beam. In the majority of directions the x-ray waves will be out of phase. This means that destructive interference will occur when the waves are combined. Atoms which are arranged in a regular manner (for example in a crystal) however will have electrons which oscillate in phase. As a result there will be constructive interference i.e. the waves will be well defined and x-ray beams will be able to exit the sample in various directions determined by the crystal lattice under study. Within the lattice, the atoms can be considered to lie in various planes or 'mirrors', separated by distance d. The path length of the x-rays differs by a distance of AB + BC, and this distance is dependent on a pre-determined angle theta. Destructive interference is said to occur when AB + BC is equal to a non-integer number. When AB + BC is equal to an integer number the waves are in phase and constructive interference will occur where they will positively reinforce one another, i.e. AB + BC equals nλ and Bragg's Law is satisfied.

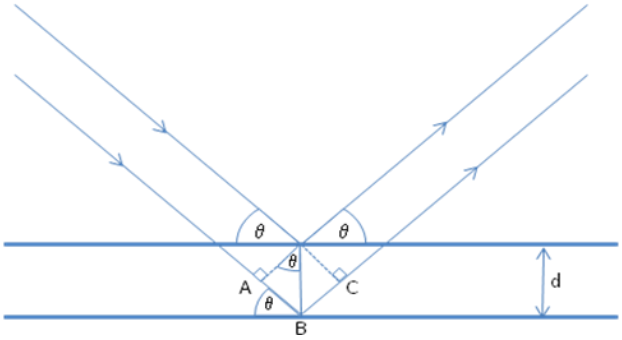

Figure 2.9 Illustration of x-ray beams reflecting off a crystal lattice.

The XRD pattern of a crystalline substance can be likened to a fingerprint as it will exhibit the same set of characteristic reflective peaks regardless of environment or whether there are additional substances present. Only if the crystalline structure itself alters will there be a change in the XRD pattern. XRD is therefore an ideal technique to determine the identity of the unknown Garamite® nanoclay utilised within this thesis.

2.8 NUCLEAR MAGNETIC RESONNACE (NMR) [12, 18, 19]

NMR allows the identification of atoms or functional groups within an unknown molecule and their positions relative to one another. The technique monitors the

interaction of nuclei after an off-resonance magnetic pulse which changes the orientation of the magnetic spin of the nuclei out of its equilibrium state. The relaxation pattern back to equilibrium is dependent on the functional groups the atom is bonded to, in addition to further spin-spin coupling which involves the coupling of the nuclear spin through valence electrons.

The interaction of nuclei is dependent on whether they possess a nuclear magnetic spin i.e. the total spin of the neutrons and protons within the nucleus is not equal to zero. If the total spin did equal zero there would be no interaction with the magnetic field.

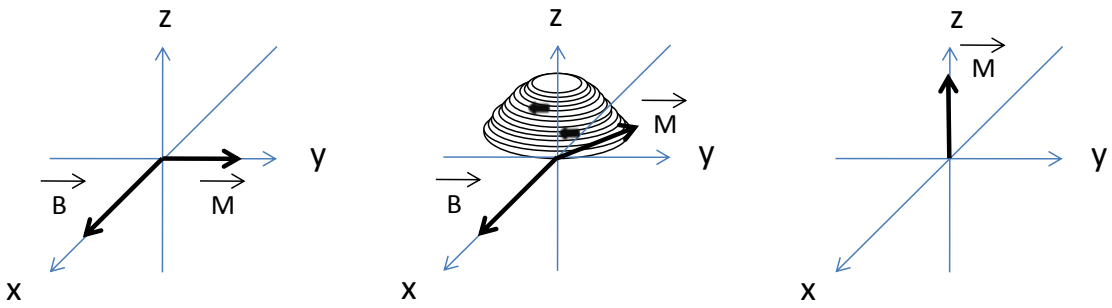

Application of a 90° magnetic pulse around the x-axis aligns the sample magnetism in the y-direction.

The magnetic field is turned off and M returns to z' by a gradual ascending spiral about z. During this process, M rotates about the z-axis several millions of times at the Lamour frequency.

After relaxation, the bulk of the magnetism has returned to its equilibrium value M_0.

Figure 2.10 Reproduced illustration of the excitation and relaxation of a magnetic field by an off-resonance pulse[10]

As the magnetic moment of a nucleus is a vector quantity it possesses both magnitude and direction. It will therefore also orientate itself in a certain manner when the magnetic field is applied. The most common nuclei to be observed are ^{1}H and ^{13}C which have a nuclear spin of half, and so the application of a magnetic field can either orientate the atoms parallel (into a low energy state) or anti-parallel (into a high energy state) with respect to the field direction.[10]

Data is then collected in the form of a sinusoidal plot of time against intensity as the magnetic moment decays back to equilibrium. As there may be hundreds of atoms under examination in varying environments the interpretation of spectra may be

difficult as many different decay patterns maybe superimposed on one another. Fourier transformation of the data simplifies interpretation through creating a line plot of the signals, with each line corresponding to a frequency of the relation (sine) wave. There are two different manners in which the off-resonance nuclei can decay back to their equilibrium state; spin-lattice and spin-spin relaxation.[10] Spin-lattice relaxation involves the transfer of energy from the nuclei to the environment of the surrounding lattice, whereas spin-spin relaxation involves direct transfer of energy to surrounding nuclei through interaction of their nuclear spins without any transfer to the lattice.

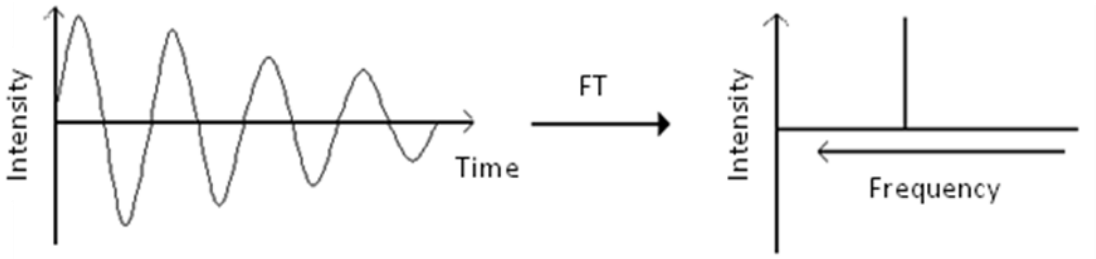

Figure 2.11 Fourier transformation of a free induction decay.

2.9 INFRARED SPECTROSCOPY [18, 19]

All atoms vibrate at temperatures above absolute zero and within a molecular environment these vibrations cause additional stretching and bending of the bonds connecting them. Infrared spectroscopy exploits these vibrations in order to identify distinct functional groups within a molecule, enhancing them through the absorption of quantized packets of energy which produce a change in the dipole moment of the molecule. It should be noted that it is only the vibrational energy state and not the electronic energy state of the molecule which changes during infrared excitation.

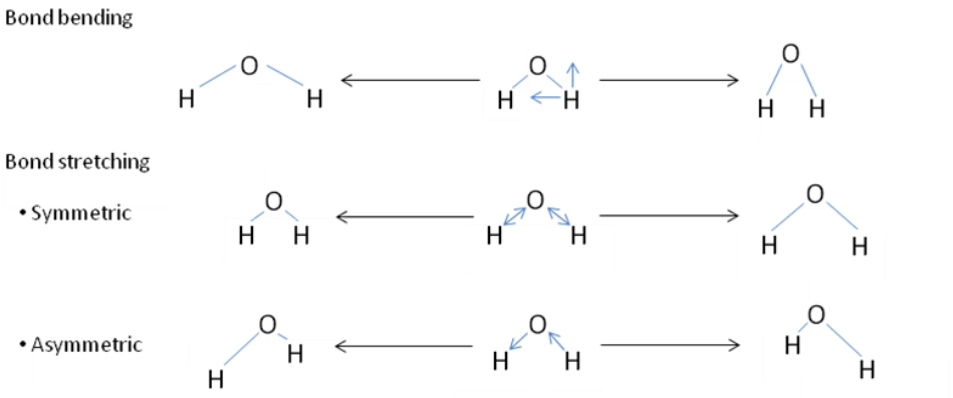

Figure 2.12 Modes of water bending and stretching in a water molecule on infrared absorption

Infrared spectroscopy can provide both qualitative and quantitative information about a sample. Qualitatively, an unknown can be determined through peak identification. Quantitative measurement involves the identification of ratios of known components within a mixture. This is achieved through the monitoring of transmittance or absorption, with the absorption determined through the logarithm of transmittance or Beer-Lambert's Law.

$$A = \log_{10}(I_0 / I) = \log_{10}T \qquad \text{Equation 2.8}$$

Beer-Lambert's Law: $A = \varepsilon bc$ Equation 2.9

where I_0 and I are the intensity of the incident and transmitted light respectively, T is therefore the transmittance of the light, ε is the molar absorptivity of the sample, b is the cell path length and c is the concentration of the sample.

An IR spectrometer consists of a source which emits light through the entire infrared frequency range, mirrors to reflect the light in the desired direction, a specimen and reference cell, a chopper, monochromator and detector. Figure 2.13 illustrates a general schematic of an IR spectrometer. Initially the light source is split into a reference and sample beam. The beams then pass through their respective cells and through a chopper which selects the beam of interest, before passing through a prism and monochromator. The prism scatters the light into individual frequencies and the monochromator allows the range of wavelengths of interest to be isolated and passed onto the detector. The

sample spectrum is produced in the case of transmittance by comparing the intensity of the light at the selected wavelengths.

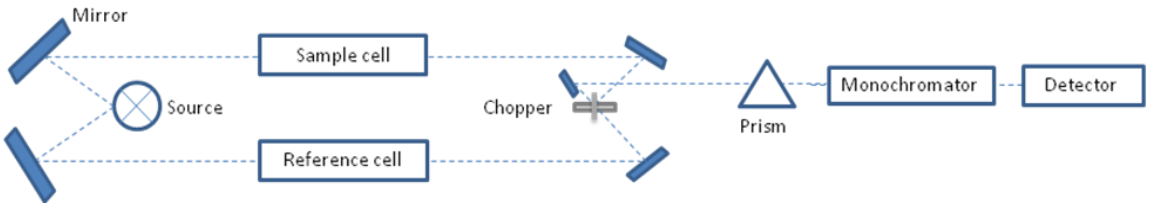

Figure 2.13 Schematic of a typical infrared spectrometer.

2.10 GEL PERMEATION CHROMATOGRAPY [19]

Gel permeation chromatography is a form of size exclusion chromatography in which the sample components are separated by molecular size due to differing hydrodynamic volumes. A dilute polymer solution is injected into the column packed with porous polymer beads. The porosity of the beads will determine the resolution in separation, with pores sizes typically in the range of 50 to 10^6 Å. The smallest molecules present are able to pass through a large proportion of the pores, which increases the retention time within the column. The largest molecules however are confined to the mobile phase and as a consequence possess a much shorter retention time. The molecules will therefore elute from the column in an order of decreasing molecular size. The molar mass may be determined through a comparison of the elution times and/or refractive index of the eluting solution with calibrant samples of a known molar mass and a similar radius of gyration.

2.11 THERMAL VOLATILISATION ANALYSIS (TVA) [20-23]

TVA is an ideal technique with which to study the degradation of polymer systems as it provides a detailed description of the degradation products and hence an insight into a polymer's degradation mechanisms. The separation and identification of the degradation products is achieved by the differential distillation of the liquid composite after the initial degradation run. The liquid composite consists of the species released during the degradation run which are condensable between ambient and cryogenic temperatures. They are heated until boiling and then the vapour is collected and

condensed into various fractions of distillate. Obviously the composition of the remaining liquid and the distillate are functions of time. Differential distillation is a technique often used in industry where small volumes of liquid are in use, separations are only performed occasionally, upstream operations are batch process, or if a feedstock varies with time or between batches. Due to the small sample sizes and also complex and potentially fluctuating composition TVA is therefore an ideal tool to examine polymer degradation.

The sub-ambient TVA line used for analysis was built in-house at the University of Strathclyde by Dr John Liggat and Dr James Lewicki. Figure 2.14 contains a schematic of the apparatus.

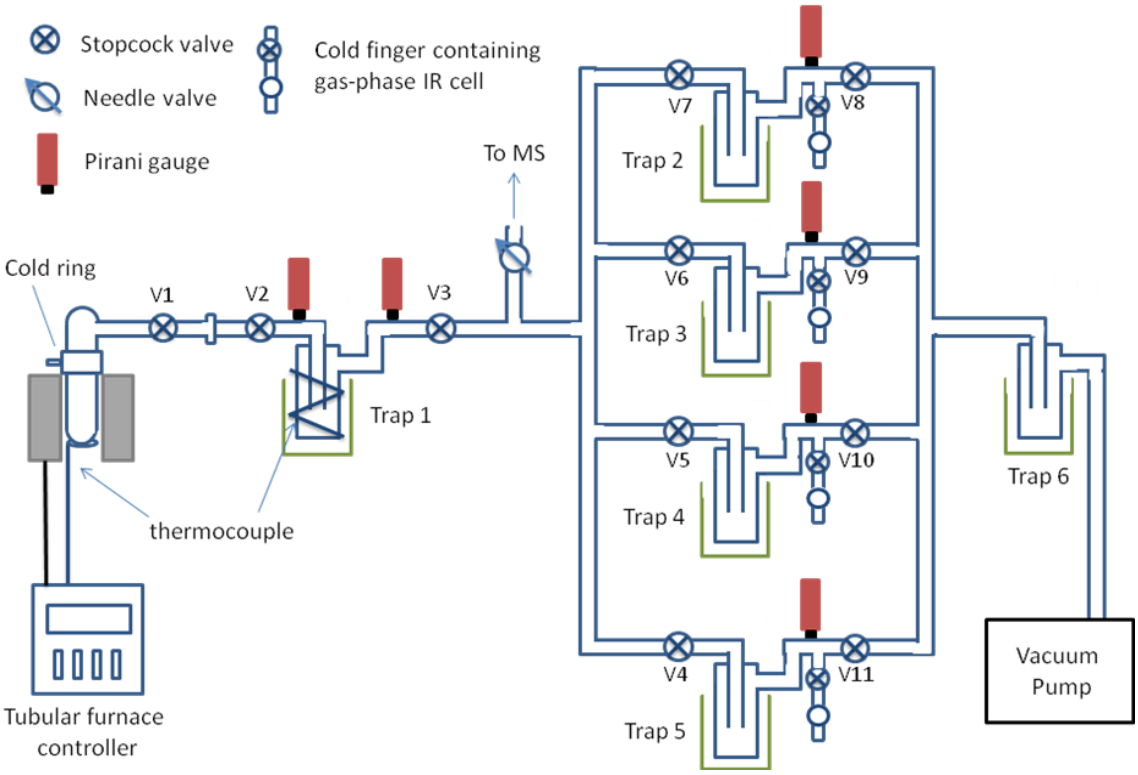

Figure 2.14 Schematic of sub-ambient TVA line.

The sample is loaded into a TVA sample tube and positioned in a tubular furnace. A thermocouple relays feedback to the controller and a ringed water jacket (or cold ring) allows cold water to encircle the tube. The cold water temperature is generally between 10°C - 14°C and the purpose is to condense the higher molar mass volatiles which do not require cryogenic temperatures. Additionally, the cold ring prevents contamination

of the TVA line with degradation products which would require an organic solvent to remove and therefore disassembling of the line.

The sample is pumped down under a high vacuum and degraded during a linear heating ramp and volatiles which are not condensable at cryogenic temperatures are detected by the mass spectrometer and pass through the vacuum line unhindered. Volatiles which are condensable at cryogenic temperatures are collected within the primary trap (trap 1) and undergo sub-ambient distillation after the degradation run is complete. The quantification of the non-condensable volatiles may therefore be achieved to some extent through the Pirani pressure gauges situated at the entrance and exit of trap 1.

Trap 1 differs from the secondary traps (traps 2-5) as it is not simply for the purpose of collecting volatiles and requires a heating element in order to distill the condensable volatiles over a linear ramp rate. Figure 2.15 contains an illustration of trap 1. A double u-tube design is also employed in order to maximise the surface area in contact with the volatiles and so ensure a homogeneous temperature throughout. A nickel-chrome alloy heating wire is coiled around the double u-tube, and the temperature is controlled through a platinum resistor wired to the heating controller. The temperature of the u-tube is recorded throughout the distillation process using a K-type thermocouple attached to the adjacent arm. PET insulating beads are also employed in order to prevent an atmospheric influence which may result in the volatiles rising or decreasing in temperature at too high a rate. During the degradation run the trap is immersed in a dewar containing liquid nitrogen. When the distillation process is initiated the dewar is removed and the nickel-chrome heating wire is set to ramp the temperature at a linear rate. A typical heating range for the trap is between -196°C and +40°C but it is generally defined by the material under investigation.

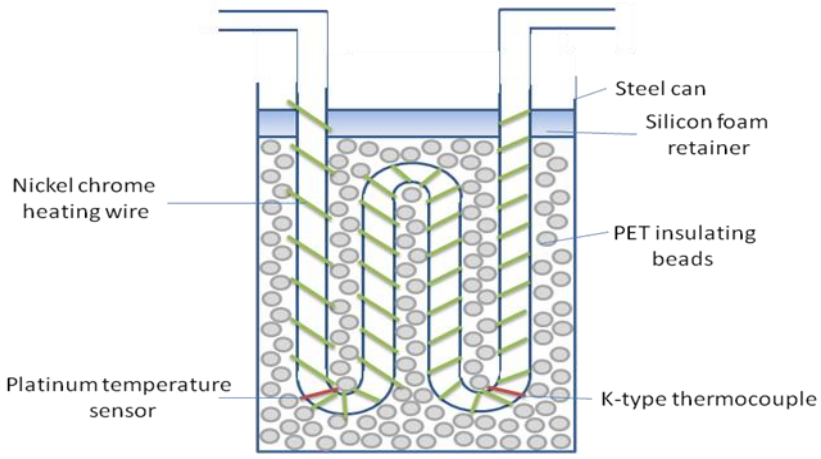

Figure 2.15 Diagram of the primary cryogenic trap (trap 1).

The secondary cryogenic traps then allow four fractions to be collected for further analysis. The temperature ranges for fraction collection are also user and material defined, and are guided by the pressure reading of the exit Pirani of trap 1. Each secondary cryogenic trap possess a cold finger which contains a built-in sodium chloride gas phase IR cell. The cold fingers within traps 2-4 are aligned with the IR cell, however within trap 5 the cold finger is attached via a perpendicular arm which allows the addition of a B10 capped extraction point. As the final trap typically contains a mixture of high molar mass species the option of an additional attempt at identification is valuable. If required the cold finger is cooled to cryogenic temperatures and the material is extracted into chloroform for analysis.

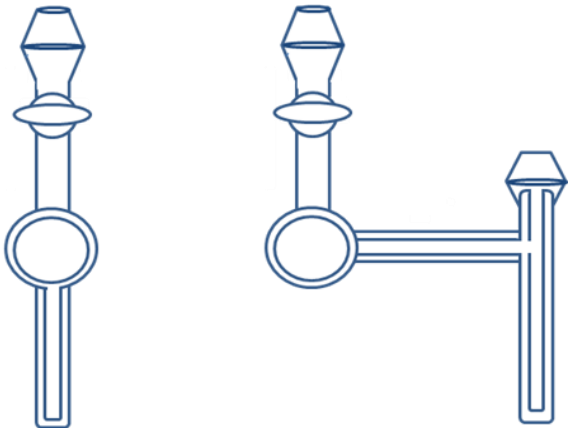

Figure 2.16 Linear cold finger on secondary traps 2-4 (left) and cold finger with B10 capped extraction point (right).

2.12 GAS CHROMATOGRAPHY – MASS SPECTROMETRY [24, 25]

Gas chromatography – mass spectrometry is a technique which combines gas-liquid chromatography and mass spectrometry. The components of a mixture are separated by gas chromatography and then a mass spectrometer is employed as the detector.

Gas chromatography is a technique employed for separating mixtures of components and can only be utilized where components are stable on vapourisation. During GC analysis a known volume of gaseous or liquid sample is injected into the head of the column. If required the sample is vapourised and carried into the column by the mobile phase (which is typically an inert gas such as helium). As the sample is carried through the column its passage is inhibited due to adsorption onto the stationary phase with which the column is packed. Each component of the sample will interact with the stationary phase to different levels and therefore separation is dependent on the interactions possible between the two phases. In addition, retention times may also be influenced through experimental parameters such as the carrier gas flow rate, the stationary phase and the temperature. After the mixture has been separated within the column it elutes through a detector, in this case a mass spectrometer.

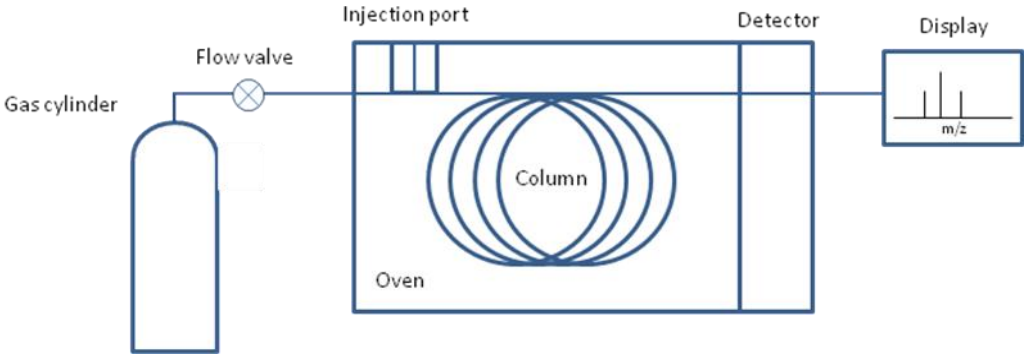

Figure 2.17 Schematic diagram of a gas chromatography instrument.

Mass spectrometry is a technique which measures the mass to charge ratio of a charged particles. A typically mass spectrometer consists of three sections: and ion source, a mass analyzer and a detector. Initially, the sample is vapourised if required then passed to the ion source which converts the gaseous molecules into ions. Various techniques may be used depending on the molecular properties and degree of fragmentation

required and hence complexity of the spectrum. Examples of commonly employed ion source techniques are chemical ionization, electrospray ionization and inductively coupled plasma. Once the sample has been ionized it is carried by magnetic or electric fields to the mass analyser which sorts the ions with respect to their mass to charge ratio. Commonly a quadrupole is employed which consists of four metal cylindrical rods to which an oscillating electrical field is applied, allowing the ions to be separated based on their stability within the oscillating electric field. Those which are more stable travel down the quadrupole via more direct route than those which are not. Obviously ions with a particular mass to charge ratio will possess a stable trajectory within a specific applied field. As a result the electric field must be varied to allow a mass spectrum of a sample to be built by the detector, which is typically an electron multiplier or Faraday cup.

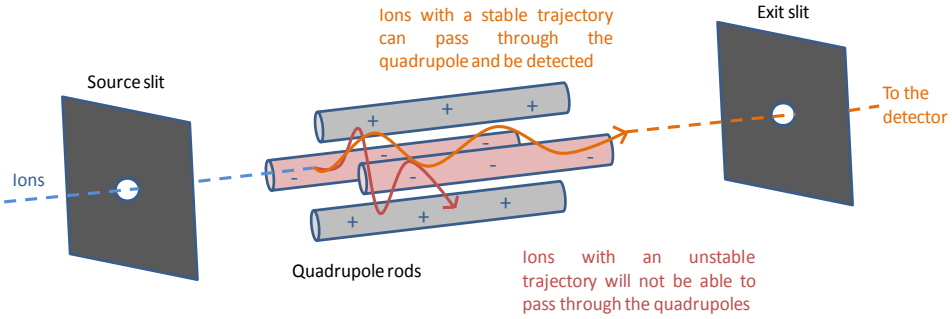

Figure 2.18 Simplified illustration of a quadrupole mass analyser.

2.13 THEORY OF KINETIC DEGRADATION MODELS

2.13.1 ARRHENIUS MODEL

The original Arrhenius equation was derived through collision theory. In an example reaction with reactants A and B, the rate of collisions is said to be proportional to their concentrations, i.e.

$$\text{Rate of collisions} \propto [A][B] \qquad \text{Equation 2.10}$$

Not all collisions however possess the minimum kinetic energy which leads to a reaction and collide along an appropriate line of approach. The rate of collisions must

then be multiplied by the fraction of collisions which possess this minimum kinetic energy and orientation. The probability of these fractions is equal to $e^{(-Ea/RT)}$.[26]

$$\text{Reaction rate} \propto [A][B]e^{(-Ea/RT)} \qquad \text{Equation 2.11}$$

It is known that a second order rate equation takes the form,

$$\text{Reaction rate} = k[A][B] \qquad \text{Equation 2.12}$$

Therefore if a pre-exponential factor is equated with reaction proportionality the rate at which reactants collide may be described through equation 2.13, the Arrhenius equation.

$$k = Ae^{(-Ea/RT)} \qquad \text{Equation 2.13}$$

Practically, the Arrhenius equation is an indirect method for determining the rate constant and provides a means to calculate the additional Arrhenius parameters; the pre-exponential factor, A, and activation energy, E_a. The Arrhenius model may be applied to data obtained during thermogravimetric analysis, where the maximum gradient in a plot of % weight against time is associated with the negative of the reaction rate, -k, at a specific temperature. If analysis is performed at a variety of heating rates and the data is manipulated into the form lnk and 1/T (where T is the temperature at which the maximum gradient occurs) then an Arrhenius plot may be generated. The values should exhibit a linear relationship with intercept lnA and gradient $-E_a/R$. Further information on the application of the Arrhenius model to a data set may be found in chapter 7.

The Arrhenius parameters are for the most part independent of temperature, and can be assumed as such during the calculation and examination of the Arrhenius model. The insignificant dependence they have on temperature is accounted for by collision theory, but both depend on the reaction under study.[27] The activation energy itself indicates the degree of temperature dependence the rate constant possesses. A high activation energy indicates a strong dependence on temperature, i.e. the reaction rate is sensitive to changes of temperature. Low activation energies alter only slightly with changes in

temperature. This is reflected in the gradients obtained in the Arrhenius plot, with a low temperature dependence resulting in a shallow gradient, and high temperature dependence a steep gradient.

2.13.2 AMERICAN STANDARD TEST METHOD E1641[28]

Whilst the Arrhenius method was described as an indirect method of determining kinetic parameters, American Standard Test Method E1641 (ASTM 1641) in comparison is substantially more direct. This description may be coined due to the assumption by the Arrhenius method that the maximum rate of weight loss equates to the maximum rate of sample degradation. As the maximum rate of weight loss is often dependent on the heating rate, analysis is dependent to a greater degree upon the analysts' judgement.

ASTM 1641 can be considered a more efficient method as the Arrhenius parameters are analysed at an identical degree of sample conversion during degradation. This is a more efficient method as theoretically, the reaction rates and mechanisms at a particular degree conversion during degradation should be directly comparable regardless of heating rate. In addition, iterative calculations allow for the refinement of the activation energy and therefore a more precise calculation of the pre-exponential factors and rate constants.

The various degrees of conversion employed during analysis were calculated via equation 2.14.[29] α is the conversion value, w_o is the initial percentage weight (100 %), w is the percentage weight at any temperature and w_α is the final percentage weight.

$$\alpha = \frac{w_0 - w}{w_0 - w_\alpha} \qquad \text{Equation 2.14}$$

Initially, calculations are performed at various degrees of conversion. ASTM 1641 recommends at least a 5%, 10%, 15% and 20% variability; however 1%, 2% and 40% were also included to ensure a thorough inspection of conversion behaviour. The presence of impurities such as the nanoclay would affect low conversion values to a

more significant extent than the larger values. At a greater degree of conversion however competing degradative mechanisms may also be observed due to differing behaviours. The potential for competing mechanisms was the key reason for recommending a conversion value no greater than 20%, and likewise a value no less than 5% due to interference by impurities. The author considered however this could potentially give a more comprehensive insight into the degradative processes underway if a more extensive conversion range was studied.

For the selected range of conversions under study, the logarithm of the heating rate, β (K min^{-1}) was plotted against the reciprocal of the temperature at that each particular degree of conversion. Linear data fitting allowed determination of the gradient which was numerically equated as $\Delta(\log \beta)/\Delta(1/T)$.

An estimated activation energy was calculated through equation 2.15. The b value was a numerical integration constant which allowed the refinement of the activation energy. The table of integration constants may be found in appendices 6 and 8. The estimated activation energy (denoted E_e) was then employed in calculating E_e/RT. E_e/RT in turn was then used to determine a new numerical constant and estimation of the b value. This procedure was iterated until there was less than 1% variability in the activation energy, where the activation energy (E_r) could be said to be suitably refined.

$$E = -\left(\frac{R}{b}\right) * \left(\frac{\Delta \log \beta}{\Delta \log(1/T)}\right) \qquad \text{Equation 2.15}$$

The pre-exponential factor was calculated according to equation 2.16, which also incorporated a numerical constant, α, which may be found within the appendices, and was determined from the refined value of E_r/RT. β' was the median heating rate under study. The Arrhenius equation was then employed to calculate the rate constant.

$$A = -\left(\frac{\beta'}{E_r}\right) * R * \ln(1-\alpha) * 10^{a} \qquad \text{Equation 2.16}$$

2.13.3 KISSINGER MODEL

The Kissinger model allows the activation energy of a dynamic degradation process to be determined via observing the shift in the maximum peak temperature when the heating rate is varied. [30] The activation energy may be calculated using the gradient of the line obtained by plotting $\ln(q/T_p^2)$ against $1/T_P$. The gradient is hence equal to $-E_a/R$, with E_a calculated through multiplication by –R. Equation 2.17 is the Kissinger equation, where E_a is the activation energy (kJ mol^{-1}), R is the universal gas constant (8.3143 J $mol^{-1}K^{-1}$), q is the heating rate (K min^{-1}), T_p is the maximum peak temperature (K) and m is the gradient of the line of best fit within the Kissinger plot.

$$E_a = -R\left[\frac{d\left(\ln\left(\frac{q}{T_p^2}\right)\right)}{d\left(\frac{1}{T_p}\right)}\right] = -Rm \qquad \text{Equation 2.17}$$

Once the activation energy has been determined the pre-exponential factor, A, can be calculated through re-arranging equation 2.18 to equation 2.19 .[31, 32] Once E_a and A have been determined, k can then be calculated through the Arrhenius equation.

$$\frac{E_a}{RT_P^2} = \frac{A}{q^2} exp\left(\frac{-E_a}{RT}\right) \qquad \text{Equation 2.18}$$

$$A = \left(\frac{\left(\frac{E_a q^2}{RT_p^2}\right)}{\exp\left(\frac{-E_a}{RT}\right)}\right) \qquad \text{Equation 2.19}$$

There are however several shortcomings of the original Kissinger model. The most apparent is the assumption that the peak maximum corresponds to the maximum degradative rate. Degradation, especially that of polyesters such as PET is complicated

and chaotic, and is very much dependent upon the heating rate. Kissinger himself recognised this with respect to differential thermal analysis in particular, and published in order to ascertain confidence that the peak maximum could reliably be assumed as the degradation maximum.[33] Other authors have also examined and verified the dependability in employing the maximum peak temperature as the maximum rate.[32] One of the key advantages to the Kissinger method however despite criticism is the ability to determine the activation energy without knowing the degradative reaction mechanism.[34]

2.13.4 AMERICAN STANDARD TEST METHOD E698 [35]

American Standard Test Method E698 (ASTM E698) is a contemporary test method developed in order to examine the dynamic degradation behaviour in polymer systems. It is similar to the previous contemporary method in the manner that the Arrhenius parameters are calculated and makes several assumptions of the degradation reaction. ATSM E698 assumes the degradation reaction follows Arrhenius behaviour, first order reaction kinetics and also assumes the extent of the reaction at the exotherm peak maximum is constant and independent of heating rate.

Samples are subjected to heating rates between 1ºC min^{-1} and 20ºC min^{-1} in order to determine the variation in maximum peak temperatures. The natural logarithms of the heating rates are then plotted against 1/T for each particular system and the gradient, $\Delta(\log \beta)/\Delta(1/T)$, may then employed in the calculation of the activation energy. Initially, an estimated activation energy is calculated (E_e) via equation 2.20 and then subsequently used to calculate E_e/RT. The approximate E_e/RT value corresponded to a particular approximation constant, D, which may then be employed within equation 2.21 which allowed a refinement of the calculated activation energy. This procedure was iterated until there was less than 1% variability in the activation energy, where the activation energy could be said to be suitably refined and may be denoted E_r. The pre-exponential factor and reaction rate were then able to be calculated via equation 2.22 and 2.23, respectively.

Nota bene. The approximation constants used within this model may be found within appendices 6 and 8.

$$E_e \cong -2.19R * \Delta(\log \beta) / \Delta(1/T_m) \qquad \text{Equation 2.20}$$

$$E = (-2.303R/D) * \Delta(\log \beta) / \Delta(1/T_m) \qquad \text{Equation 2.21}$$

$$A = \beta E e^{-Er/RT} / RT_m^{\ 2} \qquad \text{Equation 2.22}$$

$$k = A \exp\left(-\frac{E_r}{RT}\right) \qquad \text{Equation 2.23}$$

2.14 REFERENCES

1. Mason, T.J., *Practical Sonochemistry*, 1991, Ellis Horwood, New York.
2. Mason, T.J., *Sonochemistry*, 1999, Oxford Science Publications, Oxford.
3. Enomoto, H., Lerner, M.M., *Syntheses and Characterisation of Polymer/TaS_2 Layered Nanocomposites*, Journal of Physics and Chemistry of Solids, 2004, **65**(2,3), 587-590.
4. Chern, C.S., Lin, H.J., Lin, Y.L., *Kinetics of Styrene Emulsion Polymerisation in the Presence of Montmorillonite*, European Polymer Journal, 2006, **42**(5), 1033-1042.
5. Ke, Y.C., Yang, Z.B., Zhu, C.F., *Investigation of Properties, Nanostructure and Distribution in Controlled Polyester Polymerization with Layered Silicate*, Journal of Applied Polymer Science, 2002, **85**(13), 2677-2691.
6. Ferguson, J., Kemblowski, Z., *Applied Fluid Rheology*, 1991, Elsevier Applied Science, London.
7. Barnes, H.A., Hutton, J.F., Walters, K., *An Introduction to Rheology*, 1989, Elsevier Science, Amsterdam.
8. Daintith, J., *Dictionary of Chemistry*, 2000, Oxford University Press, Oxford.
9. Goodwin, J.W., Hughes, R.W., *Rheology for Chemists: An Introduction*, 2000, Royal Society of Chemistry, Cambridge.

10. Sandler, I.R., Karo, W., Bonesteel, J., Pearce, E.M., *Polymer Synthesis and Characterisation: A Laboratory Manual*, 1998, Academic Press, London.
11. Stevens, M.P., *Polymer Chemistry: An Introduction* 1999, Oxford University Press, Oxford.
12. Sandler, S.R., Karo, W., Bonesteel, J., Pearce, E.M., *Polymer Synthesis and Characterisation: A Laboratory Manual*, 1998, Academic Press, London.
13. Campbell, D., White, J., *Polymer Characterisation: Physical Techniques*, 1989, Chapman & Hall, London.
14. JOEL Limited, *Scanning Electron Microscope A To Z: Basic Knowledge For Using The SEM*, 2009, 02/02/2011, Available from: http://www.jeolusa.com.
15. Slaytor, E.M., Slater, H.S., *Light and Electron Microscopy*, 1992, Cambridge University Press, Cambridge.
16. Moore, D.M., Reynolds Jr, R.C., *X-Ray Diffraction and the Identification and Analysis of Clay Minerals* 1997, Oxford Unievrsity Press, Oxford.
17. McAlpine, M., *Synthesis and Characterisation of PMMA-clay Nanocomposites*, PhD thesis in Pure and Applied Chemistry, University of Strathclyde, Glasgow, 2006.
18. Williams, D.H., Fleming, I., *Spectroscopic Methods in Organic Chemistry*, 1995, The McGraw-Hill Companies, London.
19. Young, R.J., Lovell, P.A., *Introduction to Polymers*, 1991, Chapman and Hall, London.
20. Lewicki, J.P., *The Ageing Behaviour of Novel Poly(dimethylsiloxane) Nanocomposites*, PhD in Pure and Applied Chemistry, University of Strathclyde, Glasgow, 2008.
21. McNeill, I.C., *Thermal Volatilization Analysis of High Polymers,* European Polymer Journal 1967, **3**, 409-421.
22. McNeill, I.C., Ackerman, L., Gupta, S.N., Zulfiqar, M., *Analysis of Degradation Products by Thermal Volatilization Analysis at Subambient Temperatures,* Journal of Polymer Science: Polymer Chemistry Edition, 1977, **15**, 2381-2392.
23. McGill, W.J., Payne, L., Fourie, J., *A Technique for the Analysis of Trace Amounts of Volatile Products from Polymer Degradations,* Journal of Applied Polymer Science, 1978, **22**, 2669-2675.
24. Liebman, S.A., Levy, E.J., *Pyrolysis and GC in Polymer Analysis*, Chromatographic Science Series, Vol. 29, 1985, Marcel Dekker Inc, New York.

25. Littlewood, A.B., *Gas Chromatography: Principles, Techniques and Applications*, 1962, Academic Press, New York.
26. Atkins, P., *The Elements of Physical Chemistry*, 2001, Oxford University Press.
27. Atkins, P., Jones, L., *Chemical Principles*, 3rd ed, 2004, Freeman, New York.
28. *ASTM 1641-07: Standard Test Method for Decomposition Kinetics by Thermogravimetry*, 2010.
29. Saha, B., Goshal, A.K., *Thermal degradation kinetics of poly(ethylene terephthalate) from waste soft drinks bottles*, Chemical Engineering Journal, 2005, **111**, 39-43.
30. Kissinger, H.E., *Reaction Kinetics in Differential Thermal Analysis*, Analytical Chemistry, 1957, **28**, 1702-1706.
31. Luo, K.M., Thermochimica Acta, 1995, **255**, 241-254.
32. Zimmerman, H., *Developements in Polymer Degradation*, 1984, Applied Science Publishers, Essex.
33. Kissinger, H.E., Journal of Research of the National Bureau of Standards, 1956, **57**(4), 217-221.
34. Zhao, H., Wang, Y.Z., Wang, D.Y., Wu, B., Chen, D.Q., Wang, X.L., Yang, K.K., *Kinetics of thermal degradation of flame retardant copolyesters containing phosphorus linked pendent groups*, Polymer Degradation and Stability, 2003, **80**, 135-140.
35. *ASTM E698-05: Standard Test Method for Arrhenius Kinetic Constants for Thermally Unstable Materials Using Differential Scanning Calorimetry and the Flynn/Wall/Ozawa Method*, 2010.

CHAPTER 3 EXPERIMENTAL

3.1 MATERIALS

3.1.1 NANOCLAYS

The nanoclays employed within this thesis were in part donated by Southern Clay Products, a subsidiary of Rockwood Specialities Inc. The nanoclays were surface modified by a quaternary ammonium surfactant which varied structurally through its alkyl and aromatic substituents. The Cloisite ® and Garamite® ranges were based upon montmorillonite and an unknown blend respectively. The modifier structures and surface concentrations for each surface modified nanoclay are shown in figure 3.1.

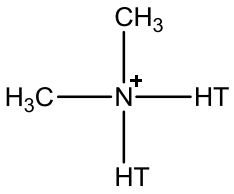

Cloisite® 6A	140 meq/100g nanoclay
Cloisite® 15A	125 meq/100g nanoclay
Cloisite® 20A	95 meq/100g nanoclay
Garamite® 1958	unknown

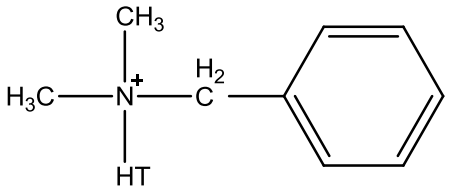

Cloisite® 10A 125 meq/100g nanoclay

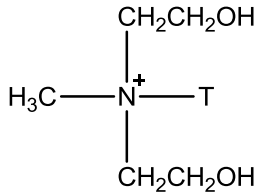

Cloisite® 30B 90 meq/100g nanoclay

Figure 3.1 Surface modifier structure and concentration

3.1.2 DISPERSANTS

All glycols and mono-functional alcohols employed within this thesis were purchased by Sigma Aldrich.

3.1.3 POLY(ETHYLENE TEREPHTHALATE) AND RESPECTIVE NANOCOMPOSITES

Two poly(ethylene terephalate) Garamite® nanocomposites at nanoclay loadings of 0.5% w/w and 1.0% w/w, and a comparative clay-free polymer sample were prepared at DuPont Teijin Film's research and development facility at Wilton. During the transesterification step a 99% antimony(III) trioxide catalyst was employed, which had a particle size of 5 micron and was purchased from Sigma Aldrich. The silicone anti-foaming agent Foamdoctor F2100 was also employed and purchased from Pennwhite Ltd.

Throughout this thesis unmodified poly(ethylene terephthalate) will be referred to as PET. PET containing 0.5% w/w and 1.0% w/w Garamite® 1958 will be referred to as PET0.5G and PET1.0G, respectively.

3.2 SUSPENSION PREPARATION

Surface modified nanoclay was stored at 40°C for two weeks prior to use in order to ensure a consistent moisture content. In order to assist moisture homogeneity the material was also stirred every 2 days. The nanoclays were exfoliated in various alcohol-based solvents. The loading levels were calculated as a % mass and loadings between 2 – 10% were examined during the course of this thesis.

The suspensions were predominantly prepared through ultrasonication. A Cole Parmer Ultrasonic Processor was set at an amplitude of 40% which translated to a power output of 8.33 J s^{-1} (see appendix 1). During this time the sample was stirred by an Ika®-Werke Eurostar stirrer at 500 rpm, which allowed the samples to be sonicated homogenously. A cooling jacket was also employed which allowed dissipation of the heat produced during sonication. Samples were sonicated for 25 minutes in 5 minute

intervals which allowed for cooling time when required. After preparation the samples were stored at 30°C for 24 hours and visually inspected prior to rheological analysis.

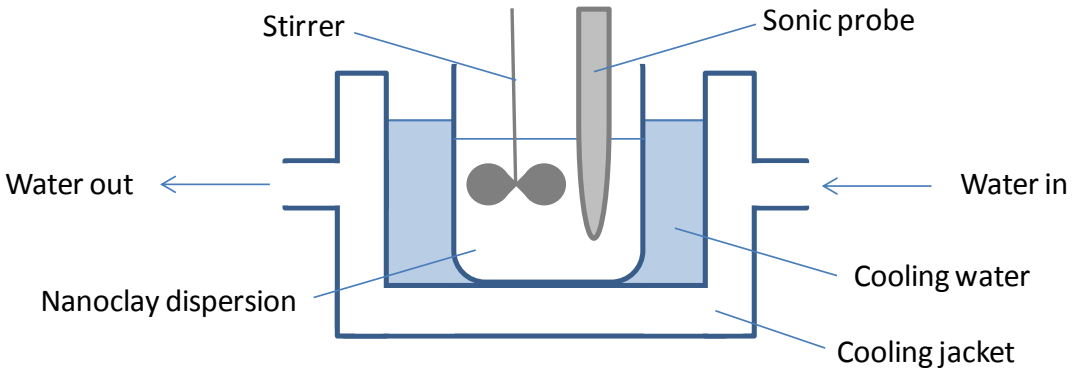

Figure 3.2 Experimental apparatus for the preparation of nanoclay and alcohol suspensions

Nota bene. The cooling jacket was essential due to the effect of temperature on the efficiency of sonication.[1] Although higher sample temperatures may result in a lower viscosity and hence easier cavitation, the shear force created on the collapse of the microbubbles is lower. In addition, if the temperature approached the boiling point of the solvent a substantial volume of smaller cavitation bubbles would form which would dampen the ability of the acoustic energy to penetrate the sample.[2]

3.3 RHEOLOGICAL ANALYSIS

Samples were analysed using a TA Rheolyst AR1000-N rheometer in conjunction with AR Instrument Control software. Data was analysed using TA Data Analysis software and plotted in OriginPro 8®. A parallel plate was chosen for analysis as it would reduce the opportunity for gap bridging by unexfoliated flocculates. An additional advantage to the parallel plate geometry is the ability to adjust the geometry gap which allows different nanoclay dispersion to be examined. The only major concern whilst using a parallel plate geometry is the variable shear rates between geometries, however this is resolved by taking measurements from the plate edge.

Prior to analysis the instrument was configured with respect to the chosen geometry through a process known as mapping which sets the air bearings. The instrument is then ‘zeroed’ to the chosen intergeometry distance. The apparatus was then set at a working temperature of 25°C and air flow of 30 psi in order to prevent bearing damage. For

standard liquid and gel-like suspensions a 40mm parallel plate geometry was selected unless otherwise stated. In a typical experiment, the shear rate was increased from 1 s^{-1} to 1000 s^{-1} whilst viscosity and shear stress were monitored. The shear range was selected as it was within the limits of the rheometers' accuracy limits and allowed a viscosity profile to be produced throughout a wide range of shear rates. During profiling 31 data points were collected and results plotted on a log scale. For each data point collected the rheometer was allowed to attain equilibrium prior to the acceptance of the measurement. This ensured consistency and accuracy within the results as the measurement was required to be within 5% of the attained data for each particular shear rate. A time limit of 1 minute 30 seconds was set in order to balance accuracy with an efficient use of instrument time.

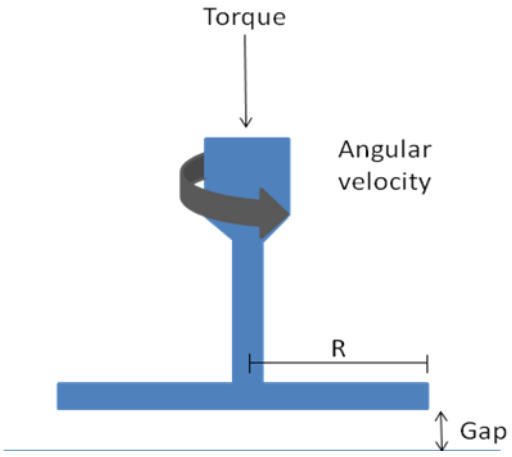

Figure 3.3 Illustration of parallel plate geometry

3.4 *IN SITU* POLYMERISATION

In situ polymerisation was performed at the DuPont Teijin Films Ltd site located within the Wilton Centre, Middlesbrough.

The Garamite® nanoclay was dispersed in ethylene glycol monomer using an Ultra-Turrax high shear disperser for 25 minutes at 16,000 rpm. 0.5 ml of anti-foam prevented foaming due to during shearing and also modifier degradation on polymerisation. The sample was sheared in 5 minute intervals to allow cooling when required.

A 7 kg reaction vessel allowed between 4.6 and 6.0 kg of polymer to be prepared. The vessels ancillary equipment consisted of a reflux valve, condenser, receiver, glycol take off line and glycol burette. The vessel temperature was also controlled through a computer controlled oil jacket, heated by a 20 kW Churchill heater. The vessel contents were agitated using a PTFE spiral agitator power by a HP motor and Kopp variator. A Genevac vacuum pump provided a vacuum of <1 mmHg during the polycondensation step. After polymerisation molten polymer lace was cooled by compressed air driers and a water casting trough, before a lace cutters chipped the polymer.

Direct esterification was performed under nitrogen and a pressure of 54 psi. The batch temperature was held between 230 °C and 255 °C. Reaction completion was determined through a decrease in temperature or a decrease in the rate of water distillation. Water distillation was initiated at temperatures between 220 °C and 235 °C during the esterification step and continued for approximately 2 hours. Polycondensation was performed under a vacuum of < 1 mm Hg and a temperature of 290°C. An antimony trioxide catalyst was dissolved in hot glycol and added to the bis-hydroxyl ethyl terephthalate prior to the temperature increase. Ethylene glycol distillate was collected by a sight received glass and the end point was determined as an increase in agitator load to 0.75 kW. Once polymerisation was complete the die at the base of the reactor was opened and the polymer lace was passed through a water trough and air shifters before being chipped.

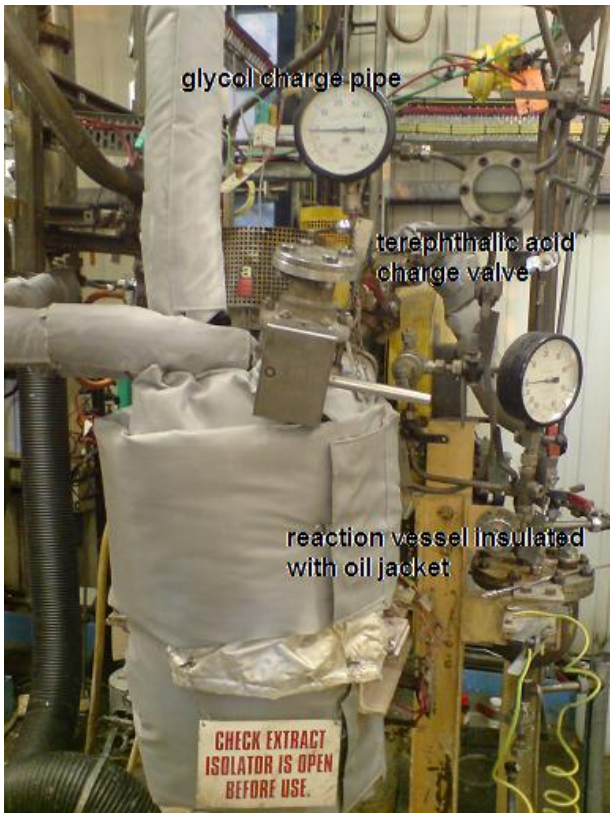

Figure 3.4 Photograph of the 7 kg (5 gallon) batch reactor used to prepare the polymer and polymer composite chip.

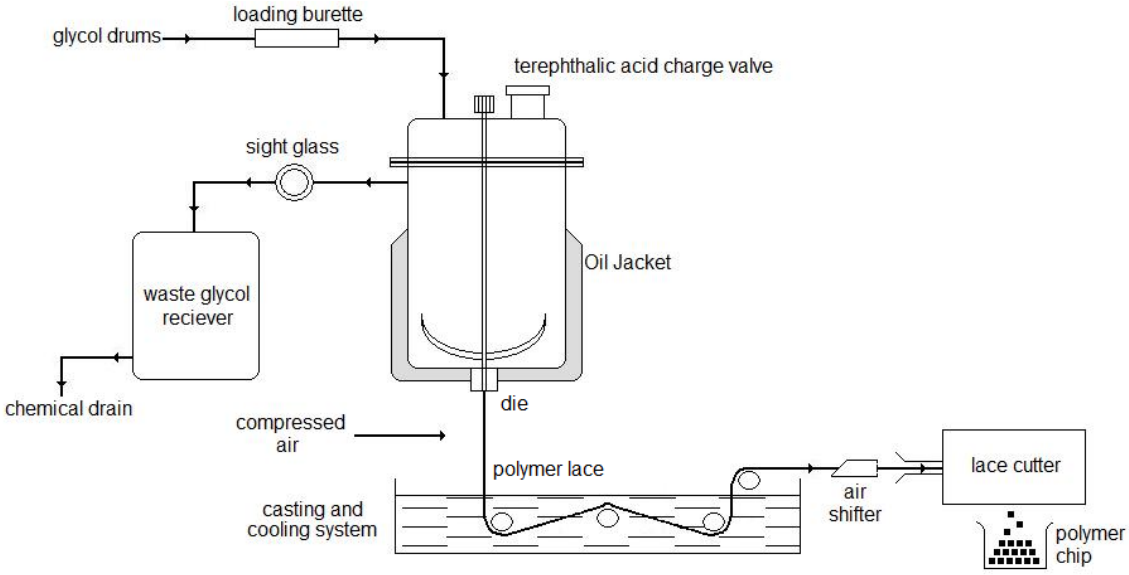

Figure 3.5 Schematic of the 7kg batch reactor used for *in situ* polymerisation.

3.5 FILM EXTRUSION

Film extrusion was performed on the mini-Meiji extrusion line at the DuPont Teijin Films Ltd research and development facility located within the Wilton Centre. Due to confidentiality the full operating procedure cannot be released however a summary is included below.

Initially the polymer or polymer composite chip was dried at 120°C for 12 hours over a bed of desiccant. This lowered the moisture content of the polymer chip to below 0.001%. The polymer remained in the drying oven until immediately prior to extrusion to minimise absorption of atmospheric moisture.

The polymer chip was loaded into the feed hopper of the heated extrusion barrel when required. A screw within the barrel compressed and sheared the polymer resulting in frictional heat which converted the chip to molten polymer. An additional oil heater held the polymer at an average temperature of 275°C. A metering section then homogenised the polymer melt and controlled the flow to the die. The polymer melt also passed through sintered metal discs prior to entering the heated die in order to remove any metal contaminants. A slit die then allowed the extrusion of a molten polymer film onto a cooled casting drum held at 17°C. The purpose of the casting drum is to cool the molten polymer as efficiently as possible. Typically the temperature decreases to below 120°C within seconds with the polymer forming a homogenous amorphous film.

The amorphous film is then drawn in the forward or machine direction to impart uniaxial orientation. The film is passed through a set of pre-heating rollers between 75°C and 85°C and then an infra-red heater in order to bring it up to the drawing temperature of 90°C. The film is then stretched by passing it through two sets of rollers, with the second set rotating faster than the first set. PET film is typically stretched 3.0 times its normal length; however ratios between 3.0 and 3.7 times are normal. At this point the PET film crystallinity is typically 20%. The film is quenched rapidly by cooling rolls before running through the fast nip, which controls the speed of the rolls after the draw.

In order to biaxially stretch the film, the uniaxial film was clamped within a T.M. Long Biaxial stretcher and pre-heated with hot air to between 80°C and 90°C. The temperature was then increased to between 100°C and 110°C and the film width gradually increased. Typically a uniaxial film may be transversely stretched to between 3.3 and 4.2 times the original width. Typically a further 5% crystallinity develops on biaxial drawing, increasing the total crystallinity to around 25%.

3.6 CHARACTERISATION

3.6.1 CHARACTERISATION OF GARAMITE® 1958

3.6.1.1 COMBINED DSC-TGA

Experiments were performed on a TA SDT 2960 Simultaneous combined TGA-DSC instrument under either an environment of either air or nitrogen at a flow rate of 30mL min^{-1}. Samples were ramped at a heating rate of 10 °C min^{-1} from between 25°C and 1100°C. TA Analysis software was employed for data analysis.

3.6.1.2 SEM

Images of the Garamite® nanoclay were obtained by a JOEL JSM-7500F FESEM equipped with a total energy detector at an accelerating voltage of 20 kV. The working distance was 7 mm achieving magnifications of between 4,000 and 100,000 times. Prior to analysis a nanoclay suspension in ethanol was prepared by ultrasonic treatment in a Cole-Parmer® WZ ultrasonic bath for 10 minutes. The suspension was then deposited on a carbon specimen mount and the ethanol removed under vacuum in a Varian V-81 Turbo Station overnight prior to analysis.

3.6.1.3 XRD

The x-ray diffraction patterns of the Garamite® nanoclay were obtained using a Philips PW 3710 instrument fitted with a Cu Kα source. The wavelength of the source was equal to 0.154 nm. The instrument operated at a generator voltage of 45kV and a tube

current of 40 mA. The diffraction pattern was collected by continuous scanning at angles between 2° and 90° at a scan step size of 0.02.

3.6.2 CHARACTERISATION OF POLY(ETHYLENE TEREPHTHALATE) GARAMITE®1958 NANOCOMPOSITES

3.6.2.1 TGA

Degradation runs were performed as previously on a Perkin Elmer TGA 7 thermogravimetric analyser and TCA 71DX thermal analysis controlled connected to a desktop PC. Samples were held isothermally at 50 °C minutes for 5 minutes prior to being ramped to 800 °C at various heating rates between 1°C min^{-1} and 20°C min^{-1}. Thermo-oxidative characterisation of samples was performed under air at a flow rate of 30mL min^{-1}. Data was compiled into a Word® Notepad and imported into Origin 8® for analysis.

2.6.2.2 NMR SPECTROSCOPY

The polymer was dissolved at a concentration of 125 mg of polymer per 1 ml of solvent mixture. The solvent mixture consisted of a 2 : 10 mass ratio of deuterated 1,1,1,3,3,3-hexafluoroisopropanol and deuterated chloroform. The sample was left overnight in order to ensure all the polymer had dissolved and was then filtered through a Pasteur pipette containing glass wool to remove any insoluble debris. Sample filtration was essential as the sepiolite nanoclay may contain iron which would interfere with the instrument.

Samples were run on an Avance 400 MHz multi-nuclear mid-field instrument based on a 9.4T Oxford unshielded magnet, BBFO-z-ATMA probe alongside a B-ACS 60 autosampler. The instrument was operated in walk-up mode using Brukers Icon NMR software and data analysis was performed on Topspin v2.0. ^{1}H and ^{13}C nuclei were examined through a 16 scan run which allowed a 1 second relaxation decay.

3.6.2.3 ATTENUATED TOTAL REFLECTANCE (ATR) – FTIR SPECTROSCOPY

Materials were characterised by an A_2 Technologies spectrometer fitted with a diamond crystal tip and Michelson interferometer. The instrument was set to perform 64/128 scans per sample within a wavelength range of 4000 – 650 cm^{-1} and resolution of 4 cm^{-1}. Data was collected as plots of absorbance against wavenumbers using Lab Condition Panorama® and Microlab PC®, also licensed by A_2 Technologies.

3.6.2.4 GPC

Gel permeation chromatography was performed by Smithers RAPRA. 20mg of sample was dissolved in 10mg of 1,1,1,3,3,3-hexafluoro-2-propanol (HFIP) solvent and 25 mM of sodium trifluoroacetate. The sample was left for 20 hours to dissolve and filtered through a 0.45 µm PTFE membrane prior to analysis. The sample was loaded onto the column at a nominal flow rate of 0.8 ml/min at a temperature of 40°C. The column was prepared with PL HFIP gel guard and PL HFIP gel. Column dimensions were 300 mm by 7.7 mm and the pore diameter was 9 µm. The molar mass was determined through measurement of the refractive index of the eluent, and data was collected and analysed using Cirrus 3.0 software.

The refractive index and molar mass relationship was ascertained prior to analysis though a set of Polymer Laboratories poly(methyl methacrylate) calibrants which possessed a low PDI and comparable radius of gyration.

3.6.2.5 SOLUTION IV

The intrinsic viscosity was determined on a Viscotek Y501C Relative Viscometer. 0.5% w/w of polymer was dissolved in ortho-chlorophenol at 25°C and the Billmeyer single point method was used to calculate the intrinsic viscosity. The intrinsic viscosity was then employed in calculating the molecular weight through the Mark Houwink equation: $[\eta] = KM^{\alpha}$.

3.6.2.6 TEM

Images of the composite chip and uniaxial film were obtained on a Philips CM12 TEM at an accelerating voltage of 120 kV. Bright-field images were collected at magnifications/scales of 50 nm and 2 μm using a Gatan Bioscan CCD digital camera. The samples were sectioned to widths of approximately 60 nm using a Drukker International diamond knife on a Reichert Ultracut-E ultramicotome. The sections were then floated in distilled water and collected on a 3 mm copper sampling grid for analysis.

3.7 CRYSTALLISATION

3.7.1 DSC

Crystallisation runs were performed on a DSC Q1000 under nitrogen. Samples were subjected to a heat-cool-reheat program between 40°C and 320°C at a rate of 10°C min^{-1}. Data was analysed using TA Universal Analysis software.

3.8 DEGRADATION

3.8.1 DSC

Degradation runs were performed as previously on a DSC Q1000. Samples were held isothermally at 40°C minutes for 5 minutes prior to being ramped to 520°C at various heating rates between 1°C min^{-1} and 20°C min^{-1}. Thermo-oxidative degradation of samples was performed under air whilst thermal degradation was performed under nitrogen, both at a flow rate of 60mL min^{-1}. Data was analysed using TA Universal Analysis software.

3.8.2 TGA

Degradation runs were performed as previously on a Perkin Elmer TGA 7 thermogravimetric analyser and TCA 71DX thermal analysis controlled connected to a desktop PC. Samples were held isothermally at 50°C minutes for 5 minutes prior to

being ramped to 800°C at various heating rates between 1°C min^{-1} and 20°C min^{-1}. Thermo-oxidative degradation of samples was performed under air whilst thermal degradation was performed under nitrogen, both at a flow rate of 30 mL min^{-1}. Data was compiled into a Word® Notepad and imported into Origin 8® for analysis.

3.8.3 TVA

3.8.3.1 DEGRADATION RUN

Prior to each run 10mg of sample was degassed overnight at room temperature. Samples were degraded under vacuum at a heating rate of 10°C min^{-1} to a temperature of 550°C under vacuum using a Carbolite® MTF tubular furnace. During the degradation run condensable volatiles were trapped at two stages. A tap water cooled o-ring situated 1 inch above the furnace allowed high molar mass volatiles to be trapped within the original sample tube. The primary cold trap (cold trap 1) then allowed the collection of lower molar mass volatiles condensable down to liquid nitrogen temperatures. Non-condensable volatiles released during degradation passed through the line and were detected continuously by means of a Hiden Analytical HPR20 mass spectrometer and a Edwards Pirani APG100-XLC gauge.

3.8.3.2 DISTILLATION OF CONDENSABLE VOLATILES

The condensable volatiles held within cold trap 1 were distilled into fractions using an in-house built heating system to allow a controlled heating regime. The liquid nitrogen was removed and a heater set at 2°C min^{-1} raised the trap temperature from -96 °C to 40 °C. Fractions were collected under liquid nitrogen in the secondary traps (cold traps 2-5) for further analysis by FT-IR and GC-MS. Typical temperature ranges for fraction collection were -196°C to -110°C, -110°C to -85°C, -85°C to -35°C and -35°C to 40°C. Fractions were monitored by mass spectroscopy continuously throughout the distillation process which allowed the degradation products to be identified. It should be noted that as the boiling point increased so did the molar mass and hence the complexity of the spectra, decreasing the certainty in identification.

3.8.3.3 FT-IR ANALYSIS OF FRACTIONS 1 - 4

Materials were characterised on a Perkin Elmer Spectrum 100 FT-IR spectrometer. Background scans were performed prior to analysis and subtracted from the sample spectrum. The instrument was set to perform 64 scans per sample within a wavelength range of 4000 – 500 cm^{-1} and resolution of 4 cm^{-1}. Data was collected as plots of % transmittance against wavelength and exported and displayed in Origin8®.

3.8.3.4 GC-MS ANALYSIS OF COLD RING FRACTION

The cold ring fraction was removed using cotton wool dampened with spectroscopy grade chloroform. The cotton wool was then placed in a small sample vial and the sample was extracted into 5 cm^3 of spectroscopy grade chloroform. The dissolved sample was then filtered through glass wool to remove any debris or material insoluble in chloroform. A further 3cm^3 of spectroscopy grade chloroform was then added to yield a dilute sample solution.

Sample solutions were transferred into vials with Teflon septum lids and analysed after a blank run in order to clear the system of potential contaminants. Samples were analysed using a Finnigan Polaris Q GC-MS under a vacuum of 10^{-6} torr and ramped between 40°C and 320°C at a rate of 20°C min^{-1}. The carrier gas was helium and a m/z range between 50 – 600 was collected over the course of the run. Data was analysed using Xcalibur software.

3.8.3.5 GC-MS ANALYSIS OF FRACTION 4

The higher molar mass volatiles were condensed in the cold finger of fraction 4 using liquid nitrogen and then dissolved in 5 cm^3 of spectroscopy grade chloroform. The sample was filtered through glass wool to remove any insoluble material and analysed without further dilution.

The experimental procedure was repeated as above.

3.9 REFERENCES

1. McAlpine, M., *Synthesis and Characterisation of PMMA-Clay Nanocomposites*, in Pure and Applied Chemistry, University of Strathclyde, Glasgow, 2006.
2. Mason, T.J., *Practical Sonochemistry*, 1991, Ellis Horwood, New York.

CHAPTER 4 DISPERSION EFFECTS

In order to prepare a nanocomposite with an even distribution of platelets throughout the polymer matrix the nanoclay must first be exfoliated or intercalated within an appropriate dispersing medium. The ability of the nanoclay to disperse within a specific medium is assessed on the most basic level through the degree of phase separation after a 24 hour settling period. A stable dispersion, i.e. suspension, is therefore a term employed throughout this chapter to describe a sample which has undergone no phase separation.

The preparation of a stable suspension is dependent upon several contributing factors that centre upon the compatibility of the dispersing medium and the nanoclay. Compatibility itself is not a simple consideration but is determined through several physical parameters, some of which are investigated within this chapter. A variety of glycols, bi- and mono-functional alcohols are examined in order to trend the data in relation to the molar mass, viscosity, dipole moment and dielectric constant. A commercially available range of organically modified nanoclays are also examined in order to determine the effect of modifier structure and surface concentration.

Within this chapter the viscosity build of the suspensions will be assessed via the relative viscosity, η_r, i.e. the ratio of the viscosity of the suspension, η, to that of the dispersant, η_s.

$$\eta_r = \frac{\eta}{\eta_s}$$

Equation 4.1

4.1 EFFECT OF NANOCLAY MORPHOLOGY AND LOADING ON EXFOLIATION

Cloisite® 10A was observed to produce the most stable montmorillonite-based suspensions with ethylene glycol, and was therefore selected to examine the effect of a plate-like morphology on viscosity build. Garamite® 1958 in comparison illustrated the effect of a more fibrous nanoclay which unravelled rather than exfoliated. Initially,

suspensions possessing a nanoclay loading of between 2 and 10% w/w were prepared, however due to phase separation the 2% w/w Cloisite® loading was not rheologically examined.

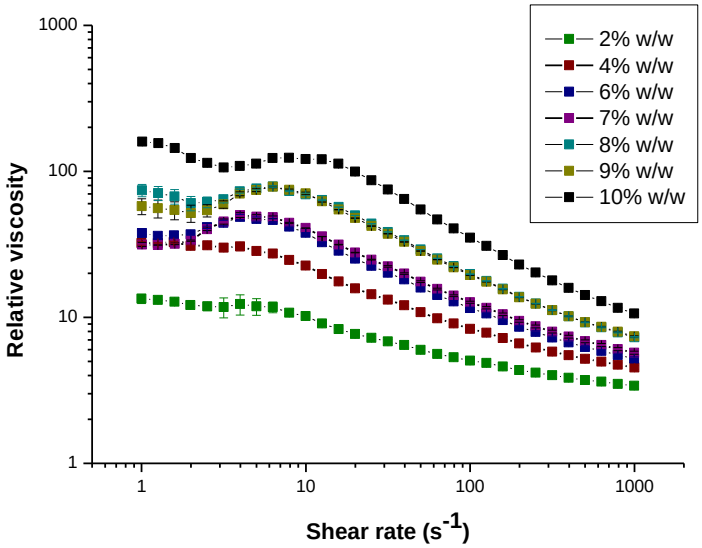

Figure 4.1 Relative viscosity versus shear rate. Cloisite® 10A suspensions in ethylene glycol at nanoclay loadings between 4 % w/w and 10 % w/w.

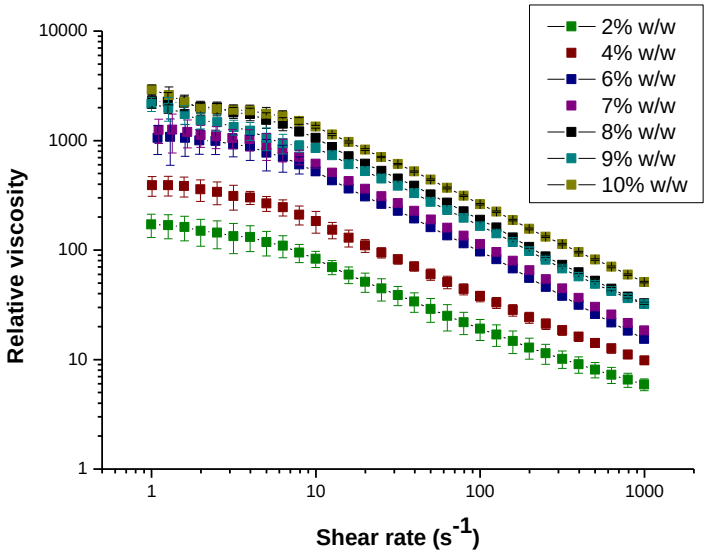

Figure 4.2 Relative viscosity versus shear rate. Garamite® 1958 suspensions in ethylene glycol at nanoclay loadings between 2 % w/w and 10 % w/w.

Figures 4.1 and 4.2 illustrate the effect of nanoclay loading on suspension viscosity for the nanoclays under study. Both profiles appear to suggest the relationship between a suspension's viscosity and the nanoclay content is not directly proportional. For example within figure 4.1 it appears that the relative viscosity is comparable for

loadings of 6 and 7 % w/w, and also 8 and 9 % w/w. It is possible this behaviour is related to specific suspension morphologies. Within the higher loading Cloisite® 10A suspensions, a decrease and subsequent increase in relative viscosity is observed shortly after the commencement of shearing, and this is to some degree proportional to nanoclay loading. Structure formation within the suspensions may therefore be assumed to have increased. It cannot be determined however whether the increase in structure is due to the extension of the interplatelet structure formed at lower loadings, or the development of a separate morphology at the higher loadings.

It is known however that montmorillonite tactoids or intercalates may form bookhouse structures which maximise attractive interplatelet forces. Theoretically, it could be suggested the apparent behavioural 'boundaries' within the rheological profiles may be due to the differing degrees of structure formation by these bookhouses. Within the Garamite® suspensions similar boundaries are observed although the rheological profiles differ. Sepiolite nanoclays possess a fibrous morphology in comparison to montmorillonite, and exist pre-exfoliation in wool-like balls.[1] As a result, they will therefore unravel as opposed to exfoliate. Although the nanoclay morphology differs the sepiolite fibre edges still possess the potential to interact with one another. It is suggested that these interactions help tease out fibres from the main bulk, with the extent and likelihood of interaction increasing with nanoclay loading. Figures 4.1 and 4.2 suggest the Garamite® disperses in ethylene glycol to a more substantial degree than Cloisite®, as the relative viscosities of Garamite® suspensions are observed on average as one order of magnitude higher than their respective Cloisite® suspensions. This may be attributed to either a greater degree of nanoclay dispersion within the medium or a greater volume of dispersant – nanoclay interactions.

4.2 EFFECT OF ORGANIC MODIFIER ON EXFOLIATION

The purpose of the organic modifier is to alter the surface chemistry of the nanoclay, increasing the compatibility between the nanoclay surface and the molecules of the dispersing medium. In order to ascertain the effect of the organic modifier and the modifier surface concentration on dispersants such as glycols, a variety of Cloisite® nanoclays were examined. Traditionally, a simple 'like dissolves like' approach to

compatibility has been taken, however suspension stability is determined by a number of variables all of which must be examined.

Varying of the modifier structure was the primary manner in which surface polarity was tuned. Incorporation of tallow groups on the ammonium modifier creates a hydrophobic nanoclay surface, and therefore exchanging a tallow for a more hydrophilic group would increase the potential for intermolecular interactions with the dispersant. The impact of modifier structure on the relative viscosity may be observed within figure 4.3 which compares Cloisite® suspensions in tetraethylene glycol. For reference, the structures of the organic modifiers have been included in below.

Table 4.1 illustrating the surface modifier structures, surface concentrations and intergallery spacings within the Cloisite® and Garamite® nanoclay range.

Nanoclay	**Modifier Structure**	**Surface Concentration / meq/100g nanoclay**	**Intergallery spacing / nm**
Cloisite® 6A	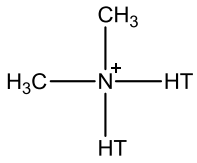	140	3.51
Cloisite® 15A		125	3.15
Cloisite® 20A		95	2.42
Garamite® 1958		unknown	N/A
Cloisite® 10A	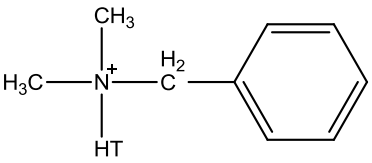	125	1.92
Cloisite® 30B	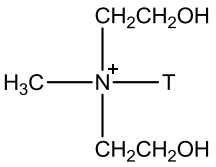	90	1.85

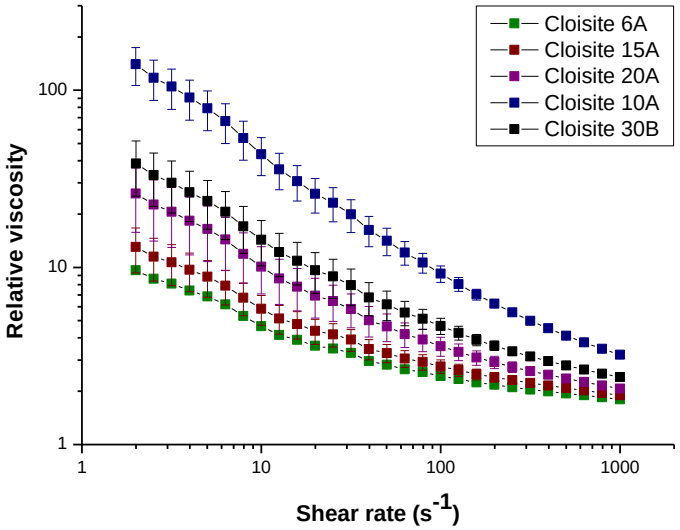

Figure 4.3 Relative viscosity versus shear rate. Various Cloisite® dispersions in tetraethylene glycol at a nanoclay loading of 6% w/w.

Figure 4.3 illustrates that suspensions prepared with more hydrophilic nanoclays exhibit a greater relative viscosity. Cloisite® 10A suspensions in tetraethylene glycol, for example, were observed to possess an initial viscosity approximately one order of magnitude greater than that of respective Cloisite® 15A suspensions. The enhanced relative viscosity of the Cloisite® 10A suspensions was attributed to the presence of an aromatic group which may create beneficial interactions with the ethylene glycol molecules i.e. the donation of π-electrons into the aromatic ring. Enhanced nanoclay – dispersant interactions would then be expected to encourage the penetration of the dispersant into the gallery spacings and increase the degree of platelet exfoliation. In addition, the intergallery spacing of Cloisite® 10A is lower than that for the analogous Cloisite® which possesses alkyl tallows. It is therefore not a physical influence such as a higher initial intergallery spacing which enhances the degree of exfoliation within the Cloisite® 10A suspension. Cloisite® 30B is also observed to produce the second highest relative viscosity for the systems under study. This is attributed to the ability of the surface modifier to hydrogen bond directly with the dispersant.

The most unstable dispersions were formed with Cloisite® 15A, however Cloisite® 10A and 15A contained the same concentration of organic modifier; 125 meq/100g. The structural difference between the Cloisite® 15A and 10A surface modifiers is illustrated within table 4.1. This further confirms the postulate that it is interactions with

the benzyl group specifically which enhance the relative viscosity. Comparison of Cloisite® 20A and 30B suspensions (at respective surface concentrations of 95 and 90 meq/100g) further highlight the need for interactive functional groups. When considering the glycol homologous family the larger glycols contain more ether lone pairs, increasing the potential for interaction with the modifier. The modifier however can only take advantage of the presence of these groups if it contains the appropriate functional groups itself. This is certainly the case when contrasting Cloisite® 20A and 30B, which possess the organic modifiers ammonium dimethyl dehydrogenated tallow (DMDHT) and methyl tallow 2-hydroxyl ethyl (MT2EtOH), respectively. DMDHT possesses no intermolecular bonding ability apart from Van der Waals forces, whereas MT2EtOH has the additional ability to initiate hydrogen bonding directly with the dispersant.

4.3 EFFECT OF MODIFIER SURFACE CONCENTRATION ON EXFOLIATION

The impact of the surface modifier concentration is shown in figure 4.4 which contains the rheological profiles of Cloisites® 6A, 15A and 20A in tetraethylene glycol. The Cloisites® under study contain the DMDHT modifier at concentrations of 140, 125 and 95 meq/100g respectively. In this instance, it is observed that the relative viscosity is related to the modifier surface concentration which further confirms the importance of a hydrophilic nanoclay surface as discussed during Section 4.2. Figure 4.4 also confirms that a larger initial intergallery spacing does not necessarily lead to a higher relative viscosity upon the preparation of a suspension.

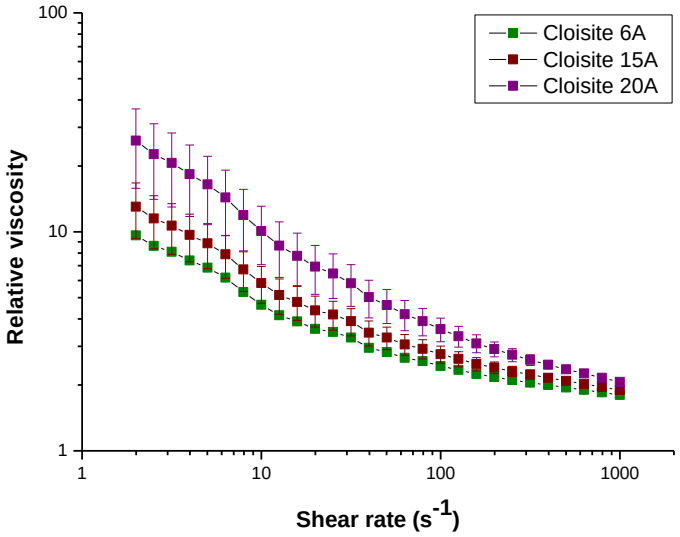

Figure 4.4 Relative viscosity versus shear rate. Suspensions of Cloisites® 6A, 15A and 20A in tetraethylene glycol. Cloisites® 6A, 15A and 20A all possess an ammonium dimethyl, dehydrogenated tallow at concentrations of 140, 125 and 95 meq/100g, respectively.

4.4 EFFECT OF DISPERSANT ON EXFOLIATION

Various glycols within the same homologous family were examined in order to identify some of the dispersant parameters which influence exfoliation. Parameters which were considered were molar mass, viscosity, dipole moment, dielectric constant and the Flory-Huggins solubility parameter. Initially, the dispersants under investigation varied through the number of ether bonds they possessed. This systematic adjustment of the dispersant structure allowed the trending of data and properties. Ethylene glycol dispersions were considered due to their association with the polymerisation of poly(ethylene terephthalate).

It is illustrated within table 4.2 and figure 4.5 that for the majority of the Cloisites® there is no significant difference in the relative viscosity when dispersant possesses an ether bond. In addition, the relative viscosities of suspensions based on bi-functional alcohols appears to scale approximately with dipole moment. The initial dispersant viscosity however is not observed to influence the suspension relative viscosity. It is proposed that the presence of an ether functional group within the higher glycols imparts an additional hydrogen bonding ability which encourages a greater degree of exfoliation. It is also proposed that the presence of a single ether bond is sufficient to

enhance nanoclay exfoliation. Only within Cloisite® 30B suspensions is there a deviation in behaviour, and this attributed to the ability of the surface modifier to interact directly with the dispersant, therefore utilising the ether bonds to a greater degree.

Table 4.2 The relative viscosity of various Cloisite® suspensions, illustrating the potential relationships between dispersant dipole moment, dispersant viscosity and suspension viscosity. Relative viscosities have been determined at a shear rate of 10 s^{-1}. PS indicates phase separation within the sample which prevented rheological analysis. [2]

Dispersant	Dispersant properties		Cloisite® suspension relative viscosity				
	Dipole moment / D	Viscosity / Pa s	6A	15A	20A	10A	30B
1-propanol	1.75	2.75×10^{-3}	114	120	140	PS	222
1-pentanol	1.66	3.20×10^{-3}	488	510	624	PS	421
Ethylene glycol	2.20	1.56×10^{-2}	PS	PS	6	17	17
1,5-pentanediol	2.37	9.45×10^{-2}	3	3	5	PS	12
Diethylene glycol	5.50	2.85×10^{-2}	7	PS	17	59	17
Triethylene glycol	5.58	3.18×10^{-2}	7	PS	15	54	33
Tetraethylene glycol	5.84	4.00×10^{-2}	6	7	13	54	40

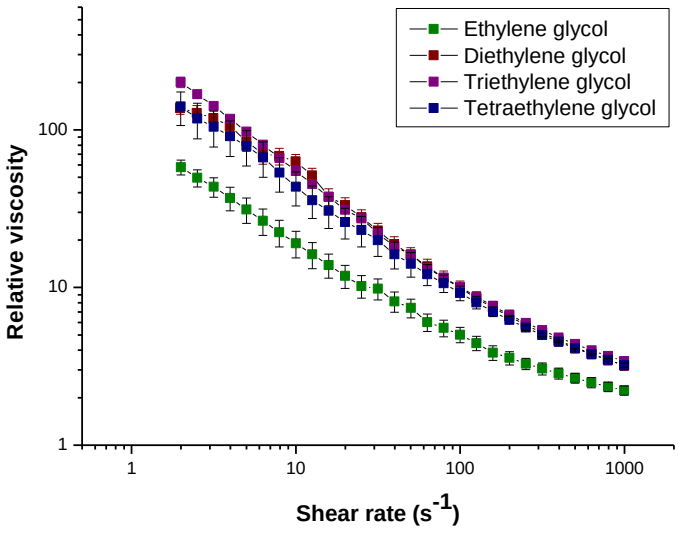

Figure 4.5 Relative viscosity versus shear rate. Suspensions of Cloisite® 10A in various glycols at a nanoclay loading of 6% w/w.

Inspection of table 4.3 however illustrates a substantial difference in molar mass between ethylene glycol and the glycols which possess an ether bond. It is therefore possible that an increase in molar mass may enhance exfoliation if suitable bonding intermolecular bonding interactions are present. In particular, a greater steric bulk has the potential to act as a physical barrier against attractive electrostatic interplatelet interactions, encouraging the nanoclay to exfoliate.

In order to assess the effects of molar mass, suspensions prepared with 1,5-pentanediol and diethylene glycol were examined. 1,5-pentanediol and diethylene glycol possessed molar masses of 104 and 106 g mol^{-1}, respectively. Although phase separation within the suspensions was still an issue, examinable suspensions exhibited a greater relative viscosity when prepared with diethylene glycol, as observed within figure 4.6 and appendix 2. This confirms the beneficial influence of an ether bond within the dispersant and also that in this instance molar mass is not a primary influence during exfoliation. Although the hydroxyls do appear to promote exfoliate to a sufficient degree, the additional ether unit is observed to enhance the viscosity. The ether may contribute to suspension formation in two manners; directly through hydrogen bonding interactions or through the improvement of suspension stability post-exfoliation. The latter contribution is attributed to the higher permittivity of the glycol as illustrated within table 4.3. Finally, the hydrophilic nanoclays were observed to exhibit a superior relative viscosity, further confirming the observations made in Section 4.2.

Table 4.3 Physical Properties of various dispersing media.[2, 3]

Dispersing medium	Molar mass / g mol^{-1}	Viscosity / Pa s	Dipole Moment, μ / D	Permittivity / -
1-propanol	60	2.75×10^{-3}	1.75	20.80
1-pentanol	88	3.20×10^{-3}	1.66	15.13
Ethylene glycol	62	15.61×10^{-3}	2.20	41.40
1,5-pentanediol	104	94.50×10^{-3}	2.37	26.20
Diethylene glycol	106	28.50×10^{-3}	5.50	31.82
Triethylene glycol	150	31.84×10^{-3}	5.58	23.69
Tetraethylene glycol	194	39.98×10^{-3}	5.84	20.44

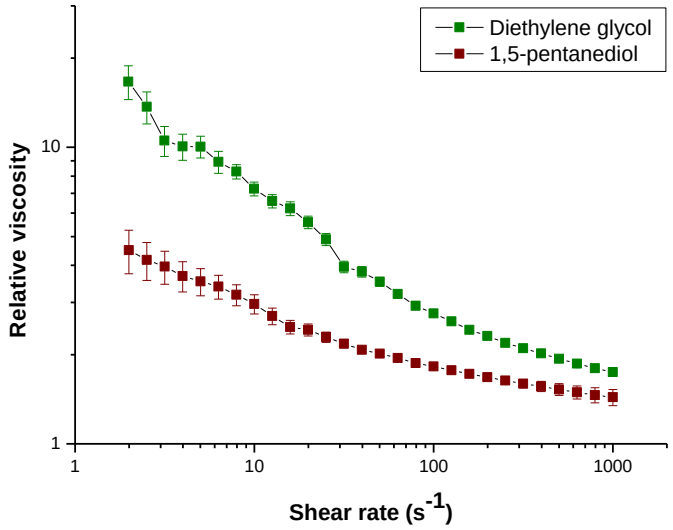

Figure 4.6 Relative viscosity versus shear rate. Suspensions of Cloisite® 6A in diethylene glycol and 1,5-pentanediol at a clay loading of 6% w/w.

In order to determine the influence of hydroxyl functionality on exfoliation suspensions prepared in mono-functional alcohols were examined via a comparison of data within figure 4.7 and table 4.2. Perhaps surprisingly, Cloisite® suspensions prepared in 1-propanol and 1-pentanol were observed to possess a significantly higher relative viscosity than those prepared with the bi-functional dispersants. In addition within the 1-pentanol suspensions shear thickening behaviour is observed, which illustrates the platelets are contributing to the relative viscosity to a greater degree than in previous suspensions. Figure 4.7 illustrates that the platelets are also able to align themselves with the shear flow direction over a shorter timescale than previously possible. This indicates the platelets have been exfoliated to a more substantial degree and the attractive forces which bind the platelets together have decreased. This is further illustrated within figure 4.8 which contained a comparison of suspensions of Cloisite® 30B in 1-pentanol and 1,5-pentanediol. It is proposed the enhanced relative viscosity suspensions prepared with mono-functional dispersants is due to a surfactant or electrical double layer effect. Surfactant-type interactions were probable due to the mono-functionality of the alcohol, and would physically force the platelets apart encouraging exfoliation. The alkyl chain length would then determine the extent of separation and increase in intergallery spacing. Bi-functional dispersants however would not be able to exfoliate the platelets in the same manner as both end-groups have the potential to interact with the modifier or platelet surface. A bi-functional dispersant

may therefore effectively bind the platelets together at an intergallery distance determined by its' chain length. It should be noted that with respect to the mono-functional alcohols that a lower permittivity therefore correlates with a greater relative viscosity. See table 4.4. In addition, although a low dispersant polarity may be assumed to indicate a greater relative this is not strictly correct. A completely non-polar dispersant would be unable to interact with the platelet surface to any substantial degree and as a result it would be highly improbable that the nanoclay would exfoliate. Caution must therefore be taken when considering the polarity of a dispersant, and it must be contemplated in conjunction with the functionality. Finally, the viscosity of the dispersant is further confirmed to be unrelated to the final relative viscosity of the suspension.

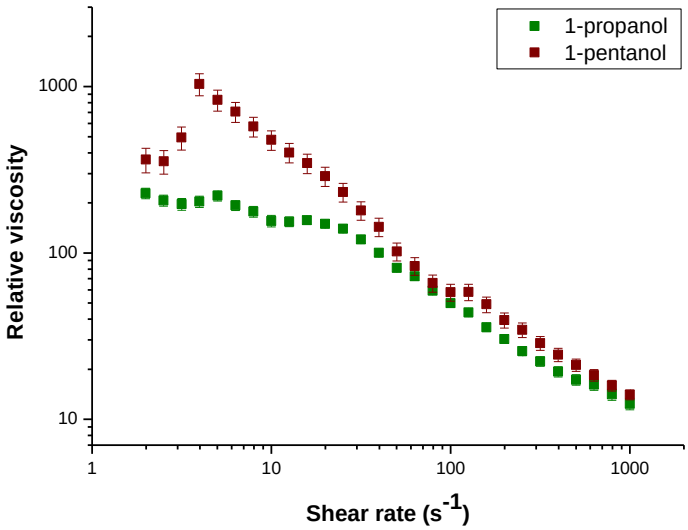

Figure 4.7 Relative viscosity versus shear rate. Suspensions of Cloisite® 20A in 1-propanol and 1-pentanol at a nanoclay loading of 6% w/w.

Table 4.4 The relative viscosity of various Cloisite® suspensions, illustrating the potential relationships between permittivity and viscosity increase. Relative viscosities have been determined at a shear rate of 10 s^{-1}. PS indicates phase separation within the sample which prevented rheological analysis.

Dispersant	Permittivity	Cloisite®				
		6A	15A	20A	10A	30B
1-propanol	20.8	114	120	140	PS	222
1-pentanol	15.13	488	510	624	PS	421
Ethylene glycol	41.4	PS	PS	6	17	17
1,5-pentanediol	26.2	3	3	5	PS	12
Diethylene glycol	31.82	7	PS	17	59	17
Triethylene glycol	23.69	7	PS	15	54	33
Tetraethylene glycol	20.44	6	7	13	54	40

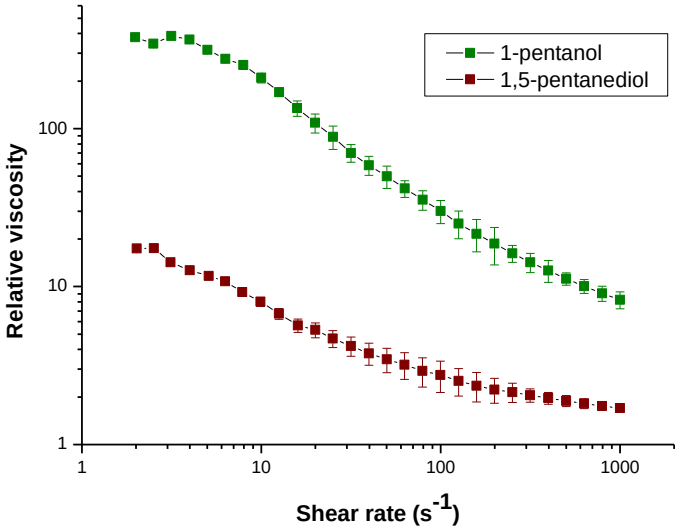

Figure 4.8 Relative viscosity versus shear rate. Suspensions of Cloisite® 30B in 1-pentanol and 1,5-pentanediol at a nanoclay loading of 6% w/w.

As the dispersant molar mass with respect to the chain length was influential within the mono-functional dispersants it was also examined within the bi-functional dispersants via figure 4.9. Phase separation was again an issue as ethylene glycol was one of the dispersants under study, and as a result only suspensions prepared with the Cloisite® 20A and 30B were examinable. In both instances, the relative viscosities of the ethylene glycol suspensions were greater than the respective 1,5-pentanediol suspensions. It is observed that although the bi-functional alcohols possess a comparable dipole moment, ethylene glycol possesses a higher relative permittivity. The permittivity may then be suggested as influential in some manner to nanoclay exfoliation, as the higher permittivity has correlated with a greater observed relative viscosity.

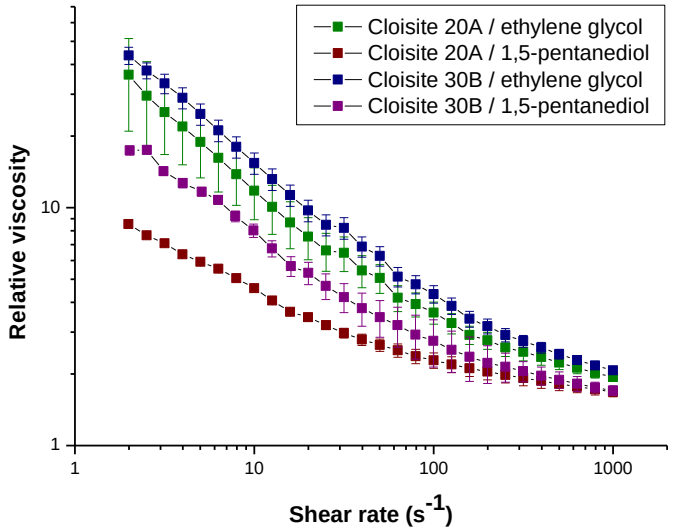

Figure 4.9 Relative viscosity versus shear rate. Suspensions of Cloisites® 20A and 30B in ethylene glycol and 1,5-pentanediol at a clay loading of 6% w/w.

In order to complete the study into attributes which are influential during exfoliation, the influence of functionality was examined through a comparison of low molar mass dispersants i.e. 1-propanol and ethylene glycol. It was observed that Cloisite® suspensions prepared in 1-propanol possessed a greater relative viscosity than the respective ethylene glycol suspensions. This further confirmed the postulate that the ability of a dispersant to act as a surfactant is more influential during exfoliation than either the polarity or permittivity. Figure 4.10 also further illustrates that exfoliation is not dependent on molar mass as the suspensions prepared in 1-propanol possessed some of highest relative viscosities observed during this study.

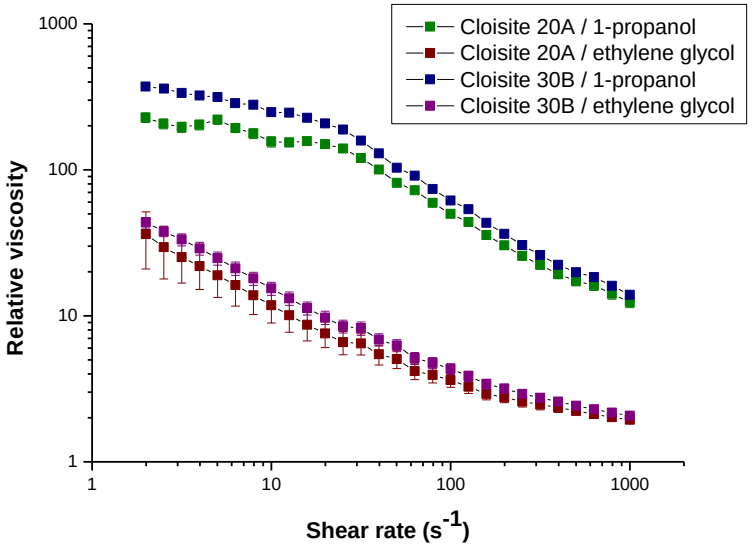

Figure 4.10 Relative viscosity versus shear rate. Suspensions of Cloisites® 20A and 30B in 1-propanol and ethylene glycol at a nanoclay loading of 6% w/w.

Throughout this chapter it has been demonstrated that the preparation of a stable Cloisite® suspension requires the nanoclay, surface modifier and dispersant to possess certain attributes. The exfoliation process is therefore not a simple matter of 'like dissolves like', for example, Cloisite® suspensions in 1-pentanol were observed to possess a greater relative viscosity than those prepared with 1,5-pentanediol. The functionality was therefore considered to determine the manner in which the dispersant was able to interact with the nanoclay. Mono-functional dispersants were observed to produce suspensions which possessed a superior relative viscosity, and a mono-functional structure therefore dominated over influences such as polarity and permittivity. When employing bi-functional dispersants however a high polarity and permittivity were considered essential.

It is also noted by the author that there still significant debate within literature over whether interactions between the dispersant and modifier and a major contribution to nanoclay exfoliation. Kotek *et al* hypothesised that it is the nanoclay surface which the solvent 'sees', regardless of the modifier polarity.[4] Within the systems under study in this thesis however this postulate has been disproven. Reflection on table 4.2 illustrates that a surface modifier does indeed affect a nanoclays ability to exfoliate.

Reflection on tables 4.2 and 4.4 also indicates that the polarity and permittivity influence nanoclay exfoliation in different manners. It has been demonstrated that a high dispersant dipole moment correlated with a high relative viscosity. The relative viscosity had also increased to the greatest extent with the most hydrophilic nanoclays and those modifiers with the ability to interact with the dispersant directly i.e. via π-electron donation or the initiation of hydrogen bonding.

In addition, a high dispersant permittivity was observed to impart stability to the suspension after the initial exfoliation of the platelets, as it is related to the dispersants' effectiveness to dampen the attractive interplatelet forces which may cause re-agglomeration. Coulomb's inverse-square law of force states: the permittivity of the dispersing medium (ε) is inversely related to the force of attraction between two charges (q′ and q″) a specific distance apart (r), which in this case originating from two platelets. The permittivity also considers the degree of polarity within a dispersant with respect to the molecule as a whole. As a consequence it may be used to rationalise the observed phase separation in several of the Cloisite® dispersions and also the apparent irreproducibility of data when low viscosities are considered.

$$F = \frac{q' q''}{4\pi\varepsilon r^2}$$

Equation 4.2

Several authors have attempted to predict the stability of a suspension by examining the solubility parameters of the nanoclay, modifier and dispersant.[5, 6] Hansen's solubility parameters in particular are often employed and define the chemical affinity between two or more molecular types through their cohesive energies of vapourisation. Flory-Huggins theory is the most commonly adopted method in literature and may be employed through equation 4.3, where χ_{AB} is the Flory-Huggins interaction parameter, and $\delta_A$and δ_B are the solubility parameters for the dispersant and modifier respectively. It must be stressed however that the Flory-Huggins interaction parameter only provides an approximate guide to the miscibility between two components.[5] This is due to the assumption that Van der Waals forces are the only interactions present, and it therefore does not take into consideration, for example, dipolar or hydrogen bonding interactions. In reality the Flory-Krigbaum theory would describe the systems under study in a more

appropriate manner, however due to the complexity of the model it is considered unsuitable.[7]

$$(\delta_A - \delta_B)^2 \approx 6\chi_{AB} \qquad \text{Equation 4.3}$$

Despite its shortcomings, Flory-Huggins theory is a commonly accepted method within literature for gauging the miscibility of a polymer or dispersant and a nanoclay.[5] As this method is accepted to some degree within literature it is consequently considered appropriate for use within this thesis. Prior to any calculation of the interaction paratemeters the effect of the surface modifier on the solubility parameter must be understood and will now be discussed.

Nanoclay surfaces are highly polar when unmodified and as a result are presumed to possess a high solubility parameter. Modification by, for example, quaternary ammonium alkyls is considered to alter the solubility parameter of the nanoclay surfaces. If the solubility parameter of the nanoclay is close to that of the dispersant, the components will have a high affinity for one another i.e. they will be miscible. In order to simplify the solubility parameters for the quaternary modifiers, calculations are based upon the alkyl chain with the greatest number of carbon units, and any contribution from the ammonium nitrogen is disregarded. The solubility parameters for the Cloisite modifiers have been reported in literature as follows: tallow, or DMDHT of Cloisites® 6A, 15A and 20A, 18 - 28 $(J/m^3)^{1/2}$; DMBHT of Cloisite® 10A, 16.2 $(J/m^3)^{1/2}$; MT2EtOH of Cloisite® 30B, 16.8 $(J/m^3)^{1/2}$.[5, 8] It is noted that although the tallow is often the greatest steric influence within the modifier it is the functionality which determines the ability of the modifier to interact with the dispersant. Previous calculations have also considered the density of the alkyl tallows to be influential and the density has been likened to that of poly(ethylene) or simple $C_{14\text{-}16}$ alkyl chains.[5, 8, 9] In reality however it is assumed the tallow density is a far more complex consideration, and is dependent on the unpredictable binding patterns of the modifier to the platelet surface and the surface modifier concentration.

Although it is apparent there are several issues with the Flory-Huggins model there is no suitable alternative at present. The Flory-Huggins interaction parameters for the

suspensions under study are therefore shown within table 4.5, allowing the calculated miscibility of the modifiers and dispersants to be examined. It should be noted that the smaller the value of χ_{AB} the greater the miscibility of the two components.

It is observed that the calculated solubility parameters for the dispersants and modifiers under study do not agree with conjecture; the suspensions which possess the greatest relative viscosity do not necessarily correlate with a lower χ_{AB} value. Throughout the chapter Cloisites® which possessed DMBHT or MT2EtOH surface modifiers were observed to form suspensions with the greatest relative viscosities; however DMDHT and dispersant interactions were calculated as possessing the lowest χ_{AB} values. If the χ_{AB} values for the DMDHT modifier are considered with the range of dispersants under study, the suspensions which possessed the greatest relative viscosities do generally appear to correlate with lower χ_{AB} values. This behaviour is not replicated in the systems which contain the DMBHT and MT2EtOH modifiers however. The apparent correlation of the experimental data and calculated interaction parameters relating to the DMDHT modifier and dispersants is considered to be due to the non-polar nature of the modifier, which may only interact with the dispersant via Van der Waals forces. The discrepancies in the interaction parameters between polar modifiers and the dispersants therefore confirm the previous assertion that the Flory-Huggins model should not be applied to systems which possess hydrogen bonding or π-electron interactions. As a final note this sub-study illustrates why literature tends not to correlate the interaction parameters with any physical observations.[5]

Table 4.5 Calculated Flory-Huggins Interaction Parameters for Cloisite® modifiers in various dispersant media.[9] A mid-range value of 23 $[J\ m^3]^{1/2}$ was employed as the DMDHT solubility parameter.

Dispersant	Solvent Solubility Parameter, δ_A / $[J\ m^3]^{1/2}$	Calculated Flory-Huggins Interaction Parameters (χ_{AB})		
		DMDHT	DMBHT	MT2EtOH
1-propanol	24.3	0.28	10.94	9.38
1-pentanol	21.7	0.28	5.04	4.00
Ethylene glycol	29.9	7.94	31.28	28.60
1,5-pentanediol	23.5	0.04	8.88	7.48
Diethylene glycol	24.8	0.54	12.33	10.67
Triethylene glycol	21.9	0.20	5.42	4.34
Tetraethylene glycol	20.3	1.22	2.80	2.04

4.5 CONCLUSIONS

When considering suspensions prepared in bi-functional dispersant the relative viscosity has been determined as dependent on both the dispersant polarity and permittivity. Polarity, expressed via the dipole moment, was an indication of the presence of polar functional groups within the dispersant and was therefore considered as an indication of the dispersants' potential for hydrogen bonding. The permittivity was considered as an indication of suspension stability during and post-exfoliation. The permittivity was associated with the ability of the dispersant to dampen attractive interplatelet forces which may cause re-agglomeration, however could not be employed as an indication of suspension relative viscosity. The permittivity could also not be employed as an indication of suspension stability when considering the mono-functional alcohols. Due to the surfactant behaviour of the mono-functional alcohols a lower permittivity was observed to produce suspensions with a higher relative viscosity. As the permittivity was inversely proportional to alkyl chain length in this instance, the dispersants with the lowest permittivity and therefore largest chain lengths were able to exfoliate the platelets to the highest degree. With respect to the mono-functional alcohols, the permittivity was therefore an indication of the dispersants ability to exfoliate the nanoclay. It should also be noted that although additional attributes such as the dispersant molar mass and viscosity were also examined throughout this chapter, they were observed to have no direct influence on the dispersants ability to exfoliate the nanoclay.

Finally, the Cloisite® nanoclays which were exfoliated in ethylene glycol were observed to exhibit stability issues which generally led in phase separation. As the preparation of a stable suspension was a pre-requisite for *in situ* polymerisation, montmorillonite was therefore deemed unsuitable for use as a filler. Sepiolite nanoclays however had been observed to form stable and reproducible suspensions within section 4.1 and were therefore suitable alternatives. As a result, Garamite® 1958 was employed in the remainder of this thesis

4.6 REFERENCES

1. Ingram, S., Dennis, H., Hunter, I., *Influence of clay type on exfoliation, cure and physical properties of in situ polymerised poly(methyl methacrylate) nanocomposites,* Polymer International, 2008, **57**(10), 1118-1127.
2. McClellan, A.L., *Tables of Experimental Dipole Moments*, 1963, W.H. Freeman & Company, London.
3. Chemical Rubber Company, *Handbook of Physics and Chemistry*, 2004, CRC Press, Boca Raton.
4. Kodek, J., Kelnar, I., Studenovsky, M., Bladrin, J., *Chlorosulphonated polypropylene: preparation and its applications as a coupling agent in polypropylene-clay nanocomposites,* Polymer, 2005, **46**, 4876-4881.
5. Jang, B.N., Wang, D., Wilkie, C.A., *Relationship between the Solubility Parameter of Polymers and the Clay Dispersion in Polymer/Clay Nanocomposites and the Role of Surfactant,* Macromolecules, 2005, **38**, 6533-6543.
6. Ho, D.L., Glinka, C.J., *Effects of Solvent Solubility Parameters on Organoclay Dispersions,* Chemical Materials, 2003, **15**(6), 1309-1312.
7. Alger, M., *Polymer Science Dictionary*, 2nd ed, 1997, Chapman & Hall, London.
8. Ho, D.L., Briber, R.M., Glinker, C.J., *Characterisation of Organically Modified Clays Using Scattering and Microscopy Techniques,* Chemistry of Materials, 2001, **13**(5), 1923-1931.
9. Brandup, J., *Polymer Handbook,* Vol. 8, 1975, John Wiley & Sons.

CHAPTER 5 CHARACTERISATION

5.1 CHARACTERISATION OF GARAMITE® 1958

5.1.1 COMBINED DSC - TGA

The analysis of the nanoclays through thermogravimetric methods allows the determination of water and organic content within the material, which is essential for determining the experimental clay loadings within the polymer nanoclay composites. In addition, characteristic mass loss at certain temperatures will also provide insight into the identity of the nanoclay. Prior to its characterisation within this thesis the Garamite® nanoclay was suspected to be a blend of sepiolite, palygorskite and montmorillonite nanoclay, surface modified by ammonium salts.[1, 2]

Figure 5.1 illustrates the thermo-oxidative degradation of sepiolite, as characterised by simultaneous TGA-DSC. It is observed that mass loss occurs in four distinct stages. The initial stage below 100°C is attributed to the loss of free or loosely bound surface water and zeolitic water. The intermediary peaks at 287°C and 507°C are attributed to the loss of co-ordinated or structural water molecules within the crystal lattice pores. After the loss of the second co-ordinated water molecule the structure collapses to form sepiolite anhydride. Dehydroxylation of the silanol functions then cause the final mass loss >800°C which is accompanied by an immediate phase change to clinoenstatite.[3] It is noted the % mass loss for the second co-ordinated water is slightly lower than that of the first although the molecules should theoretically be equivalent. It is suggested the second co-ordinated water occurs at a higher temperature due to stronger interactions between the molecule and the lattice, i.e. the lattice may co-ordinate twice as strongly as there is only one water molecule now present. The broadening of the derivative peak relating to the second co-ordinated water may also be explained due to these enhanced lattice interactions, as water loss is more difficult and therefore occurs over a larger temperature range than that observed for the first co-ordinated water molecule.

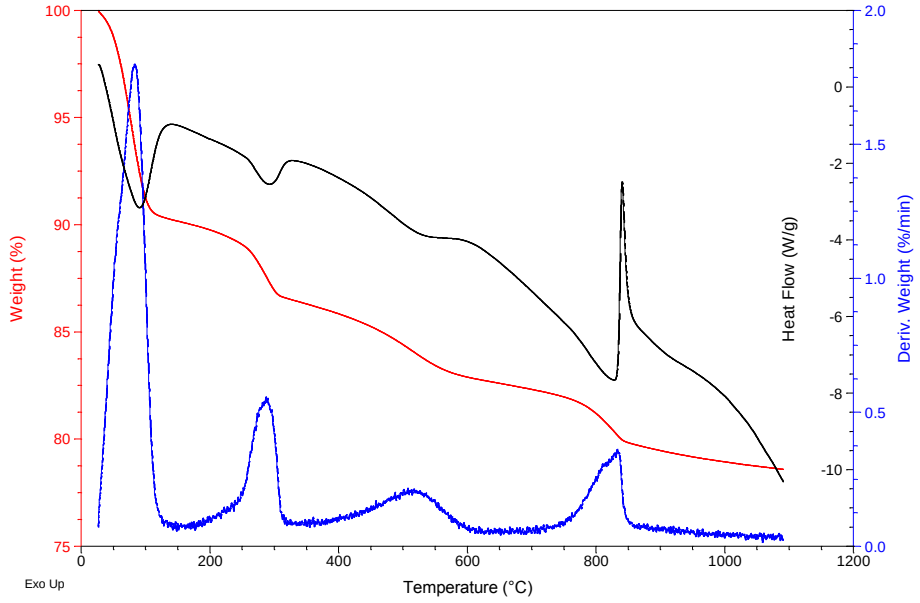

Figure 5.1 DSC-TGA plot for unmodified sepiolite nanoclay. Analysis was performed at a heating rate of 10°C min^{-1} under air

Table 5.1 Thermogravimetric data for montmorillonite nanoclay during oxidative heating. Analysis was performed under air at a rate of 10°C min^{-1}

	Stage 1	**Stage 2**	**Stage 3**	**Stage 4**
Peak Maximum / °C	82.75	286.75	507.45	832.88
% Mass Loss	10.12	4.04	3.45	3.45

The TGA data for montmorillonite is illustrated in figure 5.2, and in comparison to the sepiolite mass loss profile in figure 5.1, it is a simpler process. The loss of free or loosely bound water is observed at 64°C, approximately 20°C lower than that of sepiolite which suggests the water is bound less tightly in the case of montmorillonite. It is noted there is no detectable water loss from intergallery spaces or cation co-ordination spheres (which is generally observed between 100°C and 500°C).[4] The second significant loss in mass occurs at 645°C and is attributed to water resulting from the dehydroxylation of the crystalline lattice. The dehydroxylation of montmorillonite occurs at a significantly lower temperature than that observed for sepiolite. It is possible that this is due to the inverted, fibrous nature of sepiolite which collapses on the loss of the co-ordinated water molecules. This collapsed structure would then inhibit the diffusion of the dehydroxylation products out of the structure.

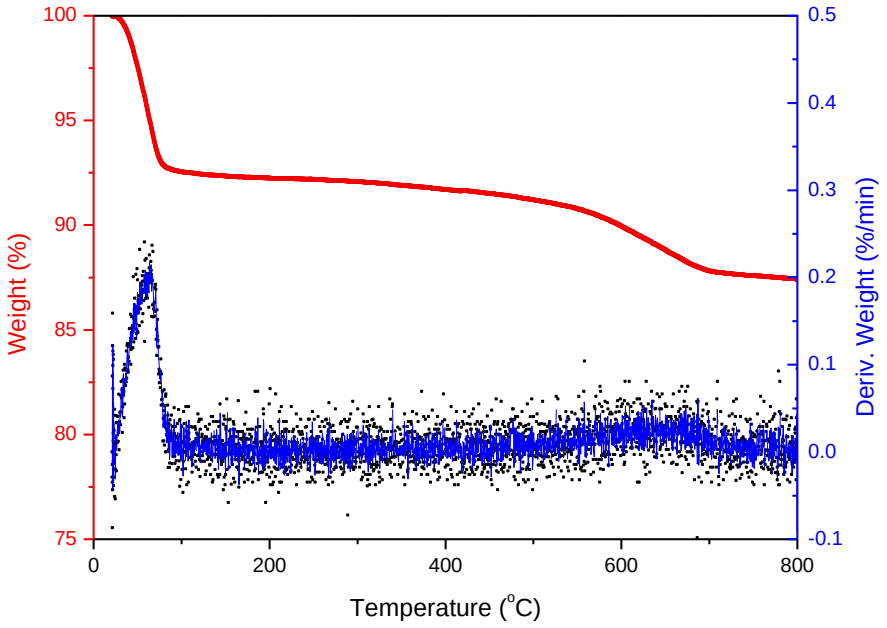

Figure 5.2 TGA plot for unmodified montmorillonite nanoclay. Analysis was performed at a heating rate of 10°C min^{-1} under air

Table 5.2 Thermogravimetric data for montmorillonite nanoclay under oxidative conditions. Heating was performed under air at a rate of 10 °C min^{-1}

	Stage 1	**Stage 2**
Peak Maximum / °C	64.58	646.15
% Mass Loss	8.11	4.45

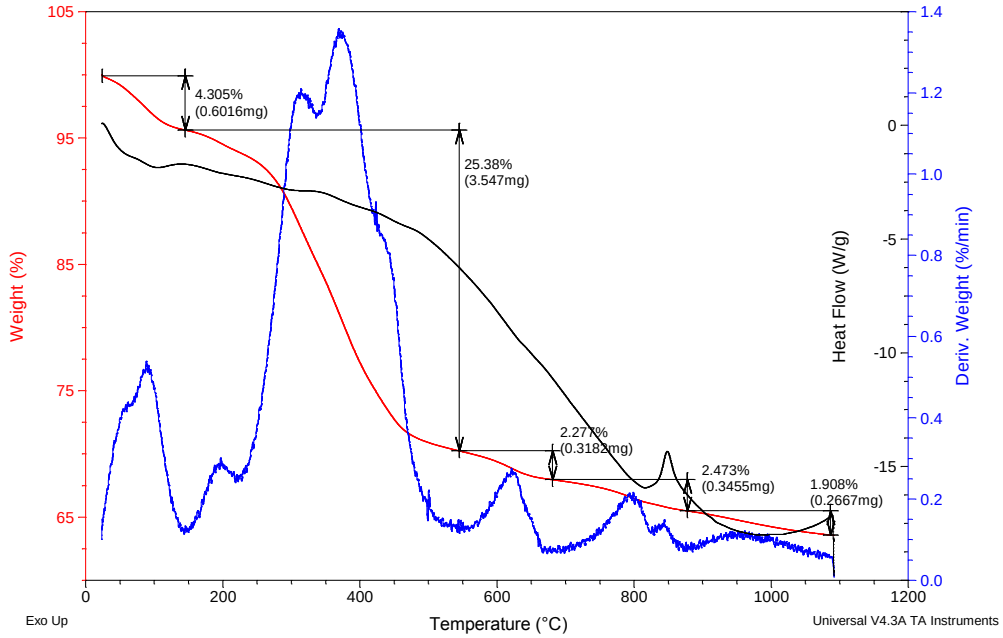

Figure 5.3 DSC-TGA plot for Garamite® 1958 nanoclay. Analysis was performed at a heating rate of 10°C min^{-1} under air.

The TGA thermogram of Garamite® indicates there are two different types of free or loosely bound water within the nanoclay. The temperatures of mass loss are observed to be relatively comparable with those observed within montmorillonite and sepiolite. Peaks associated with the degradation of the organic modifiers are observed between 199°C and 850°C, with the multiple peaks indicating that mass loss occurs in stages. Peaks identified with the dehydroxylation of montmorillonite and sepiolite may also be observed at temperatures of 620°C and 841°C respectively, which is comparable to the pure nanoclay. It is unlikely however that the dehydroxylation of montmorillonite however contributes to the degradative profile degree which is observed. It is therefore suggested that this peak is predominantly attributed to the degradation of the organic modifiers. Dehydroxylation of the sepiolite nanoclay does occur in slightly different manner within the Garamite® however this could be attributed to numerous causes. The high temperature peak is concluded to be the oxidation of the carbonaceous residue originating from the organic surface modifiers as it is not present within the TGA-DSC plots for the unmodified sepiolite.

Table 5.3 Maximum peak temperatures observed within TGA thermograms of Garamite®. Analysis was performed under air at a heating rate of 10°C min^{-1}.

Nanoclay	**Maximum Peak Temperatures / °C**								
Garamite®	60.1	89.2	199.1	314.7	368.8	620.4	794.5	841.4	956.5
% Mass Loss	4.31		25.38			2.28	2.47		1.91

If the previous % mass losses upon heating are compared with the Garamite®, the organically modified nanoclay is observed to possess a lower free water content. The water loss due to dehydroxylation is slightly higher than observed in montmorillonite and sepiolite, although due to the complexity of the Garamite® thermogram within this region it is likely due to overlapping transitions and difficulties in determining transition start and end points. The organic content is also determined as 32.04% via addition of the % mass losses attributed to the different stages in modifier degradation. It is noted that due to the relatively high organic content a substantial amount of free, unbound modifier must be present within the system.

In conclusion, thermogravimetric analysis does not definitively confirm which nanoclays are present within the Garamite® blend. The thermograms under study however do suggest that the presence of sepiolite and montmorillonite is plausible, and that the nanoclay is organically modified. In addition, due to the multiple peaks observed during the degradation of the organic modifiers, this also confirms the modification is through surface interactions only and the modifier is not grafted to the nanoclay surfaces.

5.1.2 SCANNING ELECTRON MICROSCOPY

Electron microscopy is an extremely useful technique when identifying nanoclays. As specific nanoclays tend to have characteristic shapes the identity of the Garamite® may be determined quickly whilst providing a wealth of additional information. Figures 5.4 – 5.7 contain electron micrographs of Garamite® at various magnifications.

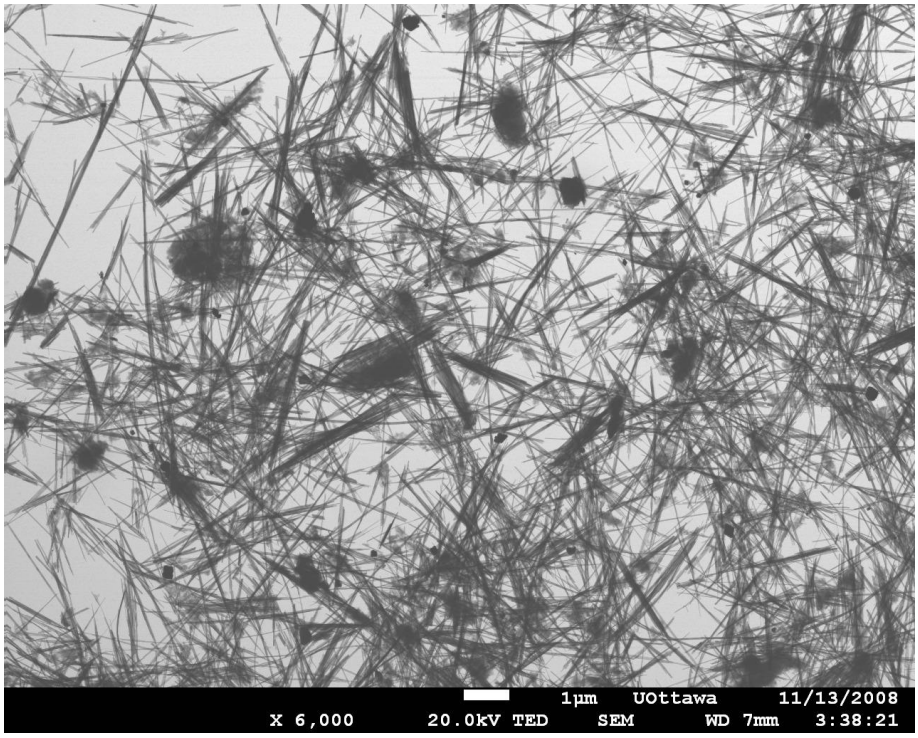

Figure 5.4 Scanning electron micrograph of Garamite® 1958 at 20.0kV and a magnitude of x 6,000.

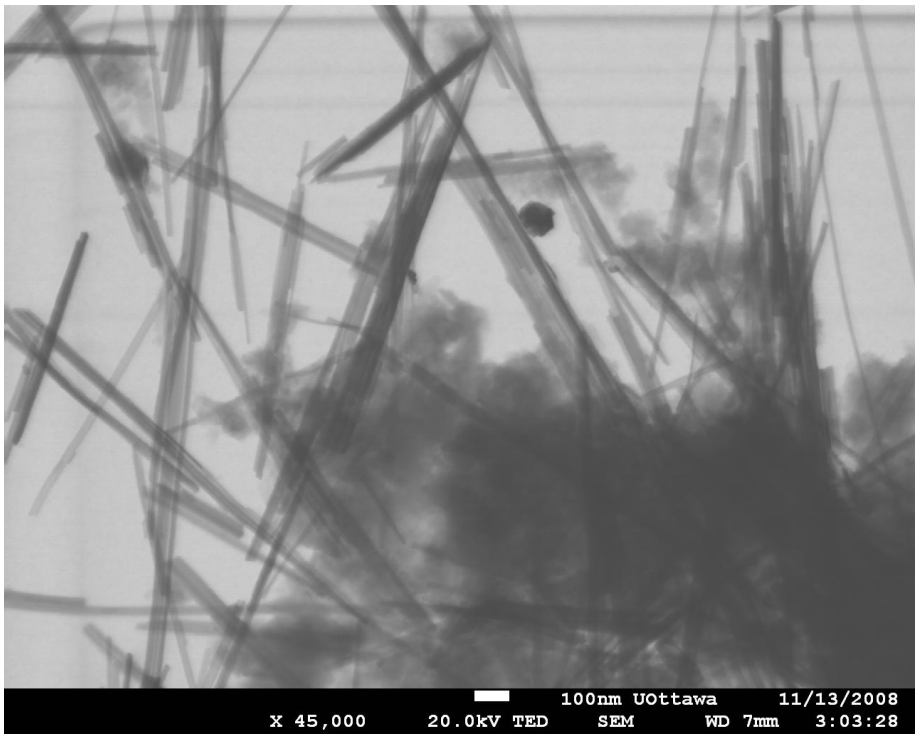

Figure 5.5 Scanning electron micrograph of Garamite® 1958 at 20.0kV and a magnitude of x45,000.

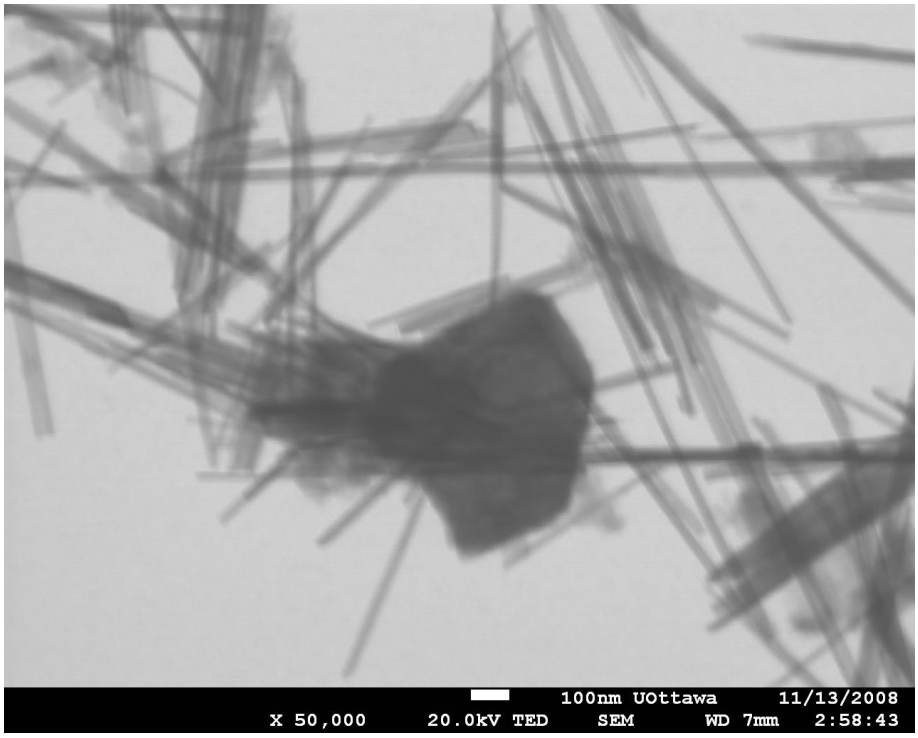

Figure 5.6 Scanning electron micrograph of Garamite® 1958 at 20.0kV and a magnitude of x50,000.

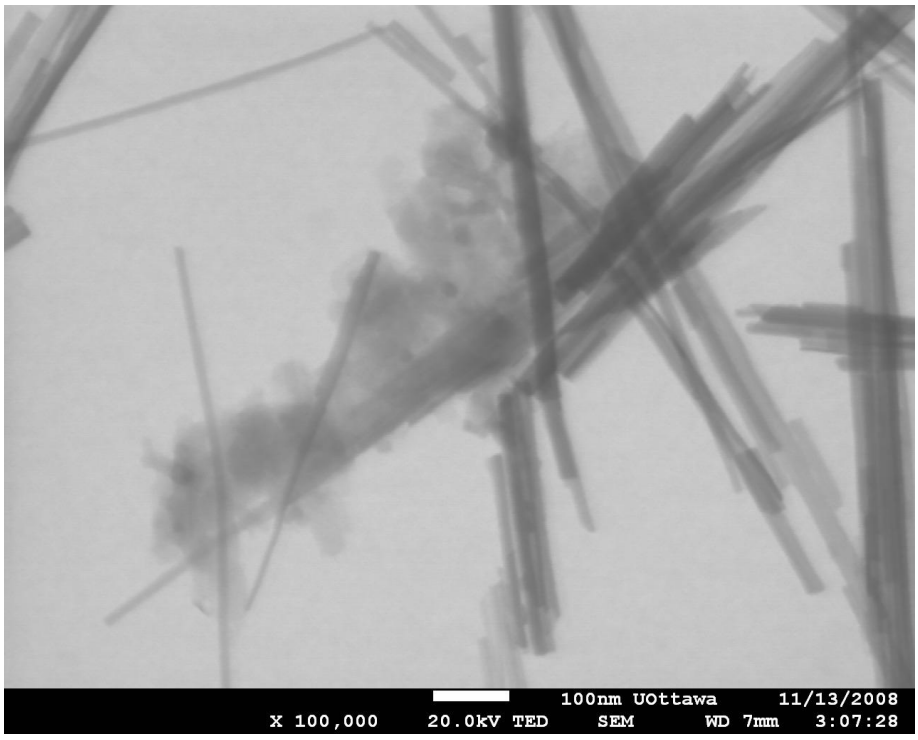

Figure 5.7 Scanning electron micrograph of Garamite® 1958 at 20.0kV and a magnitude of x100,000.

It is clear from the electron micrographs that the major constituents of Garamite® are thin, fibrous strands of material. These strands are observed to exist in exist a closely packed arrangement or loosely in clusters. The width of individual fibres was determined manually as 13.33 nm and the length varied substantially and ranged between 250 nm to 9 µm in length. The average manually determined length however was 4.11 µm. It is evident there is also an excess of organic modifier within the material, as previously suggested by thermogravimetric analysis. An excess of organic modifier is known to cause thermal instabilities in composite materials, however these instabilities are generally observed at relatively high nanoclay loadings.[5] It is possible that the low loadings employed in the systems discussed within this thesis may therefore not develop the same thermal instabilities that have been observed elsewhere.

Within figures 5.5 and 5.6 a trace material is also observed. It is suspected that due to the hexagonal platelet like-shape the material is likely to be either montmorillonite or kaolinite, although sepiolite and palygorskite nanoclays are also known to contain trace quartz impurities.[6, 7] The trace hexagonal crystals were measured manually as 108 nm and 700 nm in diameter. As these diameters are within the observed literature ranges for both nanoclays no further identification may be made.[8, 9]

5.1.3 XRD

X-ray diffraction is an extremely useful tool in the analysis of clay minerals. The Bragg plots provide not only a series of characteristic reflections which allow the identification of unknown materials, but also allow any damage or disintegration of the crystal lattice to be identified. This technique is therefore particularly useful when analysing unknown or suspect material such as Garamite® which are also known to have undergone chemical treatments such as acidification.

Figure 5.8 contains the Bragg plots for unmodified sepiolite and Garamite® nanoclay. The peak positions are comparable however the intensities are observed to differ slightly. This

is not unexpected however as spacing and intensities for sepiolite minerals are known to vary to some degree between samples.[6]

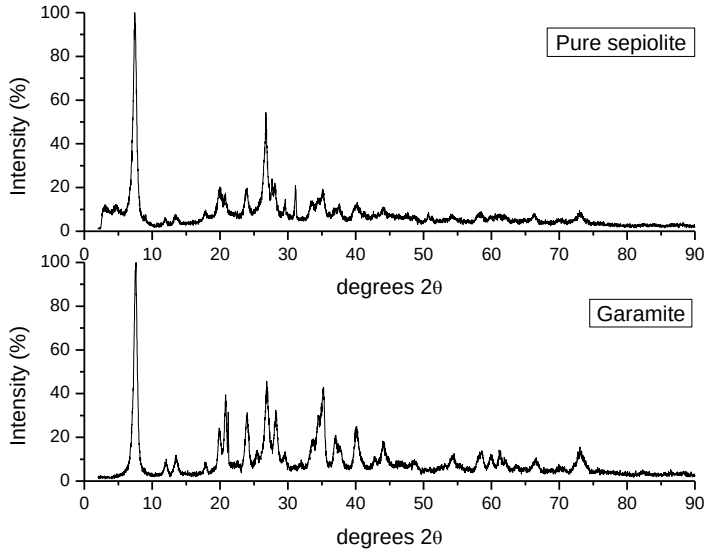

Figure 5.8 XRD spectra of unmodified sepiolite and Garamite® nanoclays between 2.0° and 90° 2θ.

Tables 5.4 and 5.5 contain the experimental XRD data and standards summarised from literature.[3, 6] The sepiolite and Garamite® data are in close agreement with each other and it is concluded that Garamite® does predominantly consist of sepiolite. It also does not appear to possess any palygorskite nanoclay as its high intensity peak at 8.5° 2θ is not observed. Within the electron micrographs a trace material was also observed that was suspected as montmorillonite or kaolinite due to the hexagonal shape. If kaolinite or montmorillonite is present with Garamite the XRD spectra will contain reflections at 12.5° and 24.9° 2θ, and 26.69° 2θ respectively. Due to sample variation however the unidentified peak at 25.47° 2θ may originate from either aluminosilicate. In addition, quartz impurities were also evident within XRD spectra of Garamite. Quartz is a common impurity within the sepiolite-palygorskite series and so was not unexpected.[6] It is therefore concluded that the trace material within the electron micrographs was most probably quartz, as opposed to montmorillonite or kaolinite.

Table 5.4 XRD spectral data from sepiolite and Garamite nanoclays between 2.0° and 90° 2θ. Data highlight in purple was identified as quartz reflective peaks whilst data highlighted in red was unidentifiable.

Garamite		Sepiolite		Garamite		Sepiolite	
2θ /°	**I / %**	**2θ /°**	**I / %**	**2θ /°**	**I / %**	**2θ /°**	**I / %**
-	-	3.05	11.94	-	-	31.17	21.19
-	-	4.68	12.30	33.66	18.97	33.51	13.58
7.66	100	7.47	100	35.28	43.21	35.17	19.56
12.11	10.19	11.92	6.44	37.09	20.96	37.66	12.65
13.51	11.59	13.36	7.85	40.11	25.06	40.23	13.47
17.85	8.43	17.89	10.19	42.83	11.01	-	-
19.89	24.00	19.96	19.44	44.11	18.38	44.00	11.12
20.83	39.46	20.87	17.45	48.64	10.19	50.75	8.67
21.21	31.38	-	-	54.53	12.53	-	-
24.04	31.38	23.89	18.85	58.57	13.47	-	-
25.43	14.05	-	-	59.96	12.41	58.45	9.02
26.87	45.78	26.72	54.80	61.21	14.40	-	-
-	-	27.66	24.00	66.64	10.42	66.38	8.20
28.19	32.67	28.15	21.90	73.02	15.46	72.91	9.60
29.62	13.35	29.58	14.75	-	-	3.05	11.94

Table 5.5 XRD spectral data obtained from literature.[3, 6]

Sepiolite		Palygorskite		Quartz	
2θ /°	**I / %**	**2θ /°**	**I / %**	**2θ /°**	**I / %**
6.9	100	8.5	100	20.80	21
11.6	4	13.8	16	26.67	100
17.4	8	16.4	11	36.57	8
20.2	35	19.9	17	39.49	8
23.6	20b	24.4	10	40.32	4
26.6	30vb	28.1	16	42.50	6
-	-	-	-	45.83	4
-	-	-	-	50.18	14
-	-	-	-	54.91	4
-	-	-	-	55.38	2
-	-	-	-	60.00	9
-	-	-	-	64.04	1

5.2 CHARACTERISATION OF POLY(ETHYLENE TEREPHTHALATE) GARAMITE® 1958 NANOCOMPOSITES

5.2.1 TGA

Degradation of the PET and PET composites is examined fully within Chapter 7, however TGA is also employed to determine the experimental Garamite® content within the composites. As the composites contained a maximum Garamite® loading of 1.0% w/w TGA may also indicate the extent at which the Garamite® has distributed throughout the sample batch.

Polymer and composite samples were heated at a rate of 10°C min^{-1} under air to ensure all polymeric material had undergone pyrolysis and oxidation. As the Garamite® nanoclay also possessed an excess of organic modifier the final weights must be corrected for organic content. As the TGA thermograms of Garamite® are complex in nature the organic content and hence Garamite® loading within the composites cannot be determined with complete certainty.

Figure 5.9 and table 5.6 contains the dynamic degradative profiles and final masses on degradation of the polymer and composite chip. In order to obtain accurate Garamite® loadings two correction factors had to be applied to the data. The first was a correction factor relating to unoxidised polymer char. On average less than 0.04% material remained after pyrolysis and oxidation of the pure polymer, and so 0.04% of each final composite weight was also attributed to unoxidised char. In addition, the Garamite® is known to possess an excess of organic surface modifier and this also must be accounted for. Within section 5.1.1 a mass loss of 33.53% was attributed to organic material and moisture when examined under the same experimental conditions. Table 5.6 illustrates that the final observed weights and corrected experimental loadings were comparable within experimental error. The corrected loadings were also comparable to the theoretical loadings indicating the Garamite® was evenly distributed throughout the samples under

study. This indicated *in situ* polymerisation was a suitable method for incorporating the Garamite® into poly(ethylene terephthalate) at the loadings under study.

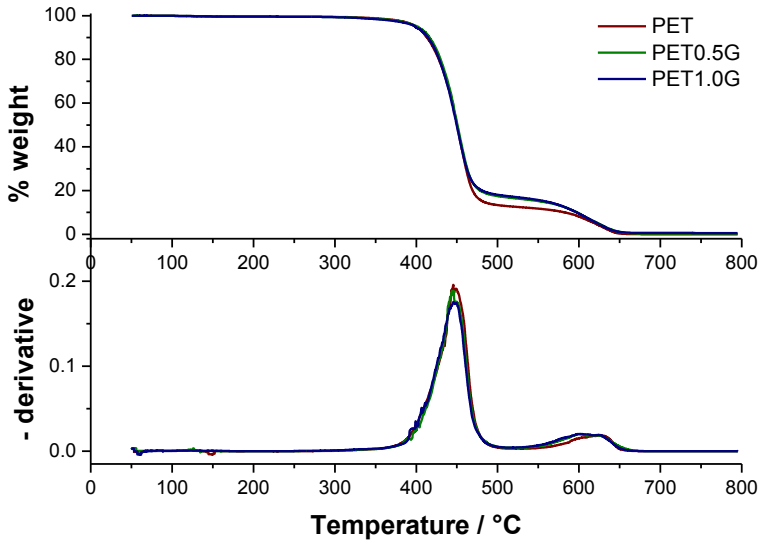

Figure 5.9 TGA thermogram of the thermo-oxidative degradation of PET and PET composites under air at a heating rate of 10°C min^{-1}.

Table 5.6 Garamite® loading data calculated from figures 5.9 and appendix 7. Errors were calculated using the standard deviation method.

Material	Sample	Replicate	Theoretical loading / % w/w	Final observed weight / %	Corrected experimental loading / % w/w
CHIP	PET	1	0.0	0.09 ± 0.06	-
		2		0.00 ± 0.06	-
		Average		0.04 ± 0.06	-
	PET0.5G	1	0.5	0.19 ± 0.02	0.22 ± 0.03
		2		0.16 ± 0.02	0.18 ± 0.03
		Average		0.17 ± 0.02	0.19 ± 0.03
	PET1.0G	1	1.0	0.89 ± 0.04	1.25 ± 0.06
		2		0.83 ± 0.04	1.16 ± 0.06
		Average		0.86 ± 0.04	1.21 ± 0.06
UNIAXIAL FILM	PET	1	0.0	0.00 ± 0.05	-
		2		0.07 ± 0.05	-
		Average		0.04 ± 0.05	-
	PET0.5G	1	0.5	0.27 ± 0.12	0.34 ± 0.18
		2		0.44 ± 0.12	0.59 ± 0.18
		Average		0.36 ± 0.12	0.47 ± 0.18
	PET1.0G	1	1.0	0.66 ± 0.04	0.91 ± 0.05
		2		0.61 ± 0.04	0.84 ± 0.05
		Average		0.63 ± 0.04	0.87 ± 0.05

5.2.2 NUCLEAR MAGNETIC RESONNANCE SPECTROSCOPY

5.2.2.1 ^{1}H NMR SPECTROSCOPY

A visual examination of the proton NMR spectra illustrates there is insignificant variance between samples. This indicates that the incorporation of Garamite® does not alter the polymerisation mechanism and therefore the chemical structure. In addition, although polymer degradation may be enhanced to some degree during melt processing the structure of the polymer is not observed to alter significantly.

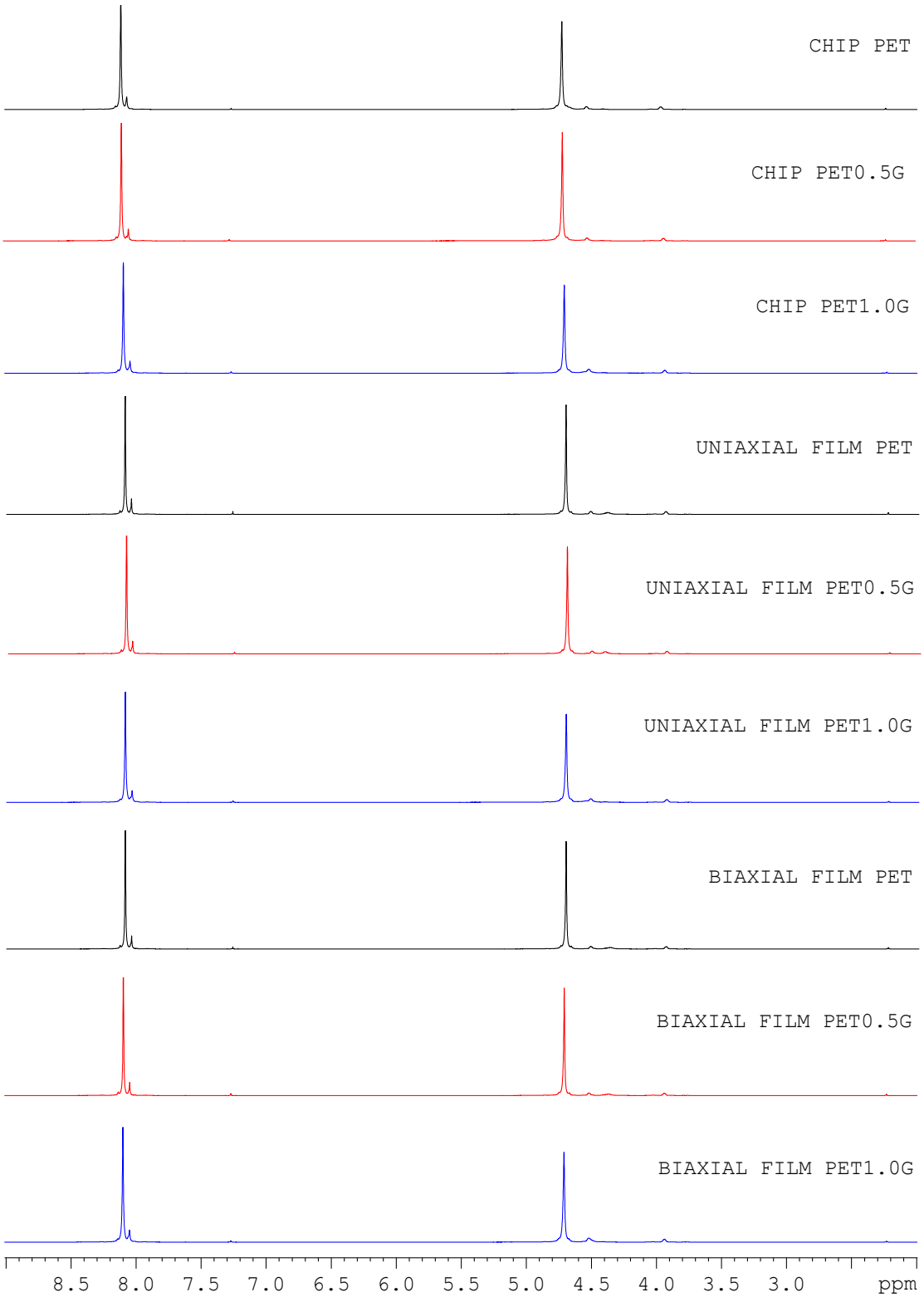

Figure 5.10 ^{1}H nmr spectra of various PET and PET composite materials in $CDCl_3$/HFIP.

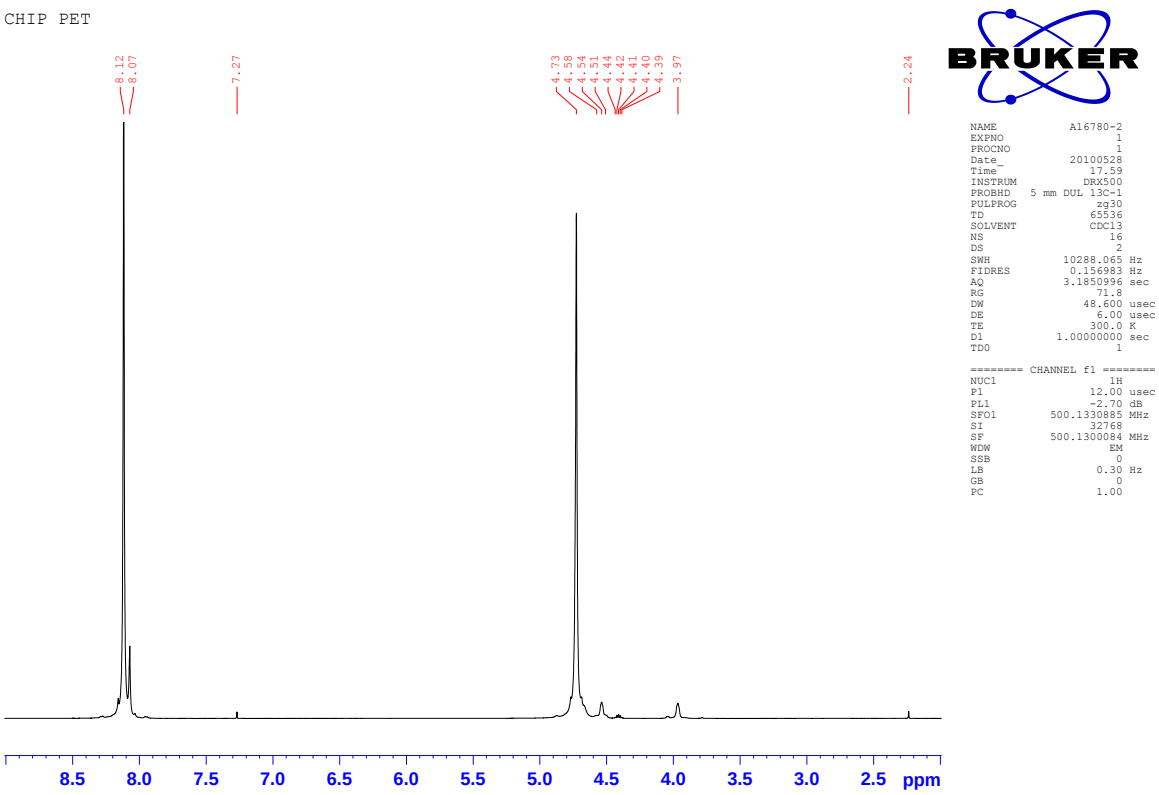

Figure 5.11 ^{1}H NMR spectra of PET CHIP in $CDCl_3$/HFIP

Table 5.7 contains the chemical shift values for the systems under study. The major peaks relating to aromatic and aliphatic protons within the polymer backbone are observed at an average of 8.099 ppm and 4.710 ppm respectively. Minor aliphatic peaks are also observed at 4.529 ppm and 3.967 ppm, and are suggested to originate from two possible sources within the polymer; glycol end groups or diethylene units as a result of side reactions. Both possible sources may be rationalised via electron density, however the glycol end group is more probable and so will now be discussed in detail. Within the repeat unit the ethylene protons are equivalent due to the balanced pull of electron density from the adjacent phthalate groups. The substitution of a phthalate group for a hydroxyl within the end groups however causes the protons to become non-equivalent as the chemical environment has altered and there is a decrease in the pull of electron density. As a result the protons experience a decrease in ppm or increase in field strength. The minor aromatic peak at 8.050 ppm may be accounted for in the same manner and is attributed to the aromatic protons within a phthalate-type end group. Deuterated chloroform and 1,1,1,3,3,3-

hexafluoro-isopropanol (HFIP) peaks are also observed as expected. It is noted however that the weak singlet is observed at 4.025 ppm and may be attribute to several sources. Hydroxyl protons are expected from both the HFIP solvent and glycol end groups. It cannot be attributed to either however with any degree of certainty.

Table 5.7 Observed chemical shifts within the ^{1}H NMR spectra of figure 5.10.

Peak no.	δ_H / ppm								
	Chip			Uniaxial film			Biaxial film		
	PET	PET0.5G	PET1.0G	PET	PET0.5G	PET1.0G	PET	PET0.5G	PET1.0G
1	8.118	8.099	8.097	8.097	8.100	8.090	8.092	8.097	8.100
2	8.073	8.045	8.046	8.050	8.053	8.040	8.050	8.048	8.049
3	7.270	7.270	7.269	7.270	7.270	7.270	7.270	7.270	7.269
4	4.728	4.709	4.708	4.708	4.713	4.700	4.708	4.708	4.710
5	4.539	4.522	4.519	4.519	4.523	4.520	4.519	4.518	4.520
6	4.412	4.402	4.403	4.401	4.414	4.400	4.403	4.401	4.406
7	4.043	4.022	4.022	4.025	4.023	4.020	4.025	4.024	4.025
8	3.967	3.932	3.935	3.939	3.944	3.930	3.939	3.938	3.938

Table 5.8 Average ^{1}H NMR chemical shift data and assignments relating to peaks within table 5.7.

Peak no.	δ_H / ppm	Peak description	Assignment
1	8.099	Strong singlet	Aromatic protons within a phthalate repeat unit
2	8.050	Weak singlet	Aromatic protons within a phthalate end group
3	7.270	Very weak	$CDCl_3$ solvent
4	4.710	Strong singlet	Methylene protons within the glycol repeat unit
5	4.522	Weak triplet	Methylene protons within the glycol end groups adjacent to the phthalate group / outer ethylene protons within a diethylene segment
6	4.405	Very weak quintuplet	Tertiary carbon proton of HFIP solvent
7	4.025	Very weak singlet	Hydroxyl proton of HFIP solvent / hydroxyl protons of glycol end group
8	3.940	Weak triplet	Methylene protons within the glycol end group adjacent to hydroxyls / inner methylene protons within a diethylene segment

Table 5.9 Peak integrations of the ^{1}H NMR spectra. A full set of spectra including integrations may be found within appendix 3, an example of which is contained within figure 5.11.

Peak no.	Integrations								
	Chip			Uniaxial film			Biaxial film		
	PET	PET0.5G	PET1.0G	PET	PET0.5G	PET1.0G	PET	PET0.5G	PET1.0G
1	3.549	3.513	3.623	3.713	3.733	3.631	3.700	3.736	3.688
2	0.452	0.422	0.507	0.435	0.434	0.547	0.458	0.430	0.540
3	-	-	-	-	-	-	-	-	-
4	4.000	4.000	4.000	4.000	4.000	4.000	4.000	4.000	4.000
5	0.253	0.224	0.494	0.208	0.210	0.340	0.209	0.168	0.418
6	-	-	-	-	-	-	-	-	-
7	0.026	0.027	0.020	0.023	0.027	0.024	0.024	0.026	0.022
8	0.184	0.158	0.207	0.186	0.159	0.203	0.184	0.160	0.203

Integrations of peaks 2, 5 and 8 appear to exhibit a slight increase within the PET1.0G samples in comparison to PET and PET0.5G. As these peak correlate to suspected end groups within the polymer chains it is reasonable to suggest they may also indicate a decreasing molar mass. Due to the number of potential end groups which may be present within the PET however is it unreasonable to employ potential end group integrations in molar mass calculations. Despite this it should be noted the data obtained through GPC and intrinsic viscosity measurements contained within Section 5.2.4 does support this hypothesis.

5.2.2.2 ^{13}C NMR SPECTROSCOPY

The ^{13}C NMR spectra within figure 5.12 were comparable between polymer and composite samples, confirming the observations made during ^{1}H NMR analysis and indicating the Garamite® did not alter the structure of the polymer during synthesis or melt processing. In addition as the structure of the polymer and composites does not alter between sample types this also suggests there is not a significant degree of thermo-oxidative degradation during melt processing.

As expected, peaks originating from the polyethylene terephthalate were observed throughout. Methylene carbons originating from polymer end groups were also observed at a slightly lower chemical shift than those within the main backbone. A small cluster of peaks was also observed within each spectrum between 68 - 70 ppm. A definite assignment could not be made, however it can be suggested that the peaks originate from a methylene proton adjacent to an oxygen atom.

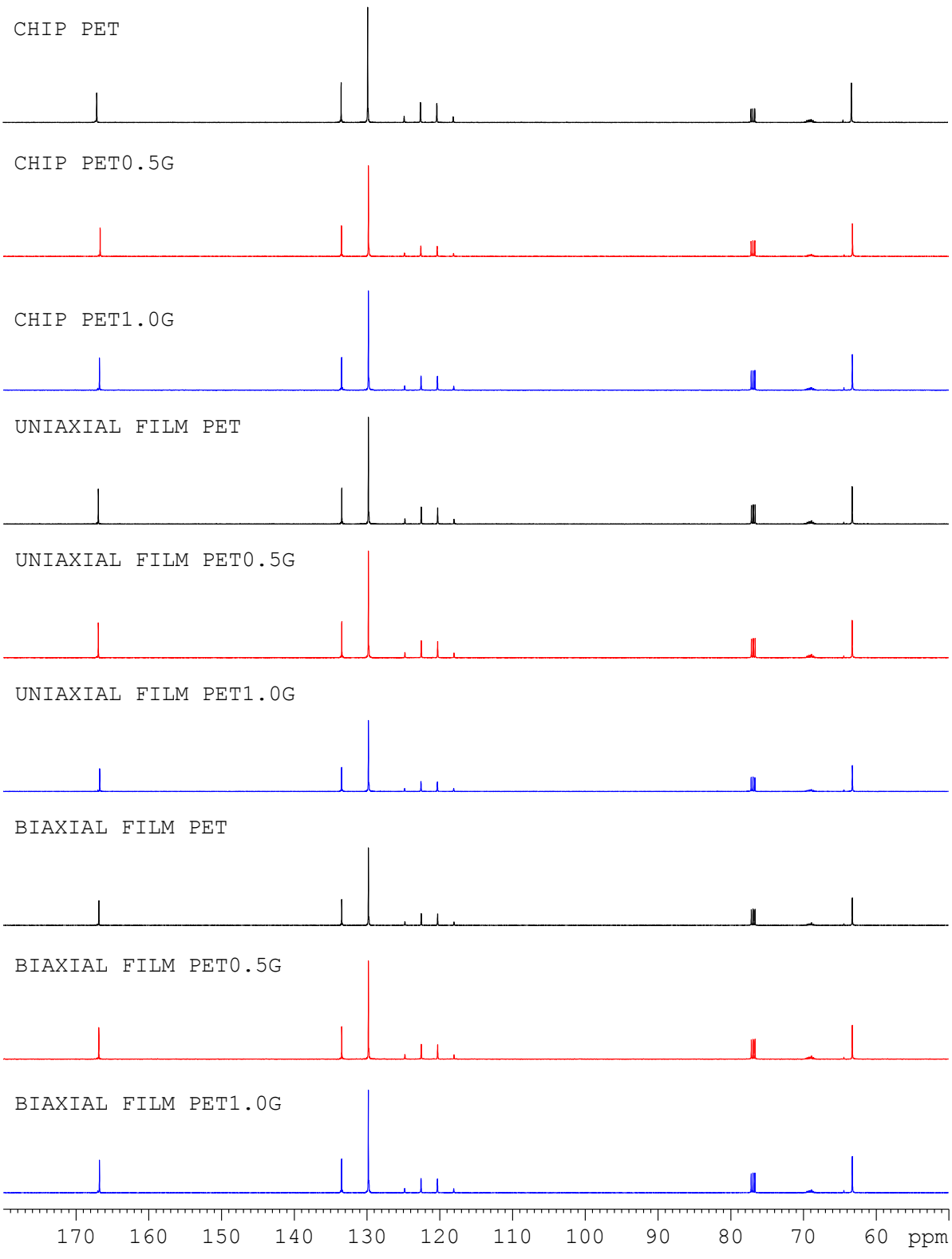

Figure 5.12 ^{13}C nmr spectra of various PET and PET composite materials in $CDCl_3$/HFIP.

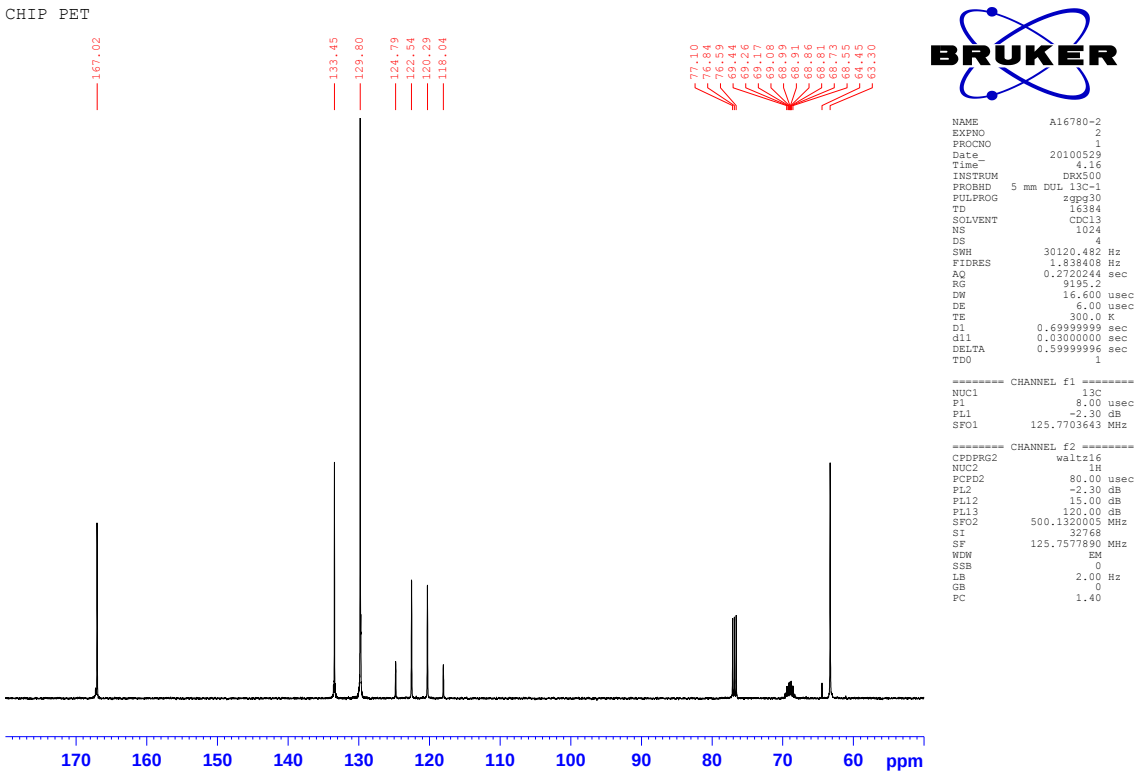

Figure 5.13 ^{13}C nmr spectrum of PET chip in $CDCl_3$/HFIP

Table 5.10 Peak assignments for average chemical shifts within figure 5.12 and table 5.12.

Peak no.	δ_C / ppm	Peak description	Assignment
1	63.138	Singlet	Methylene carbons
2	64.420	Singlet	Methylene carbons adjacent to hydroxyl end groups
3	68 – 70	Unidentified	Methyl or methylene carbon adjacent oxygen
4	76.890	Triplet	$CDCl_3$ solvent
5	123.599	Quartet	HFIP solvent
6	129.799	Singlet	Tertiary aromatic carbons
7	133.470	Singlet	Quaternary aromatic carbons
8	166.796	Singlet	Carbonyl carbon

Table 5.11 Observed chemical shifts within the ^{13}C NMR spectra of figure 5.12

Peak no.	δ_C / ppm								
	Chip			Uniaxial film			Biaxial film		
	PET	PET0.5G	PET1.0G	PET	PET0.5G	PET1.0G	PET	PET0.5G	PET1.0G
1	63.295	62.239	63.254	63.286	63.276	63.250	63.265	63.267	63.259
2	64.448	64.398	64.411	64.410	64.432	64.408	64.420	64.423	64.417
3	68-70	68-70	68-70	68-70	68-70	68-70	68-70	68-70	68-70
4	76.840	76.920	76.910	76.860	76.880	76.910	76.890	76.890	76.910
5	121.412	121.466	121.428	121.399	121.394	121.433	121.399	121.396	121.364
6	129.801	129.795	129.798	129.798	129.799	129.797	129.798	129.799	129.802
7	133.448	133.501	133.479	133.465	133.450	133.484	133.459	133.458	133.481
8	167.020	166.637	166.734	166.785	166.889	166.707	166.817	166.824	166.736

5.2.3 ATR-FTIR

Figure 5.15 illustrates that the ATR-FTIR spectra for both the polymer and composites were comparable. In addition the chip, uniaxial film and biaxial films are also comparable for each material. The observed vibrations were as expected with the high absorbance peaks originating from: aliphatic C-H stretching, carbonyl stretching, aromatic skeletal stretching, ester group stretching, in-plane aromatic vibrations and out-of plane aromatic vibrations associated with both the aromatic and carbonyl groups. These are illustrated in the ATR-FTIR spectra of PET CHIP within figure 5.14. Various additional weak vibrations were observed and are identified within table 5.12. Vibrations resulting from the nanoclay within the composites were not observed due to the low Garamite® loadings employed.

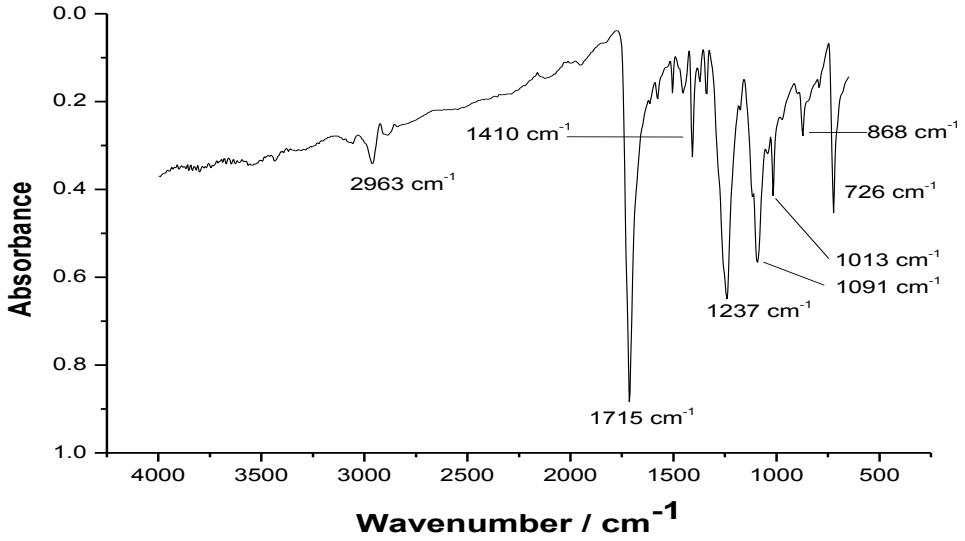

Figure 5.14 ATR-FTIR spectra of PET CHIP.

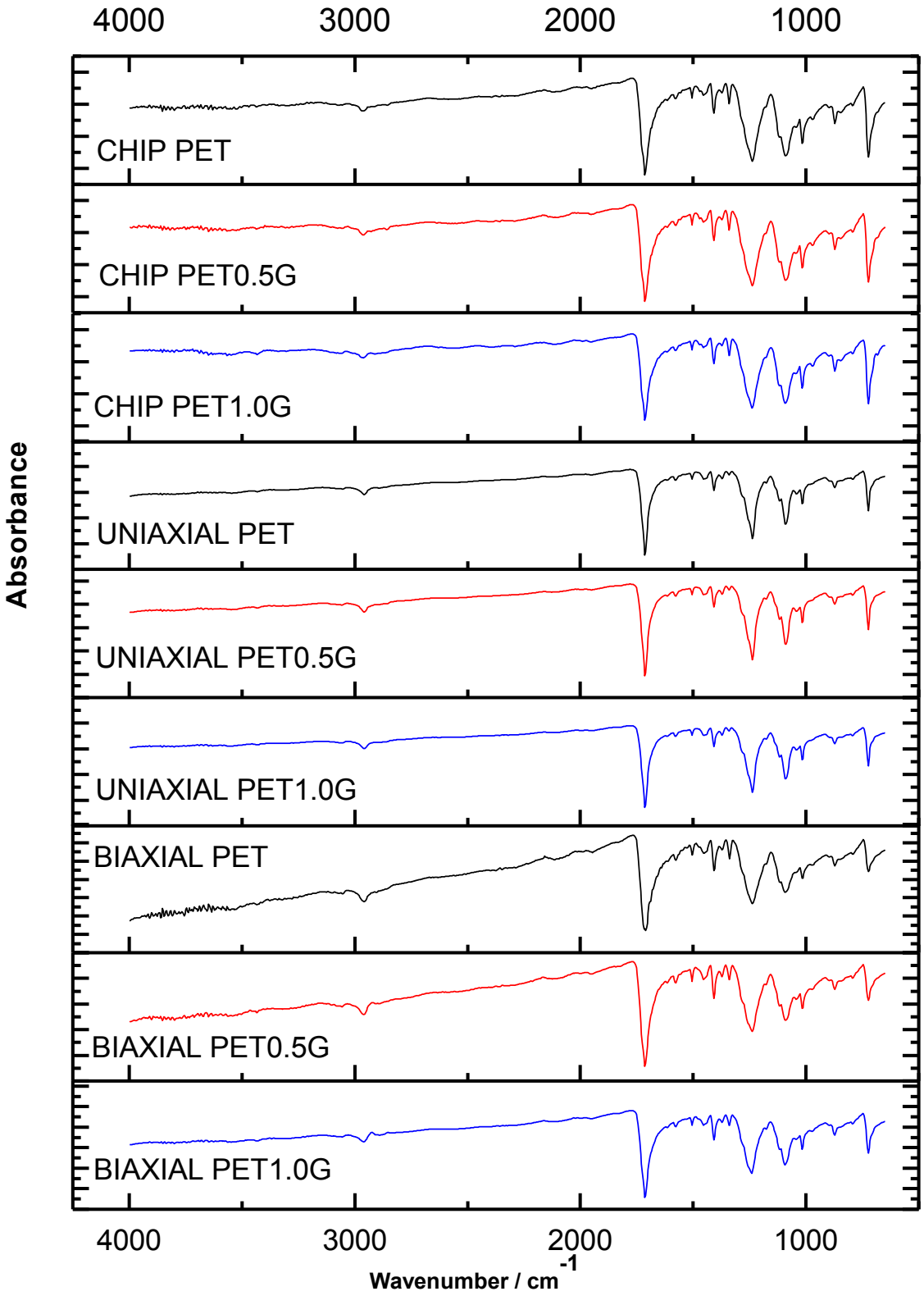

Figure 5.15 ATR-FTIR spectra of PET, PET0.5G, PET1.0G chip, uniaxial film and biaxial film.

Table 5.12 Observed peaks and their assignments within the ATR-FTIR spectra of PET, PET0.5G and PET1.0G chip, uniaxial film and biaxial film.

Wavenumber / cm^{-1}	Assignment
726	Out of plane deformations associated with the carbonyl groups of the terephthalate unit
868	Out of plane C-H deformations associated with of the aromatic group of the terephthalate unit
973	O-CH_2 stretching of ethylene unit
1013 / 1118 / 1175	In plane vibrations associated with the aromatic group, indicative of a para (1,4) di-substitution pattern
1091 / 1237	Ester C(O)-O stretching
1338	-CH_2- wagging within the ethylene unit
1410 / 1447 / 1506	Aromatic skeletal stretching
1715	Carbonyl C=O stretching
2963 / 2887	Aliphatic C-H stretching
3060	Aromatic C-H stretching
3435	O-H stretching of glycol end groups
3553	Absorbed moisture

5.2.4 MOLAR MASS DETERMINATION

The determination of a polymer's molar mass is an essential step in the material's characterisation as impacts the temperature at which, for example, thermo-physical transitions occur such as crystallisation. A polymer's molar mass itself can be altered through synthetic conditions such as catalyst choice, melt processing, and inclusion of additives or fillers. In particular, the high temperatures employed during melt extrusion are known to cause degradation and generally decrease the molar mass.[10, 11] The inclusion of organically modified nanoclays may also cause both hydrolytic or acid catalysed degradation depending on the experimental conditions.[5, 12, 13]

5.2.4.1 GPC

Gel permeation chromatography was employed as it provides not only the number and weight average molecular weights of a polymer but also the molecular weight distribution. This is extremely useful when examining the behaviour of polymer systems during processing as is may be indicative of specific degradative mechanisms.

Figure 5.16 contains an overlay for the polymer systems under study. It is evident that the chip possesses a higher molecular weight distribution than the uniaxial film. As the molecular weights follow comparable Gaussian distribution it can be concluded that the molecular weight distributions themselves have not altered during degradation on processing. Within figure 5.17 the Garamite® does not appear to have a substantial impact on molecular weight, and it is suspected that this is a direct result of the experimental conditions during synthesis. On processing to uniaxial film the degradative catalytic ability of the nanoclay is apparent, and is observed to increase with Garamite® loading. The biaxial samples were not directly comparable to the chip and uniaxial film samples as analysis had been performed under a separate system calibration. The degradative catalytic effect of the nanoclay can still be observed within the biaxial film samples however, although it cannot be ascertained whether the extent of degradation has increased on biaxial stretching.

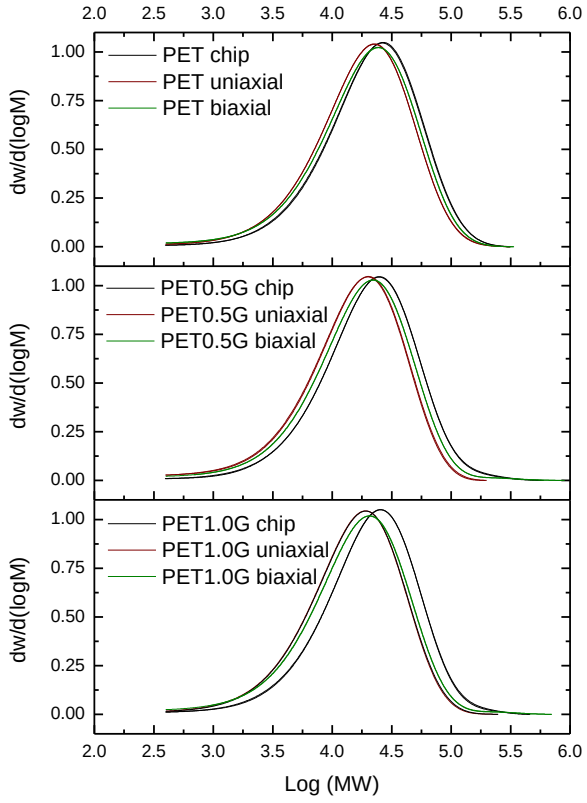

Figure 5.16 Molecular weight distributions of various polymer and composite materials highlighting the effect of Garamite® loading during processing.

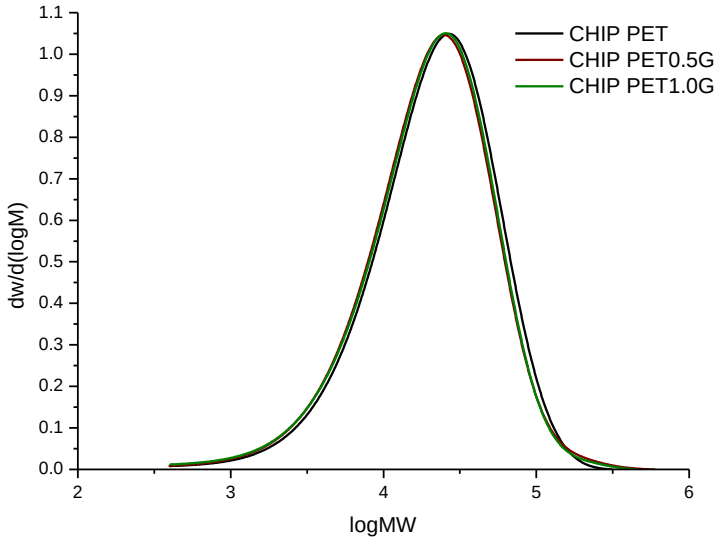

Figure 5.17 Molecular weight distribution plots of polymer and composite chip highlighting the effect of Garamite® loading on M_w values during synthesis.

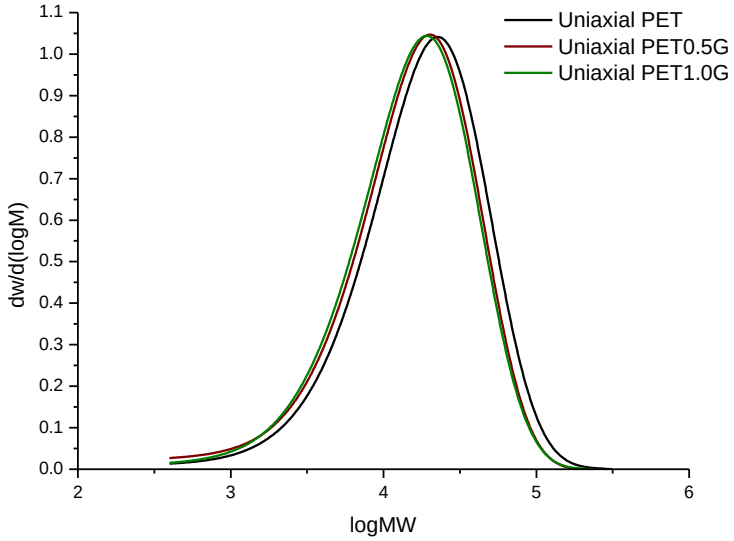

Figure 5.18 Molecular weight distribution plots of polymer and composite uniaxial film highlighting the effect of Garamite® loading on M_w values of uniaxial film.

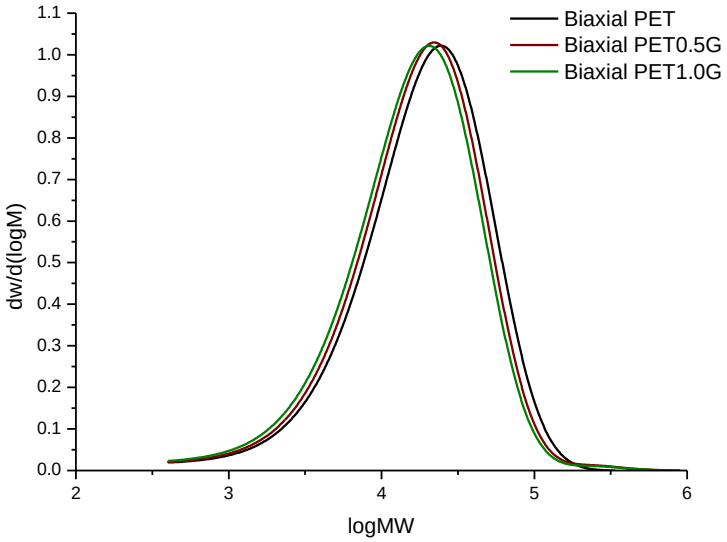

Figure 5.19 Molecular weight distribution plots of polymer and composite biaxial film highlight the effect of Garamite® loading on M_w values of biaxial film.

Table 5.13 Molecular weight data for the amorphous chip, uniaxial film and biaxial film samples. It should be noted the biaxial film samples were analysed on a separate calibration to the amorphous chip and uniaxial film.

Material	Sample	Sample no.	M_w / g mol^{-1}	M_n / g mol^{-1}	P
Amorphous chip	PET	1	32,100	13,900	2.3
		2	31,800	13,800	2.3
		average	31,950	13,850	2.3
	PET0.5G	1	31,200	13,000	2.4
		2	31,700	13,200	2.4
		average	31,450	13,100	2.4
	PET1.0G	1	31,000	12,800	2.4
		2	31,400	13,100	2.4
		average	31,200	12,950	2.4
Uniaxial film	PET	1	27,000	11,500	2.4
		2	27,100	11,500	2.4
		average	27,050	11,500	2.4
	PET0.5G	1	23,400	9,670	2.4
		2	22,900	9,480	2.4
		average	23,150	9,575	2.4
	PET1.0G	1	22,400	9,660	2.3
		2	22,800	9,850	2.3
		average	22,600	9,755	2.3
Biaxial film	PET	1	29,300	11,600	2.5
		2	29,150	11,300	2.6
		average	29,225	11,450	2.6
	PET0.5G	1	27,650	10,650	2.6
		2	27,400	10,650	2.6
		average	27,525	10,650	2.6
	PET1.0G	1	25,850	9,925	2.6
		2	25,950	9,880	2.6
		average	25,900	9,003	2.6

Table 5.14 Molecular weight data relating to sample heterogeneity within the biaxial film samples.

Sample	Data set	Replicate	M_w / g mol^{-1}	M_n / g mol^{-1}	P
PET	1	1	29,400	11,600	2.5
		2	29,200	11,600	2.5
		average	29,300	11,600	2.5
	2	1	29,200	11,300	2.6
		2	29,100	11,300	2.6
		average	29,150	11,300	2.6
	Overall average		29,225 ± 126	11,450 ± 173	2.6 ± 0.1
PET0.5G	1	1	27,800	10,700	2.6
		2	27,500	10,600	2.6
		average	27,650	10,650	2.6
	2	1	27,500	10,700	2.6
		2	27,300	10,600	2.6
		average	27,400	10,650	2.6
	Overall average		27,525 ± 206	10,650 ± 58	2.6 ± 0.0
PET1.0G	1	1	25,900	9,930	2.6
		2	25,800	9,920	2.6
		average	25,850	9,925	2.6
	2	1	25,800	9,830	2.6
		2	26,100	9,930	2.6
		average	25,950	9,880	2.6
	Overall average		25,900 ± 141	9,903 ± 49	2.6 ± 0.0

5.2.4.2 SOLUTION INTRINSIC VISCOSITY

The intrinsic viscosity of a sample is related to the molar mass via the Mark-Houwink equation (equation 5.1), with the parameters K and α specific for a given polymer solvent system. K relates to a specific molar mass range which is assumed to contain the polymer molar mass distribution, whereas α relates to the ability a solvent to solvate the polymer. α is therefore to some extent dependent on temperature. A high K value is employed when a low molar mass distribution is assumed, whereas a high α value is associated with favourable polymer-solvent interactions. For PET, values are available in the Polymer Handbook.[14-16] The intrinsic viscosity measurements are also extremely useful in this particular case as they provide a comparative molar mass to those determined through gel permeation chromatography.

$$[\eta] = KM^{\alpha} \qquad \text{Equation 5.1}$$

Tables of the standard data sets used as a comparison during analysis may be found within appendix 3, in addition to a table contain the full data sets for each individual sample.

Table 5.15 Intrinsic viscosity and calculated molar masses for PET and composite chip illustrating between sample variance. Data sets 1 and 2 relate to the average values obtained from replicate runs. K and α were determined as 4.25×10^{-4} and 0.69 respectively.

Material	Sample	Data Set	[η] / dLg^{-1}	M_w / g mol^{-1}
Amorphous Chip	PET	1	0.673 ± 0.002	43,318 ± 220
		2	0.674 ± 0.000	43,400 ± 24
		Average	0.673 ± 0.001	43,359 ± 137
	PET0.5G	1	0.658 ± 0.002	41,920 ± 182
		2	0.658 ± 0.001	41,946 ± 115
		Average	0.658 ± 0.001	41,933 ± 125
	PET1.0G	1	0.641 ± 0.001	40,412 ± 107
		2	0.641 ± 0.003	40,369 ± 269
		Average	0.641 ± 0.002	40,391 ± 169
Uniaxial Film	PET	1	0.609 ± 0.003	37,480 ± 302
		2	0.615 ± 0.002	38,021 ± 159
		Average	0.612 ± 0.004	37,750 ± 369
	PET0.5G	1	0.582 ± 0.001	35,148 ± 89
		2	0.579 ± 0.001	34,886 ± 102
		Average	0.581 ± 0.002	35,017 ± 170
	PET1.0G	1	0.552 ± 0.001	32,529 ± 69
		2	0.556 ± 0.002	32,857 ± 214
		Average	0.554 ± 0.003	32,693 ± 230
Biaxial Film	PET	1	0.598 ± 0.014	36,531 ± 1,218
		2	-	-
		Average	0.598 ± 0.014	36,531 ± 1,218
	PET0.5G	1	0.565 ± 0.004	33,613 ± 339
		2	-	-
		Average	0.565 ± 0.004	33,613 ± 339
	PET1.0G	1	0.533 ± 0.012	30,900 ± 1,036
		2	-	-
		Average	0.533 ± 0.012	30,900 ± 1,036

Table 5.15 suggests the variance between amorphous chip samples is small. This is suggestive that the nanoclay does not impact the polymer molar mass to a substantial degree during polymerisation, and is attributed to the temperature (290°C) and inert atmosphere in which the reaction occurs. During processing to uniaxial film the molar mass is observed to decrease in all samples however it is noted that degradation occurs to a more substantial degree within the composites. This enhanced level of degradation is attributed to the presence of the Garamite®, which exhibits a catalytic degradative effect on the polymer. It is noted that the largest decrease in molar mass occurs between processing from amorphous chip to uniaxial film, as opposed to during biaxial stretching. It is suggested

that the catalytic degradative ability of the nanoclay has been depleted to some degree during the initial processing stage, resulting in a reduction in the observed decrease in molar mass. It could also be suggested however that the lower temperature during biaxial stretching may also contribute to a less substantial degree of degradation. It is also observed that the nanoclay content is not directly proportional to the extent of degradation and hence decrease in molar mass which is observed during processing. If processing to uniaxial film is considered the additional 0.5% w/w nanoclay incorporated within PET1.0G only results in an additional 50% degradation on top of that observed within PET0.5G. This indicates that increasing the nanoclay content will not necessarily cause a subsequent proportional increase in degradation. A potential explanation for this behaviour may be the degree of 'unravelling' of the nanoclay fibres. At higher nanoclay loadings a lower degree of unravelling is generally expected to occur within composite systems. If this is indeed the case for these particular systems then there is a lower degree of exposed nanoclay surface and hence catalytic centres. This suggests a suppressed increase in degradative ability would be observed, which confirms the experimental data.

With respect to within sample variance, the molar masses of the biaxial films appear to fluctuate to the greatest degree in comparison to the amorphous chip and uniaxial film. It would have been valuable to obtain experimental data from an additional data set in this case, however due to the volume of sample which was required this was not possible. It could be suggested that the position of the film with respect to the stretching clamp during biaxial orientation lead to variable degrees of stress and hence potential degradation, however with the present data this cannot be either discounted or confirmed. In general the between sample variance appears negligible for the amorphous chip and uniaxial film. Variance between the polymer and polymer composite samples is observed at a maximum of ± 269 g mol^{-1} and ± 302 g mol^{-1} respectively. This suggests a homogeneous dispersion of the nanoclay within the composite samples.

5.2.5 TEM

Within images of both the PET0.5G and PET1.0G chip the sepiolite fibres are clearly visible. Within figures 5.20c, 5.20f and 5.21c the fibres are observed in clusters or bundles, and are in a similar fashion to polymer-Garamite® composites within the literature.[17, 18] Within figure 5.21e the inverted ribbon structure is also observed and the adjacent fibres appear stacked. Voids in the matrix are also visible within both polymers and commonly occur at the polymer nanoclay interface, indicating the Garamite® surface and the polymer molecules are not fully miscible. Images (found within appendix 3) of the uniaxial film also suggested that the unilateral stretching process has no effect on the degree of Garamite® exfoliation or unravelling within the polymer matrix. The fibre dimensions were measured as 13 nm in width and on average 4 μm in length, however were observed within the TEM at lengths between 250 nm and 9 μm.

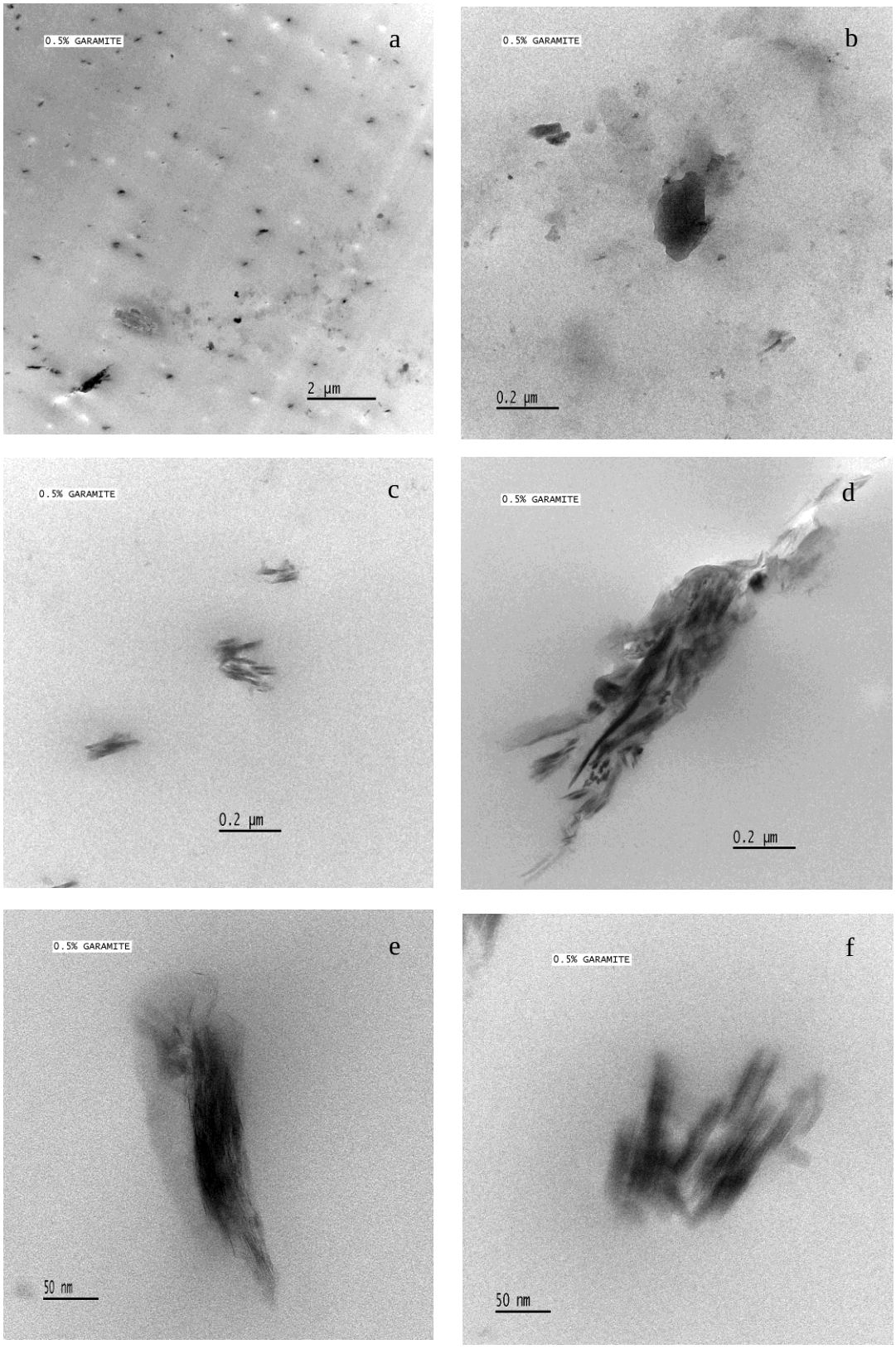

Figure 5.20 TEM images of PET0.5G chip at various magnifications

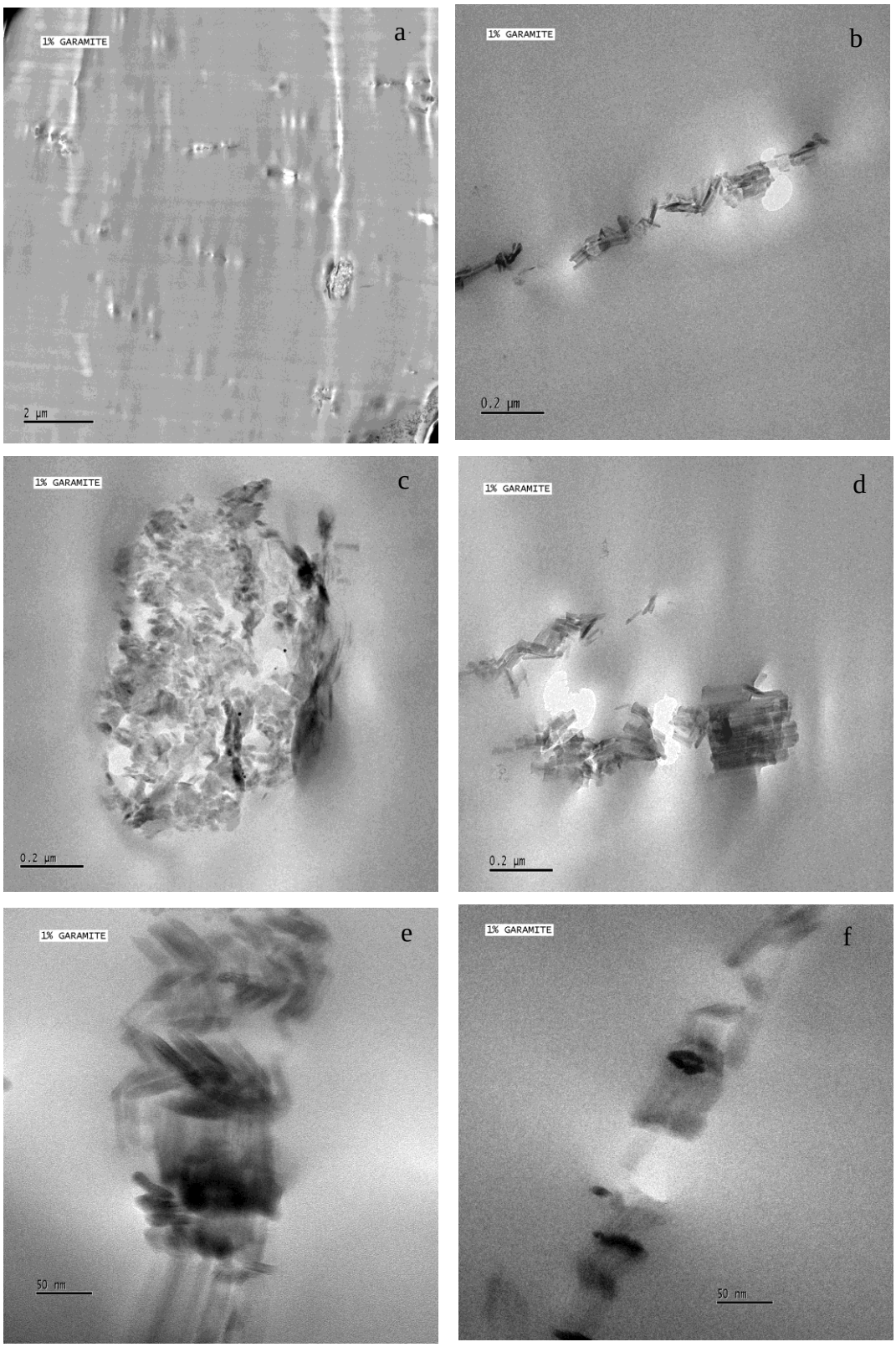

Figure 5.21 TEM images of PET1.0G chip at various magnifications

5.3 REFERENCES

1. *Garamite 1958 Mixed Mineral Thixotrope in n-methyl pyrrolidone*, 2004, http://www.scprod.com/chembriefs/ChemBrief%20V4%20I2.pdf, 22/12/2006.
2. Southern Clay Products Inc, *Why Garamite Additives?*, 2006, http://www.garamite.com, 22/12/2006.
3. Jones, B.F., Galan, E., *Hydrous Phyllosilicates (exclusive of mica) : Sepiolite and Palygorskite*, Reviews in Mineralogy, ed. Bailey, S.W., Vol. 19, 1988, Mineralogical Society of America, Michigan.
4. Xie, W., Gao, Z., Pan, W.P., Hunter, D., Singh, A., Vaia, R.A., *Thermal Degradation Chemistry of Alkyl Quaternary Ammonium Montmorillonite*, Chemical Materials, 2001, **13**, 2979-2990.
5. Xu, X., Ding, Y., Qian, Z., Wang, F., Wen, B., Zhou, H., Zhang, S., Yang, M., *Degradation of poly(ethylene terephthalate)/clay nanocomposites during melt extrusion: Effect of clay catalysis and chain extension*, Polymer Degradation and Stability, 2009, **94**, 113-123.
6. Moore, R.B., Reynolds Jr, R.C., *X-Ray Diffraction and the Identification and Analysis of Clay Minerals*, 1997, Oxford Univeristy Press, Oxford.
7. Bandli, B. *UMD Scanning Electron Microscopy Image Gallery*, 2009, Accessed 14/09/10, Available from: http://www.d.umn.edu/SEM/images.html.
8. West, S.L., White, G.N., Deng, Y., McInnes, K.J., Juo, A.S.R., Dixon, J.B., *Kaolinite, Halloysite, and Iron Oxide Influence on Physical Behaviour of Formulated Soils*, Soil Science Society of America, 2004, **68**, 1452-1460.
9. Jonas, E.C., Roberson, H.E., *Structural Charge Density as Indicated by Montmorillonite Hydration*, Clays and Clay Minerals, 1966, **13**, 223-230.
10. Cabedo, L., Plackett, D., Gimenez, E., Lagaron, J.M., *Studying the Degradation of Polyhydroxybutyrate-co-valerate during Processing with Clay-Based Nanofillers*, Journal of Applied Polymer Science, 2009, **112**(6), 3669-3676.
11. Thellen, C., Coyne, M., Froio, D., Auerbach, M., Wirsen, C., Ratto, J.A., *A Processing, Characterization and Marine Biodegradation Study of Melt-Extruded*

Polyhydroxyalkanoate (PHA) Films, Journal of Polymers and the Environment, 2008, **16**, 1-11.

12. Song, L., Hu, Y., Tang, Y., Zhang, R., Chen, Z., Fan, W., *Study on the properties of flame retardant polyurethane/organoclay nanocomposites*, Polymer Degradation and Stability, 2005, **87**, 111-116.
13. Kráčalík, M., Mikešová, J., Puffr, R., Baldrian, J., Thomann, R., Friedrich, C., *Effect of 3D nanostructures onrecycled PET/organoclay nanocomposites*, Polymer Bulletin, 2007, **58**, 313-319.
14. Sanches, N.B., Dias, M.L., Pacheco, E.B.A.V., *Comparative techniques for molecular weight evaluation of poly(ethylene terephthalate) (PET)*, Polymer Testing, 2005, **24**(6), 688-693.
15. Vyazovkin, S., Sbirrazzuoli, N., *Estimating the activation energy for non-isothermal crystallization of polymer melts*, Journal of Thermal Analysis and Calorimetry, 2003, **72**, 681-686.
16. Brandup, J., Immergut, E.H., *Polymer Handbook*, 3rd ed, 1989, John Wiley & Sons, London.
17. Ingram, S., Dennis, H., Hunter, I., *Influence of clay type on exfoliation, cure and physical properties of in situ polymerised poly(methyl methacrylate) nanocomposites*, Polymer International, 2008, **57**(10), 1118-1127.
18. Ho, M.W., Lam, C.K., Lau, K.T., Ng, D.H.L., Hui, D., *Mechanical properties of epoxy-based composites using nanoclays*, Composite Structures, 2006, **75**, 415-421.

CHAPTER 6 CRYSTALLISATION

An examination of the dynamic crystallisation process is essential as it is comparable to the conditions a material is exposed to during a real-time industrial process, examples of which are melt extrusion, film blowing and injection moulding. An understanding of the crystallisation process is essential as it is the crystallinity (and molecular orientation) which influences the physical properties.[1-3] The degree of crystallinity can be influenced in various manners, from varying experimental or processing conditions to the inclusion of inorganic fillers, catalysts or additives.[2, 4, 5] It is therefore essential individual systems are characterised in order to determine the effect of particular system selections. Smectic clays for example are well known nucleants in PET crystallisation and have been reported to increase the tenacity and Young's modulus of PET fibres when incorporated at an optimum loading.[1, 6-9] In addition, the drawing of PET in either a uniaxial or biaxial direction affects crystallisation through orientation of the polymer molecules. Polymer nanoclay composites will also have additional complexities due to the orientation of the nanoclay during the drawing process which could alter the optical properties of the material.

6.1 CRYSTALLISATION BEHAVIOUR

Figures 6.1 – 6.3 display the dynamic crystallisation thermograms for PET, PET0.5G and PET1.0G chip. Additional replicate thermograms can be found within appendix 4. Crystallisation is predominantly observed during the cooling cycle in a heat-cool-reheat sequence, however it was also observed at low temperatures within cycle 3; the reheat cycle. As the study focused on the effect of cooling rate on crystallinity any crystalline material obtained during cycle 3 was discarded. Tables 6.1 and 6.2 contain the crystallisation data for the polymer and composite chip. Precision within samples was determined to ± 0.84ºC through the standard deviation method. Instrumental error was determined as ± 1.00ºC. The total potential error was therefore ± 1.84ºC. Error within the percentage crystallinity was determined as ± 0.35 %.

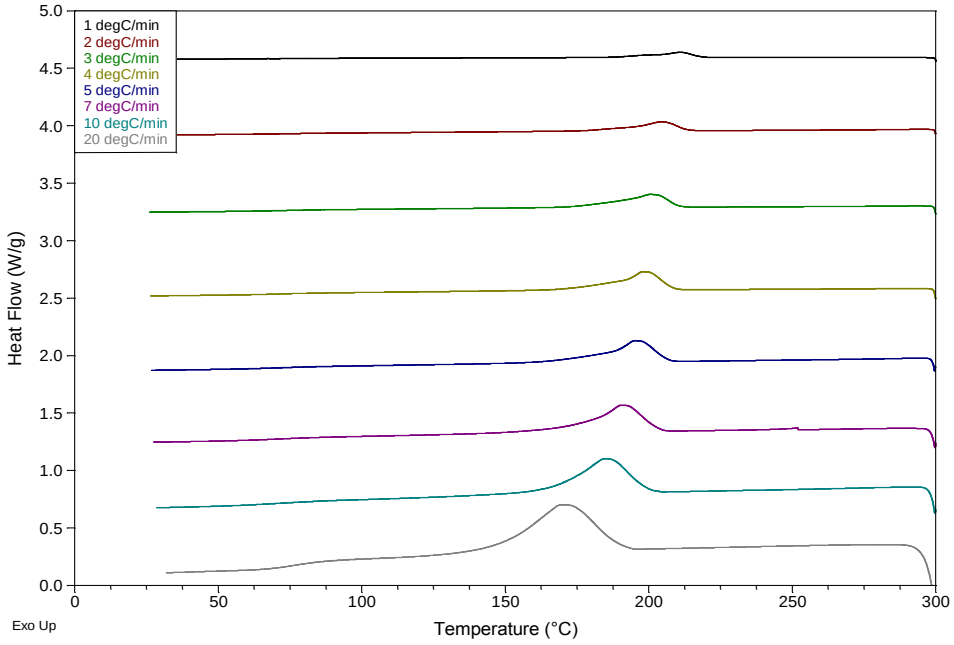

Figure 6.1 DSC thermogram of dynamic crystallisation in PET chip. Cooling rates range between 1ºC min^{-1} and 20ºC min^{-1}.

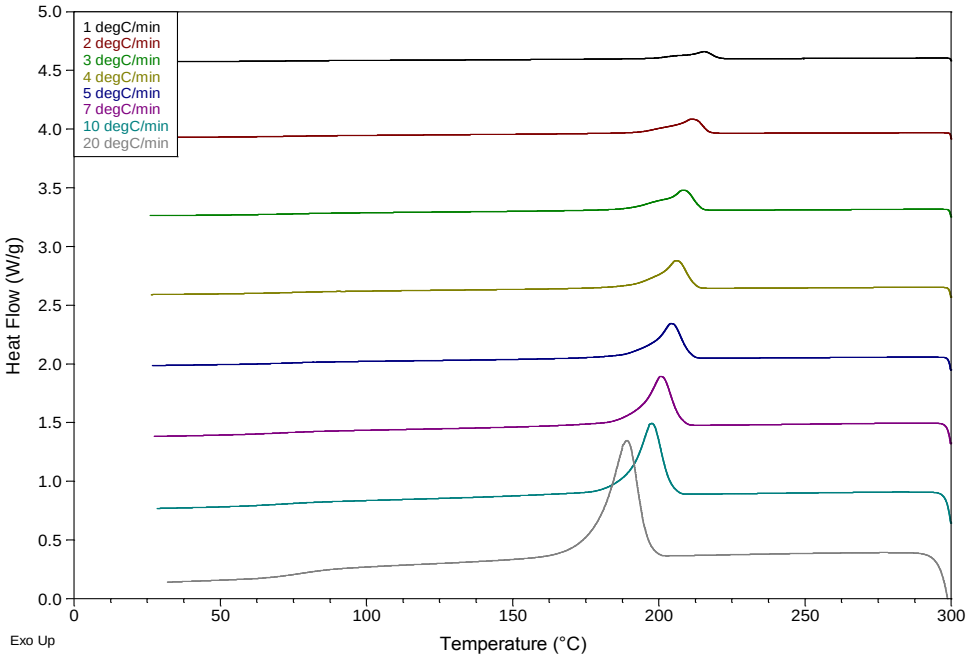

Figure 6.2 DSC thermogram of dynamic crystallisation in PET0.5G chip. Cooling rates range between 1ºC min^{-1} and 20ºC min^{-1}.

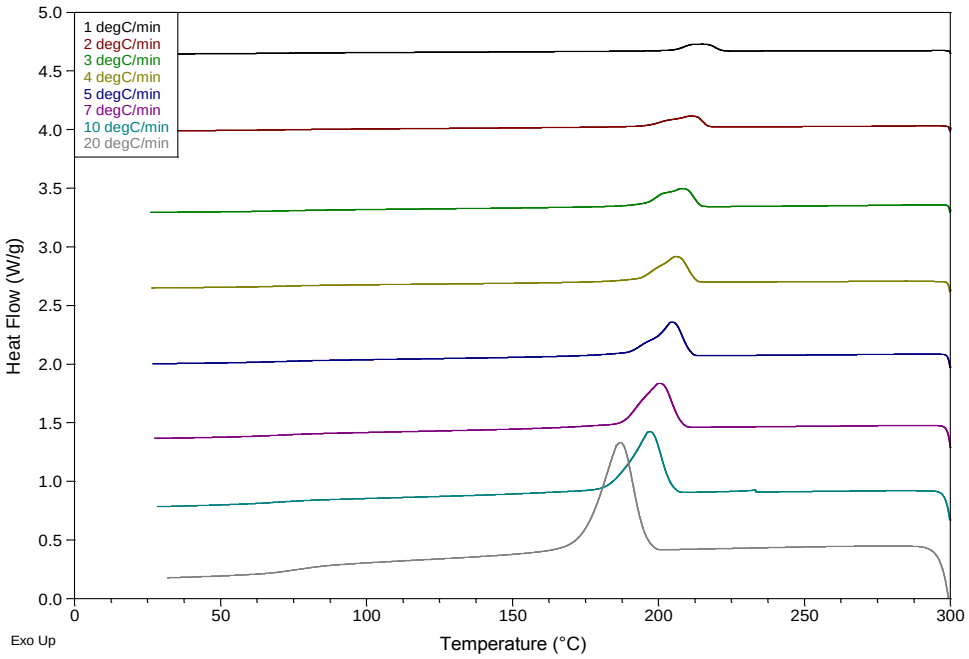

Figure 6.3 DSC thermogram of dynamic crystallisation in PET1.0G chip. Cooling rates range between 1ºC min^{-1} and 20ºC min^{-1}.

With an increase in cooling rate a broadening of the crystallisation exotherm is observed, with the peak maximum increasing in height and shifting to a lower temperature. Initially at a cooling rate of 1°C per minute, crystallisation of molten PET chip is initiated 8°C below the lowest observed crystalline melt temperature of 232°C. When the cooling rate is increased to 40°C per minute crystallisation is initiated 47°C below the lowest melt temperature. This shift to a lower onset temperature is a result of a decrease in time available for crystallisation. Literature has described the effect of the proximity of crystallisation to the crystalline melt region on spherulite size and frequency.[3] At temperatures close to the crystalline melting region nucleation is sporadic, with only a small number of larger spherulites crystallising from the melt. Lower temperatures however will yield a large number of small spherulites. An increase in cooling rate can therefore be said to decrease spherulite size and increase spherulite number. The composites are also observed to possess higher crystallisation temperatures than the polymer, indicating the nanoclay is acting as a nucleating agent. The nucleating effect may be observed visually through the formation of a shoulder within the composites after the bulk crystallisation exotherm. This indicates the polymer is undergoing a mixture of both homogenous and heterogeneous nucleation.

The chip and uniaxial film samples also appear comparable at low heating rates within experimental error; however the uniaxial film samples are consistently slightly higher in temperature. This may be attributed to the lower molar mass of the uniaxial film due to melt processing, which increases the ease at which the polymer chains can disentangle themselves from the melt and crystallise. A substantial alteration in the crystallisation temperature is only observed within the higher cooling rates for PET, such as at 20ºC min^{-1} where the uniaxial film crystallises at 181ºC as opposed to 168ºC for the chip. The lower molar mass of the film results in faster crystallisation over the smaller period of time. Within the composites only a minimal (and arguably insubstantial) increase in the crystallisation temperature is observed between the chip and uniaxial film. Due to the nucleating ability of the nanoclay the possible inhibiting effect of reduced chain mobility at the higher molar masses is therefore not as substantial.

Table 6.1 Peak maximum crystallisation temperatures for samples under various cooling rates.

Cooling rate / ºC min^{-1}	**Replicate**	**T_c / ºC**					
		Amorphous chip			**Uniaxial film**		
		PET	**PET0.5G**	**PET1.0G**	**PET**	**PET0.5G**	**PET1.0G**
1	1	211	215	213	209	216	213
	2	210	215	210	207	205	214
	average	210	215	211	208	210	213
2	1	204	211	211	207	215	212
	2	204	212	212	205	212	212
	average	204	211	211	206	213	212
3	1	200	208	208	201	210	210
	2	201	208	208	199	211	210
	average	201	208	208	200	211	210
4	1	198	206	206	199	208	208
	2	196	206	206	199	209	208
	average	197	206	206	199	209	208
5	1	195	204	204	197	207	208
	2	193	204	205	196	207	207
	average	194	204	204	197	207	207
7	1	190	201	200	193	204	204
	2	190	201	201	194	203	204
	average	190	201	201	194	203	204
10	1	184	198	197	191	200	200
	2	184	197	198	190	200	200
	average	184	197	198	191	200	200
20	1	169	189	187	181	193	192
	2	169	189	187	181	192	191
	average	169	189	187	181	193	192

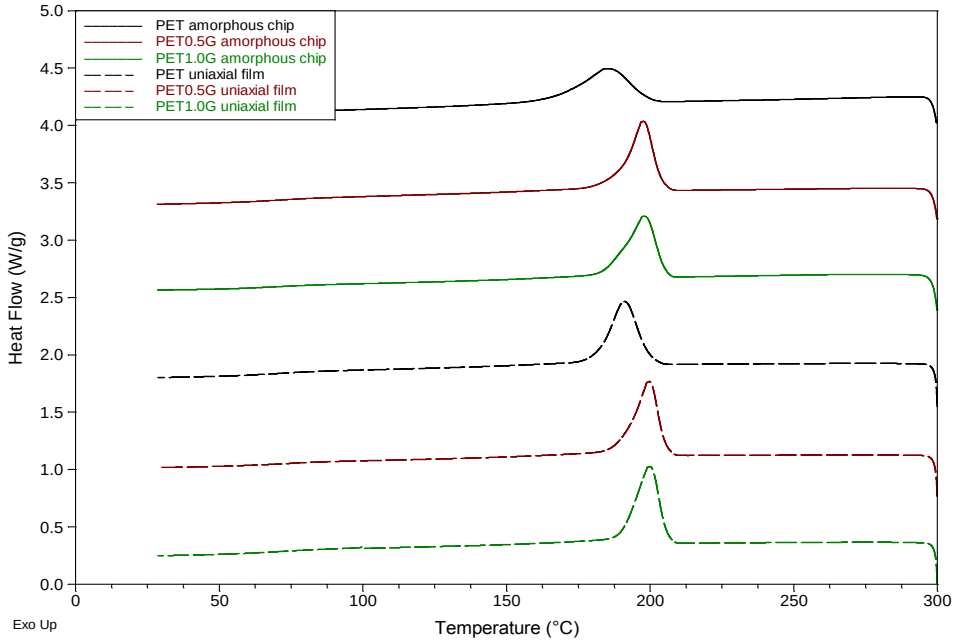

Figure 6.4 Comparison plot of crystallisation exotherms of PET, PET0.5G and PET1.0G amorphous chip and uniaxial film, at a cooling rate of 10 ºC min^{-1}.

Measurement of the crystalline melting region provides an accurate determination of the crystalline content of a polymeric material, however due to the possibility of additional crystallisation at low temperatures during the final reheat cycle the crystallisation enthalpy is also considered extremely important. Table 6.2 contains the percentage crystallinity for the systems under study. A decrease in percentage crystallinity is observed within samples when the cooling rate rises above 7ºC min^{-1}. As the period of time in which the crystallisation process may occur will decrease with increasing cooling rate, the decrease in available time at 7°C min^{-1} is deemed sufficient to prevent the polymer crystallising to its full potential. It is also observed that the decrease in crystallinity due to increasing cooling rate is buffered to some degree by the nucleating ability of the nanoclay. In addition, the uniaxial film samples exhibit a smaller decrease in percentage crystallinity than their amorphous chip counterparts, again illustrating the effect of lower molar mass on the ease of polymer crystallisation.

Table 6.2 Percentage crystallinities for samples under various cooling rates. Polymer composites have been corrected for Garamite® content.

Cooling rate / °C min^{-1}	Replicate	% Crystallinity					
		Amorphous chip			Uniaxial film		
		PET	PET0.5G	PET1.0G	PET	PET0.5G	PET1.0G
1	1	51	57	54	48	47	50
	2	52	55	53	49	52	48
	average	52	56	53	48	49	49
2	1	50	57	50	50	52	49
	2	50	57	55	48	51	51
	average	50	57	52	49	52	50
3	1	52	52	53	52	53	52
	2	51	55	52	47	52	50
	average	51	53	52	50	53	51
4	1	52	53	50	48	52	50
	2	50	50	48	48	51	53
	average	51	51	49	48	52	51
5	1	51	52	49	45	49	51
	2	52	47	49	46	49	50
	average	52	50	49	46	49	50
7	1	49	50	50	47	47	49
	2	50	47	49	46	47	50
	average	50	49	49	46	47	50
10	1	46	49	48	47	48	49
	2	45	45	47	46	47	50
	average	45	47	47	46	47	50
20	1	37	46	45	42	44	45
	2	38	44	45	41	43	44
	average	37	45	45	42	44	44

6.2 CRYSTALLINE MELTING BEHAVIOUR

Figures 6.5 - 6.7 contain the crystalline melting isotherms of PET, PET0.5G and PET1.0G chip, at a heating rate of 10ºC min^{-1}. Additional isotherms for the uniaxial film samples and replicates can be found in appendix 4.

It is noted that due to the heat-cool-reheat regime, crystallisation may still take place within the reheat cycle which contains the crystalline melting data. It is therefore possible that the additional opportunity to crystallise would result in larger enthalpies for crystalline melting and is considered on analysis. Precision within samples was determined to ± 0.21ºC through the standard deviation method. Instrumental error was determined as ± 1.00ºC. The total potential error was therefore ± 1.21ºC. Error associated with the crystalline melt enthalpy was determined as ± 0.82 J g^{-1}.

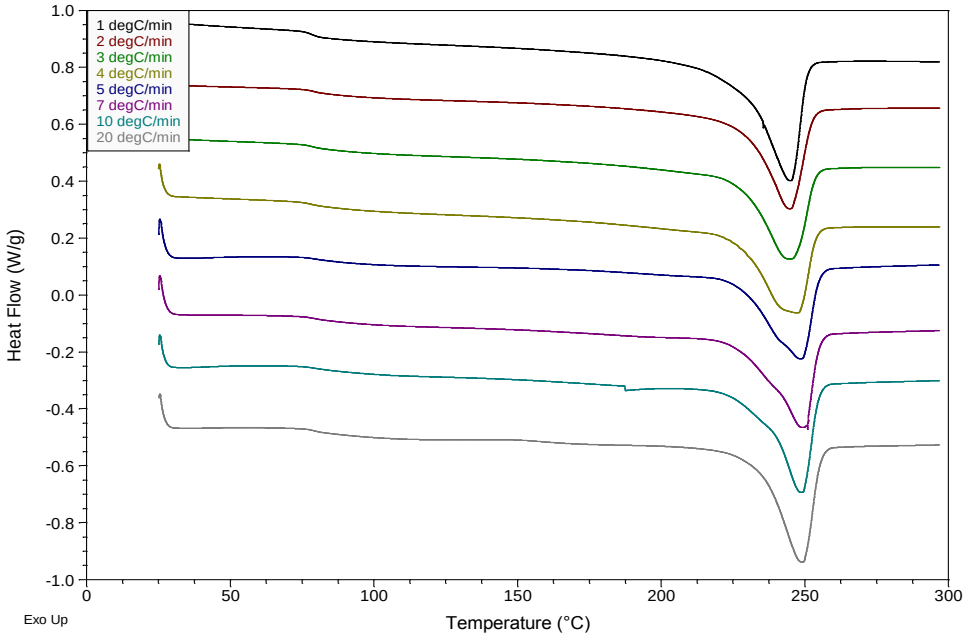

Figure 6.5 DSC thermogram of crystalline melting region of PET chip. Samples were heated at a rate of 10ºC min^{-1}. Cooling rates during crystallisation ranged between 1ºC min^{-1} and 20ºC min^{-1}.

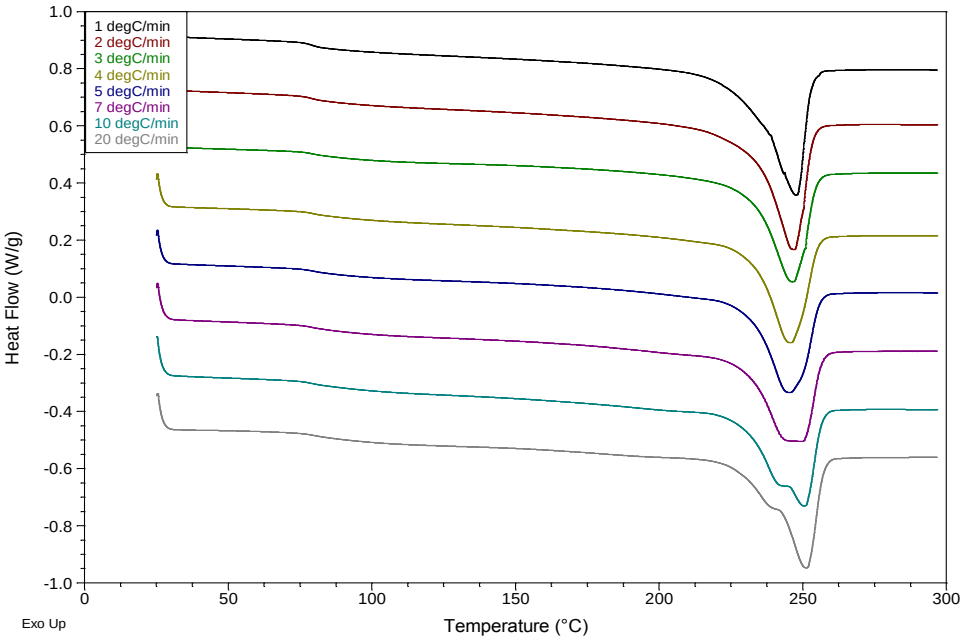

Figure 6.6 DSC thermogram of crystalline melting region of PET0.5G chip. Samples were heated at a rate of 10ºC min^{-1}. Cooling rates during crystallisation ranged between 1ºC min^{-1} and 20ºC min^{-1}.

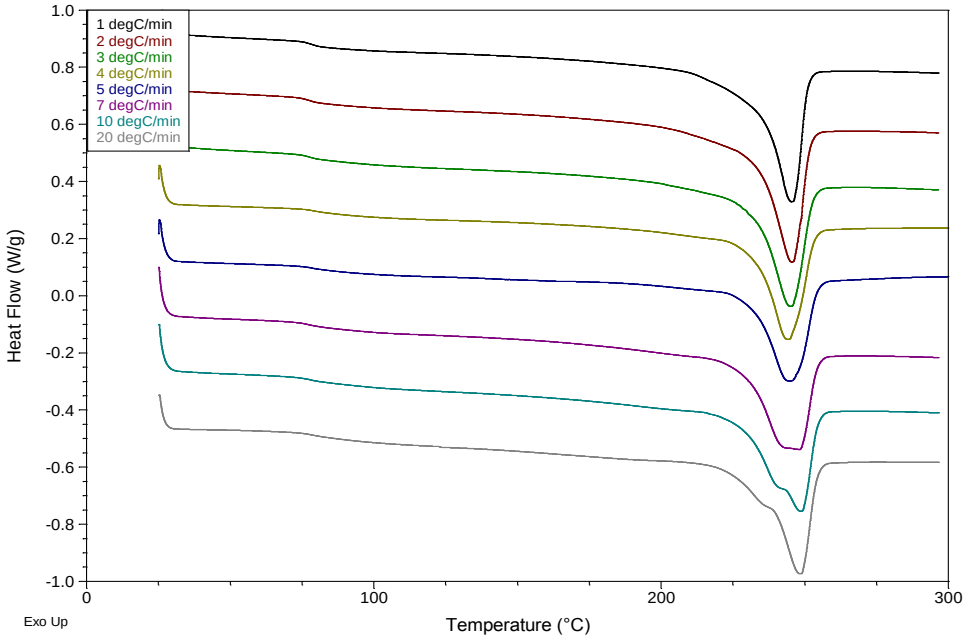

Figure 6.7 DSC thermogram of crystalline melting region of PET1.0G chip. Samples were heated at a rate of 10ºC min^{-1}. Cooling rates during crystallisation ranged between 1ºC min^{-1} and 20ºC min^{-1}.

Although the melt temperatures were relatively comparable as the cooling rate was increased, a visual examination suggests there is a change in the crystallisation process, and that the slight fluctuations in melt temperature are perhaps significant. Within the composite samples the melt peaks are observed to decrease slightly, broaden and begin to split into two melt peaks. The highest temperature peak then becomes dominant. It is noted that within the polymer samples there is an identical broadening of the melt peak as the crystallisation rate is increased, however only a small shoulder develops adjacent to the dominant high temperature peak before it is again observed to sharpen. As the cooling rate is increased there is a decrease in crystallisation time which will push crystallisation to lower temperatures and as a result form thinner lamellae. Thinner lamellae are less thermally stable, and so the crystalline melt temperature would also be expected to decrease. Recrystallisation may then occur in increasing extents in proportion to the available crystallisation time, resulting in an additional crystalline melt peak in the case of the composites. This is due to the nanoclay acting as a heterogeneous nucleant within the polymer melt. It is observed however that the crystalline melting temperatures of the polymer and composite are comparable. This would indicate that the incorporation of the nanoclay and a decrease in molar mass does not affect the fundamental crystalline morphology.

The melt enthalpies are also comparable between samples for each particular cooling rate. As the cooling rate increased, the crystalline melt enthalpy was observed to decrease by up to 8 J g^{-1} between rates of 1ºC min^{-1} and 20ºC min^{-1}. The data was also in agreement with the crystallisation enthalpies which suggested the crystalline content was lowered at high cooling rates. Percentage crystallinities were calculated according to equation 6.1, where ΔH_m was the melt enthalpy of the sample, ΔH_m^0 was the melt enthalpy of the perfectly crystalline polymer and ø was the weight fraction of the filler. The melt enthalpy of perfectly crystalline PET was obtained defined as 117.6 J g^{-1} in literature.[10]

$$\%\chi = \frac{\Delta H_m}{\Delta H_m^0 (1 - \phi)} \; x \; 100$$

Equation 6.1

Table 6.4 illustrates at a standard cooling rate of 10ºC min^{-1} the percentage crystallinities were comparable and varied between 32% and 34%. This suggested that as both the polymer and composites were comparable, in both chip and uniaxial film samples, the nanoclay could therefore be concluded to nucleate the polymer without altering the observed crystalline content. This was in agreement with the literature.[11]

Table 6.3 Maximum crystalline melt temperatures for samples under various cooling rates.

Heating rate / °C min^{-1}	Replicate	T_m / °C					
		Amorphous chip			Uniaxial film		
		PET	PET0.5G	PET1.0G	PET	PET0.5G	PET1.0G
1	1	245	248	246	244	246	246
	2	244	247	245	243	242	245
	average	244	247	246	243	244	246
2	1	245	247	247	244	247	245
	2	245	247	245	242	245	245
	average	245	247	246	243	246	245
3	1	245	246	245	242	245	244
	2	245	247	245	242	246	244
	average	245	247	245	242	246	244
4	1	248	246	244	248	245	244
	2	248	247	244	241	245	243
	average	248	246	244	244	245	243
5	1	249	246	244	248	244	243
	2	248	246	245	247	245	243
	average	248	246	244	247	245	243
7	1	249	247	247	248	243	242
	2	249	249	248	248	243	242
	average	249	248	248	248	243	242
10	1	249	251	249	248	250	248
	2	249	250	249	248	250	248
	average	249	251	249	248	250	248
20	1	249	251	248	248	251	249
	2	249	251	248	248	250	249
	average	249	251	248	248	250	249

Table 6.4 Enthalpies of the crystalline melt region for samples under various cooling rate.

Cooling rate / °C min^{-1}	Replicate	ΔH_c / J g^{-1}					
		Amorphous chip			Uniaxial film		
		PET	PET0.5G	PET1.0G	PET	PET0.5G	PET1.0G
1	1	46	46	45	41	42	47
	2	43	44	44	40	37	40
	average	45	45	44	40	40	43
2	1	38	44	35	42	44	40
	2	39	42	44	41	42	42
	average	39	43	40	41	43	41
3	1	39	40	41	42	41	40
	2	39	41	40	40	41	32
	average	39	40	40	41	41	36
4	1	39	40	39	39	40	39
	2	38	39	38	37	40	39
	average	39	40	39	38	40	39
5	1	40	40	38	37	40	41
	2	37	41	38	37	39	38
	average	39	41	38	37	39	39
7	1	37	42	40	37	38	39
	2	38	40	36	37	38	36
	average	38	41	38	37	38	37
10	1	38	40	38	38	38	39
	2	37	40	38	37	40	38
	average	38	40	38	38	39	39
20	1	37	38	37	37	38	38
	2	38	37	37	36	37	37
	average	37	38	37	37	37	37

Table 6.5 % Crystallinities calculated from the melt endotherms for samples under various cooling rates. The sample heating rate was 10°C min^{-1}. Composites have been corrected for Garamite® content.

Cooling rate / °C min^{-1}	Replicate	% Crystallinity					
		Amorphous chip			Uniaxial film		
		PET	PET0.5G	PET1.0G	PET	PET0.5G	PET1.0G
1	1	39	39	39	34	36	40
	2	37	38	38	34	33	35
	average	38	39	38	34	34	37
2	1	32	38	30	35	37	34
	2	33	36	38	35	36	36
	average	33	37	34	35	37	35
3	1	33	34	35	35	35	35
	2	33	35	34	34	35	27
	average	33	34	35	35	35	31
4	1	33	34	34	33	34	34
	2	32	34	33	31	34	33
	average	33	34	33	32	34	34
5	1	34	34	32	32	34	35
	2	32	35	33	31	33	32
	average	33	35	33	32	34	34
7	1	32	36	34	31	32	33
	2	33	34	31	31	32	31
	average	32	35	33	31	32	32
10	1	32	34	33	33	32	34
	2	32	34	33	32	34	33
	average	32	34	33	32	33	33
20	1	31	33	32	32	32	32
	2	32	32	32	31	32	31
	average	32	32	32	31	32	32

6.3 CRYSTALLISATION KINETICS

6.3.1 MODIFIED AVRAMI MODEL

The modified Avrami model allows the crystallisation kinetics of a polymer to be examined under dynamic circumstances. The temperature region over which crystallisation occurs is converted to time, and a graduated integration of the crystallinity is performed allowing construction of plots of ln[-ln(1-χ(t)] against ln(t).[12] Equation 6.2 is the modified Avrami equation, and figures 6.8a and 6.8b contain a set of modified Avrami plots for the polymer and composite chip material. Additional plots can be found within appendix 4.

$$\ln\left[-\ln\left(1-\chi(t)\right)\right] = \ln Z_t + n\ln(t)$$

Equation 6.2

The modified Avrami model may only be used to examine primary crystallisation prior to crystallite infringement; if a system either does not follow or diverges from a primary crystallisation route then non-linearity of data will occur and the kinetic model cannot be employed successfully. It can be observed within figure 6.8a that non-linearity does occur within the PET and PET composite systems at the lowest and highest crystallinities. The red horizontal line indicates a crystallinity of 40% which is generally considered the limit of the Avrami model. As a result of the divergence the model was re-focused on the primary crystallisation region as illustrated in figure 6.8b, visually deemed to occur between crystallinities of 1% and 40%. The non-linearity of data during modified Avrami analysis is typical of poly(ethylene terephthalate) and has also previously been encountered by authors such as Durmus *et al*.[11]

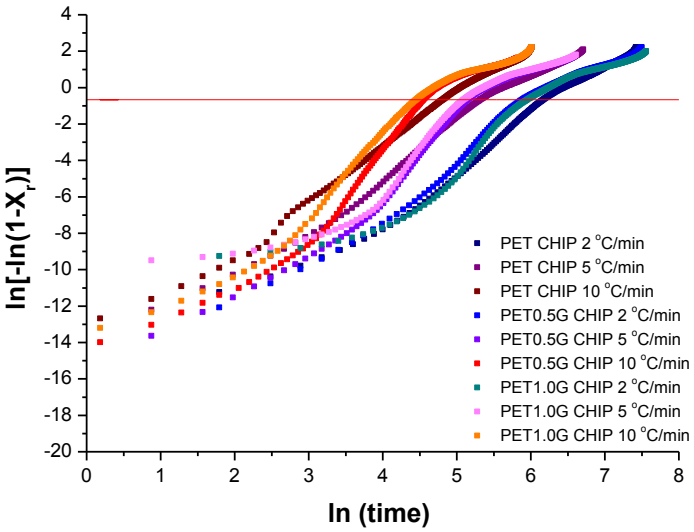

Figure 6.8a Modified Avrami plots relating to the dynamic crystallisation of PET, PET0.5G and PET1.0G chip. The red line represents a crystallinity of 40% and the limits of the Avrami model.

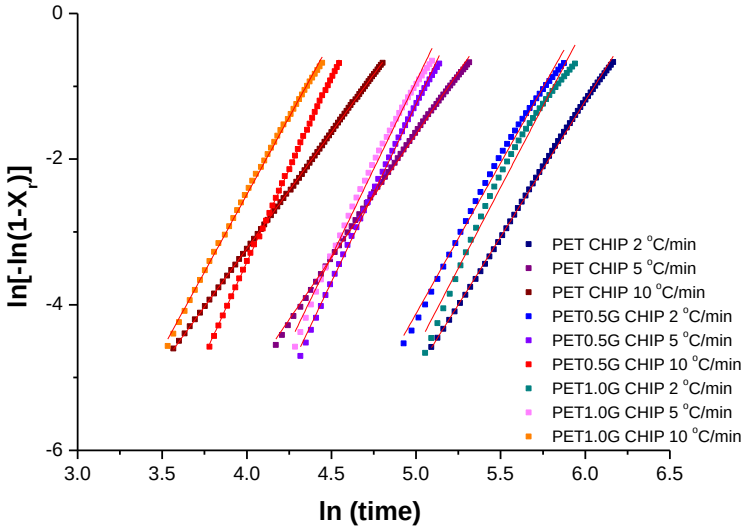

Figure 6.8b Modified Avrami plots relating to the dynamic crystallisation of PET, PET0.5G and PET1.0G chip at crystallinities of between 1% and 40%.

Tables 6.6, 6.7 and 6.8 indicate that the homogeneously nucleated polymer is likely to possess a disc or spherulitic morphology. The polymer composites, which crystallise via a combination of homogeneous and heterogeneous nucleation, are observed to possess a more sheaf-like morphology due to the adsorption of polymer chains onto the fibrous sepiolite surface. It is noted that the chip materials illustrate this difference in nucleation methods in a more clearly defined manner than is observed for the uniaxial films. This may be attributed to a more comparable molar mass range within the chip. Several of the Avrami exponents are also higher than expected and may be attributed to

the poor reproducibility which can be observed when comparing the original Avrami plots within figure 6.8a to those within appendix 4.

Table 6.6 Avrami constants of PET and PET composite chip and uniaxial films.

Sample Type	Sample	Replicate	Avrami Constant at various cooling rates		
			2°C min^{-1}	5°C min^{-1}	10°C min^{-1}
CHIP	PET	1	3.72 ± 0.01	3.40 ± 0.02	3.19 ± 0.00
		2	3.49 ± 0.01	2.82 ± 0.00	3.43 ± 0.01
		Average	3.61 ± 0.01	3.11 ± 0.01	3.31 ± 0.01
	PET0.5G	1	4.14 ± 0.05	4.88 ± 0.04	5.10 ± 0.01
		2	4.79 ± 0.07	4.29 ± 0.02	5.21 ± 0.02
		Average	4.47 ± 0.06	4.59 ± 0.03	5.16 ± 0.02
	PET1.00G	1	4.45 ± 0.10	4.81 ± 0.06	4.25 ± 0.02
		2	4.20 ± 0.10	3.56 ± 0.03	3.21 ± 0.01
		Average	4.33 ± 0.10	4.19 ± 0.05	3.73 ± 0.01
UNIAXIAL FILM	PET	1	4.66 ± 0.02	3.71 ± 0.01	3.47 ± 0.02
		2	4.86 ± 0.02	6.53 ± 0.05	4.02 ± 0.02
		Average	4.76 ± 0.02	5.12 ± 0.03	3.75 ± 0.02
	PET0.5G	1	6.10 ± 0.07	4.09 ± 0.01	4.39 ± 0.01
		2	6.47 ± 0.15	4.41 ± 0.02	3.28 ± 0.01
		Average	6.29 ± 0.11	4.25 ± 0.02	3.84 ± 0.01
	PET1.00G	1	4.77 ± 0.08	3.69 ± 0.02	3.12 ± 0.02
		2	3.86 ± 0.05	3.82 ± 0.02	3.14 ± 0.02
		Average	4.32 ± 0.07	3.76 ± 0.02	3.13 ± 0.02

Table 6.7 Avrami exponents for predetermined and sporadic nucleation[3]

Crystallite growth	Avrami exponent, n	
	Predetermined nucleation	Sporadic nucleation
Fibril	1	2
Disc	2	3
Spherulite	3	4
Sheaf	5	6

Table 6.8 Lamellae morphologies for the Avrami constants within table 6.6.

Material	Sample	Lamellae morphology at various cooling rates		
		2°C min^{-1}	5°C min^{-1}	10°C min^{-1}
CHIP	PET	Disc/spherulite	Disc	Disc
	PET0.5G	Sheaf	Sheaf	Sheaf
	PET1.0G	Sheaf	Sheaf	Sheaf
UNIAXIAL FILM	PET	Spherulite	Spherulite/sheaf	Spherulite
	PET0.5G	Sheaf	Sheaf	Spherulite/Sheaf
	PET1.0G	Sheaf	Spherulite/Sheaf	Spherulite

6.3.2 OZAWA MODEL

The Ozawa model is an alternative approach derived from the Avrami equation, and is commonly employed to examine the crystallisation kinetics of polymer systems.[11, 13] Similar to the modified Avrami equation, it describes crystallisation under a primary nucleation process, and therefore non-linearity in data may indicate the presence of secondary nucleation. In order to apply the Ozawa model to a particular system, fractional crystallinity plots as a function of temperature must first be generated. Figures 6.9 – 6.11 contain the fractional crystallinity plots for the polymer and composite chip. Equation 6.3 is the Ozawa equation.

$$\ln[-\ln(1-\chi)] = \ln[K(T)] + m\ln[\frac{1}{dT/dt}] \qquad \text{Equation 6.3}$$

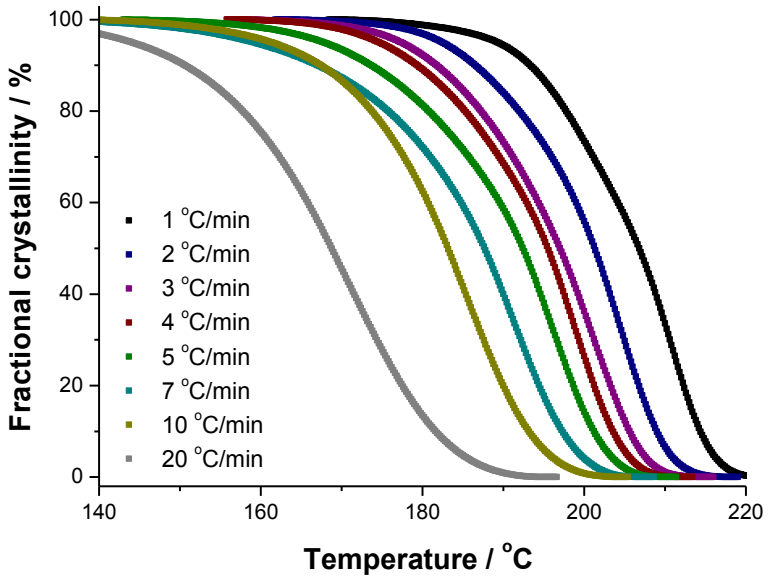

Figure 6.9 Fractional crystallinity during the dynamic crystallisation of PET chip at various cooling rates.

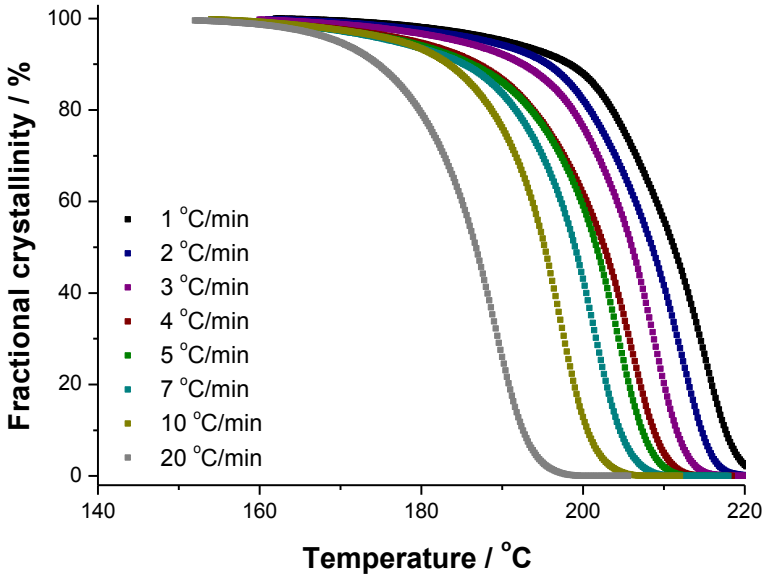

Figure 6.10 Fractional crystallinity during the dynamic crystallisation of PET0.5G chip at various cooling rates.

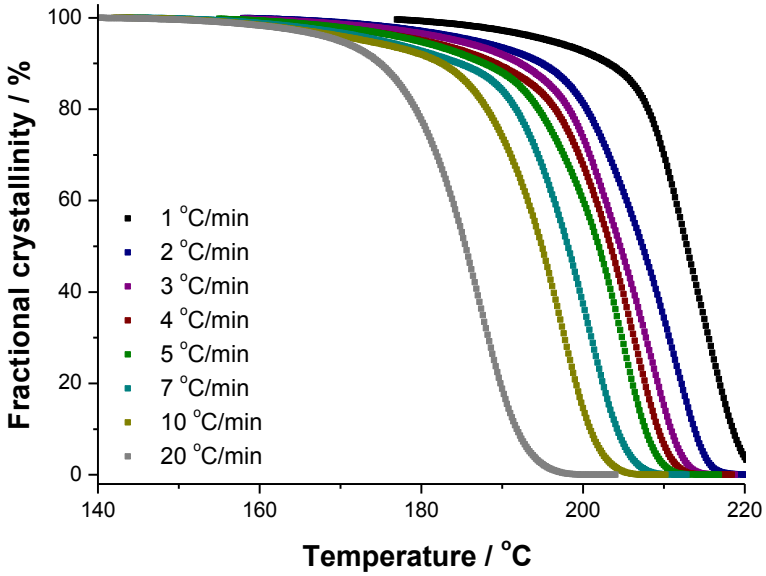

Figure 6.11 Fractional crystallinity during the dynamic crystallisation of PET1.0G chip at various cooling rates.

The fractional crystallinity plots are inspected to determine a suitable temperature range for comparison. In all plots it was observed that crystallisation at a cooling rate of 20ºC min^{-1} exhibited too low a crystallisation range for comparison, therefore only cooling rates between 1ºC min^{-1} and 10ºC min^{-1} were examined. The most appropriate temperature range was between 190 - 200ºC. The crystallinity at each particular temperature was noted, and used to calculate ln[-ln(1-(χ/100))], required in the Ozawa

plots of ln[-ln(1-χ/100))] against ln(cooling rate). Figures 6.12 – 6.14 contain the Ozawa plots for the polymer and composite chip.

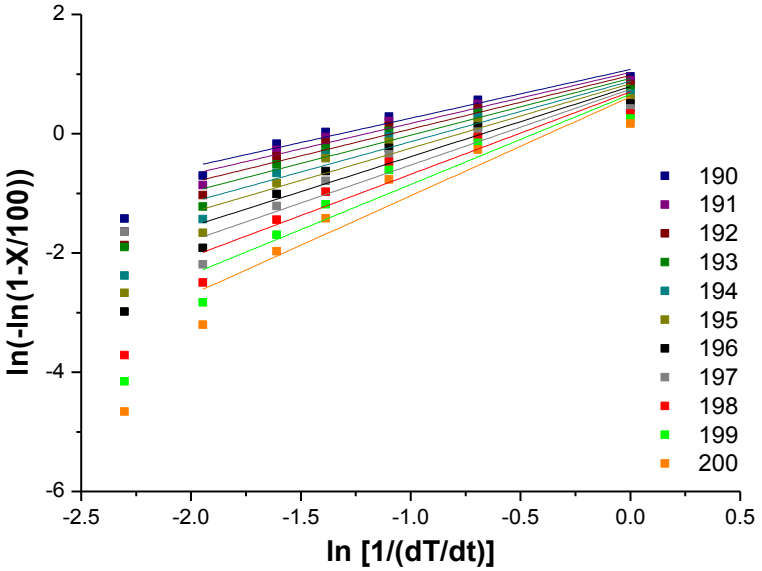

Figure 6.12 Ozawa plot of PET chip at various temperatures (ºC).

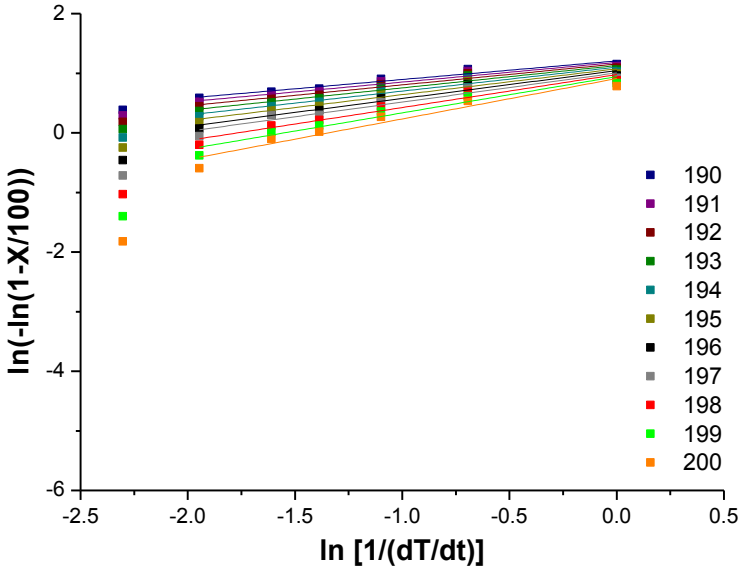

Figure 6.13 Ozawa plot of PET0.5G chip at various temperatures (ºC).

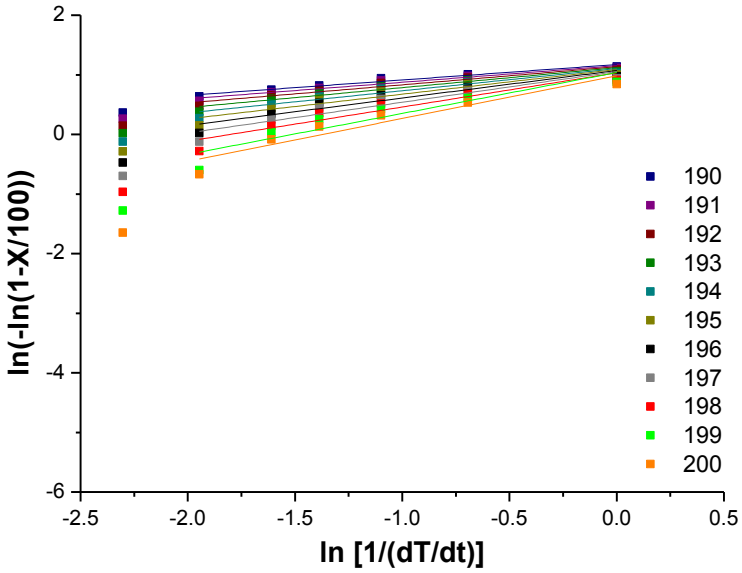

Figure 6.14 Ozawa plot of PET1.0G chip at various temperatures (ºC).

At low cooling rates (which equate to greater ln[1/(dT/dt)] values) the data from the temperatures under study are comparable. As the cooling rate increases the data is observed to become less comparable, with the extent of decrease in the y-values dependent on the temperature of examination. The variance in data at higher cooling rates may be attributed to a greater variance in crystallinity at the higher temperatures as the bulk crystallisation process is still ongoing. Data at the lower cooling rates and temperatures under study are therefore comparable as a substantial period of time has elapsed in which crystallisation may occur and the majority of the crystallisation process is hence complete.

As a result the Ozawa exponent is observed to increase and crystallisation rate decrease as the examination temperature increases. If one refers to the fractional crystallinity plots it is indicated that the majority of the crystalline material is present at 190ºC and the crystalline growth process is near completion. The data values at 200ºC are therefore more reflective of the crystallisation process when at a constant rate. It should be noted that temperatures higher than 200ºC were considered however the opposite predicament was encountered. At the higher temperatures the crystallisation rates were not yet constant and some samples had yet to begin crystallisation growth. This was especially evident within the higher cooling rate samples (or lower ln[1/(dT/dt)] values). The resulting Ozawa values were not comparable to literature values and as a

result discarded. The Ozawa plots for temperatures up to 210ºC however may be found within appendix 4.

Table 6.9 contains the Ozawa constants and crystallisation rates for the chosen comparative temperature of 200ºC. The Ozawa constant and therefore mode of nucleation is observed to differ between the composites and the polymer, which is as expected. The polymer should undergo sporadic nucleation from the melt as there is no significant material which could act as crystallisation seeds. The composites in comparison will undergo a combination of both predetermined and sporadic nucleation due to the presence of nanoclay which acts as a nucleant. For the purpose of this analysis, predetermined nucleation will be assumed dominant, however some degree of variance from the expected literature values will be expected.

It is noted that the Ozawa values for PET in particular are substantially higher than the standard sets of values cited within the literature and contained within table 6.10. According to Zhang *et al.* an expected value for the Ozawa constant during sporadic nucleation of a spherulitic crystallite is 0.75.[14] The values obtained experimentally and quoted within table 6.9 for PET chip and uniaxial film however are over twice this value. Ozawa constants experimentally derived within literature published by Durmus *et al*. and Jiang *et al*. on the other hand illustrate this variance should not be unexpected and cite values of 2.07 and 3.54, respectively.[11, 13] In contrast, the values determined for the nanocomposite materials are relatively comparative to the standard literature values for pre-determined nucleation, especially for the nanocomposite chip. Melt processing does appear to impact the crystallisation process and values are notably lower in the case of the uniaxial film samples. This may indicate a decrease in crystalline growth dimensions from a spherulitic to disc-like growth morphology within the composites. As the Ozawa constants for the polymer however are substantially higher than the standard set of values contained with table 6.10 no conclusion for these samples may be drawn other than a possible sheaf-like morphology. The Ozawa model is therefore not appropriate for considering the dimensional growth of the pure polymer system in particular. In addition, the morphologies obtained for the polymer composites are unexpected due to the fibrous nature of the sepiolite nanoclay, and it must therefore

be questioned whether the Ozawa model is in addition suited to the polymer nanocomposites.

If the crystallisation rate is considered the uniaxial film is observed to crystallise at a faster rate than the amorphous chip at the temperature under study. The increase in rate is attributed to the lower molar mass of the uniaxial film which improves chain mobility and hence increases the ease of crystallisation. The nucleant behaviour of the Garamite® nanoclay is also evident within the composite chip systems. In addition it appears that heterogeneous nucleation at the loadings under study increases the crystallisation rate to a comparable extent imparted by the decrease in molar mass on melt processing. It is noted however that the nucleant behaviour is not mirrored within the uniaxial film systems and the crystallisation rate appears to decrease within the nanocomposites samples. It is suspected that the combined effect of the Garamite® nucleant and the decrease in molar mass on melt processing has increased the crystallisation rate to such a degree that the crystallisation process is near completion at the temperature under study.

Table 6.9 Kinetic data for the crystallisation of PET and PET composites obtained through the Ozawa model

Material	Sample	m	Z(200)
CHIP	PET	1.66 ± 0.30	4.15 ± 2.46
	PET0.5G	0.68 ± 0.09	8.15 ± 1.31
	PET1.0G	0.72 ± 0.12	9.65 ± 1.41
UNIAXIAL FILM	PET	1.55 ± 0.27	10.62 ± 2.23
	PET0.5G	0.29 ± 0.15	5.28 ± 1.57
	PET1.0G	0.38 ± 0.08	5.28 ± 1.28

Table 6.10 Significance of Ozawa values with relation to crystalline growth.[14]

Crystallite growth	Ozawa exponent, m	
	Predetermined nucleation	Sporadic nucleation
Fibril	0	$^1/_2$
Disc	$^1/_2$	$^2/_3$
Spherulite	$^2/_3$	$^3/_4$

The Ozawa model appears to possess some the same issues which faced the modified Avrami model. The Ozawa model was developed in view of dynamic crystallisation, however the extent of the crystalline growth process at a particular temperature will vary depending on, for example, molar mass or nanoclay loading. It is therefore not ideal for use as a comparative tool. The Ozawa model may also only be employed

during the initial stages of primary crystallisation before crystallite infringement has occurred, which is typically considered before 40% crystallinity. Low crystallinity levels however required high temperatures of examination, which have been observed to lead to high Ozawa constants as observed within appendix 4. The examination of the systems therefore required a compromise between temperature of examination and % crystallinity in order to achieve values of any significance.

6.3.3 COMBINED AVRAMI-OZAWA MODEL

A combined model of the Avrami and Ozawa approaches was developed by Liu *et al.* in 1997.[15] Various authors had previously suggested modifications to the Avrami equation for reasons such as poor fitting when concerning more crystalline polymers.[16] Ozawa in particular modified the Avrami equation to allow dynamic crystallisation conditions.[17] Liu then merged Ozawa's modification with the Avrami equation, forming the combined Avrami-Ozawa model. Equations 6.4 – 6.5 contain combined and rewritten versions of the Avrami-Ozawa model.

$$\log Z_t + n\log(t) = \log K(T) - m\log\left[\frac{1}{dT/dt}\right]$$

Equation 6.4

Rewritten to,

$$\log\left[\frac{1}{dT/dt}\right] = \log F(T) - a\log(t)$$

Equation 6.5

The combined Avrami-Ozawa model may be applied to a system through plotting various extents of crystallinity at various cooling rates against log time. The intercept and gradient obtained through line-fitting provides logF(T) and –a respectively. F(T) equates to $[K(T)/Z]^{1/m}$, whereas a is the ratio of the Avrami and Ozawa exponents, n/m. Plots were generated at crystallinities of 10%, 20%, 40%, 60% and 80%. Figure 6.15 contains the combined plots for PET, PET0.5G and PET1.0G chip at 10% crystallinity. Due to visual similarities between all Ozawa plots produced, only a sample is presented below.

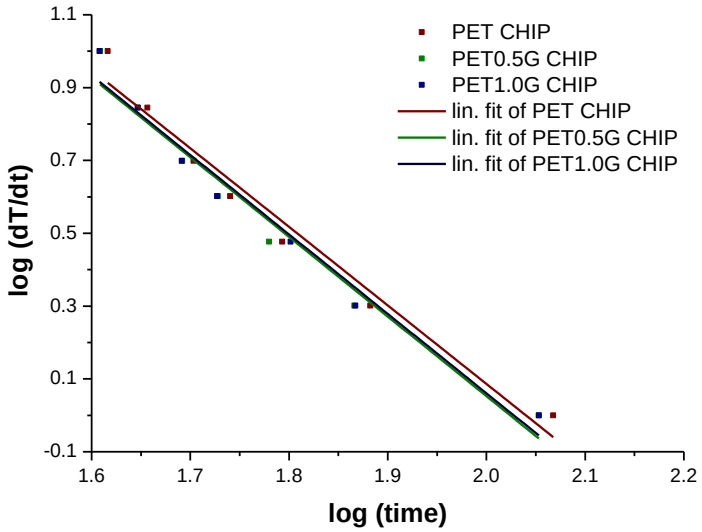

Figure 6.15 Combined Avrami-Ozawa plots for PET, PET0.5G and PET1.0G chip at 10% crystallinity.

As previously stated the slope equates to –a, where a = n/m. According to the combined Avrami-Ozawa model for these particular systems, the Avrami exponent is approximately double the value of the Ozawa exponent as illustrated within table 6.11. Examination of table 6.12 also indicates the logF(T) values are comparative within experimental error, and therefore crystallisation can be concluded to be occurring at a consistent rate between crystallinities of 10% and 80%. Both parameters are slightly higher than those observed within the literature.[11] Data from this particular model indicates the presence of nanoclay does not enhance the nucleation rate.

Table 6.11 Avrami-Ozawa exponents obtained from the gradient of the combined Avrami-Ozawa plots.

Material	**Sample**	**Avrami – Ozawa Exponent, a**				
		10%	**20%**	**40%**	**60%**	**80%**
Amorphous Chip	PET	2.16 ± 0.16	1.93 ± 0.21	2.02 ± 0.18	2.07 ± 0.16	2.08 ± 0.14
	PET0.5G	2.19 ± 0.17	2.13 ± 0.17	2.06 ± 0.16	2.03 ± 0.19	2.10 ± 0.16
	PET1.0G	2.19 ± 0.17	1.93 ± 0.21	2.02 ± 0.18	2.07 ± 0.16	2.08 ± 0.14
Uniaxial Film	PET	2.19 ± 0.17	2.13 ± 0.17	2.06 ± 0.16	2.03 ± 0.19	2.10 ± 0.16
	PET0.5G	2.19 ± 0.17	1.93 ± 0.21	2.02 ± 0.18	2.07 ± 0.16	2.08 ± 0.14
	PET1.0G	2.19 ± 0.17	2.13 ± 0.17	2.06 ± 0.16	2.03 ± 0.19	2.10 ± 0.16

Table 6.12 Log F(T) values obtained from the y-intercept of the combined Avrami-Ozawa plots.

Material	Sample	Log F(T)				
		10%	**20%**	**40%**	**60%**	**80%**
Amorphous Chip	PET	4.40 ± 0.29	4.18 ± 0.32	4.35 ± 0.30	4.26 ± 0.29	4.37 ± 0.22
	PET0.5G	4.40 ± 0.29	4.18 ± 0.32	4.27 ± 0.28	4.31 ± 0.26	4.37 ± 0.22
	PET1.0G	4.40 ± 0.29	4.18 ± 0.32	4.35 ± 0.30	4.26 ± 0.29	4.37 ± 0.22
Uniaxial Film	PET	4.40 ± 0.29	4.18 ± 0.32	4.27 ± 0.28	4.31 ± 0.26	4.37 ± 0.22
	PET0.5G	4.40 ± 0.29	4.18 ± 0.32	4.35 ± 0.30	4.26 ± 0.29	4.37 ± 0.22
	PET1.0G	4.40 ± 0.29	4.18 ± 0.32	4.27 ± 0.28	4.31 ± 0.26	4.37 ± 0.22

6.4 CALCULATION OF THE ACTIVATION ENERGIES

The activation energy could be determined through methods derived from either Kissinger or Ozawa.[18] As the Ozawa model has previously been employed in the investigation of the crystallisation kinetics it seemed the most appropriate method to follow. Equation 6.6 is the method Ozawa suggested; Ø is the cooling rate (ºC min^{-1}), T_p the peak maximum of crystallisation (ºC), E_a is the activation energy (kJ mol^{-1}) and R the gas constant (8.314 J K^{-1} mol^{-1}).

$$\frac{d(\log\phi)}{d(\frac{1}{T_p})} = -0.457\frac{E_a}{R}$$

Equation 6.6

Table 6.13 contains the calculated activation energies for the systems under study. The values obtained for chip samples are in agreement with those observed in literature, especially with respect to the study performed by Wang *et al.*.[18, 19] The apparent negative activation energies also imply that there is an increase in crystallisation rate with a decrease in temperature. This behaviour is as expected for a polymer system as there are various contributing thermodynamic factors involved in the crystallisation process.[20] Crystallisation is also known to require an entropy penalty on the formation of the crystalline nuclei. The larger exothermic values for the composites with respect to the polymer indicate that the nanoclay pays this entropy penalty during crystallisation, allowing the more substantial release in energy.

Table 6.13 Activation energies of crystallisation calculated through the Ozawa method.

Material	Sample	E_a (kJ mol^{-1})
Amorphous Chip	PET	-122
	PET0.5G	-202
	PET1.0G	-216
Uniaxial Film	PET	-192
	PET0.5G	-301
	PET1.0G	-244

6.5 CONCLUSIONS

Throughout the crystallisation studies the Garamite® nanoclay was observed to act as a nucleant, due to the higher crystallisation temperatures observed during the cooling cycle within the heat-cool-reheat regime. At higher cooling rates there was a substantial difference in the crystallisation temperatures of the amorphous chip and uniaxial film materials, especially with respect to the pure polymer. The pure polymer exhibited a 12ºC decrease in the crystallisation temperature between the uniaxial film and chip, illustrating the inhibition of crystallisation due to high molar mass and low chain mobility. The molar mass effects were also observed to be buffered to some extent by the presence of nucleating material. This illustrates the presence of nanoclay rather than molar mass is the dominant influence on crystallisation, which in turn has significant influence on the use of the dynamic crystallisation models.

During crystalline melting the nucleant ability of the nanoclay was confirmed as it increased the ability of the polymer to re-crystallise from the melt. This was observed through the emergence of a secondary crystalline melt peak. The uniaxial film samples were also observed to crystallise faster than the amorphous chip. This was attributed to the lower molar mass of the uniaxial film samples. For example, PET chip was observed to have a mass of 31,950 g mol^{-1} compared with a molar mass of 27,050 g mol^{-1} for the respective PET uniaxial film sample, when determined through gel permeation chromatography.

The crystallisation kinetics were examined in order to investigate the mode of crystalline growth. Non-linearity was initially observed within the modified Avrami model due to a low crystalline content during the induction period and crystallite infringement at higher crystalline contents. A more suitable crystalline range of between 1 - 40% provided linearity, and expressed a change from disc-like to spherulitic crystalline morphologies on melt processing for the pure polymer and a sheaf-like crystalline morphology for the polymer composites. The sheaf-like crystalline morphology was attributed to the fibrous nature of the sepiolite nanoclay which nucleated the polymer chains. Both the Ozawa and combined Avrami-Ozawa models exhibited linearity of data and the combined Avrami-Ozawa model suggested

there was no significant difference in the rate of crystallisation. The Ozawa model was also suggestive that within the pure polymer chip and uniaxial film the crystallisation growth process occurred in the same manner i.e. a sheaf-like growth. Therefore crystalline growth was concluded to remain constant for the pure polymer despite a lower molar mass. On the contrary, composite crystalline growth was observed to decrease in dimensions on processing, i.e. from spherulitic to disc-like lamellae. As a result, the Ozawa method was concluded as the least suitable kinetic model to examine the PET and PET composite systems within this thesis.

Finally, the calculated activation energies for the materials under study were in good agreement to those previous observed within literature.[18, 19] The nucleating ability of the nanoclay was illustrated through a lower activation energy of crystallisation when comparing both chip and uniaxial film materials. The polymers with the lower molar mass also exhibited similar behaviour to those which were heterogeneously nucleated as a low molar mass generally coincides with a greater ease of organisation from the melt.

7.6 REFERENCES

1. Calcagno, C.I.W., Mariani, C.M., Teixeira, S.R., Mauler, R.S., *The effect of organic modifier of the clay on morphology and crystallization properties of PET nanocomposites,* Polymer, 2007, **48**, 996-974.
2. Rojanapitayakorn, P., Lather, P.T., Goldberg, A.J., Weiss, R.A., *Optically transparent self-reinforced poly(ethylene terephthalate) composites: molecular orientation and mechanical properties,* Polymer, 2005, **46**, 761-773.
3. Cowie, J.M.G., *Polymers: Chemistry and Physics of Modern Materials*, 1991, Chapman & Hall, London.
4. Pilati, F., Toselli, M., Messori, M., Manzoni, C., Turturro, A., Gattiglia, E.G., *On specific factors affecting the crystallization of PET: the role of carboxyl terminal groups and residual catalysts on the crystallization rate,* Polymer, 1997, **38**, 4469-4476.

5. Gümther, B., Zachmann, H.G., *Influence of molar mass and catalysts on the kinetics of crystallization and on the orientation of poly(ethylene terephthalate),* Polymer 1983, **24**, 1008-1014.
6. Chung, J.W., Son, S.E., Chun, S.W., Kang, T.J., Kwak, S.Y., *Non-isothermal Crystallisation Behaviour of Exfoliated Poly(ethylene terephthalate)-Layered Silicate Nanocomposites in the Presence and Absence of Organic Modifier* Journal of Polymer Science: Part B: Polymer Physics, 2008, **46**, 989-999.
7. Ou, C.F., Ho, M.T., Lin, J.R., *The Nucleating Effect of Montmorillonite on Crystallization of PET/Montmorillonite Nanocomposite,* Journal of Polymer Research, 2003, **10**, 127-132.
8. Ke, Y., Long, C., Qi, Z., *Crystallization, Properties, and Crystal and Nanoscale Morphology of PET-Clay Nanocomposites,* Journal of Applied Polymer Science 1999, **71**, 1139-1146.
9. Litchfield, D.W., Baird, D.G., *The role of nanoclay in the generation of poly(ethylene terephthalate) fibres with improved modulus and tenacity,* Polymer 2008, **49**, 5027-5036.
10. Arencon, D., Velasco, J.I., *The Influence of Injection-Moulding Variables and Nucleating Additives on Thermal and Mechanical Properties of Short Glass Fiber/PET Composites,* Journal of Thermoplastic Composite Materials, 2003, **16**, 365-380.
11. Durmus, A., Ercan, N., Soyubol, G., Deligoz, H., Kasgoz, A., *Non-isothermal Crystallization Kinetics of Poly(ethylene terephthalate)/Clay Nanocomposites Prepared by Melt Processing,* Polymer Composites, 2010, **31**(6), 1056-1066.
12. Li, G., Yang, S., Jiang, J., Jin, J., Wu, C., *The Complicated Influence of Branching on Crystallization Behavior of Poly(ethylene terephthalate),* Journal of Applied Polymer Science, 2008, **110**(3), 1649-1655.
13. Jiang, X.L., Luo, S.J., Sun, K., Chen, X.D., *Effect of nucleating agents on crystallization kinetics of PET,* Express Polymer Letters, 2007, **1**(4), 245-251.
14. Zhang, Z., Xiao, C., Dong, Z., *Comparison of the Ozawa and modified Avrami models of polymer crystallization under non-isothermal conditions using a computer simulation method,* Thermochimica Acta, 2007, **466**, 22-28.

15. Liu, T., Mo, Z., Wang, S., Zhang, H., *Non-isothermal Melt and Cold Crystallization Kinetics of Poly(Aryl Ether Ether Ketone Ketone),* Polymer Engineering and Science, 1997, **37**(3), 568-575.
16. Di Lorenzo, M.L., Silvestre, C., *Non-isothermal crystallization of polymers,* Progress in Polymer Science, 1999, **24**, 917-950.
17. Ozawa, T., *Kinetics of non-isothermal crystallisation*, Polymer, 1971, **12**(3), 150-158.
18. Wang, Y., Shen, C., Li, H., Li, Q., Chen, J., *Nonisothermal Melt Crystallization Kinetics of Poly(Ethylene Terephthalate)/Clay Nanocomposites,* Journal of Applied Polymer Science, 2003, **91**(1), 308-314.
19. Vyazovkin, S., Sbirrazzuoli, N., *Estimating the activation energy for non-isothermal crystallization of polymer melts,* Journal of Thermal Analysis and Calorimetry, 2003, **72**, 681-686.
20. Atkins, P., Paula, J., *Atkins' Physical Chemistry*, 7th ed, 2002, Oxford University Press, Oxford.

CHAPTER 7 DEGRADATION

7.1 THERMAL DEGRADATION

7.1.1 DYNAMIC TGA

Dynamic TGA provided insight into the mass loss effects during degradation. Various heating rates were examined in order to determine the effect of the nanoclay on thermal diffusion, and also the nanoclays' impact on volatile loss during degradation. Figure 7.1 illustrates the mass loss as temperature is increased for PET uniaxial film under helium. Additional plots for the composites and the amorphous chip counterparts can be found within the appendices. It should be noted that due to time constraints 1ºC min^{-1} and 20ºC min^{-1} heating rates were not performed on PET and PET composite chip. Precision between samples was determined as follows: ± 0.4 % for residual mass and ± 1.4ºC for temperatures observed at the maximum degradation rate.

The thermal degradation of PET, PET0.5G and PET1.0G is observed to occur through a single step mass loss which then plateaus at higher temperatures. Polymer or composites which were degraded at the higher heating rates were observed to possess higher maximum temperatures due to the decrease in the time available for degradation. It was noted however that the final mass loss was comparable between samples and therefore the heating rate is not observed to impact the extent of degradation.

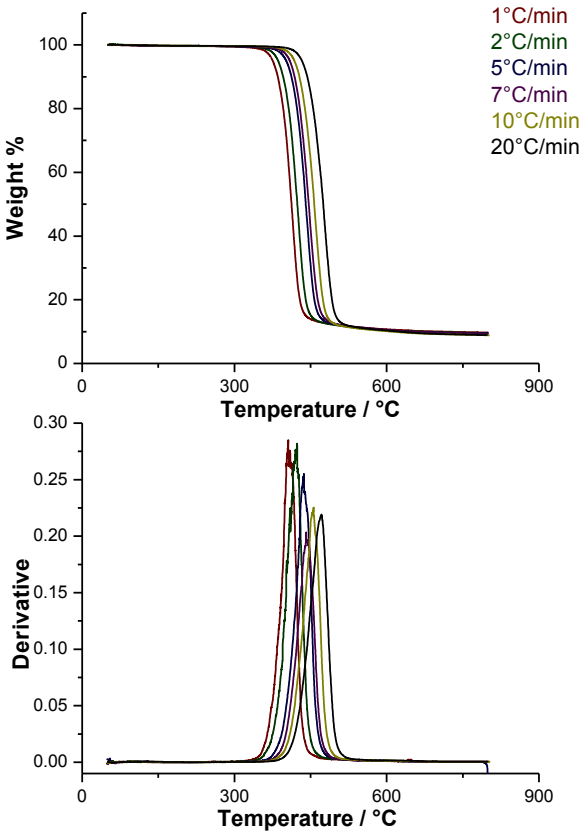

Figure 7.1 TGA thermogram for PET uniaxial film during thermal degradation under helium.

Table 7.1 illustrates the temperatures at the maximum rate of degradation are comparable for the polymer and composite samples, which suggests the nanoclay has no impact on the degradative rate. Table 7.1 also indicates the polymer possesses a lower final mass post-degradation in comparison to the polymer composites. This increase in char material cannot, however, be attributed solely to the presence of the Garamite® and the nanoclay may therefore be suggested to enhance char formation in some manner. It is noted that there is a significant increase of at least 3.4% in residual char in the PET0.5G samples in comparison to the pure polymer. Further increasing the Garamite® loading to 1.0% w/w however only increases the residual mass by an additional 1.0%. This suggests the enhancement of char formation is predominantly achieved by the initial 0.5% w/w Garamite®.

Table 7.1 Average final % mass loss values for PET and PET composite uniaxial film and chip samples during thermal TGA degradation.

Material	Sample	Replicate	Heating rate / ºC min^{-1}				Residual mass / %
			2	5	7	10	
Amorphous Chip	PET	1	8.68	9.09	8.43	8.23	8.61
		2	8.21	8.11	8.36	8.74	8.36
		average	8.45	8.60	8.40	8.49	**8.48**
	PET0.5G	1	13.94	13.24	12.76	13.29	13.31
		2	13.61	13.01	13.21	12.99	13.21
		average	13.78	13.13	12.99	13.14	**13.26**
	PET1.0G	1	14.47	14.25	14.04	14.17	14.23
		2	15.04	14.37	13.99	13.43	14.21
		average	14.76	14.31	14.02	13.80	**14.22**
Uniaxial film	PET	1	9.52	9.82	9.34	8.85	9.38
		2	9.86	9.88	9.22	9.02	9.50
		average	9.69	9.85	9.28	8.935	**9.44**
	PET0.5G	1	13.15	12.81	12.85	12.64	12.86
		2	12.30	13.06	13.03	12.83	12.81
		average	12.73	12.94	12.94	12.74	**12.83**
	PET1.0G	1	13.77	13.82	13.66	14.40	13.91
		2	13.63	13.67	13.60	13.58	13.62
		average	13.70	13.75	13.63	13.99	**13.77**

Tables 7.2 Temperatures at the maximum degradation rate during thermal TGA degradation of PET and PET composite chip and uniaxial film samples.

Material	Sample	Replicate	Heating rate / ºC min^{-1}			
			2	**5**	**7**	**10**
Amorphous Chip	PET	1	427.55	443.19	455.53	455.80
		2	427.55	444.20	452.27	459.84
		average	427.55	443.70	453.90	457.82
	PET0.5G	1	424.02	440.67	450.00	458.07
		2	421.24	441.42	447.73	455.55
		average	422.63	441.05	448.87	456.81
	PET1.0G	1	422.76	442.43	447.98	449.50
		2	424.52	442.18	448.99	456.31
		average	423.64	442.31	448.49	452.91
Uniaxial film	PET	1	420.99	434.87	442.94	454.54
		2	416.96	436.63	441.42	455.30
		average	418.98	435.75	442.18	454.92
	PET0.5G	1	424.78	438.65	447.48	454.79
		2	421.24	443.95	447.98	455.30
		average	423.01	441.30	447.73	455.05
	PET1.0G	1	419.98	438.40	443.49	450.00
		2	421.75	436.71	446.16	453.53
		average	420.87	437.56	444.83	451.77

7.1.2 DYNAMIC DSC

Dynamic DSC runs were performed in order to investigate the energetic behaviour of both the polymer and composites during thermal degradation. Due to the volume of samples and instrument run time required, analysis via DSC was only performed on chip samples. The onset of degradation and temperature at the energetic maximum of degradation in particular were examined. This would provide insight into how the nanoclay affected the stability of the polymer at the nanoclay-polymer interfaces, and also whether the degradation of the bulk polymer matrix was altered in any manner. The samples were prepared and subjected to the procedures previously outlined in Chapter 3. Figures 7.2 - 7.4 contain the dynamic thermal degradation curves for the polymer and composites. Precision was determined as ± 3.30ºC for the onset temperatures and ± 2.00ºC for the degradation maximums. An additional ± 1.00ºC was attributed in each case to account for instrumental variance.

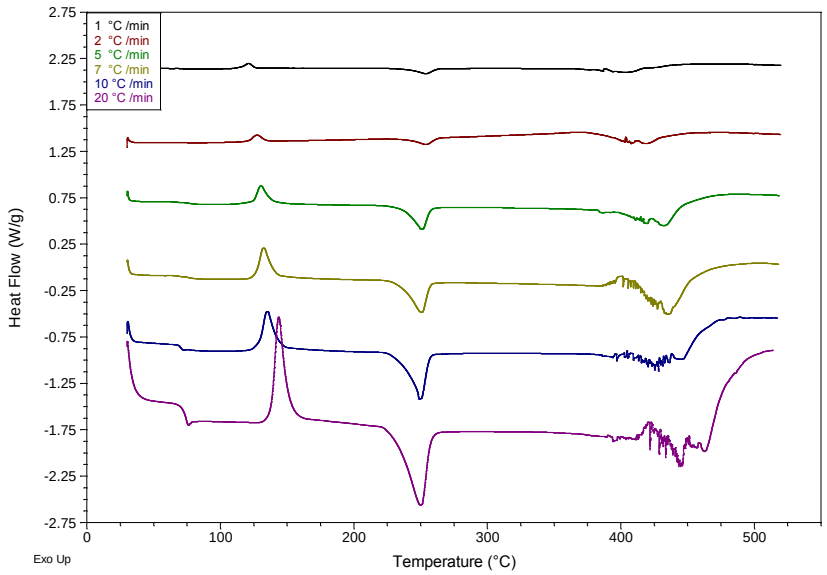

Figure 7.2 Dynamic thermal degradation profiles of PET at various heating rates under nitrogen.

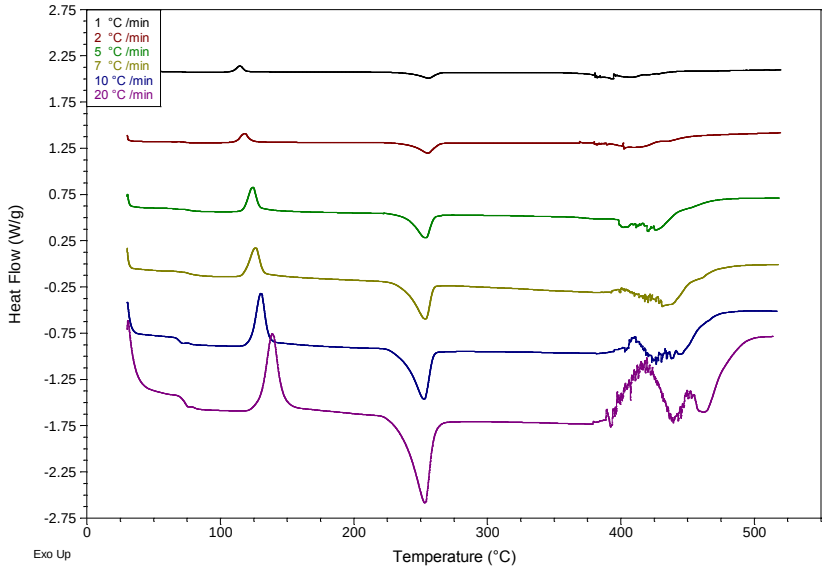

Figure 7.3 Dynamic thermal degradation profiles of PET0.5G at various heating rates under nitrogen.

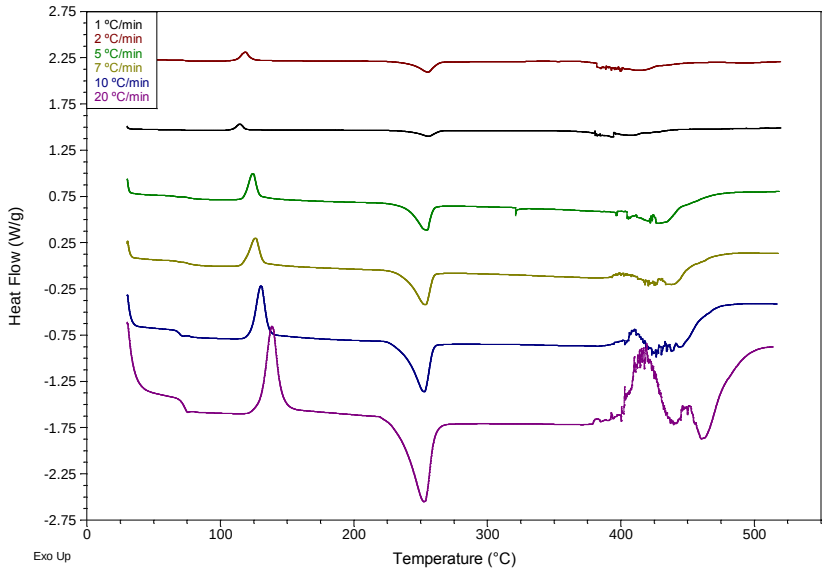

Figure 7.4 Dynamic thermal degradation profiles of PET1.0G at various heating rates under nitrogen.

Visual examination of the plots suggests a similar energetic behaviour during the degradation of the polymer and composites. It is noted however that degradation at the higher heating rates does appear to become slightly more erratic and energetic within the composite samples. The erratic baseline during degradation is due to the evolution of volatile species which result in rapid fluctuations in heat flow.

Tables 7.3 and 7.4 contain the onset and maximum peak temperatures for energetic degradation. The onset temperatures are extremely valuable when examining composite systems as minor alterations in the degradation process can be observed. For example within polymer-nanoclay composites the bulk of the polymer matrix has no contact with the nanoclay, only a small percentage of the polymer will be present at a nanoclay interface. Due to the highly sensitive nature of the DSC technique, minor changes in system stability can be observed through changes in the onset temperature. The maximum peak temperatures are representative of the degradation of the bulk of the polymer matrix which is not in contact with the nanoclay, and therefore are not expected to substantially change by the presence of nanoclay at such small loadings.

Table 7.3 Comparative table of polymer and composite temperatures for the onset of thermal degradation.

Heating rate /°C min^{-1}	**Onset temperature / ºC**		
	PET	**PET0.5G**	**PET1.0G**
1	367.11	360.22	362.18
1	363.31	358.46	360.15
1	365.21	359.34	361.17
2	377.07	378.97	375.70
2	375.05	374.15	389.87
2	376.06	376.56	382.79
5	382.57	394.36	350.09
5	377.10	402.99	355.62
5	379.84	398.70	352.86
7	385.80	389.51	370.64
7	380.84	389.56	352.39
7	383.32	389.54	361.52
10	385.71	394.63	371.25
10	390.87	389.33	361.88
10	388.29	391.98	366.57
20	408.78	385.60	394.15
20	417.30	395.04	391.24
20	413.04	390.32	392.70

Table 7.4 Comparative table of polymer and composite temperatures for the main degradation peak temperature during thermal degradation.

Heating rate /°C min^{-1}	Maximum temperatures of degradation /°C		
	PET	PET0.5G	PET1.0G
1	399.56	407.51	407.63
1	403.07	402.48	404.57
1	401.32	405.00	406.10
2	421.2	411.96	402.56
2	418.92	412.43	402.23
2	420.06	412.20	405.97
5	431.83	420.62	433.89
5	418.86	421.78	432.12
5	425.35	421.20	433.01
7	433.95	433.49	434.93
7	428.66	430.91	435.81
7	431.31	432.20	435.37
10	443.78	444.84	444.80
10	440.79	444.01	443.39
10	442.29	444.43	444.10
20	462.67	461.30	456.22
20	458.85	460.61	458.59
20	460.76	460.96	457.41

The onset of degradation of PET was observed to increase with heating rate due to the time constraints imposed on degradation as the heating rate increased. Also, although the same overall trend was observed within the composites, there were complexities within the trends. At low heating rates there was no detectable impact by the nanoclay. This was not unexpected, as degradation is allowed to occur over a rather fsubstantial period of time. For example, a 20ºC range at a heating rate of 1ºC min^{-1} would occur over 20 minutes, as opposed to 2 minutes at 10ºC min^{-1}. As the heating rate increased degradation occurred over a shorter timescale, allowing the effect of the nanoclay to be detected. A substantial drop in the onset temperature of PET1.0G was observed in comparison to PET and PET0.5G at a 5ºC min^{-1} heating rate. This heating rate appears to be the optimum rate in which to observe the influence of the nanoclay on degradation. As the heating rate increases further the onset temperatures increase until they are comparable with PET0.5G at a heating rate of 20ºC min^{-1}. At the higher heating rates, the onset of polymer degradation will occur over a relatively short period of time. Any alteration to the degradative behaviour at the polymer-Garamite® interface may then be too subtle for detection. Overall, as expected, the effects of the Garamite® on the onset of degradation were observed to a more significant degree within the composite with the higher Garamite® loading.

The maximum peak temperatures, however, did not exhibit the same fluctuations in trend as the onset temperatures. A definitive increase in T_{max} was observed with an increase in heating rate for both the polymer and composites. The range of observed temperatures within both duplicate samples and between nanoclay loadings, illustrated that no significant alterations occurred within the degradation of the bulk polymer matrix due to incorporation of nanoclay at either of the examined loadings. The fluctuations in temperatures were therefore attributed to experimental error.

7.1.3 THERMAL VOLATILISATION ANALYSIS

Thermal Volatilisation Analysis (TVA) and Sub-Ambient Thermal Volatilisation Analysis (SATVA) were employed due to the wealth of information which may be collected over a relatively short period of time. As already discussed in Chapter 2, some of the benefits of TVA include insight into the ratios of condensable and non-condensable volatiles and the identification of product ratios and temperatures of formation. The techniques employed in order to deliver this information were FT-IR, MS and GC-MS, in addition to pirani pressure measurements. The full procedure for this technique can be found in Chapter 3.

Uniaxial film was examined prior to the chip. This could be considered an improper order for analysis; however, polymer film was considered a more appropriate starting medium for examining degradation under the experimental conditions of TVA. The film would not contain trapped atmospheric gases such as oxygen or moisture which may give erroneous results. In addition it would melt and degrade within the sample tube in a more uniform and reproducible manner, which is of particular importance when examining the timing and temperatures of volatile release. It is also noted that during analysis of the composite samples, there were no degradation products which could be identified as originating from the organic modifiers within the Garamite®. All products detected through FTIR, MS and GC-MS were therefore attributed to the degradation of the polymer.

7.1.3.1 DEGRADATION RUN

7.1.3.1.1 PRESSURE MEASUREMENTS

The collection of pressure measurements during the degradation run would give an indication of the volume of condensable and non-condensable volatile materials released during degradation. A considerable volume of non-condensables in comparison to condensable volatiles may indicate a particular degradation mechanism at particular temperatures. This indication would of course have to be confirmed by mass spectrometry.

Figure 7.5 is an example of the typical pressure measurements which were collected during analysis. The solid line plot represents the pressure measurements obtained at the entrance of the sub-ambient trap, therefore indicating the total pressure rise due to both condensable and non-condensable volatiles. The dashed line plot represents the pressure measurement at the exit of the cold trap, and therefore the detection of only the non-condensable volatiles. Additional plots of the composites and replicate samples may be found in appendix 5. Error was determined as ± 5.06ºC and ± < 10^{-2} Torr for temperature and pressure measurements respectively.

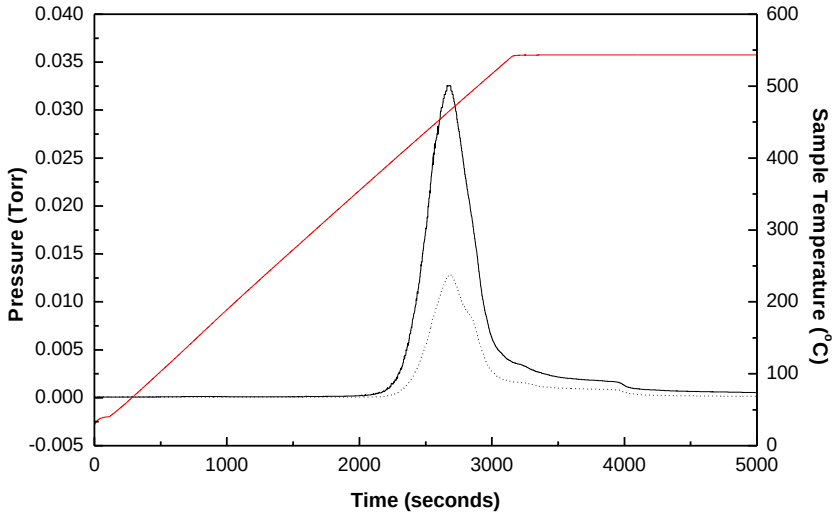

Figure 7.5 Pressure measurements from the pre- and post-sub-ambient trap during thermal degradation of PET1.0G uniaxial film. The solid and dashed plots represent pressure measurements pre- and post- sub-ambient trap, respectively. The red plot represents the furnace temperature.

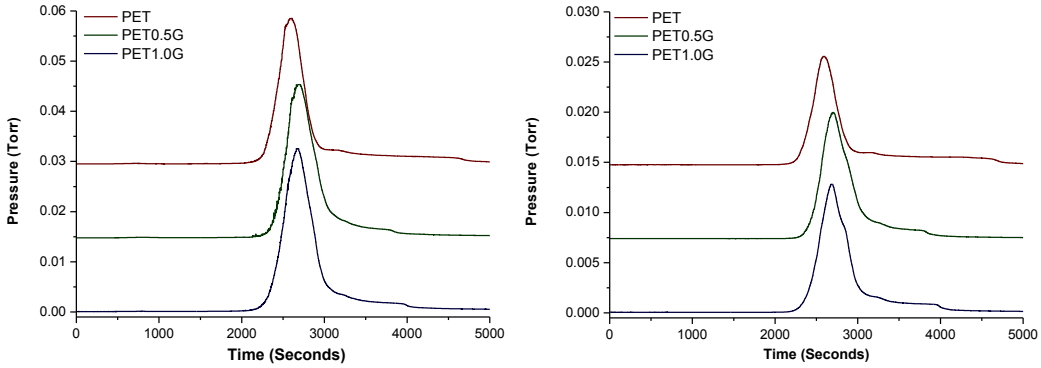

Figures 7.6 and 7.7 Pressure readings of pre-subambient and post-subambient traps, respectively, during the thermal degradation of PET. Replicate sample data may be found in appendix 5.

Degradation process within the pressure plots shown in figure 7.5 can be sectioned into four regions; the onset of degradation (prior to the maximum degradation rate being reached), the maximum degradation region, a post-maximum degradation region (where degradation is still underway but at a slower rate) and a tail-off period where a low concentration of the final volatile remnants are evolved.

Figure 7.7 in particular illustrates that within the composite samples a shoulder is present in the post-maximum region, which is indicative of peak separation. The shoulder is observed to increase in size with an increase in nanoclay loading. Table 7.5 contains the temperatures at which the maximum volumes of volatiles are being evolved. Within the chip materials the T_{max} values are comparable; indicating the release of volatiles in the bulk state is not affected by the nanoclay. Figure 7.7 however suggests the release of the non-condensable volatiles is impeded or extended to some degree within the composite chip. As the P_{max} values are observed to increase within the composites it is more probable an increase in non-condensable volatiles in particular has occurred.

With respect to the volatile release during the degradation of the uniaxial film samples, the polymer film possesses relatively comparable T_{max} values in comparison to the amorphous chip. The composites however are slightly higher in temperature, suggesting the drawing process also affect the release of volatiles in the bulk state on degradation. In addition P_{max} is also observed to increase slightly for all uniaxial film samples. It is probable the increase in the volatile content is due to the lower molar mass of the uniaxial film which would allow degradation to occur be initiated faster and perhaps to

a greater degree. The increase in T_{max} can most likely be attributed to an increase in the degree of exfoliated Garamite® due to shearing during melt processing. A more highly dispersed nanoclay would be expected to impede volatile diffusion to a greater extent. Literature has suggested the nanoclay impedes the evolution of volatiles during the degradation process through the temporary adsorption of volatiles onto the nanoclay surface or into the nanoclay pores.[1] Char formation may also account for the volatile impediment to a certain degree, and is a commonly known occurrence during composite degradation.[2] The composites are also observed to possess a greater maximum pressure which may be attributed to a greater rate of release of volatiles on degradation. The nanoclay may be affecting the volatile release in two manners. The degradation of thermally unstable alkyl ammonium surface modifiers is known to leave acidic sites on the nanoclay surface which catalyse polyester degradation and may increase the volume of volatiles produces. In addition the degradation of the surface modifiers themselves may be a direct cause of the increase in volatile production. Mass spectrometry will now give insight into the identity of volatiles within each particular region.

Table 7.5 Maximum temperatures and pressures of condensable and non-condensable volatiles, and non-condensable volatiles during thermal degradation.

Material	Sample	Replicate	Condensable and non-condensable volatiles		Non-condensable volatiles	
			T_{max} / °C	P_{max} / Torr	T_{max} / °C	P_{max} / Torr
Amorphous Chip	PET	1	446.88	0.022	451.87	0.009
		2	441.36	0.023	446.53	0.009
		Average	444.12	0.023	449.20	0.009
	PET0.5G	1	452.33	0.028	453.47	0.012
		2	452.76	0.027	454.54	0.011
		Average	452.55	0.028	454.01	0.012
	PET1.0G	1	444.39	0.029	446.52	0.013
		2	450.26	0.028	451.87	0.013
		average	447.33	0.029	449.20	0.013
Uniaxial Film	PET	1	451.61	0.029	451.34	0.011
		2	457.57	0.025	462.91	0.010
		Average	454.59	0.027	457.13	0.011
	PET0.5G	1	467.18	0.031	468.96	0.013
		2	467.00	0.033	468.78	0.013
		Average	467.09	0.032	468.87	0.013
	PET1.0G	1	464.69	0.033	467.00	0.013
		2	462.37	0.030	464.15	0.012
		average	463.53	0.032	465.58	0.013

7.1.3.1.2 MASS SPECTROMETRY OF NON-CONDENSABLE VOLATILES

Mass spectrometry is an extremely valuable analytical tool in determining the products and hence mechanistic pathways of a polymer's degradation. Pressure measurements during degradation have indicated a significant increase in both condensable and non-condensable volatiles evolved from the polymer composites in comparison to the polymer, however provide no indication of molecular content. Mass spectrometry is therefore an appropriate tool to identify the volatiles in real time in conjunction with pressure measurements.

Spectral data was comparable between both the polymer and polymer composite samples, for both chip and uniaxial film samples and between the replicates. One full set of spectra are contained within figures 7.8 – 7.11, with additional spectra within appendix 5.

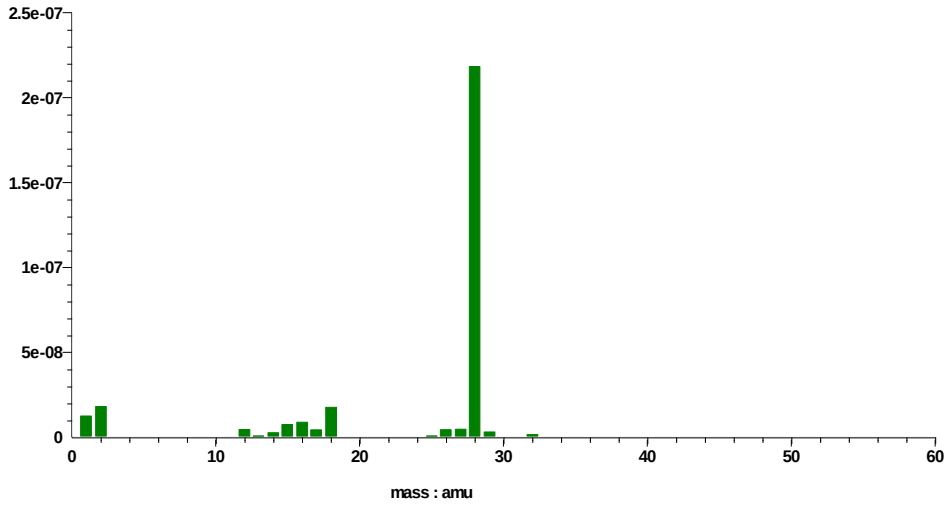

Figure 7.8 Mass spectrum of non-condensable volatiles during the onset region of PET1.0G degradation by TVA.

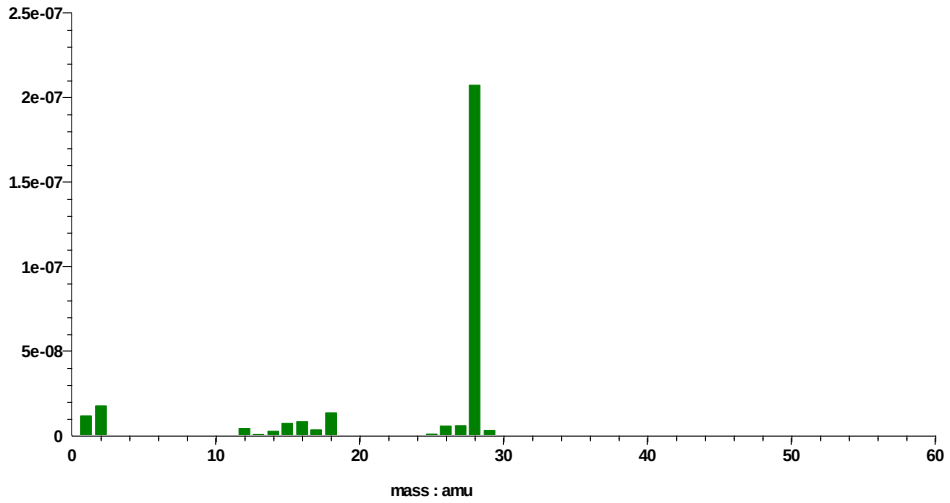

Figure 7.9 Mass spectrum of non-condensable volatiles within the maximum degradation region during PET1.0G degradation by TVA.

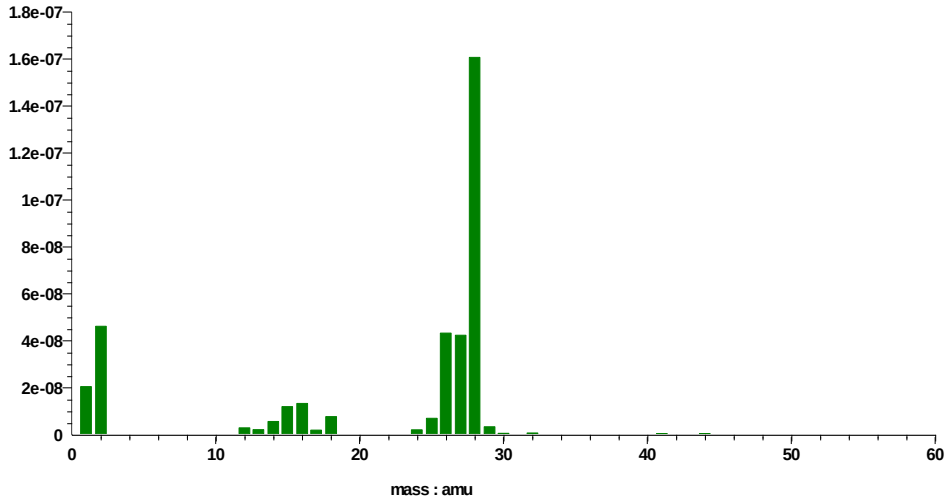

Figure 7.10 Mass spectrum of non-condensable volatiles after the maximum degradation region during PET1.0G degradation by TVA.

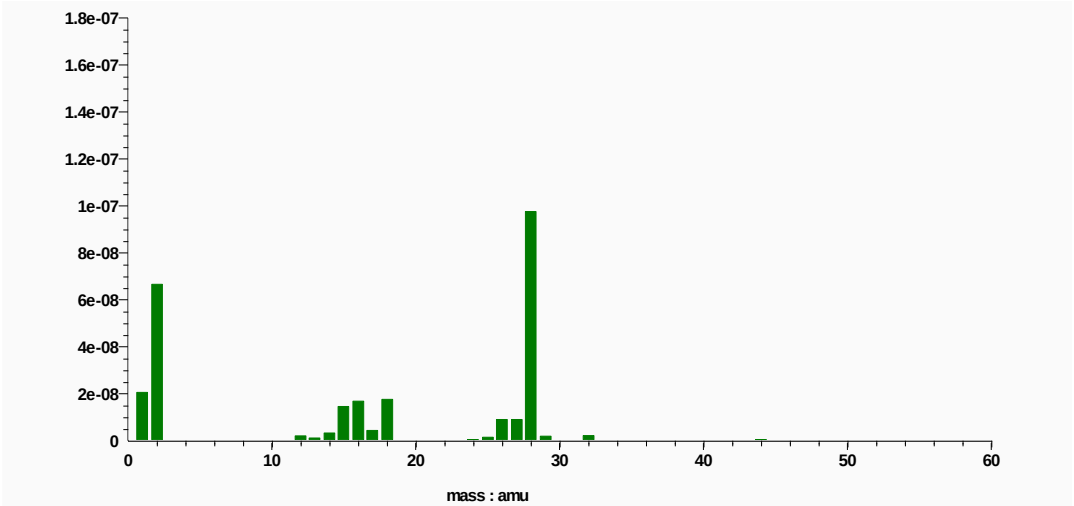

Figure 7.11 Mass spectrum of non-condensable volatiles during the tail-off shoulder region during PET1.0G degradation by TVA.

During polymer and composite degradation carbon monoxide was the predominant non-condensable volatile, in addition to traces of small organic molecules such as methane, ethylene and acetylene. Hydrogen and water were at background levels throughout. Within the post-degradation region (where peak separation occurred), organic volatiles were observed to increase, and were accompanied by a decrease in carbon monoxide evolution. Peaks which also may be attributed to ethylene and acetylene were observed at 26 and 27 atomic mass units, and were considered minor products detected in the latter stages of degradation. The shoulder within the composites was specifically attributed to these minor organics. It is noted that ethylene and acetylene are both condensable at cryogenic temperatures and theoretically should not have been detected with non-condensable volatiles such as methane and carbon monoxide. Cryogenic trapping however is not 100% effective in removing condensable volatile species, especially those at low concentrations or at low boiling points.[3] As suspected from the pressure measurements, it is likely the nanoclay physically slows the transport of the organics out of the degrading polymer rather than through a chemical influence. Finally, as both the polymer and composites produced identical volatile materials on degradation, it was concluded the primary degradation pathways of PET were not altered due to the presence of the nanoclay.

Table 7.6 Observed non-condensable volatiles and respective spectral peak masses.

Non-condensable volatile	Mass / amu
H_2	1,2
CO	12,16,28,29
CH_4	12,13,14,15,16
C_2H_2	24,25,26,27
C_2H_4	24,25,26,27,28,29

Table 7.7 Observed non-condensable volatiles during polymer and polymer composite degradation. x indicates the volatile has been observed.

Material	Sample	Non-condensable volatiles				
		H_2	CO	CH_4	C_2H_2	C_2H_4
Amorphous Chip	PET	x	x	x	x	x
	PET0.5G	x	x	x	x	x
	PET1.0G	x	x	x	x	x
Uniaxial Film	PET	x	x	x	x	x
	PET0.5G	x	x	x	x	x
	PET1.0G	x	x	x	x	x

7.1.3.2 ANALYSIS OF CONDENSABLE VOLATILES

Sub-ambient thermal volatilisation analysis (SATVA) has been described in detail within Chapter 2. In summary, during the degradation of a polymer both condensable and non-condensable volatiles are evolved. Those which are non-condensable at cryogenic temperatures are detected in real time by the mass spectrometer. Condensable volatiles are cryogenically trapped and analysed in fractions during a controlled heating regime post-degradation. Analysis of the condensable degradation products is commonly more complex than the non-condensable products due to the variety of higher molar mass degradation products.

7.1.3.2.1 PRESSURE MEASUREMENTS

Typical pressure measurements for the polymer and composite sub-ambient runs can be observed within figure 7.12. All samples possessed four main product fractions collected within the following temperature ranges -154ºC to -110ºC, -110 ºC to -85ºC, -85ºC to -55ºC and -55ºC to +40ºC. Fractions 1 and 2 are observed to be the major condensable products, with the heavier fractions formed in minor quantities. Peak overlap prohibited an accurate integration and hence comparison of fractions between samples. Inspection of the maximum observed pressures for the major products however does indicate that in general the ratios of fraction 1 to fraction 2 differ between the polymer and composites within the uniaxial film samples. Within the polymer, fraction 1 is the dominant non-condensable volatile, however within the composites fraction 2 is dominant. This indicates that the nanoclay alters the degradative pathway of poly(ethylene terephthalate) in some manner, driving the production of the products contained within fraction 2.

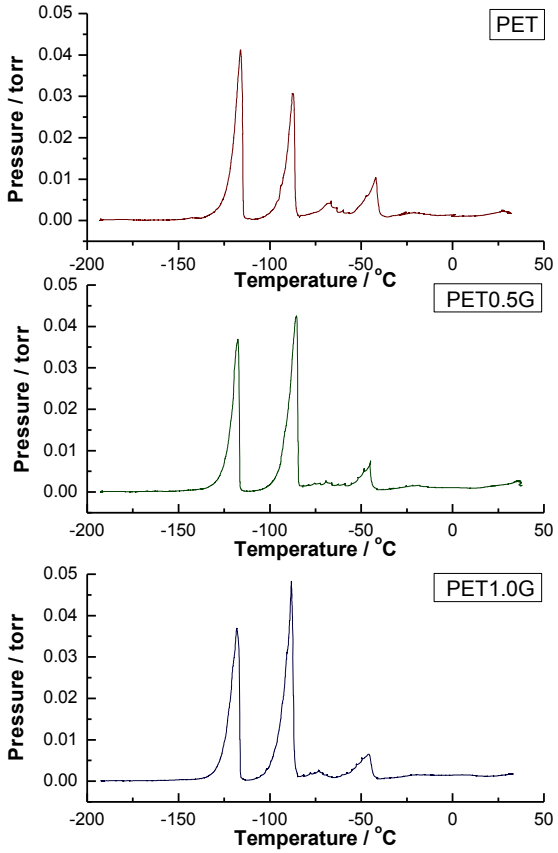

Figure 7.12 Pressure measurements during the subambient TVA run of PET, PET0.5G and PET1.0G uniaxial film. The subambient run is performed under a 4ºC min^{-1} heating rate from -196 ºC to +40 ºC.

Table 7.8 Maximum observed pressures for condensable fractions 1 and 2 during the SATVA run.

Material	Sample	Replicate	P_{max} / torr	
			Fraction 1	Fraction 2
Amorphous Chip	PET	1	0.0161	0.0195
		2	0.0228	0.0271
		Average	0.0195	0.0233
	PET0.5G	1	0.0226	0.0449
		2	0.0286	0.0432
		Average	0.0256	0.0441
	PET1.0G	1	0.0640	0.0548
		2	0.0321	0.0413
		Average	0.0481	0.0481
Uniaxial Film	PET	1	0.0414	0.0307
		2	0.0317	0.0296
		Average	0.0366	0.0302
	PET0.5G	1	0.0371	0.0427
		2	0.0327	0.0433
		Average	0.0349	0.043
	PET1.0G	1	0.0372	0.0433
		2	0.0326	0.0476
		Average	0.0349	0.0455

7.1.3.2.2 MASS SPECTROMETRY

The degradation products which were condensable at cryogenic temperatures were consistent throughout both the polymer and composite samples, and uniaxial film and chip samples. As previously stated all samples consisted of four primary fractions. The primary volatile in fraction 1 was carbon dioxide, in addition to traces of small organics such as methane, ethylene, acetylene, propene, carbon monoxide and water.

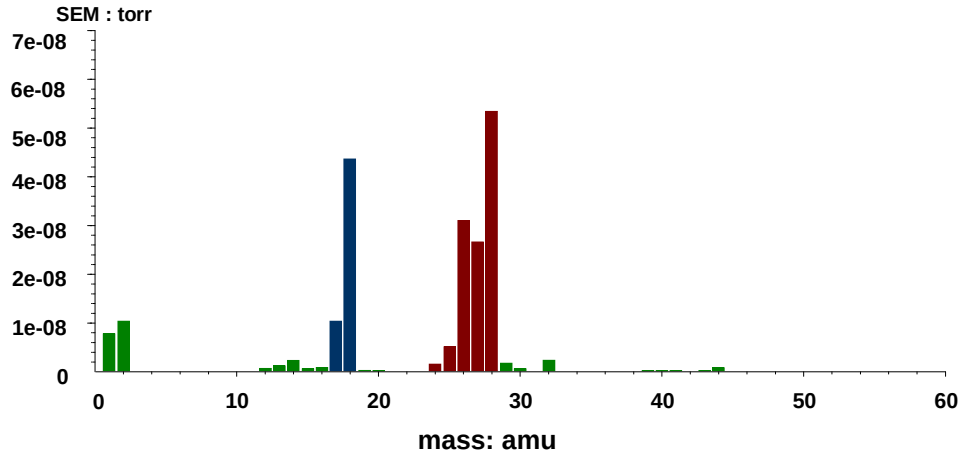

Figure 7.13 Mass spectrum illustrating the presence of water and ethene within fraction 1. Water and ethene are represented by blue and red bars respectively.

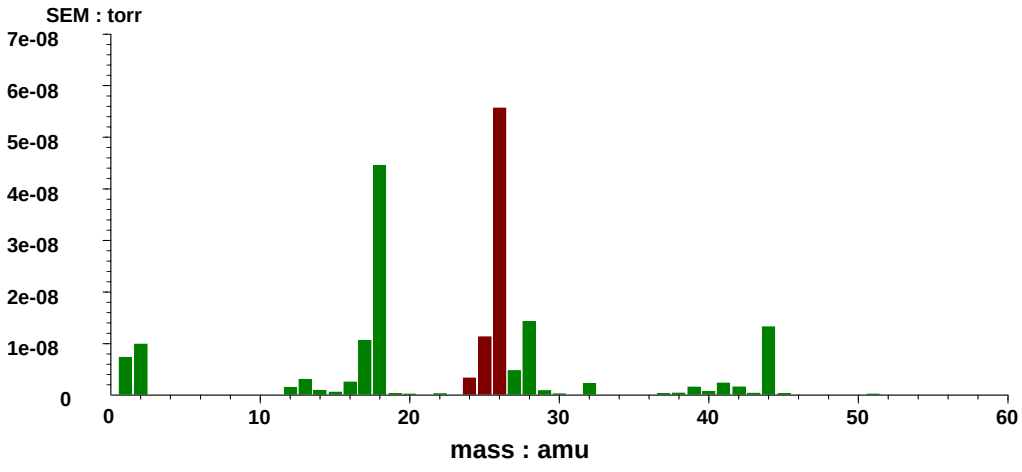

Figure 7.14 Mass spectrum illustrating the presence of acetylene within fraction 1. Acetylene is represented by the red bars.

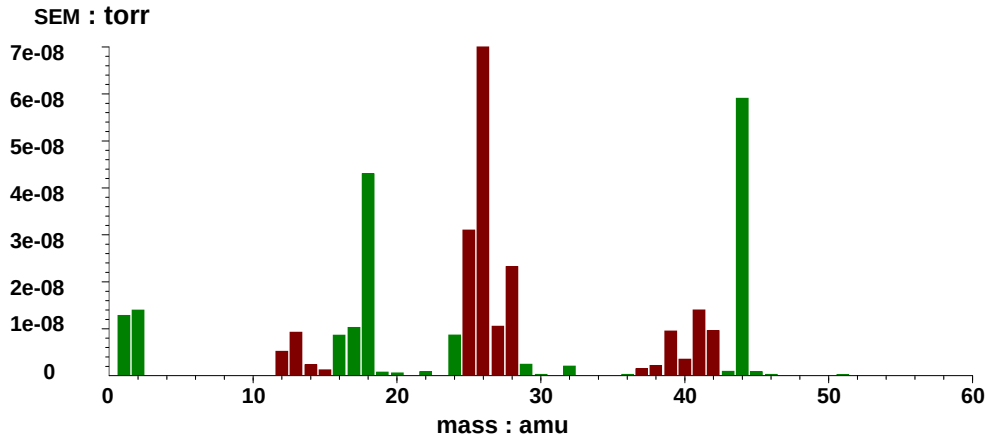

Figure 7.15 Mass spectrum illustrating the presence of propene within fraction 1. Propene is represented by the red bars.

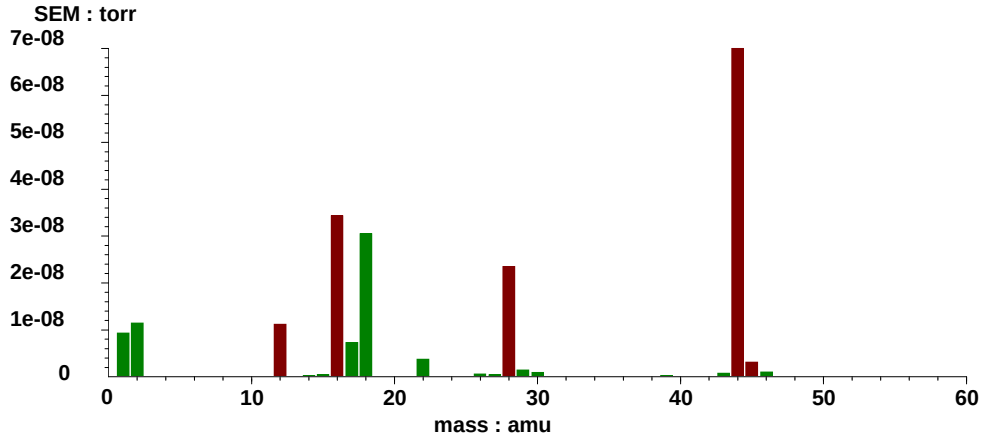

Figure 7.16 Mass spectrum illustrating the presence of carbon dioxide within fraction 1. Carbon dioxide is represented by the red bars.

Fraction 2 consisted of acetaldehyde and was identified primarily through the major primary peaks observed at 15, 29 and 44 atomic mass units. It may now be concluded that the presence of the nanoclay preferentially drives the production of acetaldehyde, however this will be discussed further within section 7.3. Fractions 3 and 4 consisted predominantly of water and benzaldehyde, respectively, in addition to various aromatic volatiles. Due to significant peak overlap at the lower masses, the detection of the aromatic materials was primarily achieved through the identification of prominent and characteristic high mass peaks. Peaks highlighted in mass spectra relating to aromatic volatiles are therefore not expected to originate exclusively with the identified product at the lower masses. Evidence for aromatics such as furan, benzene, toluene and trace amounts of styrene have been observed in the following figures.

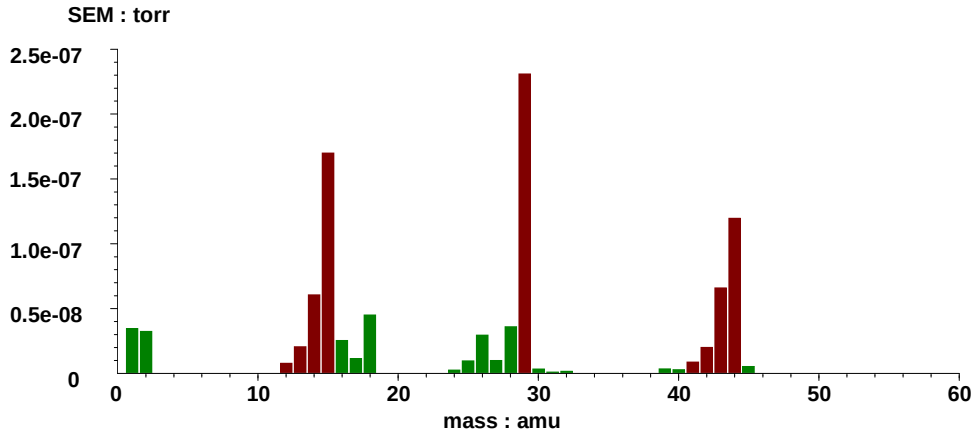

Figure 7.17 Mass spectrum illustrating the presence of acetaldehyde within fraction 2. Acetaldehyde is represented by the red bars.

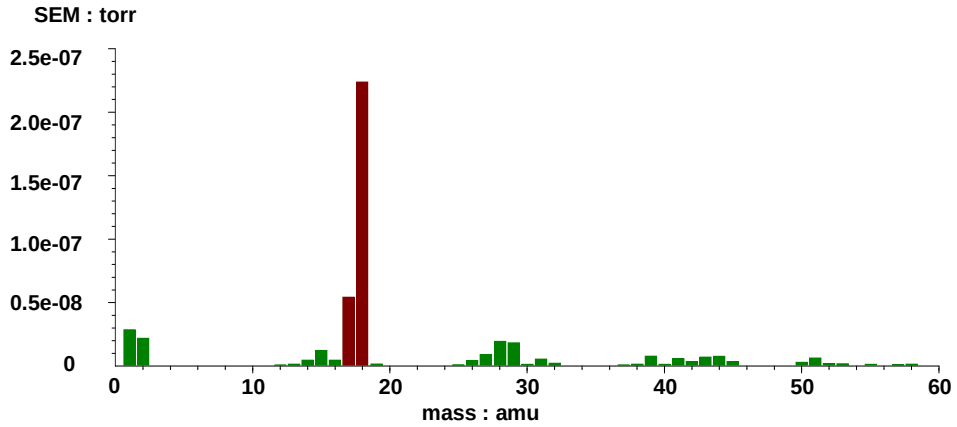

Figure 7.18 Mass spectrum illustrating the presence of water within fraction 3. Water is represented by the red bars.

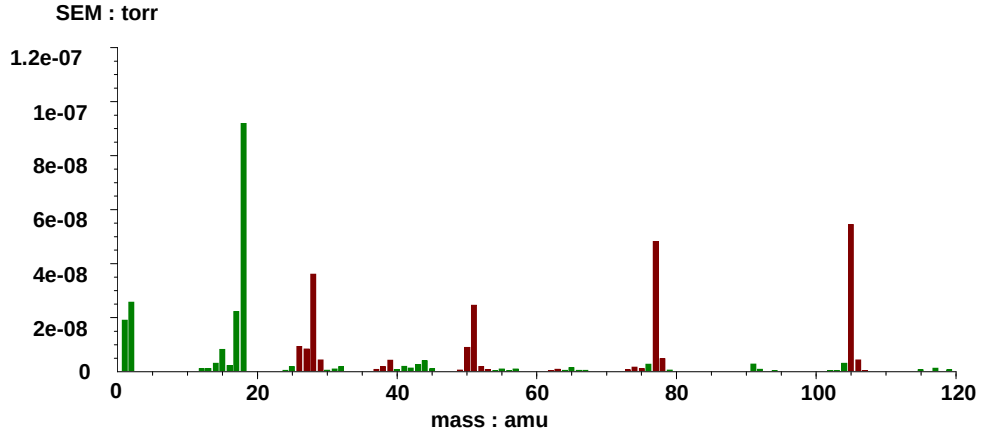

Figure 7.19 Mass spectrum illustrating the presence of benzaldehyde within fraction 4. Benzaldehyde is represented by the red bars.

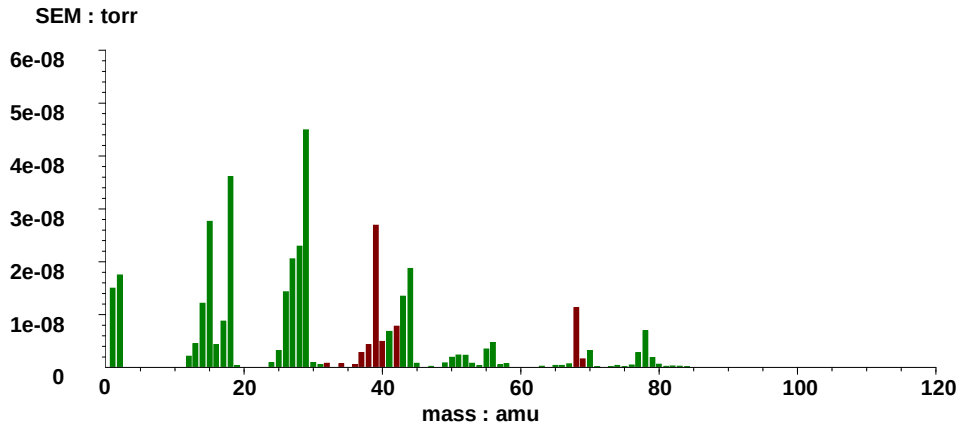

Figure 7.20 Mass spectrum illustrating the presence of furan within fraction 3/4. Furan is represented by the red bars. Major peaks are at 39 amu and 68 amu, in addition the minor and trace peaks are present at the expected ratios.

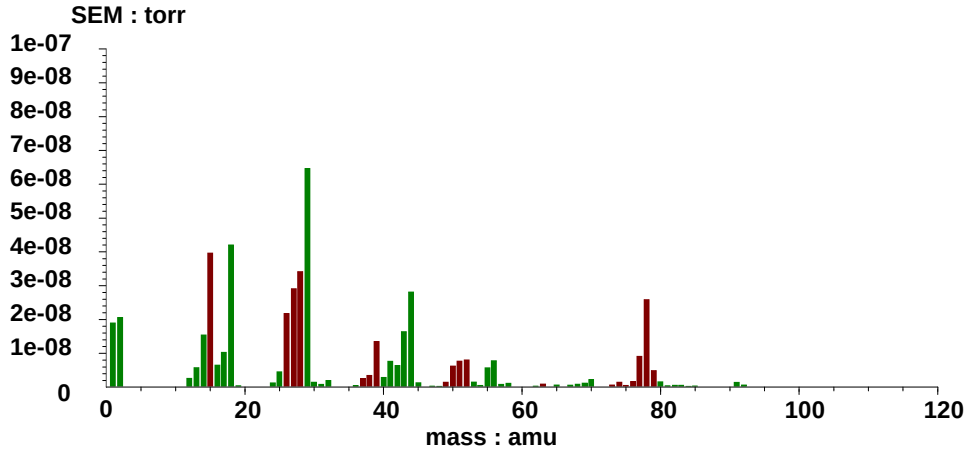

Figure 7.21 Mass spectrum illustrating the presence of benzene within fraction 3/4. Benzene is represented by the red bars. Major peaks are at 77-78 amu, and additional expected peaks are present at 49-52 amu and 36-38 amu.

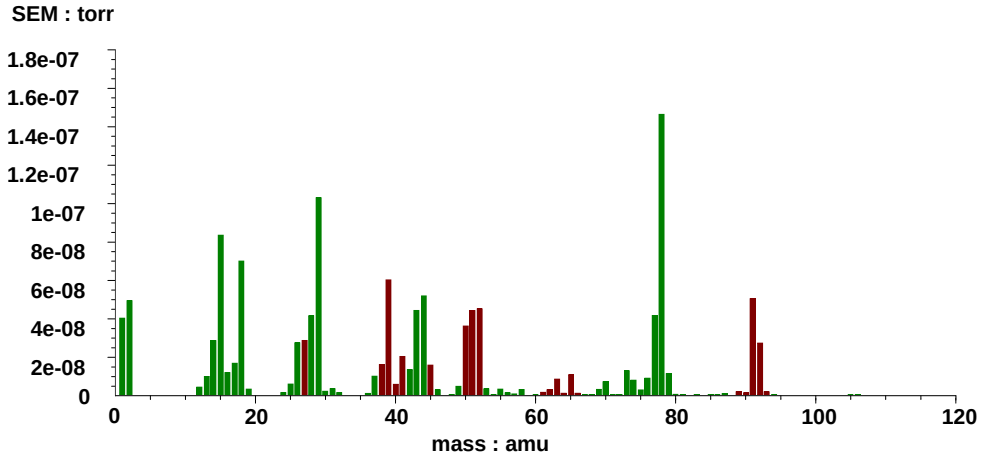

Figure 7.22 Mass spectrum illustrating the presence of toluene within fraction 3/4. Toluene is represented by the red bars. Major peaks are at 91-92 amu, and additional expected peaks are present at 61-66 amu, 51-53 amu and 38-41 amu.

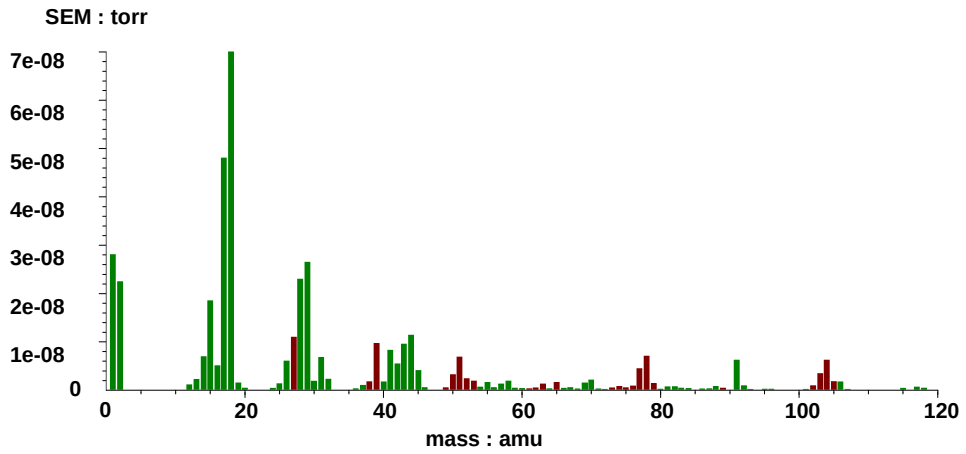

Figure 7.23 Mass spectrum illustrating the presence of styrene within fraction 3/4. Styrene is present in trace amounts and its' presence is arguable. Peak ratios between 102-105 amu and ratios also between 78 amu and 104 amu however in the authors' opinion strongly indicate the presence of styrene.

Fraction 4 contains the highest molar mass molecules and hence most complex molecular structures and fragmentation patterns. It is therefore extremely difficult to characterise mixtures of minor/trace volatiles. Figure 7.23 contains mass spectral data during the later stages of volatile evolution from fraction 4. Particular attention is paid to spectral peaks between 115 amu and 123 amu. Although their identity cannot be confirmed conclusively, it is clear they are substituted aromatics. Potential degradation products are 1-methyl, 2-vinylbenzene, 2-hydroxy benzaldehyde and/or benzoic acid. See table 7.9. The final and largest product which could be identified within fraction 4 was biphenyl, see figure 7.24.

Table 7.9 Potential degradation products relating to mass spectral peaks between 115 amu and 123 amu.

Degradation product	**Molar mass / amu**	**Structure**	**High amu mass spectral peaks** (underline denotes major peaks)
1-methyl, 2-vinylbenzene	118	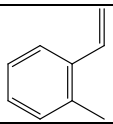	115, 116, 117, 118, 119 102, 103, 105 86, 87, 89, 90, 91, 92
2-hydroxy benzaldehyde	122	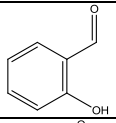	121, 122, 123 105, 106 92, 93, 94
Benzoic acid	122	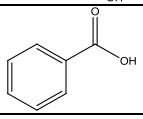	122, 123 105, 106

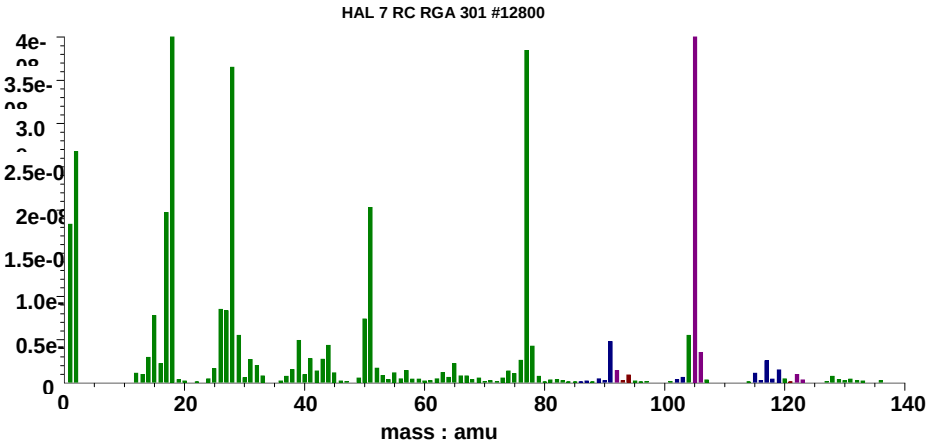

Figure 7.24 Mass spectrum of potential substituted aromatic degradation products. The red bars represent 1-methyl, 2-vinyl benzene, the blue bars represent 2-hydroxy benzaldehyde and the purple represent benzoic acid and overlap peaks of the previous two aromatic products.

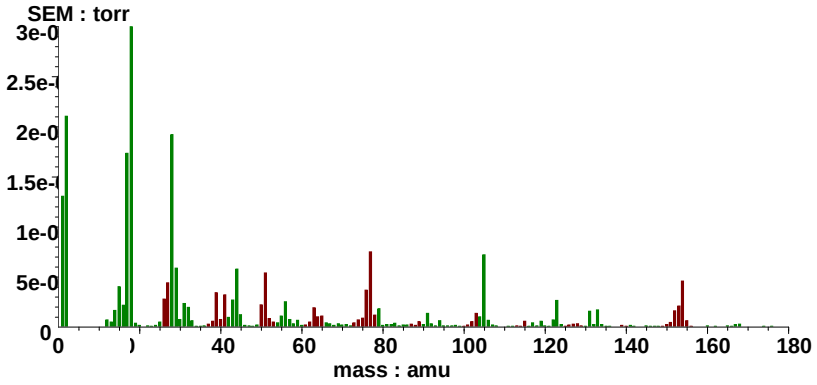

Figure 7.25 Mass spectrum of illustrating the presence of biphenyl within fraction 4. Biphenyl is represented by the red bars.

7.1.3.2.3 FOURIER TRANSFORM INFRARED SPECTRSCOPY

Infrared spectroscopy was performed on each fraction collected after mass spectroscopy allowing direct comparison and to an extent the corroboration of degradation products. Spectra were comparable throughout; therefore only one set of spectra has been included. Additional spectra can be found within the appendices.

Within fraction 1 carbon dioxide was the predominant product, observed at approximately 2350 cm^{-1}. A significant volume of hydrogen bonded hydroxyl groups

were also present within the spectra originating from PET, however these were less evident within the composite fractions. In addition, bands and stretches relating to alkyl and aromatic species were observed. Methyl and methylene stretching was observed at 2920 cm^{-1} to 2850 cm^{-1}. Bands within the fingerprint region, specifically mono- and *para*-substituted aromatics were observed at low frequencies. The presence of alkyl and aromatic species are therefore evident within fraction 1, however carbon dioxide is dominant. The alkyl material can most likely be attributed to trace quantities of acetaldehyde and other small organics, however to the author's knowledge the presence of alkyls and aromatic material has not previously been reported within fraction 1 during the degradation of poly(ethylene terephthalate).

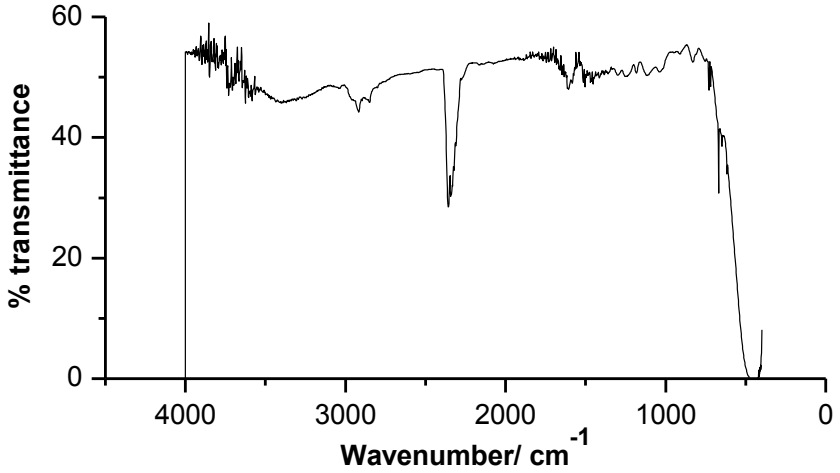

Figure 7.26 FTIR spectrum of fraction 1 during PET1.0G uniaxial film degradation.

Fraction 2 consisted primarily of acetaldehyde, confirmed through C=O stretches associated with a saturated aliphatic aldehyde at 1768 cm^{-1}, aliphatic C-H stretches between 2920 - 2730 cm^{-1}, anti-symmetric C-H rocking at 1417 cm^{-1} and 1370 cm^{-1} and C-H deformations at 918 cm^{-1}. In addition, CO-O bending at 1120 cm^{-1} and C-O stretching at 1100 cm^{-1} relating to acidic groups are also observed, suggesting more complex degradation products are present than solely acetaldehyde.

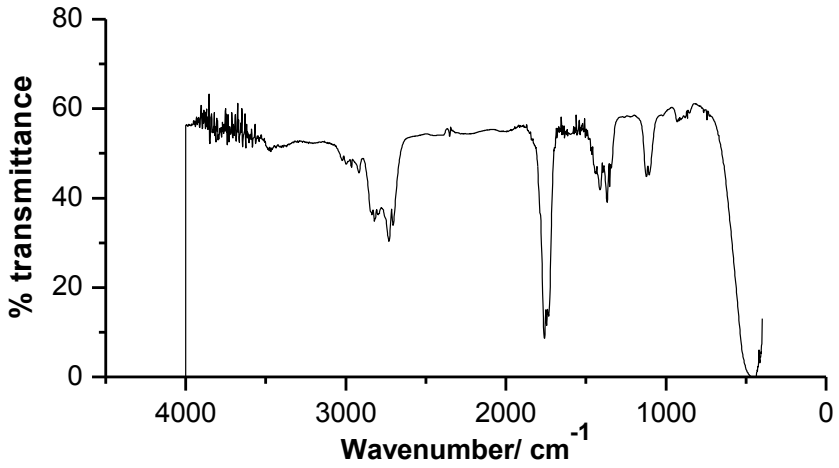

Figure 7.27 FTIR spectrum of fraction 2 during PET1.0G uniaxial film degradation.

Fraction 3 possessed the weakest set of bands. This was expected due to the low pressure measurements taken during the SATVA run. Evidence of aliphatic, aldehydic and aromatic stretching was observed at 2915 - 2945 cm^{-1}, 2735 cm^{-1} and 1750 cm^{-1}, and 1595 cm^{-1}, respectively. In addition weak CO-O bending at 1125 cm^{-1} and aromatic C-H out-of-plane deformations at 930 cm^{-1} were observed. Water was observed as a primary product within this fraction through mass spectrometry, however little evidence of water was observed within the FTIR spectra. Due to the low intensity of the peaks little more can be taken from fraction 3 other than confirmation of the presence of aromatic-based degradation products.

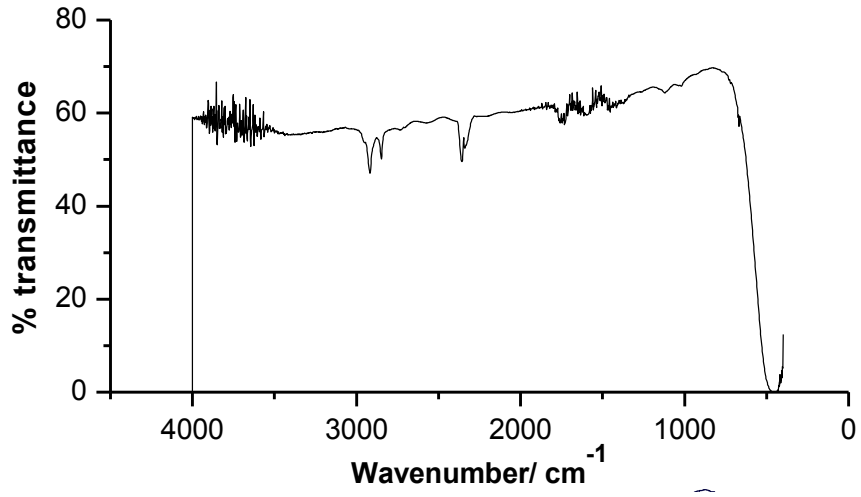

Figure 7.28 FTIR spectrum of fraction 3 during PET0.5G uniaxial film degradation.

Fraction 4 contained the highest molar mass species. Benzaldehyde was identified through the presence of aldehydic stretches, aromatic skeletal stretches and aromatic C-H deformations. Additional aliphatic bands, alkyl C-H deformations and bands relating to weakly hydrogen bonded hydroxyl groups were observed, indicating high molar mass and more complex aromatic degradation products.

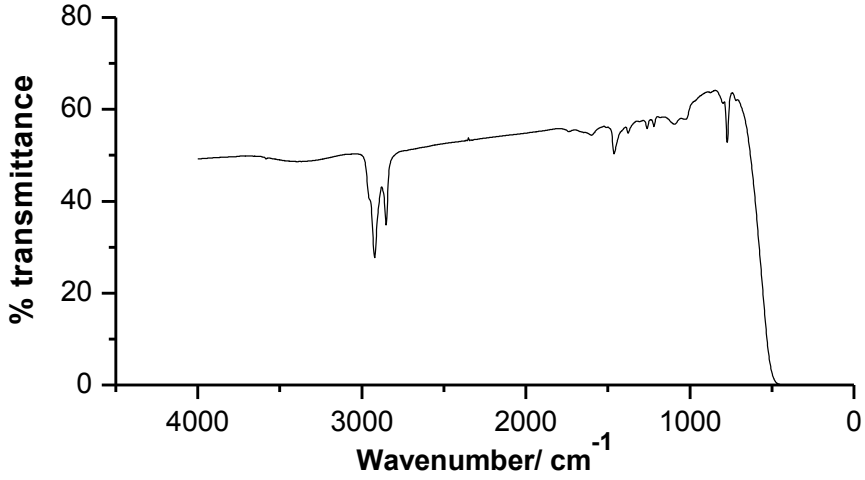

Figure 7.29 FTIR spectrum of fraction 4 during PET1.0G uniaxial film degradation.

7.1.3.2.4 GAS CHROMATOGRAPHY MASS SPECTROMETRY

Fraction 4 contained higher molar mass species and was therefore able to condense into chloroform and be analysed by GCMS, however very little information on the higher molar mass by-products was obtained. The majority of peaks were either unidentifiable or attributed to column degradation products. In addition, by-products which were

identified were identified with an extremely low probability, and therefore even their detection is questionable.

Hex-1-enyl benzene was identified in both the polymer and composite samples at a retention time of 9.66 to 9.77 minutes and probability of between 22.64 and 30.88%. Cyclohexylbenzene and a conjugated aromatic system were also detected at retention times of 9.71 and 18.95 minutes, and probabilities of 11.39% and 7.11%, respectively. Although the probabilities for cyclohexylbenzene were low, the mass spectra do indicate an aromatic moiety within the degradation product. In addition the chromatograms within appendix 5 also indicate PET contains the largest amount of high molar mass material. The composites appear to produce a lower amount of high molar mass degradation products, and this may be attributed to the catalytic effect of the nanoclay. All additional peaks within the PET chromatograms and those of the composites however were unidentifiable. The majority of library 'matches' contained conjugated alkenes or alkyl ring systems, and so in the least some indication of the structural characteristics can be taken from GC-MS analysis.

7.1.3.3 ANALYSIS OF COLD RING FRACTION

7.1.3.3.1 GAS CHROMATOGRAPHY MASS SPECTROSCOPY

The cold ring fraction contained the highest molar mass volatiles which condensed under tap water temperatures, usually between 5ºC and 15ºC. No identifiable products were observed however during analysis, and the chromatogram was visually consistent with that of a standard chloroform run.

7.1.4 THERMAL DEGRADATION KINETICS

The degradation kinetics of polymer systems are most easily determined through a loss in mass or the energetic flow in and out of a system during degradation. Classical models are those of Arrhenius and Kissinger, however American Standard Test Methods (ASTM) offer a more contemporary means of calculating the Arrhenius parameters. Both classical and contemporary methods will be examined. Examples of

data treatment and full sets of numerical results are included in the following section for each particular model, however the interpretation of data will be contained in section 7.1.4.3.

7.1.4.1 GRAVIMETRIC KINETICS MODELS

7.1.4.1.1 ARRHENIUS MODEL

7.1.4.1.1.1 SELECTION OF ISOTHERMAL TEMPERATURES

Initially, dynamic TGA runs were performed in order to select the appropriate temperatures for isothermal measurements. Figure 7.30 contains the dynamic thermal analysis for the polymer and composites.

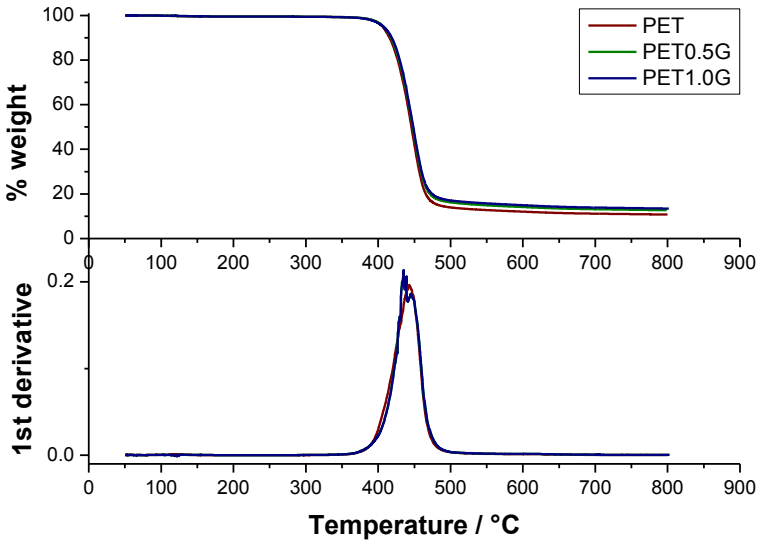

Figure 7.30 Dynamic, non-oxidative degradation TGA plots for PET, PET0.5G and PET1.0G uniaxial film. Analysis was performed under helium at a heating rate of 10ºC min^{-1}.

The isothermal temperature range selected for study was 390ºC to 420ºC, over 10ºC increments. This incorporated the onset of mass loss until the maximum rate of loss was reached. The narrow temperature range would also to some degree limit the influence of any competing degradation mechanisms, potentially complicating the kinetics.

7.1.4.1.1.2 ARRHENIUS MODEL

The Arrhenius model is a classical model which may be employed to examine degradation within an isothermal degradation process assuming zero order kinetics. The maximum observed gradient over a plot of % mass against time equates to – k (– reaction rate), at a specific degradation temperature. An Arrhenius plot of lnk against 1/T provides a gradient of $-E_a/R$ and y-intercept lnA. Replicate k values were averaged prior to the Arrhenius plot to increase accuracy in calculated E_a and lnA values.

Figure 7.31 is an example isothermal plot of PET uniaxial film at temperatures between 390ºC and 420ºC. All additional duplicates may be found in appendix 5. The linear region of the plots with the steepest gradient represented the maximum degradation rate in relation to mass loss. This region varied depending upon the isothermal temperature; the higher the hold temperature the faster mass loss and hence degradation. A 10ºC range was therefore selected depending on the isothermal temperature. The region of maximum mass loss is graphed within figure 7.32.

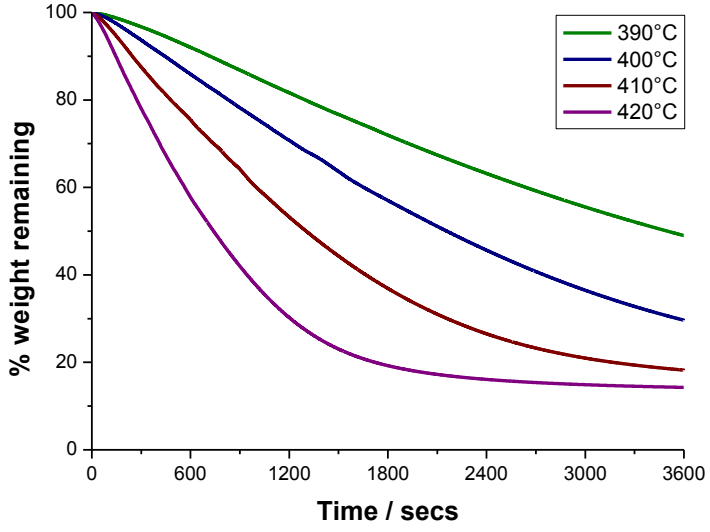

Figure 7.31 Isothermal degradation plots for PET uniaxial film between 390ºC and 420ºC. The isothermal was held for 1 hour. Analysis was performed under helium.

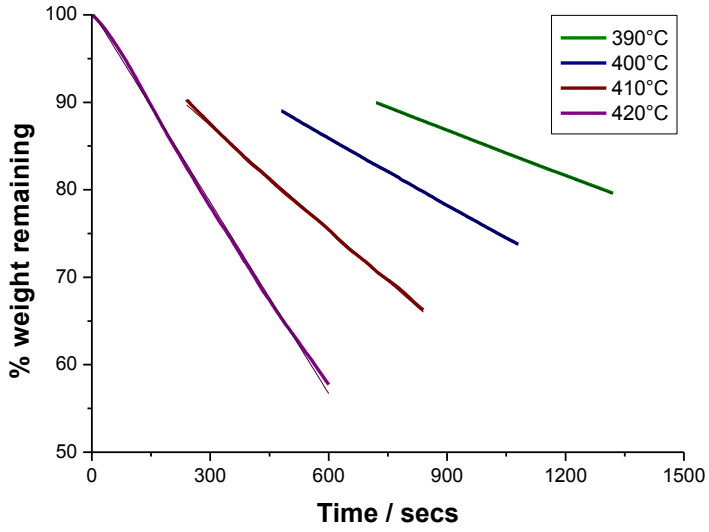

Figure 7.32 Regions of maximum rate of mass loss during the isothermal degradation plots for PET uniaxial film between 390ºC and 420ºC. Analysis was performed under helium. Linear fittings were also performed.

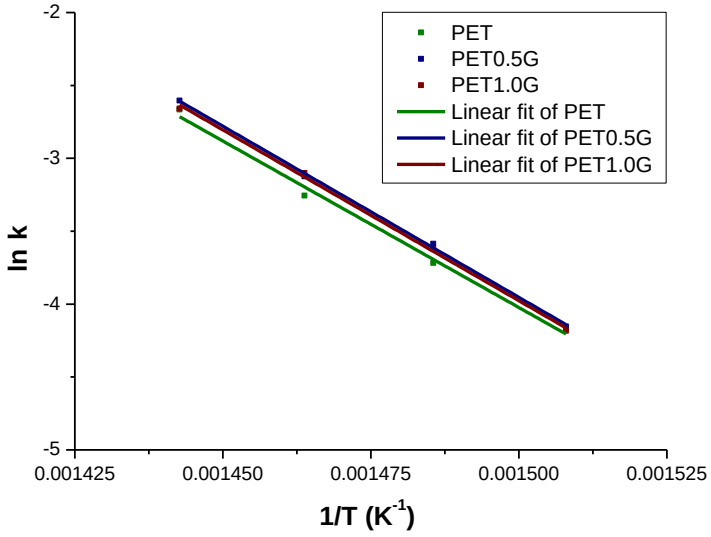

Figure 7.33 Arrhenius plot for PET, PET0.5G and PET1.0G uniaxial film.

Figure 7.33 contains the Arrhenius plot of lnk against 1/T. The Arrhenius factors were extracted from the plot data and presented within table 7.10. k at a temperature of 700K was calculated via equation 7.1; the Arrhenius equation.

$$k = A\exp\left(-\frac{E_A}{RT}\right) \qquad \text{Equation 7.1}$$

Table 7.10 Calculated Arrhenius parameters during thermal degradation of PET, PET0.5G and PET1.0G uniaxial film. k represents the rate constant at 700K.

Sample	m	Ea / kJ mol^{-1}	lnA	k / s^{-1}
PET	-2.2 x 10^4	185.5 ± 2.3	29.5 ± 2.4	3.9 x 10^{-2}
PET0.5G	-2.4 x 10^4	199.2 ± 1.2	31.9 ± 0.2	4.3 x 10^{-2}
PET1.0G	-2.3 x 10^4	194.5 ± 3.8	31.2 ± 0.7	4.3 x 10^{-2}

7.1.4.1.2 AMERICAN STANDARD TEST METHOD E1641

ASTM 1641 is a contemporary method for determining the Arrhenius parameters from dynamic thermogravimetric analysis runs, and possesses similarities with the Flynn, Wall and Ozawa methods.[4, 5] It has been described as a more efficient method for analysis as the degree of conversion during degradation is employed as the basis for comparison, as opposed to the maximum peak temperature which may not equate to the maximum degradation rate. Initially, samples are subjected to heating rates between 1ºC min^{-1} and 20ºC min^{-1} and the maximum peak temperatures are determined. The thermal degradation plots from which the temperatures were extracted may be found within section 7.1 and appendix 6. The natural logarithms of the heating rates are then plotted against the reciprocal of the maximum peak temperature at various degrees of conversion, α, and linear data fitting is applied.

Figure 7.34 contains a conversion plot for the thermal degradation of PET0.5G uniaxial film. Conversions between 0.01 (1%) and 0.40 (40%) were examined in order to determine the period where there is a constant degradation rate. A constant and maximum rate is assumed when the gradients are comparable, for example in this particular case between a 0.10 and 0.20 conversion.

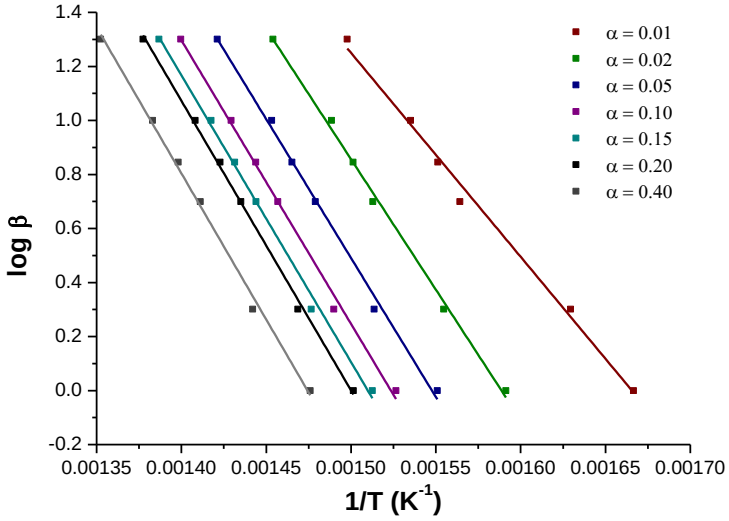

Figure 7.34 Conversion plot for PET0.5G uniaxial film. Conversion factors between 0.01 (1%) and 0.40 (40%) have been included. The gradients for the linear data fittings are contained in table 7.11.

Table 7.11 Gradients (Δ(log β)/Δ(1/T)) for the linear data fittings in figure 7.34.

α	**Δ(log β)/Δ(1/T)**
0.01	-6447
0.02	-9502
0.05	-10276
0.10	-10585
0.15	-10628
0.20	-10690
0.40	-10855

To ensure consistency a constant conversion factor was employed throughout the samples under study. Conversion plots of duplicate samples and the additional polymer and composite samples were also examined and these plots may be found in appendix 6. A conversion of 0.15 was selected and experimental temperatures at this conversion were noted, see table 7.12.

Table 7.12 Gradients **(**Δ(log β)/Δ(1/T)) and temperatures relating to a 0.15 conversion during thermal degradation. The average error is obtained through Origin software and is with respect to linearity of data within the line fitting process.

Material	**Sample**	**Δ(log β)/Δ(1/T)**				**Temperature / K**		
		1	**2**	**Average**	**Average Error**	**1**	**2**	**Average**
Amorphous Chip	PET	-11301	-10254	-10778	± 413	694.27	693.53	693.90
	PET0.5G	-10828	-10471	-10649	± 174	692.02	690.87	691.45
	PET1.0G	-10556	-11423	-10990	± 165	692.85	691.81	692.33
Uniaxial Film	PET	-10579	-11001	-10790	± 288	690.01	691.10	690.56
	PET0.5G	-10638	-10619	-10628	± 302	693.31	692.49	692.90
	PET1.0G	-11109	-11082	-11095	± 145	689.57	688.77	689.17

The gradient, $\Delta(\log\beta)/\Delta(1/T)$, was then employed in iterative calculations which initially estimated the activation energy via equation 7.2, and then refined using equation 7.3, where R is the universal gas constant (8.314 J K^{-1} mol^{-1}) and b is an approximation constant. The activation energy was described as suitably refined when the variability between the calculated activation energies was less than 1%, at which point it was denoted E_r. The pre-exponential factor can then be calculated via equation 7.4 through employing the refined activation energy, β' which is the heating rate at the midpoint of the experimental heating rates under study, and a second approximation constant, a. The reaction rate may then be calculated through the Arrhenius equation. The Arrhenius parameters derived from this method are contained within table 7.13.

$$E_{approx} \cong -(R/0.457) * \Delta(\log\beta)/\Delta(1/T) \qquad \text{Equation 7.2}$$

$$E = -(R/b) * \Delta(\log\beta)/\Delta(1/T) \qquad \text{Equation 7.3}$$

$$A = -(\beta'/E_r) * R * \ln(1-\alpha) * 10^a \qquad \text{Equation 7.4}$$

Nota bene. A table of the approximation constants employed within this method may be found within appendix 6. .

Table 7.13 Arrhenius parameters for thermal degradation calculated through employing the ASTM 1641 model.

Material	Sample	E_{approx} / kJ mol^{-1}	E_r / kJ mol^{-1}	lnA	k / s^{-1}
Amorphous Chip	PET	196.1	195.2	30.8	6.7 x 10^{-2}
	PET0.5G	193.7	199.1	31.9	6.7 x 10^{-2}
	PET1.0G	199.9	192.9	30.8	1.0 x 10^{-1}
Uniaxial Film	PET	196.3	195.4	30.8	6.4 x 10^{-2}
	PET0.5G	193.4	191.7	29.8	4.3 x 10^{-2}
	PET1.0G	201.9	201.0	31.9	6.9 x 10^{-2}

7.1.4.2 ENERGETIC (DSC) KINETICS MODELS

7.1.4.2.1 KISSINGER MODEL

The Kissinger model is a classical method which was initially developed to allow the calculation of activation energies within dynamic degradation processes. The Kissinger

model was employed for the reasons outlined in the instrumental chapter. Kissinger plots are generated of $\ln(q/T_{max}^2)$ against $1/T_{max}$ through various heating rates. Linear data fitting then provides the activation energy in the form $-E_a/R$ from the gradient and the lnA value from the y-intercept. Tables 7.14 – 7.16 contain the DSC data required to graph the Kissinger plot, figure 7.35 of $\ln(q/T_{max}^2)$ against $1/T_{max}$.

Table 7.14 Kissinger data for degradation of PET degradation subjected to various heating rates.

Heating Rate/K min^{-1}	Temperature / K			$1/T_{max}$ / K^{-1}	$\ln(q/T_{max}^2)$
	1	2	Average		
1	672.71	676.22	674.47	1.48 x 10^{-3}	-13.03
2	694.35	692.07	693.21	1.44 x 10^{-3}	-12.39
5	704.98	692.01	698.50	1.43 x 10^{-3}	-11.49
7	707.10	701.81	704.46	1.42 x 10^{-3}	-11.17
10	716.93	713.94	715.44	1.40 x 10^{-3}	-10.84
20	735.82	732.00	733.91	1.36 x 10^{-3}	-10.20

Table 7.15 Kissinger data for degradation of PET0.5G degradation subjected to various heating rates.

Heating Rate/K min^{-1}	Temperature / K			$1/T_{max}$ / K^{-1}	$\ln(q/T_{max}^2)$
	1	2	Average		
1	680.66	675.63	678.15	1.47 x 10^{-3}	-13.04
2	685.11	685.58	685.35	1.46 x 10^{-3}	-12.37
5	693.77	694.93	694.35	1.44 x 10^{-3}	-11.48
7	706.64	704.06	705.35	1.42 x 10^{-3}	-11.17
10	717.99	717.16	717.58	1.39 x 10^{-3}	-10.85
20	734.45	733.76	734.11	1.36 x 10^{-3}	-10.20

Table 7.16 Kissinger data for degradation of PET1.0G degradation subjected to various heating rates.

Heating Rate/K min^{-1}	Temperature / K			$1/T_{max}$ / K^{-1}	$\ln(q/T_{max}^2)$
	1	2	Average		
1	680.78	679.25	680.02	1.47 x 10^{-3}	-13.04
2	682.85	675.38	679.12	1.47 x 10^{-3}	-12.35
5	707.04	705.27	706.16	1.42 x 10^{-3}	-11.51
7	708.08	708.96	708.52	1.41 x 10^{-3}	-11.18
10	708.96	716.54	712.75	1.40 x 10^{-3}	-10.84
20	717.95	731.74	724.85	1.38 x 10^{-3}	-10.18

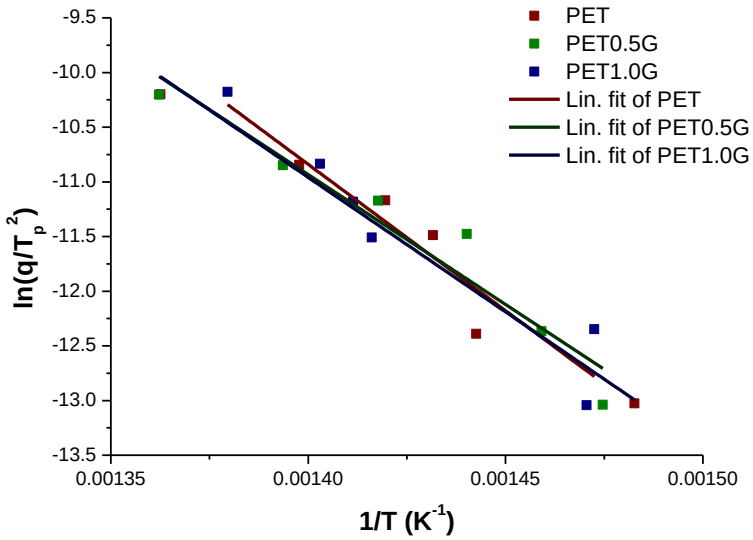

Figure 7.35 Kissinger plot for the thermal degradation of PET, PET0.5G and PET1.0G. Linear data fitting has been applied to each data set.

Table 7.17 contains the Arrhenius parameters. The activation energy was obtained by multiplying the gradient values by –R (gas constant) and lnA values required no manipulation and equated to the y-intercept. The reaction rate was determined for a temperature of 700 K. Although incorporation of the nanoclay appears to decrease the Arrhenius parameters of the composites in comparison to the polymer, the calculated values are comparable within error. The nanoclay can therefore be considered to not affect the degradation kinetics with regards to the Kissinger model.

Table 7.17 Arrhenius parameters for thermal degradation calculated through the Kissinger model. The error is obtained through Origin software and is with respect to linearity of data within the line fitting process.

Sample	Ea / kJ mol^{-1}	lnA	k / s^{-1}
PET	222.5 ± 31.3	38.6 ± 5.4	1.5
PET0.5G	197.5 ± 26.0	34.4 ± 4.5	1.6
PET1.0G	204.6 ± 25.5	35.1 ± 4.4	0.9

7.1.4.2.2 AMERICAN STANDARD TEST METHOD E698

ASTM E698 is a contemporary test method developed in order to examine the degradation behaviour in dynamic systems. It is similar to the previous contemporary method in the manner that the Arrhenius parameters are calculated.

Samples are subjected to heating rates between 1ºC min^{-1} and 20ºC min^{-1} in order to determine the variation in maximum peak temperatures. Plots of these dynamic heating runs may be found within section 7.1.2 and appendix 6. The natural logarithms of the heating rates are then plotted against 1/T for each particular system.

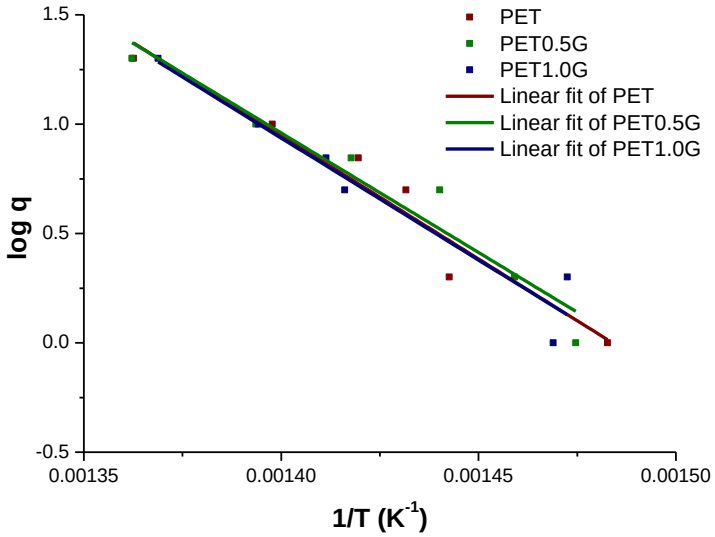

Figure 7.36 ASTM E698 plot for the thermal degradation of PET, PET0.5G and PET1.0G.

The gradient, $\Delta(\log \beta)/\Delta(1/T)$, is then employed in the estimation and then refinement of the activation energy, via an equations 7.5 and 7.6 respectively, and with an approximation constant, D, also employed in the latter. A table of approximation constants may be found within appendix 6. The pre-exponential factor and reaction rate may then also be calculated via equation 7.7 and the Arrhenius equation, respectively.

$$E_{approx} \approx -2.19R * \Delta(\log\beta)/\Delta(1/T) \qquad \text{Equation 7.5}$$

$$E = (-2.303R/D) * \Delta(\log\beta)/\Delta(1/T) \qquad \text{Equation 7.6}$$

$$A = \beta E e^{-Ea/RT} / (RT_m^2) \qquad \text{Equation 7.7}$$

$$k = Ae^{-Ea/RT} \qquad \text{Equation 7.8}$$

As in previous determinations of k, a temperature of 700 K was employed. It is noted that the approximate and refined values of E_a do not vary substantially.

Table 7.18 Arrhenius parameters for thermal degradation calculated using the ASTM E98 method. The refined activation energy, E_r, was achieved after three iterations.

Sample	E_{approx} / kJ mol^{-1}	E_r / kJ mol^{-1}	lnA	k / s^{-1}
PET chip	205.7	204.7	33.5	1.9 x 10^{-2}
PET0.5G chip	199.0	197.6	32.3	1.9 x 10^{-2}
PET1.0G chip	203.2	201.8	33.0	1.9 x 10^{-2}

7.1.4.3 COMPARISON OF KINETIC MODELS APPLIED TO THERMAL DEGRADATION

A comparison between chip and film materials illustrates there is no significant variation in the Arrhenius parameters for thermal degradation outwith experimental error; neither is there any significant distinction between the polymer and composite samples. The classical and contemporary gravimetric kinetics methods were observed to be reliable and comparable, especially with regards to the pre-exponential factor and reaction rate. Either method is therefore concluded suitable for the calculation of the Arrhenius parameters during thermal degradation.

Table 7.19 Comparison of Arrhenius parameters for the thermal degradation of chip and uniaxial films samples calculated using the ASTM 1641 model.

Material	Sample	E_r / kJ mol^{-1}	lnA	k / s^{-1}
Amorphous Chip	PET	195	30.8	6.7 x 10^{-2}
	PET0.5G	199	31.9	6.7 x 10^{-2}
	PET1.0G	193	30.8	1.0 x 10^{-1}
Uniaxial Film	PET	195	30.8	6.4 x 10^{-2}
	PET0.5G	192	29.8	4.3 x 10^{-2}
	PET1.0G	201	31.9	6.9 x 10^{-2}

Table 7.20 Comparison of Arrhenius parameters for thermal degradation calculated by the Arrhenius and ASTM 1641 gravimetric kinetic methods. The samples under study were uniaxial film.

Material	Sample	E_r / kJ mol^{-1}	lnA	k / s^{-1}
Arrhenius	PET	186	29.5	7.1 x 10^{-2}
	PET0.5G	199	31.9	7.1 x 10^{-2}
	PET1.0G	194	31.2	7.1 x 10^{-2}
ASTM 1641	PET	195	30.8	6.4 x 10^{-2}
	PET0.5G	192	29.8	4.3 x 10^{-2}
	PET1.0G	201	31.9	6.9 x 10^{-2}

Parameters calculated via energetic models were not as comparable as those from gravimetric models. The reaction rates varied for example between one and two orders of magnitude. The Kissinger model appeared to produce values higher than the other

models for lnA and k in particular, with the majority of the E_a values comparable with gravimetric values. As the reaction rate is extremely sensitive to variations in lnA and E_a, both of which are co-dependent, larger k values are therefore not unexpected. In contrast, the parameters obtained through employing the contemporary method were all extremely comparable to those obtained within the gravimetric models. It is concluded the classical model is therefore not as reliable when determining the Arrhenius parameters and the contemporary model is preferred. It should be noted however that DSC as an instrumental technique to characterise degradation is problematic. The identification of the onset of degradation and the maximum peak temperatures is often difficult due to the highly energetic nature of the degradation process, as can be illustrated through the previous thermograms in figures 7.2 – 7.4 and appendix 4.

Table 7.21 Comparison of Arrhenius parameters for thermal degradation calculated by the Kissinger and ASTM E698 energetic kinetic methods. The samples under study were chip material.

Material	Sample	E_r / kJ mol^{-1}	lnA	k / s^{-1}
Kissinger	PET	223	38.6	1.5
	PET0.5G	198	34.4	1.6
	PET1.0G	205	35.1	0.9
ASTM E698	PET	205	33.5	1.9×10^{-2}
	PET0.5G	198	32.3	1.9×10^{-2}
	PET1.0G	202	33.0	1.9×10^{-2}

7.2 THERMO-OXIDATIVE DEGRADATION

7.2.1 DYNAMIC TGA

Dynamic TGA provided insight into the mass loss behaviour of the polymer and composites during thermo-oxidative degradation. Various heating rates were examined in order to determine the effect of the nanoclay on thermal and oxidative diffusion, in addition to the nanoclays' impact on volatile loss during degradation. Precision between samples was determined as follows: ± 0.2 % for final mass percentages, ± 0.2 % for data relating to the integration of derivative curves and ± 2.7ºC for temperatures observed at the maximum degradation rate. Figure 7.37 illustrates the mass loss during degradation for PET uniaxial film under air, additional plots can be found within the appendices.

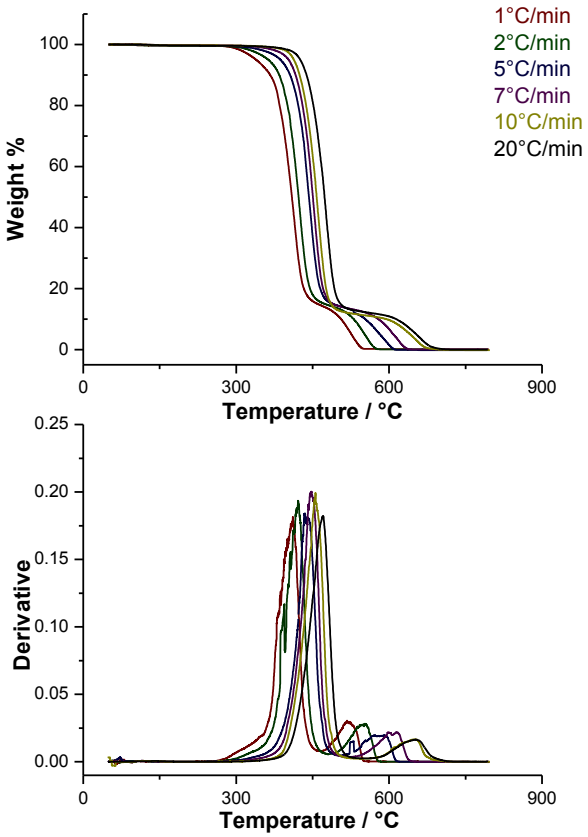

Figure 7.37 TGA thermogram for PET uniaxial film during thermo-oxidative degradation under air.

The thermo-oxidative degradation of the polymer and composites were observed to occur in two stages. The major degradation stage was attributed to the pyrolysis of the polymer backbone, whereas the later was due to the pyrolysis and oxidation of combustible material such as carbonaceous char to carbon dioxide.

Final % mass for the polymer and composite represented the non-oxidisable material present within the materials. Although the values were not strictly in line with the theoretical final values, they did reflect an increasing nanoclay content. Due to the overlapping of the main degradation process and the oxidation of carbonaceous char material the derivative areas could not be employed in the same manner as for thermal degradation.

The temperatures at maximum degradation were lower for the uniaxial film in comparison to the chip. This was due to a lower molar mass within the uniaxial film as a result of melt processing, which allowed a faster rate of oxygen diffusion. Composite samples were also observed to possess higher T_{max} values due to impedance of oxygen

diffusion by the nanoclay i.e. there was a barrier effect. It was noted the barrier effect within the uniaxial PET1.0G uniaxial film sample appeared to be counteracted as the heating rate increased. It is suggested that in addition to the inhibiting barrier effect the nanoclay possessed an accelerating catalytic effect on degradation. It is also suggested that this catalytic effect may only be substantial enough to be observed at loadings of 1.0% and over, and within lower molar mass samples such as the uniaxial films.

Table 7.22 Average final % masses for PET and PET composite uniaxial film and chip materials during thermo-oxidative degradation by TGA under air

Material	Sample	Replicate	Heating rate / ºC min^{-1}				Average
			2	5	7	10	
Amorphous Chip	PET	1	0.08	0.62	0.00	0.09	0.20
		2	0.00	0.10	0.18	0.00	0.07
		average	0.04	0.36	0.09	0.05	**0.13**
	PET0.5G	1	0.92	0.62	0.59	0.19	0.58
		2	0.81	0.65	0.53	0.16	0.54
		average	0.87	0.64	0.56	0.18	**0.56**
	PET1.0G	1	1.00	0.95	0.91	0.89	0.94
		2	1.30	0.94	0.65	0.83	0.93
		average	1.15	0.95	0.78	0.86	**0.93**
Uniaxial film	PET	1	0.00	0.00	0.00	0.00	0.00
		2	0.00	0.06	0.04	0.07	0.04
		average	0.00	0.03	0.02	0.04	**0.02**
	PET0.5G	1	0.39	0.32	0.37	0.27	0.34
		2	0.49	0.48	0.40	0.44	0.45
		average	0.44	0.40	0.39	0.36	**0.40**
	PET1.0G	1	0.75	0.75	0.72	0.61	0.71
		2	0.66	0.65	0.64	0.66	0.65
		average	0.71	0.70	0.68	0.64	**0.68**

Tables 7.23 Temperatures at the maximum degradation rate during thermo-oxidative TGA degradation of PET and PET composite chip and uniaxial film samples

Material	Sample	Replicate	Heating rate / ºC min^{-1}			
			2	**5**	**7**	**10**
Amorphous Chip	PET	1	427.55	443.69	453.03	464.63
		2	430.58	437.39	456.56	458.32
		average	429.07	440.54	454.80	461.48
	PET0.5G	1	434.61	454.79	458.83	466.90
		2	436.63	456.28	456.31	467.40
		average	435.62	455.54	457.57	467.15
	PET1.0G	1	440.16	458.07	467.40	469.67
		2	437.55	455.08	461.10	474.97
		average	438.86	456.58	464.25	472.32
Uniaxial film	PET	1	421.75	436.88	447.23	454.04
		2	424.15	435.62	450.34	456.22
		average	422.95	436.25	448.79	455.13
	PET0.5G	1	428.05	444.20	452.27	461.10
		2	428.56	448.23	449.50	462.11
		average	428.31	446.22	450.89	461.61
	PET1.0G	1	425.03	441.42	443.95	451.95
		2	427.25	440.16	449.50	456.31
		average	426.14	440.79	446.73	454.13

It was observed during thermo-oxidative degradation that a shoulder or additional peak emerged prior to the main degradation peak, and that this peak was not present in the equivalent thermally degraded sample. This was most notable within the lower heating rates and highest nanoclay loadings. During thermo-oxidative degradation lower heating rates will result in higher melt viscosities within the molten polymer, which will impede oxygen diffusion to a greater degree. Thermo-oxidative degradation will therefore be determined by the extent of oxygen diffusion throughout the polymer melt and it will only occur as far as the oxygen has diffused throughout the sample, hence an initial shoulder or minor peak is produced.

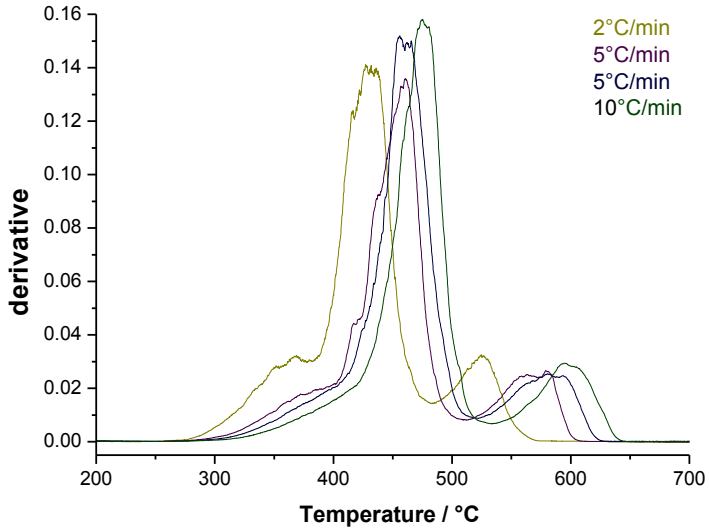

Figure 7.38 Derivative of the TGA thermo-oxidative degradation plot of PET1.0G chip

A comparison of derivative plots between the polymer and composites also suggest the secondary peak relating to the pyrolysis and oxidation of the degradation residues occurs at a faster rate for the composites. It has been previously suggested in literature that nanoclay fibres may act as a scaffold at this stage, allowing a more porous char material to be formed. This would then allow oxygen and volatile diffusion in and out of the degrading sample at a faster rate, accelerating degradation.[6]

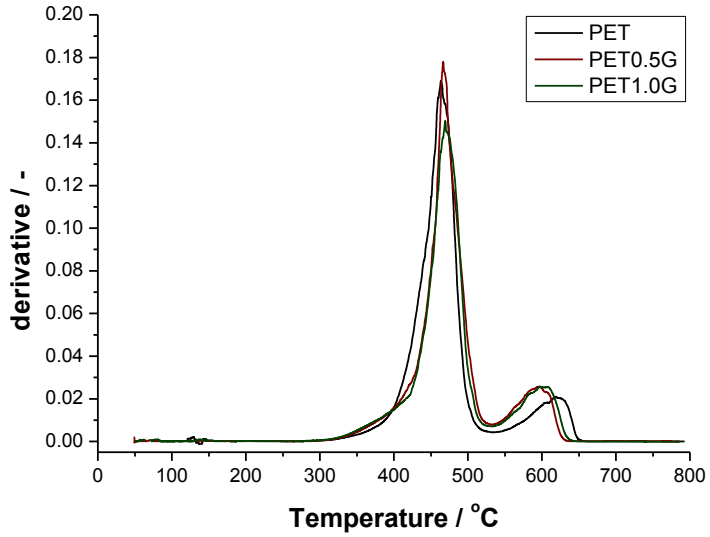

Figure 7.39 Derivative of the TGA thermo-oxidative degradation plots of polymer and composite chip degraded at 10°C min^{-1}.

7.2.2 DYNAMIC DSC

Dynamic DSC analysis was performed in order to investigate the energetic behaviour of both the polymer and composites at various heating rates under a thermo-oxidative environment. The onset of degradation and temperature at maximum degradation in particular were examined, providing insight into how the initiation and the main thermo-oxidative degradation processes were altered by incorporation of nanoclay into the polymer. The samples were prepared and subjected to the procedures previously outlined in Chapter 3. Figures 7.40 – 7.42 illustrate the dynamic, thermo-oxidative degradation curves for the polymer and composites. Precision was determined as ± 3.8ºC for the onset temperatures and ± 1.6ºC for the degradation maximums. An additional ± 1.0ºC was attributed in each case to account for instrumental variance.

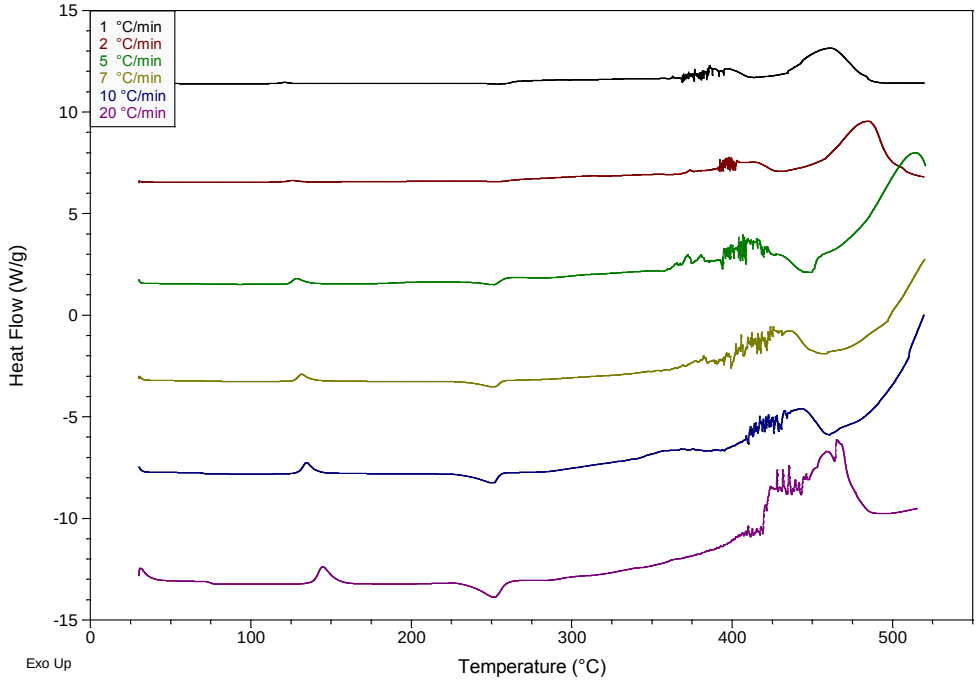

Figure 7.40 Dynamic thermo-oxidative degradation profile of PET at various heating rates. Analysis was performed under air.

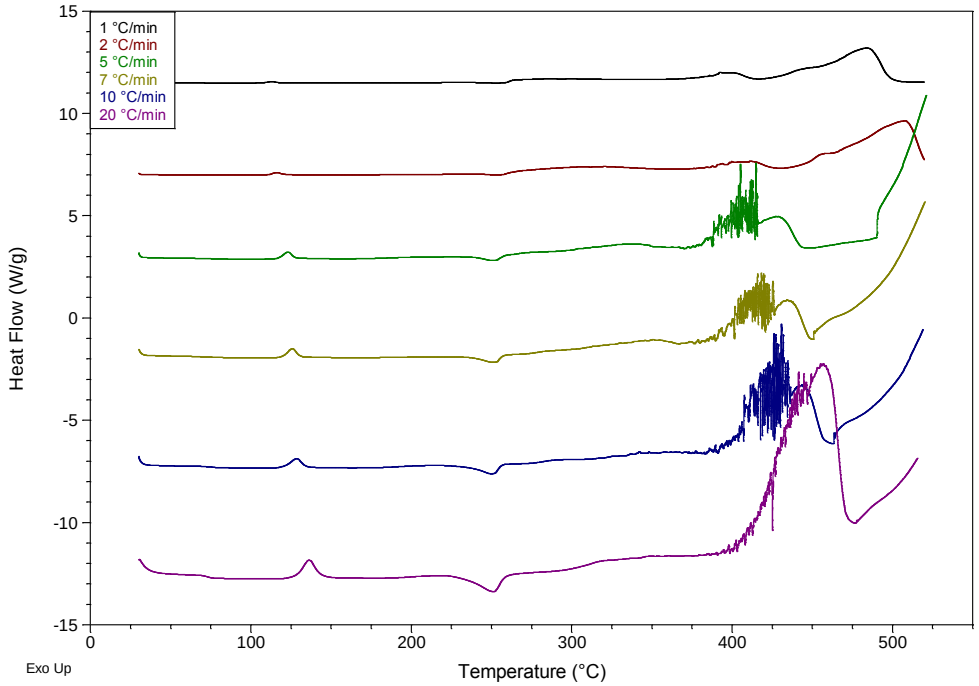

Figure 7.41 Dynamic thermo-oxidative degradation profile of PET0.5G at various heating rates. Analysis was performed under air.

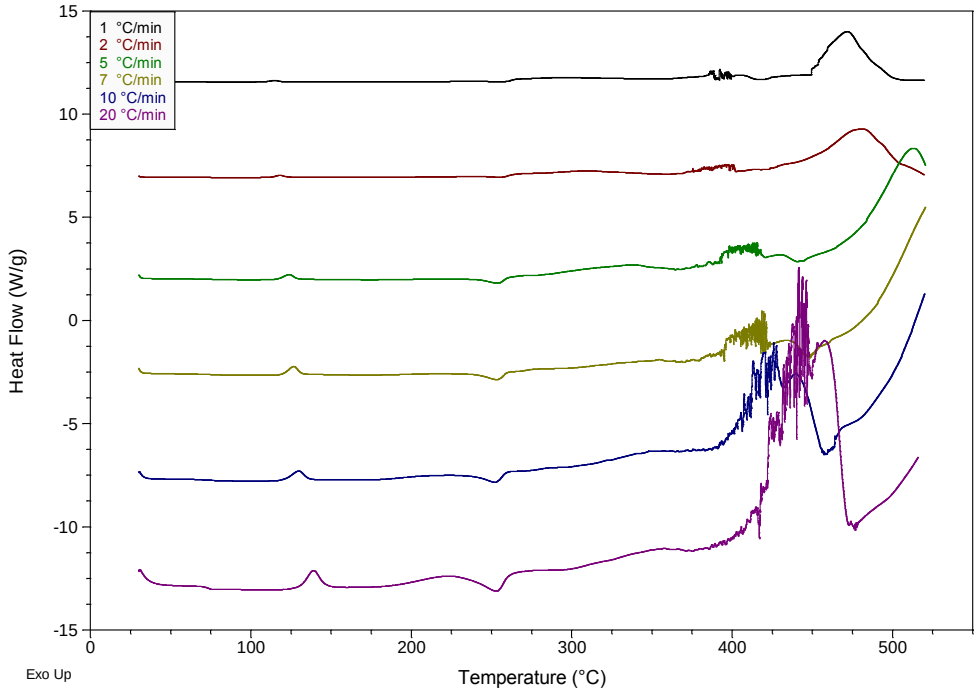

Figure 7.42 Dynamic thermo-oxidative degradation profile of PET1.0G at various heating rates. Analysis was performed under air.

In the preliminary visual examination two main exotherms are evident during thermo-oxidative degradation. Each system follows the same pattern of behaviour, indicating the nanoclay does not alter the main degradation processes. As heating rate is increased, the primary exotherm increases in energy and is driven to higher temperatures. Erratic behaviour at the onset of this exotherm also increases. The secondary exotherm is also driven to higher temperatures, to such an extent it is no longer observable. It is noted that the erratic nature of the composites in particular increases to a more substantial degree as the heating rate is increased. As enhanced char formation may allow an increase in the rate at which volatiles and oxygen diffuse though the material this is a possible cause. In addition, if the nanoclay possesses a catalytic effect a more erratic exotherm may also be expected.

Table 7.24 Comparative table for the onset temperatures of thermo-oxidative degradation

Heating rate /°C	PET	PET0.5G	PET1.0G
1	339.29	362.39	356.46
1	335.22	350.64	369.6
1	337.26	356.52	363.03
2	345.99	355.75	373.64
2	347.70	375.01	361.22
2	346.85	365.38	367.43
5	356.26	368.36	372.05
5	353.40	370.66	374.12
5	354.83	369.51	373.09
7	348.84	370.83	381.99
7	351.69	379.65	383.80
7	350.26	375.24	382.90
10	358.56	387.95	387.03
10	357.40	385.20	383.11
10	357.98	386.58	385.07
20	364.81	384.46	396.01
20	363.09	380.66	396.47
20	363.95	382.56	396.24

Table 7.25 Comparative table of polymer and composite temperatures for the main degradation peak temperature

Heating rate /°C	PET	PET0.5G	PET1.0G
1	398.15	404.80	400.69
1	396.51	402.58	403.66
1	397.33	403.69	402.18
2	413.79	410.57	409.15
2	412.83	408.11	407.54
2	413.31	409.34	408.35
5	426.06	429.06	431.96
5	428.27	424.40	428.14
5	427.17	426.73	430.05
7	434.15	433.97	435.28
7	436.26	431.25	434.50
7	435.21	432.61	434.89
10	443.72	439.65	442.20
10	442.58	442.41	443.06
10	443.15	441.03	442.63
20	457.32	457.95	455.16
20	458.62	452.31	456.62
20	457.97	455.13	455.89

The onset values are observed to increase within each particular system with an increase in heating rate. This is attributed to a decrease in time available for degradation as previously described in section 7.1.2. Lower onset values for the polymer than during thermal degradation illustrate the catalytic effect of oxygen on degradation. It is also noted that the composite values are significantly higher than those of the polymer. It is therefore suggested that the nanoclay inhibits thermo-oxidative degradation in some manner, possibly due the hindrance of oxygen diffusion through the melt.

Temperatures at the maximum degradation rate also exhibit a linear increase in T_{max} with an increase in heating rate. Temperatures are comparable therefore the nanoclay is not said to alter the energetic degradation of the bulk polymer matrix.

7.2.3 THERMO-OXIDATIVE DEGRADATION KINETICS

Classical and contemporary methods will again be employed and compared when examining the thermo-oxidative kinetics of degradation. Thermo-oxidative degradation is more complex than thermal degradation due to the requirement of oxygen diffusion throughout the polymer matrix. The rate of oxygen diffusion may therefore be the rate-determining step within the systems, especially within the low heating rates where the melt viscosity is higher for a relatively substantial period of time.

Examples of data treatment and full sets of numerical results are again included in the following section for each particular model, however the interpretation of data will be contained in section 7.2.3.3.

7.2.3.1 GRAVIMETRIC KINETICS MODELS

7.2.3.1.1 ARRHENIUS MODEL

7.2.3.1.1.1 SELECTION OF ISOTHERMAL TEMPERATURES

As for the thermal degradation TGA runs, dynamic measurements were performed initially in order to select the appropriate temperatures for isothermal measurements. Figure 7.43 contains the dynamic oxidative analysis for the polymer and composites.

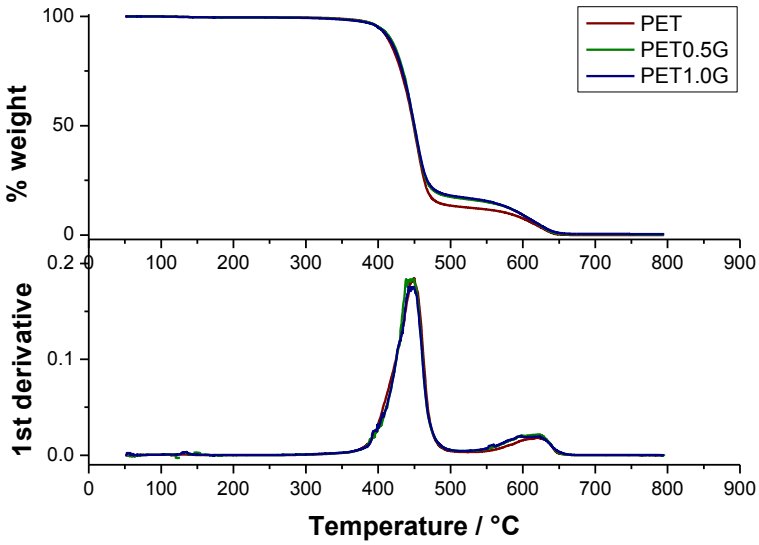

Figure 7.43 Dynamic, thermo-oxidative degradation TGA plots for PET, PET0.5G and PET1.0G uniaxial film. Analysis was performed under air.

The isothermal temperature range selected for study was 390ºC to 420ºC, over 10ºC increments. This incorporated the initiation of mass loss until the maximum rate of loss was reached. The narrow temperature range would also to some degree inhibit the influence of any competing degradation mechanisms, potentially complicating the kinetics.

7.2.3.1.1.2 ARRHENIUS MODEL

The Arrhenius model was the classical gravimetric model employed. The maximum observed gradient over a plot of % mass against time equates to – k (–reaction rate), at a specific degradation temperature and assuming zero order kinetics. An Arrhenius plot of lnk against 1/T provides a gradient of $-E_a/R$ and y-intercept lnA. Replicate k values were averaged prior to the Arrhenius plot to increase accuracy in E_a and lnA.

Figure 7.44 is an isothermal plot of PET at the pre-determined temperatures. Duplicate plots and those of the composites can be found in appendix 8. Figure 7.44 and those within the appendix indicate that the higher the isothermal the faster the rate of mass loss, and hence degradation rate.

Again, the linear region of the plots with the steepest gradient represented the maximum degradation rate in relation to mass loss and this region varied with temperature. A 10ºC range was selected depending on the isothermal hold temperature. The region of maximum mass loss is graphed in figure 7.45.

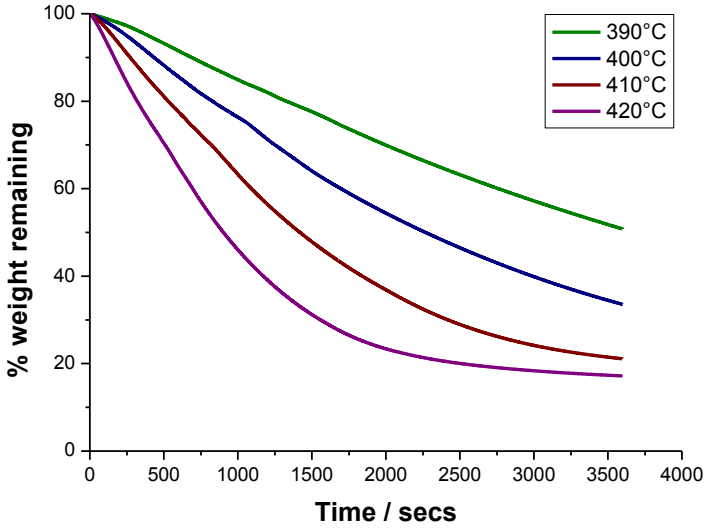

Figure 7.44 Isothermal thermo-oxidative degradation plots for PET uniaxial film between 390ºC and 420ºC. The isothermal was held for 1 hour. Analysis was performed under air.

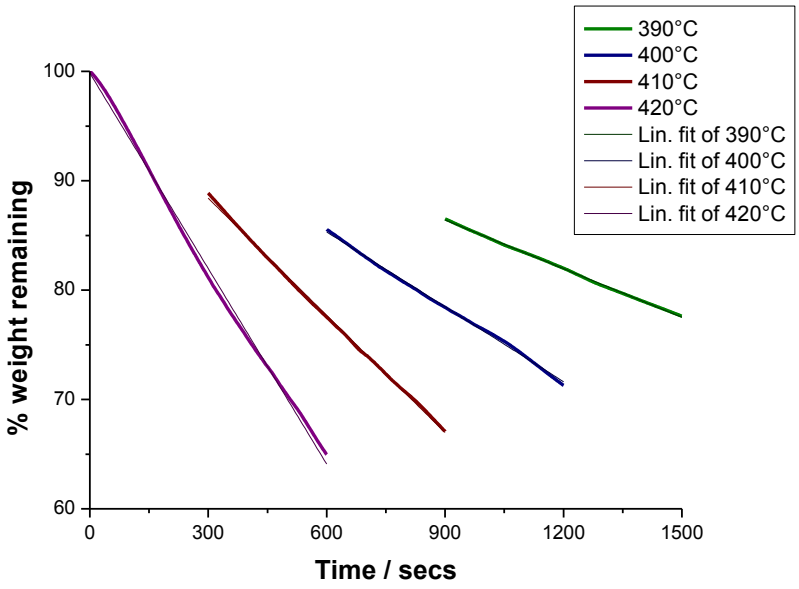

Figure 7.45 Regions of maximum mass loss during the isothermal degradation plots for PET uniaxial film between 390ºC and 420ºC. Analysis was performed under air. Linear fittings were also performed.

As before the linear region of maximum mass loss equates to the –k. The k values are used to graph an Arrhenius plot, shown in figure 7.46. The gradient was equal to $-E_a/R$

and y-intercept lnA, allowing the Arrhenius parameters to be calculated. A temperature of 700 K was used when calculating k.

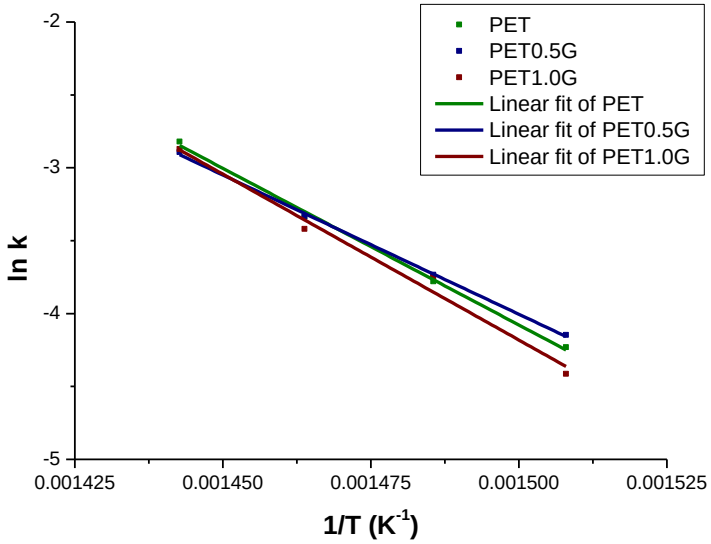

Figure 7.46 Arrhenius plot for the thermo-oxidative degradation of PET, PET0.5G and PET1.0G uniaxial film

$$k = A\exp\left(-\frac{E_A}{RT}\right) \qquad \text{Equation 7.1}$$

Table 7.26 Calculated Arrhenius parameters during thermo-oxidative degradation of PET, PET0.5G and PET1.0G uniaxial film. k represents the reaction rate at 700 K.

Sample	m	Ea / kJ mol^{-1}	lnA	k / s^{-1}
PET	-2.4 x 10^4	197.8 ± 13.8	31.6 ± 2.4	8.8 x 10^{-2}
PET0.5G	-1.9 x 10^4	157.6 ± 2.1	24.4 ± 0.4	6.8 x 10^{-2}
PET1.0G	-2.1 x 10^4	174.0 ± 5.8	27.3 ± 1.0	7.2 x 10^{-2}

7.2.3.1.2 AMERICAN STANDARD TEST METHOD E1641

Samples were subjected to heating rates between 1ºC min^{-1} and 20ºC min^{-1} and maximum peak temperatures determined. Thermo-oxidative degradation plots may be found within section 7.2.1. and appendix 7. The natural logarithms of the heating rates are then plotted against the reciprocal of temperature at various degrees of conversion, α, and linear data fitting is applied.

Figure 7.47 contains a conversion plot for the thermal degradation of PET uniaxial film. Conversions between 0.01 (1%) and 0.40 (40%) were examined in order to determine

the period where there is a constant degradation rate. A constant and maximum rate is assumed when the gradients are comparable, for example in this particular case between a 0.10 and 0.20 conversion.

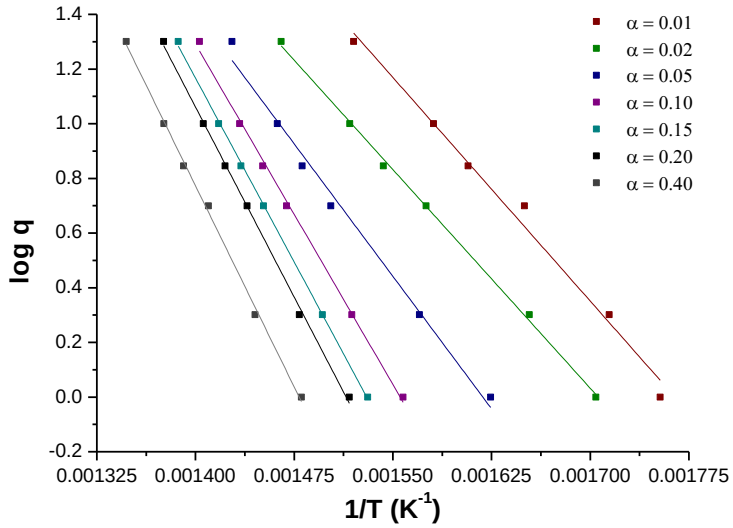

Figure 7.47 Conversion plot for PET uniaxial film during therm-oxidative degradation. Conversion factors between 0.01 (1%) and 0.40 (40%) have been included. The gradients for the linear data fittings are contained in table 7.27.

Table 7.27 Gradients for the linear data fittings in figure 7.47.

α	Δ(log β)/Δ(1/T)
0.01	-5454
0.02	-5333
0.05	-6461
0.10	-8303
0.15	-8968
0.20	-9270
0.40	-9809

To ensure consistency a constant conversion factor was employed throughout the samples under study, therefore conversion plots of duplicate samples and the additional polymer and composites sample were also examined. These plots may be found in appendix 8. A conversion of 0.15 or was selected and experimental temperatures at this conversion were noted.

Table 7.28 Gradients **(**Δ(log β)/Δ(1/T)) and temperatures relating to a 0.15 conversion during thermal degradation. The average error is obtained through Origin software and is with respect to linearity of data within the line fitting process.

Material	Sample	Δ(log β)/Δ(1/T) / -				Temperature / K		
		1	2	Average	Average Error	1	2	Average
Amorphous Chip	PET	-9391	-6492	-7942	± 413	689.37	689.70	689.54
	PET0.5G	-5480	-5254	-5367	± 174	687.86	688.61	688.24
	PET1.0G	-5391	-5117	-5254	± 165	687.89	699.96	693.93
Uniaxial Film	PET	-8999	-8968	-8983	± 288	688.36	688.85	688.61
	PET0.5G	-8292	-7201	-7746	± 302	693.17	689.07	691.12
	PET1.0G	-8312	-8009	-8160	± 145	688.93	689.47	689.20

The gradient, $\Delta(\log\beta)/\Delta(1/T)$, was then employed in iterative calculations which initially estimated the activation energy via equation 7.2, and then refined using equation 7.3, where R is the universal gas constant (8.314 J K^{-1} mol^{-1}) and b is an approximation constant. The activation energy was described as suitably refined when the variability between the calculated activation energies was less than 1%, at which point it was denoted E_r. The pre-exponential factor can then be calculated via equation 7.4 through employing the refined activation energy, β' which is the heating rate at the midpoint of the experimental heating rates under study, and a second approximation constant, a. The reaction rate may then be calculated through the Arrhenius equation. The Arrhenius parameters derived from this method are contained within table 7.13.

$$E_{approx} \cong -(R/0.457) * \Delta(\log\beta)/\Delta(1/T) \qquad \text{Equation 7.2}$$

$$E = -(R/b) * \Delta(\log\beta)/\Delta(1/T) \qquad \text{Equation 7.3}$$

$$A = -(\beta'/E_r) * R * \ln(1-\alpha) * 10^a \qquad \text{Equation 7.4}$$

Nota bene. A table of the approximation constants employed within this method may be found within appendix 6. .

Table 7.29 Arrhenius parameters for thermal degradation calculated through employing the ASTM 1641 model

Material	Sample	E_{approx} / kJ mol^{-1}	E_r / kJ mol^{-1}	ln A	k / s^{-1}
Amorphous Chip	PET	144.5	140.8	21.6	7.3 x 10^{-2}
	PET0.5G	97.6	91.4	12.1	2.8 x 10^{-2}
	PET1.0G	95.6	89.5	12.2	4.0 x 10^{-2}
Uniaxial Film	PET	163.4	160.6	24.7	5.3 x 10^{-2}
	PET0.5G	140.9	137.0	20.5	4.8 x 10^{-2}
	PET1.0G	148.5	144.7	21.5	3.6 x 10^{-2}

7.2.3.2 ENERGETIC KINETICS MODELS

7.2.3.2.1 KISSINGER MODEL

The Kissinger model was again employed for the reasons outlined previously. To summarise, Kissinger plots are generated of $\ln(q/T_{max}^2)$ against $1/T_{max}$ through various heating rates. Linear data fitting then provides the activation energy in the form $-E_a/R$ from the gradient and the lnA value from the y-intercept.

Tables 7.30 – 7.32 contain the DSC data required to graph the Kissinger plot, figure 7.48 below, of $\ln(q/T_{max}^2)$ against $1/T_{max}$.

Table 7.30 Kissinger data for the thermo-oxidative degradation of PET at various heating rates.

Heating Rate/K min^{-1}	Temperature / K			$1/T_{max}$ / K^{-1}	$\ln(q/T_{max}^2)$
	1	2	Average		
1	671.30	669.96	670.63	1.49 x 10^{-3}	-13.02
2	686.94	685.98	686.46	1.46 x 10^{-3}	-12.37
5	699.21	701.42	700.32	1.43 x 10^{-3}	-11.49
7	707.39	709.41	708.40	1.41 x 10^{-3}	-11.18
10	716.87	715.73	716.30	1.40 x 10^{-3}	-10.85
20	730.47	731.77	731.12	1.37 x 10^{-3}	-10.19

Table 7.31 Kissinger data for the thermo-oxidative degradation of PET0.5G at various heating rates.

Heating Rate/K min^{-1}	Temperature / K			$1/T_{max}$ / K^{-1}	$\ln(q/T_{max}^2)$
	1	2	Average		
1	677.95	675.73	676.84	1.48 x 10^{-3}	-13.034
2	681.26	681.26	681.26	1.47 x 10^{-3}	-12.36
5	702.21	697.55	699.88	1.43 x 10^{-3}	-11.49
7	707.12	704.40	705.76	1.42 x 10^{-3}	-11.17
10	712.80	715.56	714.18	1.40 x 10^{-3}	-10.84
20	731.10	725.46	728.28	1.37 x 10^{-3}	-10.19

Table 7.32 Kissinger data for the thermo-oxidative degradation of PET1.0G at various heating rates.

Heating Rate/K min^{-1}	Temperature / K			$1/T_{max}$ / K^{-1}	$\ln(q/T_{max}^2)$
	1	2	Average		
1	673.84	676.81	675.33	1.48 x 10^{-3}	-13.03
2	682.30	680.69	681.50	1.47 x 10^{-3}	-12.36
5	705.11	701.29	703.20	1.42 x 10^{-3}	-11.50
7	708.43	707.65	708.04	1.41 x 10^{-3}	-11.18
10	715.35	716.21	715.78	1.40 x 10^{-3}	-10.84
20	728.31	729.77	729.04	1.37 x 10^{-3}	-10.19

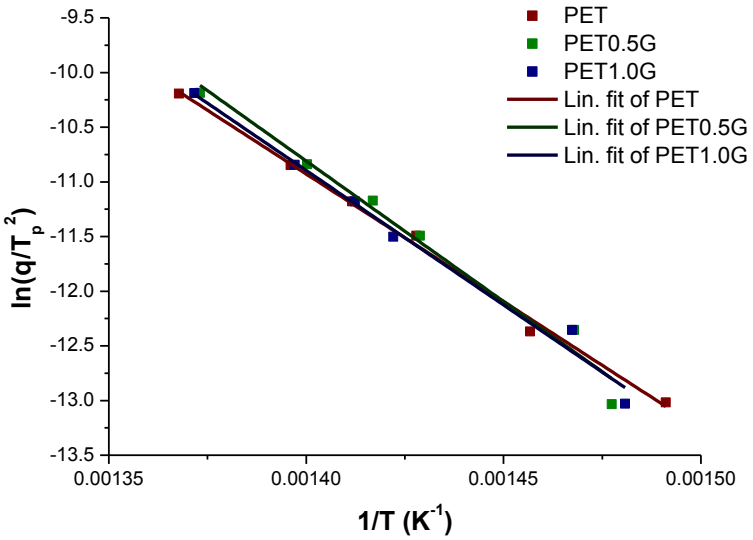

Figure 7.48 Kissinger plot for the thermo-oxidative degradation of PET, PET0.5G and PET1.0G. Linear data fitting has been applied to each data set.

Table 7.33 contains the Arrhenius parameters. The activation energy was obtained by multiplying the gradient values by –R (gas constant) and the lnA value required no manipulation. K was determined for a temperature of 700K.

Table 7.33 Arrhenius parameters for thermal degradation calculated through the Kissinger model. The average error is obtained through Origin software and is with respect to linearity of data within the line fitting process.

Sample	Ea / kJ mol^{-1}	lnA	k / s^{-1}
PET	193.9 ± 6.1	33.5 ± 1.1	1.19
PET0.5G	213.7 ± 15.4	37.0 ± 2.6	1.31
PET1.0G	204.5 ± 11.4	35.2 ± 2.0	1.24

7.2.3.2.2 AMERICAN STANDARD TEST METHOD E698

As previously the samples were subjected to heating rates between 1ºC min^{-1} and 20ºC min^{-1} in order to determine the variation in maximum peak temperatures. Plots of these dynamic heating runs may be found within section 7.2.2 and appendix 7. The natural logarithms of the heating rates are then plotted against 1/T for each particular system.

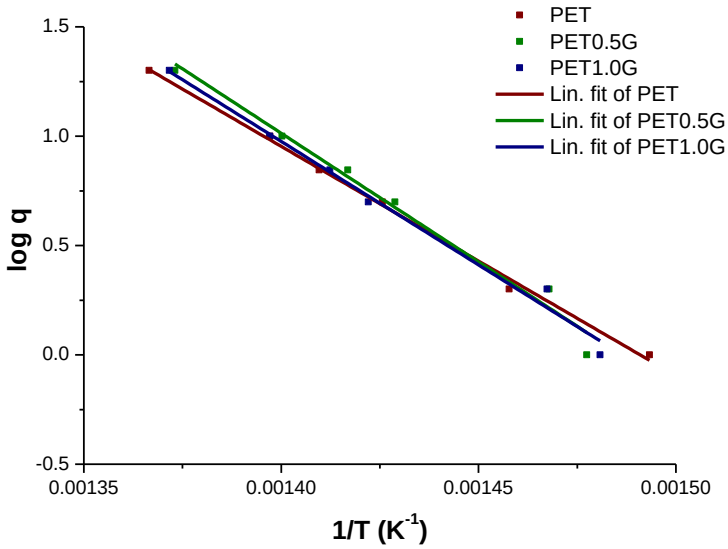

Figure 7.49 ASTM E698 plot for the thermo-oxidative degradation of PET, PET0.5G and PET1.0G.

The gradient, $\Delta(\log\beta)/\Delta(1/T)$, is then employed in the estimation and then refinement of the activation energy, via an equations 7.5 and 7.6 respectively, and with an approximation constant, D, also employed in the latter. A table of approximation constants may be found within appendix 6. The pre-exponential factor and reaction rate may then also be calculated via equation 7.7 and the Arrhenius equation, respectively.

$$E_{approx} \approx -2.19R * \Delta(\log\beta)/\Delta(1/T) \qquad \text{Equation 7.5}$$

$$E = (-2.303R/D) * \Delta(\log\beta)/\Delta(1/T) \qquad \text{Equation 7.6}$$

$$A = \beta E e^{-Ea/RT} / (RT_m^2) \qquad \text{Equation 7.7}$$

$$k = Ae^{-Ea/RT} \qquad \text{Equation 7.8}$$

As in previous determinations of k, a temperature of 700K was employed. It is noted that the approximate and refined values of E_a do not vary substantially.

Table 7.34 Arrhenius parameters for thermo-oxidative degradation calculated using the ASTM E698 method. The refined activation energy, E_r, was achieved after three iterations.

Sample	E_{approx} / kJ mol^{-1}	E_r / kJ mol^{-1}	lnA	k / s^{-1}
PET	190.9	189.0	30.8	1.8 x 10^{-1}
PET0.5G	214.3	213.5	35.1	2.0 x 10^{-1}
PET1.0G	205.6	204.5	33.5	1.9 x 10^{-1}

7.2.3.3 COMPARISON OF KINETIC MODELS APPLIED TO THERMO-OXIDATIVE DEGRADATION

There was substantial variation within the chip materials in comparison to the uniaxial film during thermo-oxidative degradation. With regards to the application of the E1641 model, both the chip composites were observed to drop 50 kJ mol^{-1} in activation energy in relation to the polymer, as opposed to a drop of up to 20 kJ mol^{-1} for the uniaxial film. The pre-exponential factor was also observed to follow the same trend. This observed drop in E_a and lnA within sets of chip and uniaxial film samples is attributed to the catalytic effect of the nanoclay on degradation. It is also noted that the effect of the nanoclay on the Arrhenius parameters is not as substantial within the uniaxial material as observed within the chip. This decrease in the effectiveness of the nanoclay is attributed to the degradation of ammonium surface modifiers during melt processing, which effectively decreases the catalytic effect on processing.[7]

Table 7.35 Arrhenius parameters for thermo-oxidative degradation calculated through employing the ASTM 1641 model.

Material	Sample	E_a / kJ mol^{-1}	lnA	k / s^{-1}
Amorphous Chip	PET	141	21.6	7.3 x 10^{-2}
	PET0.5G	91	12.1	2.8 x 10^{-2}
	PET1.0G	90	12.2	4.0 x 10^{-2}
Uniaxial Film	PET	161	24.7	5.3 x 10^{-2}
	PET0.5G	137	20.5	4.8 x 10^{-2}
	PET1.0G	145	21.5	3.6 x 10^{-2}

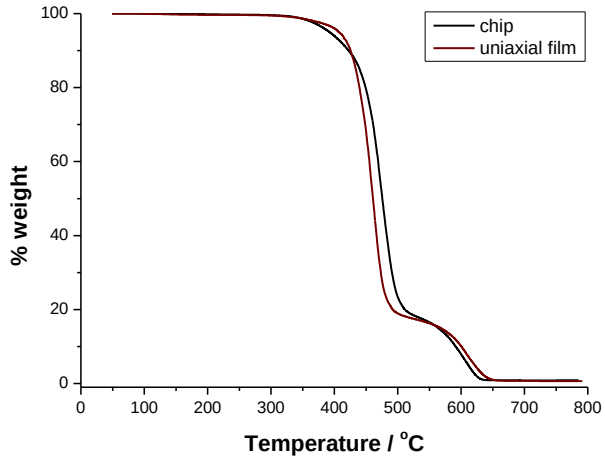

Figure 7.50 TGA thermogram of PET chip and uniaxial film during thermo-oxidative degradation.

Both gravimetric models exhibit the same trends within the uniaxial film i.e. a drop in E_a and lnA due to the catalytic effect of the nanoclay. The classical model illustrates this effect to a more substantial degree through higher values and greater discrepancies between the polymer and composites. Reaction rates are comparable however despite the variation in the other parameters.

Table 7.36 Comparison of the Arrhenius parameters for thermo-oxidative degradation calculated using the Arrhenius and ASTM 1641 gravimetric models. The material under study was uniaxial film.

Material	Sample	E_a / kJ mol^{-1}	lnA	k / s^{-1}
Arrhenius	PET	198	31.6	8.8 x 10^{-2}
	PET0.5G	158	24.4	6.8 x 10^{-2}
	PET1.0G	174	27.3	7.2 x 10^{-2}
ASTM 1641	PET	161	24.7	5.3 x 10^{-2}
	PET0.5G	137	20.5	4.8 x 10^{-2}
	PET1.0G	145	21.5	3.6 x 10^{-2}

The energetic models are extremely comparable when considering the activation energy and pre-exponential factors. Values again appear to be high in relation to the gravimetric models however, and energetic stabilisation is observed in contrast to the destabilisation observed within the gravimetric models.

Table 7.37 Comparison of the Arrhenius parameters for thermo-oxidative degradation calculated using the Kissinger and ASTM E698 energetic models. The material under study was chip.

Material	Sample	E_a / kJ mol^{-1}	lnA	k / s^{-1}
Kissinger	PET	194	33.5	1.2
	PET0.5G	214	37.0	1.3
	PET1.0G	205	35.2	1.2
ASTM E698	PET	189	30.8	1.8 x 10^{-1}
	PET0.5G	214	35.1	2.0 x 10^{-1}
	PET1.0G	205	33.5	1.9 x 10^{-1}

The activation energies appear to suggest a stabilising effect on degradation. The energetic onset values during thermo-oxidative degradation also indicated the nanoclay possessed an inhibiting effect, however this is not replicated within the maximum peak temperatures during the bulk of degradation. As the degradation of the bulk polymer matrix is not affected it is assumed some manner of inhibition or stabilisation occurs at the polymer-nanoclay interfaces. It is suggested that the nanoclay is hampering oxygen diffusion through a barrier effect. This has previously been observed within literature for PET/palygorskite nanocomposite systems, which comparable to the Garamite®-based nanocomposites.[6]

7.3 DISCUSSION

Thermogravimetric analysis illustrated the thermal degradation of PET and PET nanoclay composites occurred within one degradation step, due to the pyrolysis of the PET backbone into a residual char material. Gravimetric and energetic measurements during thermal degradation illustrated an acceleration in degradation only within the energetic onset at the highest clay loading of 1.0% w/w. The maximum degradation peaks in both gravimetric and energetic measurements possessed no significant alterations on the incorporation of nanoclay, therefore the bulk of the polymer matrix with no contact with the nanoclay is concluded to remain unaffected on degradation.

Kinetic calculations indicate the Arrhenius parameters are comparable within error with relation to the degradation behaviour of the chip material, and within the nanoclay loadings under study for E_a and lnA. The parameters calculated are observed to be less comparable with respect to E_a and lnA, however more so with respect to k. The nanoclay can therefore be concluded to accelerate thermal degradation in some manner. In addition, at the mass loadings under study the effect of the nanoclay on the degradation kinetics is comparable. This is perhaps suggestive that at a loading as low as 1.0% w/w the nanoclay has already reached the maximum loading at which it may affect the degradative behaviour of poly(ethylene terephthalate). The Arrhenius parameters for the polymer and composites varied as follows; the polymer possessed activation energies between 141 - 198 $kJmol^{-1}$, lnA values between 21.6 – 33.5 and reaction rates between 5.27 x 10^{-2} – 1.19 s^{-1}; the composites possessed activation energies between 90 - 205 $kJmol^{-1}$, lnA values between 20.5 – 35.2 and reaction rates between 1.93 x 10^{-2} - 1.31 s^{-1}. The values for the activation energies and pre-exponential factors for thermal degradation compared well with literature values.[8-10]

Thermogravimetric analysis during thermo-oxidative degradation illustrated the amorphous chip possessed higher maximum temperatures of degradation than the uniaxial film. This was due to a lower molar mass and hence melt viscosity within the uniaxial film as a result of processing, which allowed a faster rate of oxygen diffusion. Composite samples were also observed to possess higher T_{max} values due to impedance of oxygen diffusion by the nanoclay i.e. there was a barrier effect. It was noted the

barrier effect within the uniaxial PET1.0G uniaxial film sample appeared to be counteracted as the heating rate increased. It is suggested that in addition to the inhibiting barrier effect the nanoclay possessed an accelerating catalytic effect on degradation, and that this catalytic effect may only be substantial at a loading over 1.0%. The stabilisation was also observed through delays in the energetic onset of degradation within differential scanning calorimetry. No effect on the bulk energetic degradation was observed however, indicating the energetic rate was neither inhibited nor catalysed, and only the physical transport of oxygen and small organic molecules was affected. The competing effects can be observed clearly through the degradation kinetics. In the Arrhenius model/ASTM 1641 the catalytic effect of the nanoclay is clearly observed, whereas the Kissinger model/ASTM E698 the physical barrier effect is observed. Both gravimetric and energetic thermograms however illustrated the barrier effect of the nanoclay, but only the thermogravimetric analysis was able to illustrate the catalytic effect of nanoclay at the higher loading though alterations in the observed trends. It is concluded the catalytic effect of the nanoclay is most efficiently observed gravimetrically rather than energetically. Both gravimetric and energetic kinetic models are therefore extremely useful when applied to the thermo-oxidative degradation of PET. The Arrhenius parameters for the polymer and composites varied as follows; activation energies were between 91 – 214 $kJmol^{-1}$, lnA values between 12 – 35 s^{-1} and reaction rates 1.82 x 10^{-1} – 1.31 s^{-1}. The activation energies and pre-exponential factors were comparable with those in literature, however values appeared to vary substantially between authors.[6, 11-13]

The kinetic calculations within the degradation chapter employed both classical and contemporary, energetic and gravimetric models. The gravimetric models (Arrhenius and ASTM 1641) were extremely comparable in all kinetic parameters. It had been noted that the Arrhenius method was relatively indirect in comparison to ASTM 1641, due to the assumption that the region of maximum mass loss equated to the maximum degradation rate. This was problematic however as this region varied with heating rate. ASTM 1641 on the other hand employed data at a specific percentage of conversion. This was initially assumed as a more accurate method, as degradation rates and mechanisms should be comparable at specific degrees of conversion regardless of heating rate. It has been proved however that within these polymeric systems at least

the assumption made within the Arrhenius equation is valid, and either kinetic model can be employed. Classical and Contemporary energetic methods however were observed to be not as comparable as their gravimetric counterparts. The classical Kissinger method was observed to produce slightly higher activation energies and pre-exponential factors, which resulted in reaction rates two orders of magnitude higher than the average. The Kissinger method was therefore concluded as less reliable within the systems under study. Activation energies and pre-exponential factors were however still comparable within error with those of the contemporary method. ASTM E698 however was determined as the more reliable method, and in addition was comparable to the gravimetric models.

It should be noted that the only ASTM 1641 was performed on both chip and uniaxial film in both thermal and thermo-oxidative environments, and kinetic parameters were determined comparable. The Arrhenius gravimetric model was performed only on uniaxial film, and the energetic models only on amorphous chip. As ASTM 1641 parameters were comparable, comparisons and assumptions were then made between other kinetic models.

Finally, thermal volatilisation analysis (TVA) provided insight into the thermal degradation products and mechanisms. Non-condensable volatiles released during degradation contained primarily carbon monoxide, in addition to traces of small organic molecules such as methane, ethene, acetylene and propene. The pressure traces of the composite also exhibited a shoulder after the degradation maximum. It was concluded that the evolution of ethene and acetylene was inhibited due to the barrier effect of the nanoclay, which slowed the physical transport of the volatiles through the polymer matrix. Condensable volatiles primarily included carbon dioxide, acetaldehyde, water and benzaldehyde. Various other organic molecules were detected due to the variety of mechanistic pathways available to the degradation by-products. Furan, benzene, toluene, styrene and other conjugated aromatics were detected within the higher molar mass fractions.

Mass spectrometry has also revealed that the presence of the nanoclay drives the production of acetaldehyde during degradation, and therefore alters the degradation

mechanisms of poly(ethylene terephthalate) in some manner. If the degradation pathways within the introduction chapter are considered it may be expected that if a homolytic mechanism is dominant, an increase in the evolution of both acetaldehyde and carbon monoxide would be observed due to a 1:1 product ratio (see figures 1.21 and 1.22 within Chapter 1), however this is not the case. If degradation was predominantly initiated via a heterolytic mechanism however it would be expected that acetaldehyde production may increase without the accompanying increase in carbon dioxide. Although the literature provides evidence to support both mechanisms, it is rational that a heterolytic mechanism is suggested as dominant in this particular case.[14, 15]

The presence of the surface modified nanoclay has been suggested to catalyse the degradation of a polymer through various manners within the literature. The catalytic activity of the nanoclay may be attributed to the hydroxyl groups on the nanoclay edges which act as Brønsted acid sites. Brønsted acid sites were also produced during the degradation of the ammonium surface modifiers through the Hoffman elimination. The presence of Brønsted acid sites is significant as a polyester may undergo acid catalysed ester hydrolysis when free protons are available.

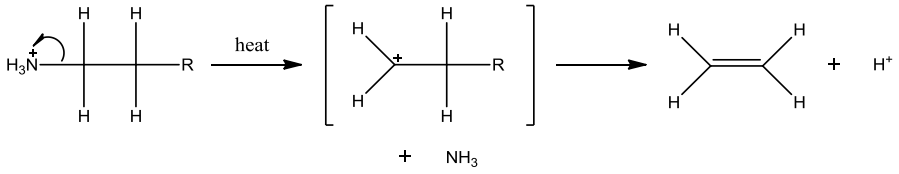

Figure 7.51 Mechanism of the Hoffman elimination which the ammonium surface modifiers undergo on processing.

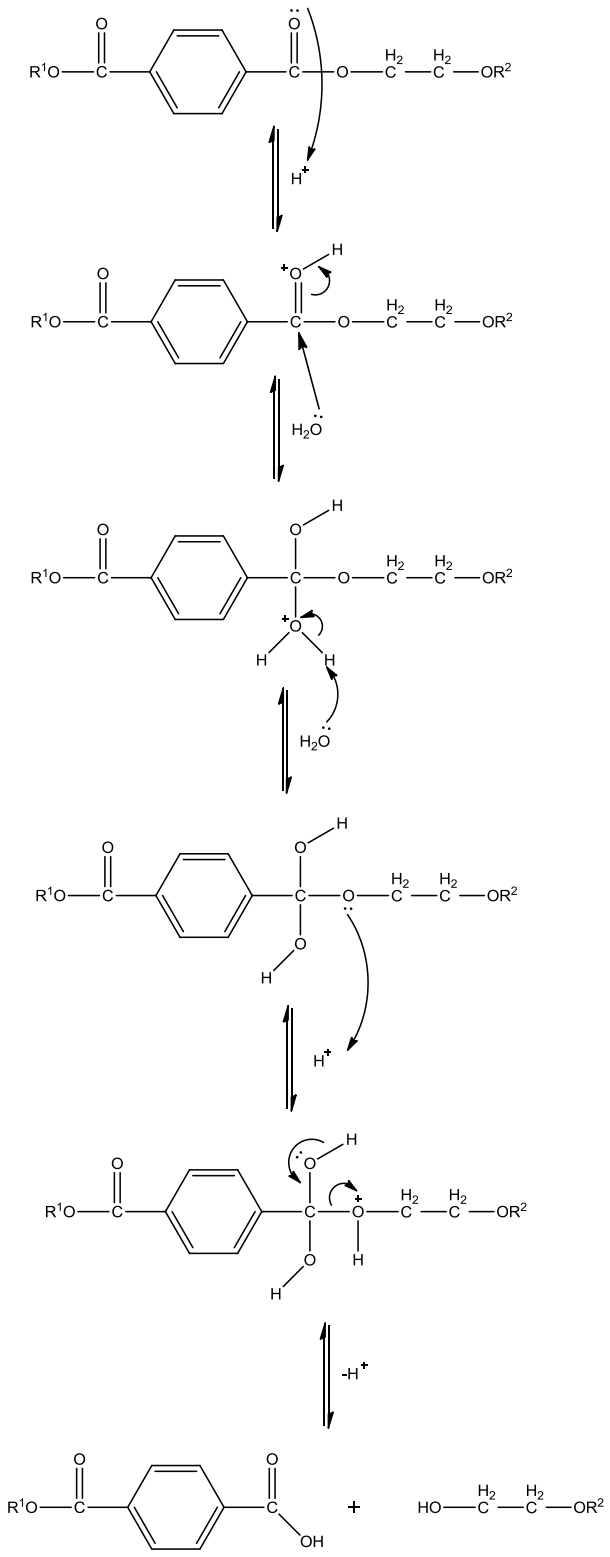

Figure 7.52 Acid catalysed hydrolysis of PET.

Hydrolysis has also been suggested to occur with the assistance of a metal catalyst i.e. the unexchanged sodium counter ions, which may remain on the nanoclay surface at

concentrations of up to 15% of the total surface ion concentration.[16, 17] In addition aminolysis may occur due to the tertiary amines produced during the Hoffman elimination, leading to the formation of peptide linkages.[18] The presence of α-olefins and other by-products are also often suggested to contribute, however no mechanisms are generally suggested within the literature.[16]

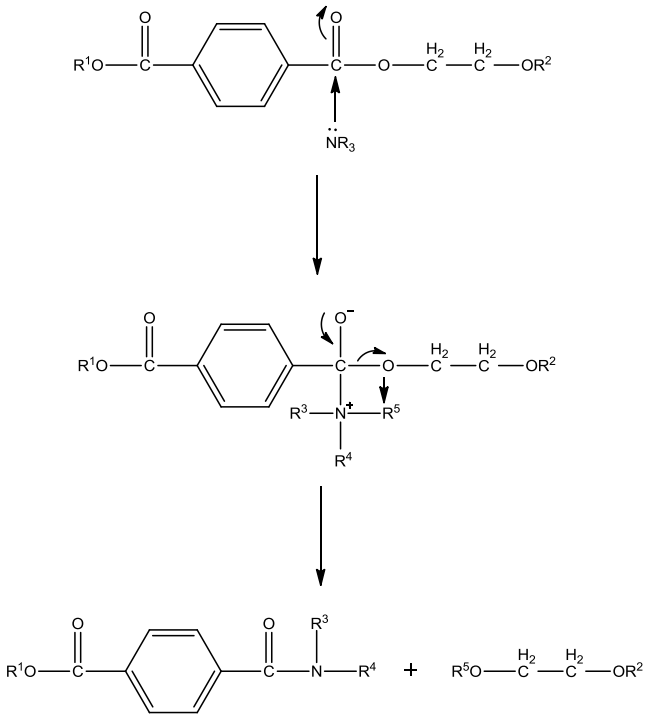

Figure 7.53 Aminolysis of PET through the tertiary amine produced during the Hoffman elimination.

As previously discussed the presence of the Garamite® nanoclay preferentially drives the formation of acetaldehyde. The suggested catalytic mechanism must therefore account for this observation. Within Chapter 1, it was illustrated that acetaldehyde is formed from vinyl benzoate end groups during both a homolytic and heterolytic initiation mechanisms. Acid catalysed hydrolysis and aminolysis however produce products which cannot directly account for an increase in the acetaldehyde yield. In addition if the nanoclay catalysed degradation through either of the mechanisms discussed an increase in ethylene glycol formation would be expected and this is not observed experimentally. It may be suggested that if the acid catalysed degradation of poly(ethylene terephthalate) does occur the free ethylene glycol product may attack the vinyl benzoate moiety and preferentially catalyse this particular step, driving the

formation of acetaldehyde and replacing the vinyl ester end group with a glycol (or hydroxyl ethyl) end group. Brønsted acids may also catalyse the degradation of vinyl benzoate moieties to carboxylic acid. An increase in acetaldehyde production in particular has been observed experimentally and supports this hypothesis.

7.4 REFERENCES

1. Bilotti, E., *Polymer/Sepiolite Nanocomposites*, PhD in School of Engineering and Materials Science, Queen Mary, University of London, London, 2009.
2. Zammarano, M., Franceschi, M., Bellayer, S., Gilman, J.W., Mariani, S., *Preparation and flame resistance properties of revolutionary self-extinguishing epoxy nanocomposites based on layered double hydroxides*, Polymer, 2005, **46**, 9314-9328.
3. Wijmans, J.G., Membrane Technology and Research Inc, *Process for Removing Condensable Products from Gas Streams*, Office, U.S.P., 1993,
4. Ozawa, T., *Kinetic Analysis of Derivative Curves in Thermal Analysis*, Journal of Thermal Analysis, 1970, **2**, 301-324.
5. Flynn, J.H., Wall, L.A., *A quick, direct method for the determination of activation energy from thermogravimetric data*, Polymer Letters, 1966, **4**, 323-328.
6. Yuan, X., Li, C., Guan, G., Xiao, Y., Zang, D., *Thermal degradation investigation of poly(ethylene terephthalate)/fibrous silicate nanocomposites*, Polymer Degradation and Stability, 2008, **93**, 466-475.
7. Xu, X., Ding, Y., Qian, Z., Wang, F., Wen, B., Zhou, H., Zhang, S., Yang, M., *Degradation of poly(ethylene terephthalate)/clay nanocomposites during melt extrusion: Effect of clay catalysis and chain extension*, Polymer Degradation and Stability, 2009, **94**, 113-123.
8. Saha, B., Goshal, A.K., *Thermal degradation kinetics of poly(ethylene terephthalate) from waste soft drinks bottles*, Chemical Engineering Journal, 2005, **111**, 39-43.
9. Holland, B.J., Hay, J.N., *The thermal degradation of PET and analogous polyesters measured by thermal analysis-fourier transform infrared spectroscopy*, Polymer, 2002, **43**(6), 1835-1847.

10. Vassilious, A.A., Chrissafis, K., Bikiaris, D.N., *In situ preparation of PET nanocomposites: effect of organically modified MMT and fumed silica nanoparticles on PET physical properties and thermal degradation kinetics,* Thermochimica Acta, 2010, **500**, 21-29.
11. Zimmerman, H., *Developments in Polymer Degradation* 1984, Applied Science Publishers, Essex.
12. Wu, B., Wang, Y.Z., Wang, X.L., Yang, K.K., Jin, Y.D., Zhao, H., *Kinetics of thermal oxidative degradation of phosphorus-containing flame retardant copolyesters,* Polymer Degradation and Stability, 2002, **76**, 401-409.
13. Du, X.H., Zhao, C.S., Wang, Y.Z., Zhou, Q., Dang, Y., *Thermal oxidative degradation behaviours of flame-retardant thermotropic liquid cryatl copolyesters/PET blends,* Materials Chemitry and Physics, 2006, **98**, 172-177.
14. Grassie, N., Gerald, S., *Polymer Degradation and Stabilisation*, Vol. 5, 1985, Cambridge University Press, Cambridge.
15. McNeill, I.C., Bounekhel, M., *Thermal Degradation Studies of Terephalate Polyesters: 1. Poly(alkylene terephthalate),* Polymer Degradation and Stability, 1991, **34**, 187-204.
16. Fornes, T.D., Yoon, P.J., Paul, D.R., *Polymer matrix degradation and colour formation in melt processed nylon 6/clay nanocomposites,* Polymer, 2003, **44**, 7545-7556.
17. Davis, R.D., Gilman, J.W., VanderHart, D.L., *Processing degradation of polyamide 6/montmorillonite clay nanocomposites and clay organic modifier,* Polymer Degradation and Stability, 2003, **79**, 111-121.
18. Achilias, D.S., Tsintzou, G.P., Nikolaidis, A.K., Bikiaris, D.N., Karayannidis, G.P., *Aminolytic depolymerisation of poly(ethylene terephthalate) waste in a microwave reactor,* Polymer International, 2011, **60**, 500-506.

CHAPTER 8 FINAL CONCLUSIONS

One of the primary objectives of this thesis was to explore the exfoliation process of surface modified nanoclays. From an academic point of view, this was to provide an insight into the attributes which encourage a high degree of not only platelet or fibre separation but also suspension stability post-exfoliation. Industrially, this study would also provide an insight into the most compatible nanoclay for the preparation of a poly(ethylene terephthalate) based nanocomposite via an *in situ* polymerisation process. Specifically, the study highlighted a need for a dispersant which possessed both a high permittivity and polarity. The permittivity was considered as a means to describe the ability of a dispersant to shield or dampen the attractive interplatelet forces which would result in the reformation of tactoids. A high dispersant permittivity was therefore associated with an effective shielding ability. The polarity provided an indication of the extent of interactions possible with the nanoclay surface and/or surface modifiers through interactions such as hydrogen bonding or Van der Waals. An examination of the Cloisite® range also highlighted the need for a surface modifier which had the ability to interact with the dispersant directly. Modifier functional groups such as benzyls and those capable of hydrogen bonding were therefore identified as the most beneficial to nanoclay exfoliation.

Characterisation of the Garamite® itself was performed at the University of Ottawa after the polymer nanocomposites had been prepared. Data obtained through XRD measurements and TEM illustrated that the Garamite® did not possess a platelet morphology as previously assumed. Instead the Garamite® was determined to be of a more fibrous nature and was identified as a surface modified sepiolite nanoclay.

Characterisation of the PET nanocomposites prepared at Wilton then allowed the affect of the Garamite® on the polymer properties to be determined. Various methods confirmed there was no affect on the polymeric structure, and hence the synthetic mechanism can be assumed to be unaffected by the Garamite® as far as reasonably possible. The presence of the Garamite® was however observed to enhance the decrease in molar mass on melt

processing, and was therefore assumed to possess some degree of catalytic effect during degradation.

A study into the crystallisation behaviour was an essential aspect to this thesis due to possibility of commercial applications which would require the impact of a filler on the crystalline properties to be assessed. This was especially important when melt processing amorphous chip to either a uniaxially or biaxially drawn film as there must be a controlled level of crystallinity. Fillers such as nanoclays are known to be heterogeneous nucleating agents and the Garamite® was found to be no exception. Examination of the crystallisation kinetics through the modified model identified a sheaf-like mode of crystalline growth for the polymer nanocomposites which did not alter as a result of melt processing. The polymer in contrast exhibited an increase in crystalline growth dimensions on melt processing from a disc-like to spherulitic morphology.

Finally, an investigation into the degradation behaviour was performed. If the polymer nanocomposites were suitable for commercialisation their thermal stability would determine which applications they were suitable for. During thermal degradation, the Garamite® was observed to have no affect on the thermogravimetric and energetic degradation of the bulk polymer matrix. Only the onset of energetic degradation was lowered, suggesting that the Garamite® encouraged degradation only when in direct contact with the polymer matrix. Calculation of the Arrhenius parameters with respect to the thermal degradation kinetics also suggested there was insignificant variation between the polymer and composites.

An investigation into the thermo-oxidative degradation behaviour illustrated that the most stable materials possessed a higher molar mass, which may be associated with a higher melt viscosity. A high melt viscosity would be expected to slow oxygen diffusion and therefore delay the degradation process. Samples which contained the Garamite® nanoclay were also observed to possess a higher maximum temperature of degradation which was suspected to be due to the further impedance of oxygen diffusion. It was noted at the highest Garamite® loading that the barrier effect was counteracted within the uniaxial film

samples (which possessed the lowest molar masses), suggesting the Garamite® accelerated the thermo-oxidative process. In addition stabilisation was observed through a delay in the energetic onset of degradation however there was no effect on the degradation of the bulk polymer matrix. This indicated that the degradation of the bulk polymer matrix was neither inhibited nor catalysed and only the physical transport of the oxygen and small organics was affected. These competing influences were also observed in the degradation kinetics.

Examination of the polymer and polymer nanocomposites through thermal volatilisation analysis also illustrated that the Garamite® impeded the transport of small organics through the molten polymer matrix, specifically the minor degradation products ethene and acetylene. Mass spectrometry allowed the qualitative identification of the standard degradation products of poly(ethylene terephthalate) which were carbon monoxide, carbon dioxide, acetaldehyde, water and benzaldehyde. It was noted that an increase in acetaldehyde production was observed during degradation. This was attributed to the catalytic effect of the amine and Brønsted acid sites formed during the degradation of the surface modifiers. Subsequent aminolysis or acid catalysed hydrolysis of the polymer backbone resulted in an excess of ethylene glycol which was able to participate in further transesterification reactions with vinyl benzoate moieties, creating acetaldehyde as a by-product.

In summary, the studies performed within this thesis provide insight into both the prerequisites for an *in situ* polymerisation process and also the impact of a modified sepiolite nanoclay on polymer properties. The studies have analysed the materials in order to determine behaviour during melt processing and predict stability in thermal applications. For completion the author would also have liked to incorporate mechanical, dynamic light scattering and x-ray scattering studies within this thesis, however due to time restraints this was not possible.